5-6-2019

Synthesis and Characterization of Fluorescent Silica Nanoparticles with Large Stokes Shifts for Multiplexed Assays and Imaging

Gala M. Chapman
Georgia State University

SYNTHESIS AND CHARACTERIZATION OF FLUORESCENT SILICA NANOPARTICLES WITH LARGE STOKES SHIFTS FOR MULTIPLEXED ASSAYS AND IMAGING

by

GALA CHAPMAN

Under the Direction of Gabor Patonay, Ph. D.

ABSTRACT

Modern approaches to biological and biomedical analysis demand ever-increasing levels of sensitivity, selectivity, and throughput. This challenge has been addressed in the work described herein via the synthesis, characterization, and proofs of concept of a series of single and multidye copolymerized fluorescent silica nanoparticles with large Stokes shifts and near infrared fluorescence. The prepared fluorescent probes exhibit substantially enhanced fluorescence signals relative to their constituent dyes, good indicators of biocompatibility, and readily distinguishable fluorescence signals, promoting the simultaneous detection of multiple targets and reducing both the cost and time per assay.

A novel NIR-fluorescent aminocyanine dye was designed for incorporation into silica nanoparticles, then synthesized and characterized as detailed in the second chapter. Spectroscopic characterization confirmed the intended dye structure and revealed a large Stokes

shift, near infrared fluorescence, and a relatively high quantum yield, indicating the suitability of this compound for bioanalytical applications and incorporation into silica nanoparticles as either a standalone fluorophore or as a resonance energy transfer acceptor for other UV-visible dyes.

In the third chapter, the incorporation of the novel dye and other commercial dyes into silica nanoparticles is discussed, along with characterization and proofs of concept for *in vivo* and *in vitro* applications of the resultant fluorescent labels. Nanoparticle synthetic approaches, dye concentrations, and surface coating densities were optimized for fluorescence intensities and biocompatibility. Nanoparticles containing single and multiple dye species were synthesized per the optimal parameters, producing a series of fluorescent tags with distinct fluorescence signatures and large Stokes shifts. Synthesized nanoparticles were characterized in terms of sizes, synthetic yields, quantum yields, limits of detection, stability, and synthetic reproducibility. The suitability of surface modified nanoparticles to *in vitro* and *in vivo* applications was demonstrated via biotin linkage to streptavidin microbeads and fluorescence microscopy imaging, hemocompatibility studies, and protein binding studies.

Finally, in the fourth chapter, resonance energy transfer characteristics of multidye copolymerized nanoparticles were characterized. Energy transfer efficiencies between donor-acceptor pairs, numbers of dye molecules per nanoparticle, and average distances between dye molecules were calculated, then Förster radii for different donor-acceptor pairs were estimated using two approaches and compared.

INDEX WORDS: Aminocyanine dyes, Fluorescent silica nanoparticles, Large Stokes shift, Resonance energy transfer, Biocompatible nanoparticles, Multiplexed assay, Intermolecular distance, Förster radius

SYNTHESIS AND CHARACTERIZATION OF FLUORESCENT SILICA NANOPARTICLES WITH LARGE STOKES SHIFTS FOR MULTIPLEXED ASSAYS AND IMAGING

by

GALA CHAPMAN

A Dissertation Submitted in Partial Fulfillment of the Requirements for the Degree of

Doctor of Philosophy

in the College of Arts and Sciences

Georgia State University

2019

SYNTHESIS AND CHARACTERIZATION OF FLUORESCENT SILICA NANOPARTICLES WITH LARGE STOKES SHIFTS FOR MULTIPLEXED ASSAYS AND IMAGING

by

GALA CHAPMAN

Committee Chair: Gabor Patonay

Committee: Gangli Wang

Zhen Huang

Electronic Version Approved:

Office of Graduate Studies

College of Arts and Sciences

Georgia State University

May 2019

DEDICATION

This dissertation is dedicated to Maksim Kvetny. Thank you for understanding me, making me laugh, listening to me, nerding out with me, making things, fixing things, and feeding me on a regular basis. I absolutely would not have been able to manage five plus years of simultaneous homeownership, full time work, and doctoral pursuit without your patience and support. You probably deserve some sort of medal, but I'm hoping I can skate by on these measly words for the time being. I love you.

ACKNOWLEDGEMENTS

I would like to express my profound gratitude to Dr. Gabor Patonay for his mentorship and encouragement through my years at Georgia State. Thank you for giving me ample space to cultivate my independence as a scientist, for challenging me to think critically about my work, and for countless wonderful conversations and laughs! I'd also like to thank you for allowing me the opportunity to begin a rewarding career at CDC early in my doctoral studies, despite the significant amounts of additional difficulty this has created for us both. On this note, I would also like to thank Dr. Giovanni Gadda for allowing me to take this unusual path and both Rita Sandra Bennett and Kedayne King for the substantial amount of extra help they have provided me in dealing with work/study logistics. On the subject of logistics, I'm very grateful to the Georgia State University Research Services & Administration for funding my Dissertation Grant proposal. This grant was of tremendous assistance in providing many of the starting materials I needed for this project.

I would also like to sincerely thank Dr. Gangli Wang and Dr. Zhen Huang for serving on my committee and helping me develop my project. I have so appreciated the opportunity to learn from both of you! Dr. Huang, I'd like to specifically thank you for sparking my ongoing fascination with the possible origins of life on Earth and for continuing to believe in me and take interest in my work. Dr. Wang, I'd like to thank you for allowing me to use your laboratory's microscope, for deepening my understanding of electrochemistry, and for all of the extra time, advisement, kindness, and moral support you have provided me throughout my doctorate.

On this note, I would also like to express my deep gratitude to Dr. Kathryn Grant, who has written numerous recommendation letters on my behalf, reviewed a manuscript for me, provided support to me when I've gone through difficulties, and advised me on matters of both

career and education. Thank you for being a teacher, a mentor, and above all such a tremendous friend and a bright light when things were the most difficult. Thank you for helping me land my job and improve my standing at work. Thank you for lifting me up and helping me get through this. I would never be where I am without you!

Similarly, I would never have been able to finish my doctorate without the tremendous support and understanding of my coworkers and supervisors at CDC. In particular, I would like to express deep gratitude to my present and past supervisors, Dr. Liza Valentin and Dr. Clifford Watson, for providing me with both the flexibility and space I needed to complete this work. Thank you both for understanding my unique position, for encouraging my studies, and for believing in me. I am also deeply indebted to my present and past team leads Dr. Megan McGuigan, Dr. Roberto Bravo, and Dr. Rayman Stanelle for their unequivocal support and for consistently pushing me to prioritize school and finish my degree. Rayman, you have my particularly deep gratitude for your service on my committee during our time together at CDC (especially given your multitude of other responsibilities), for your extremely generous offer of reviewing this tome despite the fact that those responsibilities have since multiplied, for your ongoing support, and for your repeated dire warnings of lifelong regret should I abandon the pursuit of my doctorate!

There are a number of individuals both at GSU and at CDC that I would also like to acknowledge for making contributions to this work. I would like to sincerely thank Dr. Robert Simmons for the many hours spent acquiring and providing all of the transmission electron microscopy images used in this work. Thank you dearly for accommodating me despite our funding challenges. I hope your retirement is joyful and filled with creative pursuits! I'd also like to extend my gratitude to Dr. Markus Germann for obtaining multiple NMR spectra of a

problematic sample on my behalf. Thank you for your wit and your generosity with your time! To Sharon Flores and Gyliann Peña: thank you both for providing me with friendship, laughs, encouragement, and red blood cell samples. To Stephanie Negrete, Dr. Jonas Perez, and Dr. Rudolph Johnson: this work would not have been possible without the use of your fluorometer. Your generosity and access to modern technology easily saved me hundreds of hours in combined travel and data processing. To Juliana Giraldo Junco: your wonderful sense of humor, delightful cooking, warm heart, and excellent work ethic allowed us to make miracles happen at CDC despite my split attention span and off-the-charts stress levels; thank you for being a partner in method development and a great friend.

I'm deeply indebted to so so many of my friends and coworkers at GSU and CDC for their moral support throughout this trying season of my life. I would like to express my gratitude to all of my peers within the Patonay lab. To Dr. Garfield Beckford: you're hilarious, a brilliant scientist, a wonderful father, and a superb human being. I cannot ever repay you for the tremendous support you provided me through my formative years as a scientist. Infinite thanks as well to my former Patonay lab co-conspirator and current coworker Erica Lewis. Your intelligence, work ethic, diversity of skills, and positive attitude are inspiring and formidable, and your friendship, kindness, support, patience, and sense of humor are absolute treasures. I'd be remiss if I didn't also acknowledge my other coworkers née Patonay lab students Amy Watson, Kristin Dortch, Phuong Ngac, and Peter Kuklenyik. Thank you all from the bottom of my heart for your support, for sharing your own experiences of working full-time through your graduate degrees, for showing me that it CAN be done, for your consistent offers of help, for checking up on me, and for pushing me to just finish already (Amy: seriously, thank you).

Last, but certainly not least, I would like to thank my family and close friends for their incredible patience with me through this marathon. I want to thank my father, Robb Chapman, for believing in me and nurturing my love for science, my late mother, Leslie Uhl, for loving me unconditionally and teaching me the value of stubbornness, my stepfather, John Hagler, for his attention to detail and his resolute and unwavering support, and my stepmother, Sarah Hosford, for her superhuman work ethic and organizational abilities. I want to thank my brothers Jesse Chapman and Will Chapman for keeping my spirits high with quality memes and my sister Lela Chapman for being a lifeline through my hardest struggles as well as the person on Earth who best understands me. I have such deep gratitude for my lifelong friends Emilia Pasalic, Aleta Christensen, Kasumi Kato, and Johnna Szegda. I'm overwhelmed at your infinite patience and the depth of your love, you ladies are turtles all the way on down the line. My deep appreciation also to Ross and Kelly Terrell for their top-notch anxiety-busting skills and for giving me nothing but support and opportunities for fun. Thank you all for loving me from afar, for continuing to invite me out, and for understanding when I haven't been able to make it. Someday I hope I can maybe be half as good a friend as each of you has been to me. Thank you all, a million times, from the bottom of my heart.

TABLE OF CONTENTS

ACKNOWLEDGEMENTS ..... **v**

TABLE OF CONTENTS ..... **ix**

LIST OF TABLES ..... **xiv**

LIST OF FIGURES ..... **xvi**

LIST OF ABBREVIATIONS ..... **xxi**

1 Introduction **1**

1.1 The Discovery of Fluorescence **1**

1.2 Modern Fluorescence Techniques in Bioanalytical Chemistry **2**

1.3 Fluorescent dyes **3**

1.3.1 UV-visible dyes ***3***

1.3.2 NIR dyes ***13***

1.3.3 Functionalization of dyes for solubility and bioconjugation ***20***

1.4 Particle-based fluorescent tags **22**

1.4.1 Noble metal nanoparticles and nanoclusters ***23***

1.4.2 Nanorods ***25***

1.4.3 Quantum dots ***26***

1.4.4 Organic polymer nanoparticles ***29***

1.4.5 Dendrimers ***31***

1.4.6 Micelles and vesicles *33*

1.4.7 Silica nanoparticles *35*

1.5 References **40**

2 Design, Synthesis, and Characterization of a Novel NIR Dye: **57**

2.1 Introduction **57**

2.1.1 Chemical interactions with light *57*

2.1.2 Molecular orbital theory *60*

2.1.3 Absorbance and molar absorptivity *63*

2.1.4 Fluorescence spectra and quantum yield *65*

2.1.5 Cyanine dye spectral characteristics *68*

2.1.6 Aminocyanine dyes *71*

2.1.7 Overview *74*

2.2 Experimental **76**

2.2.1 Reagents, materials, and instrumentation *76*

2.2.2 Synthesis of novel dye GC-1-23 ..... *77*

2.2.3 Spectroscopic characterization of novel dye GC-1-23 ..... *82*

2.3 Results and discussion **84**

2.3.1 Determination of molar absorptivity and quantum yield of GC-1-23 ..... *84*

2.3.2 Spectroscopic characterization and Stokes shift of GC-1-23 ..... *85*

2.3.3 Quantum yield of GC-1-23 ..... *88*

2.4 Conclusions 89

2.5 References 89

3 Silica Nanoparticle Synthesis and Characterization 94

3.1 Introduction 94

3.1.1 Importance of silica nanoparticles 94

3.1.2 Synthesis of silica nanoparticles 95

3.1.3 Surface modification of nanoparticles for biocompatibility and bioconjugation 98

3.1.4 Overview 101

3.2 Preliminary work 102

3.2.1 Introduction 102

3.2.2 Experimental 103

3.2.3 Results and Discussion 112

3.2.4 Conclusions 132

3.3 NIR-fluorescent multidye silica nanoparticles with large Stokes shifts for versatile biosensing applications 132

3.3.1 Abstract 133

3.3.2 Introduction 134

3.3.3 Experimental 136

3.3.4 Results and discussion 141

3.3.5 Conclusions *163*

3.4 References **164**

4 Resonance Energy Transfer Characteristics of Multidye-Doped Nanoparticles ...

.... 178

4.1 Introduction **178**

4.1.1 Förster resonance energy transfer *178*

4.1.2 Spectral overlap and the Förster distance *179*

4.1.3 Energy transfer efficiency *183*

4.1.4 Overview *184*

4.2 Experimental **185**

4.2.1 Determination of energy transfer efficiency *185*

4.2.2 Determination of number of dye molecules per NP *186*

4.2.3 Estimation of average distance between dye molecules *191*

4.2.4 Determination of Förster distance using spectral overlap *192*

4.2.5 Determination of Förster distance using energy transfer efficiency *192*

4.3 Results and discussion **193**

4.3.1 Determination of energy transfer efficiency *193*

4.3.2 Determination of number of dye molecules per NP *197*

4.3.3 Estimation of average distance between dye molecules *201*

4.3.4 Determination of Förster distances using spectral overlap *203*

4.3.5 Determination of Förster distance using energy transfer efficiency 205

4.4 Conclusions 208

4.5 References 210

APPENDICES 212

Appendix A – NMR and HRMS spectra 212

Appendix A.1 - ^{1}H NMR 212

Appendix A.2 - ^{13}C NMR 215

Appendix A.3 – HRMS 218

Appendix B – Supplementary information to Section 3.3 220

Appendix B.1 - Reproducibility of dye incorporation 220

Appendix B.2 – Dye leaching 220

Appendix B.3 – Quantum yield of NPs 221

Appendix B.4 – Fluorescence enhancement of dye copolymerized NPs 222

Appendix B.5 – Binding of BPNPs to streptavidin microspheres 222

Appendix B.6 – Hemolysis assay 223

Appendix B.7 – Protein adsorption study 224

LIST OF TABLES

Table 3.1: Mole percentages of dye-silane conjugates as a function of TEOS, synthetic approaches, and TEM radii for NP syntheses discussed in this section 123

Table 3.2.a: Optimization of total PEG-silane coverage (as specific surface area/SSA) by calculation of fluorescence intensity as a percentage of that of the maximum fluorescence intensity observed (%I_F^{MAX}) 125

Table 3.2.b: Optimization of percent Bio-PEG-Sil coverage by calculation of fluorescence intensity as a percentage of the maximum observed fluorescence intensity (%I_F^{MAX})……..…....125

Table 3.3: Theoretical mol% of each dye in various dye molar ratios used in this text 127

Table 3.4: Calculation of percentage of solvent-accessible dyes in dye-copolymerized NPs from relative fluorescence change in PB vs EtOH 128

Table 3.5: Synthesis yields and TEM radii for NPs with different dye combinations 150

Table 3.6: Quantum yields calculated for dye-silane conjugates and dye copolymerized NPs (n = 3) 153

Table 3.7: Calculated average LOD values for NPs and dye-silane conjugates (n = 3) and their ratios..... 157

Table 4.1: Quantum yields (ϕ, n = 3) of donor dyes in single and multidye NPs and corresponding FRET efficiencies (E) for these dye combinations 196

Table 4.2: Summary of molar absorptivity values calculated for dye-silane conjugates in nanoparticle synthesis solution at wavelengths of interest (n = 3) 198

Table 4.3: Calculated number of dyes per nanoparticle (N) for 1:1:1 nanoparticles and selected nanoparticles in the 1:1:2 series, and average number of dye molecules/NP (± standard deviation) across different sample syntheses 199

Table 4.4: Comparison of estimated and observed limits of detection for dye-copolymerized NPs 200

Table 4.5: Determination of average distance between all dye molecules in NPs (R) 201

Table 4.6: Determination of average distance between dyes of same species in NPs (R_X) 202

Table 4.7: R_0 values calculated from overlap integrals for hetero-FRET and homo-FRET in multidye-copolymerized NPs 203

Table 4.8: Determination of per-dye fluorescence intensities as a percentage of the maximum for individual dyes in multidye nanoparticles containing varying mole percentages (mol%) of dye relative to TEOS 205

Table 4.9: R_0 values calculated from intermolecular distances and energy transfer efficiency in multidye-copolymerized NPs 206

Table 4.10: Comparison of R_0 values calculated using different approaches 207

LIST OF FIGURES

Figure 1.1: Ionization equilibria of fluorescein: quantum yields and pKa values[15, 16] 5

Figure 1.2: General structures of xanthene dyes 7

Figure 1.3: Structures of (a) Rhodamine B, (b) Rhodamine 6G, and (c) Rhodamine 101 9

Figure 1.4: (a) Structures of phenanthridine dyes ethidium bromide and propidium iodide, (b) illustration of ethidium bromide intercalated into duplex DNA 10

Figure 1.5: Structures of (a) 4H-1,4-oxazine, (b) phenoxazine backbone, and representative structures of oxazine dyes (c) Nile Blue and (d) Nile Red 11

Figure 1.6: Basal structures of (a) porphyrins, (b) phthalocyanines, (c) naphthalocyanines 14

Figure 1.7: Basic structures of different cyanine dye classes: (a) streptocyanines, (b) hemicyanines, (c) closed-chain cyanines 15

Figure 1.8: Heterocyclic backbones and common derivatives used as termini in closed-chain cyanines: pyrroles (a-e), pyridines (f-g), imidazoles (h-i), oxazoles (j-k), and thiazoles (l-n) 17

Figure 1.9: Representative structures of equivalent (a) cyanine, (b) squaryllium and (c) croconium dyes 19

Figure 1.10: TEM image of gold nanorods illustrating approximate size and morphology[85] 26

Figure 1.11: Illustration of the quantum confinement effect in QDs with respect to size, bandgap separation, and emission color[89] 28

Figure 1.12: Sol-gel condensation of tetraethyl orthosilicate (TEOS) 35

Figure 2.1: A representative Jablonski diagram[1] 57

Figure 2.2: Relative energy levels of molecular orbitals and allowed electronic transitions 62

Figure 2.3: Relative HOMO and LUMO energy differentials (ΔE) for (a) ethene, (b) 1,3-butadiene, and (c) 1,3,5-hexatriene; ground state electronic configurations indicated 63

Figure 2.4: Effect of chosen excitation wavelengths (points A-E) on the emission spectra (corresponding spectra A-E); emission spectral intensity changes but the spectrum itself does not 67

Figure 2.5: Typical Jablonski diagram for a polymethine dye[11] 69

Figure 2.6: Dewar-Knott substitution positions for a heptamethine cyanine dye..... 70

Figure 2.7: Example of a chlorocyclohexenyl ring-stabilized heptamethine dye (IR-786 iodide)73

Figure 2.8: Structure of the designed NIR aminocyanine dye (GC-1-23)..... 75

Figure 2.9: Structure of bis-cyanine side product resulting from reaction of IR-786 with putrescine 82

Figure 2.10: Absorption at 629 nm as a function of concentration for GC-1-23 in methanol..... 85

Figure 2.11: Normalized absorption and fluorescence spectra of (a) parent dye IR-786 and (b) aminocyanine derivative GC-1-23, with labeled Stokes shifts..... 87

Figure 3.1: Representative nanoparticle synthetic approaches: (a) monophasic Stöber process; (b) biphasic reverse microemulsion process[12] 95

Figure 3.2: Examples of different approaches for dye incorporation into silica nanoparticles: (a) noncovalent incorporation of hydrophilic dye indocyanine green (ICG) via biphasic reverse microemulsion synthesis; (b) covalent incorporation of isothiocyanate-modified fluorescein (FITC) via formation of silane conjugate (FITC-APTES) followed by monophasic Stöber synthesis 97

Figure 3.3: Structures of (a) free biotin and (b) streptavidin bound to biotin[50] 100

Figure 3.4: Bioconjugation of antibodies (Ab) to NPs: (a) direct conjugation of Ab to surface; (b) direct binding of streptavidin to NP surface and conjugation using biotinylated Ab; (c) use of streptavidin as a "bridge" to link PEG-biotin bound NPs to biotinylated Ab[51] ... 101

Figure 3.5: Representative TEM image of reverse microemulsion NPs (scale bar: 1 μm) 114

Figure 3.6: Representative TEM image of Stober NPs prepared using uncontrolled addition of TEOS and a prehydrolysis time of 1 minute (scale bar: 200 nm)..... 116

Figure 3.7: Representative TEM image of Stöber NPs copolymerized with 5 μmol FITC-APTES prepared using controlled addition of TEOS (0.29 mL/h; 14.5 μmol/h; scale bar: 1 μm) 118

Figure 3.8: Representative TEM image of Stöber NPs copolymerized with 5 μmol GC-1-23-ICPTES prepared using controlled addition of TEOS (0.29 mL/h; 14.5 μmol/h; scale bar: 1 μm)..... 120

Figure 3.9: Representative TEM image of Stöber NPs copolymerized with 62.5 nmol FITC-APTES, 62.5 nmol TR-APTES, and 127 nmol GC-1-23-ICPTES; prepared using controlled addition of TEOS (0.29 mL/h; 14.5 μmol/h; scale bar: 500 nm) 122

Figure 3.10: Normalized fluorescence intensities (I_F) at wavelengths of maximum emission (λ_{EM}) for individual dyes in multidye nanoparticles containing varying mole percentages (mol%) of dye relative to TEOS 127

Figure 3.11: Comparison of dye spectra in solution to spectra in dye-copolymerized NPs: (a) fluorescein in 0.1 M NaOH vs. FITC-NPs in EtOH; (b) TR in EtOH vs. TR-NPs in EtOH; (c) GC-1-23 in EtOH vs GC-1-23-NPs in EtOH..... 131

Figure 3.12: Normalized absorption (solid) and fluorescence (dashed) spectra from single dye copolymerized NPs: (a) FITC-NPs (1:0:0 dye ratio), (b) TR-NPs (0:1:0 dye ratio), (c) GC-1-23-NPs (0:0:2 dye ratio) 144

Figure 3.13: Comparison of single- and multidye-copolymerized NP samples under (a) ambient lighting and (b) ultraviolet lighting (365 nm). Dye molar ratios (FITC:TR:GC-1-23) for these samples were: (I) 0:1:0, (II) 1:1:0, (III) 1:0:0, (IV) 1:0:2, (V) 0:0:2, (VI) 0:1:2, and (VII) 1:1:2 147

Figure 3.14: Fluorescence spectra for NPs copolymerized with FITC:TR:GC-1-23 in the ratios (a) 1:0:0, (b) 1:1:0, (c) 0:1:0 obtained using an excitation wavelength (λ_{EXC}) of 450 nm 148

Figure 3.15: Fluorescence spectra for NPs copolymerized with FITC:TR:GC-1-23 in the ratios (a) 1:0:2, (b) 1:1:2, (c) 0:1:2, (d) 0:0:2 obtained using an excitation wavelength (λ_{EXC}) of 450 nm 149

Figure 3.16: Representative TEM image of prepared NPs (scale bar: 200 nm) 151

Figure 3.17: Normalized absorption (solid) and emission (dashed) spectra for fluorescein species in different environments: (a) fluorescein standard in base solution, (b) FITC-APTES copolymerized NPs in EtOH (1:0:0), and (c) FITC-APTES conjugate in EtOH 156

Figure 3.18: Fluorescence microscopy images of streptavidin microbeads conjugated with BPNPs with FITC:TR:GC-1-23 dye ratios of (a) 1:0:0, (b) 1:1:0, (c) 1:0:2, (d) 1:1:2; corresponding images of blank streptavidin microbeads are provided in (e). For all samples, the excitation filter nominal wavelength was 470 nm and the emission filter nominal wavelengths were (f) 525 nm, (g) 607 nm, (h) 750 nm. Combined emission spectra overlaid on brightfield images are provided in column (i); scale bar: 10 μm 159

Figure 3.19: Absorption spectra of (a) IgG and (b) HSA solutions following incubation with bare 1:1:2 NPs, PEGylated 1:1:2 PNPs, and 1:1:2 BPNPs functionalized with both PEG and biotin 162

Figure 4.1: (a) Schematic illustration of resonance energy transfer between donor D and acceptor A; (b) Jablonski diagram of FRET; (c) adapted illustration of overlap integral (grey shaded area, J) between D fluorescence spectrum (blue, F_D) and A absorption spectrum (green, ε_A)^2 180

Figure 4.2: Variation of FRET efficiency (E) with radius (R) for a hypothetical donor-acceptor pair with a Förster radius (R_0) of 50 Å 183

Figure 4.3: Representative absorption spectra of dye-silane conjugates in NP synthesis solution 188

Figure 4.4: Spectral deconvolution of FITC dye absorption from nanoparticle scattering in 1:0:0 nanoparticles 194

Figure 4.5: Linear relationship between NP scattering and volume of NP solution added (in this case volume is proportional to NP concentration) 195

Figure 4.6: Graphical representation of calculated Förster radii (R_0) versus intermolecular distances between dye molecules (R) for donor-acceptor pairs, with included average R_0 values (horizontal lines) and energy transfer efficiencies (E) 206

LIST OF ABBREVIATIONS

APTES	(3-Aminopropyl)triethoxysilane
Bio-PEG-Sil	Biotin-polyethylene glycol-silane (molecular weight 3400)
BPNP	Nanoparticles with biotin-polyethylene glycol-silane and methoxypolyethylene glycol-silane surface modifiers
EtOH	Ethanol
FITC	Fluorescein isothiocyanate
FRET	Förster resonance energy transfer (also known as fluorescence resonance energy transfer)
GC-1-23	2-(2-[2-(1,4-Diaminobutyl)-3-(1,3-dihydro-1,3,3-trimethyl-2H-indol-2-ylidine]ethylidine)-1-cyclohexen-1-yl]ethenyl)-1,3,3-trimethylindolium iodide
ICPTES	3-(Triethoxysilyl)propyl isocyanate
ICT	Intramolecular charge transfer
mol %	Mole percent
MeOH	Methanol
mPEG-Sil	Methoxypolyethylene glycol-silane (mPEG-Sil, molecular weight 2000)
MW	Molecular weight
N_A	Avogadro's number (6.022×10^{23} mol^{-1})
NIR	Near-infrared
NMR	Nuclear magnetic resonance
NP	Nanoparticle
PB	Phosphate buffer (pH 7.4, 11.8 mM phosphate)
PEG	Polyethylene glycol

pI	Isoelectric point
PNP	Nanoparticles with methoxypolyethylene glycol-silane surface modifiers
r	Radius
R	Distance between dye molecules in nanoparticles
R_0	Förster distance or Förster radius (intermolecular distance at which energy transfer efficiency between dyes is 50%)
s	Standard deviation
SSA	Specific surface area (in m^2/g)
TEOS	Tetraethyl orthosilicate
TEM	Transmission electron microscopy
TR	Texas Red (sulforhodamine 101 acid chloride)
TEM	Transmission electron microscopy
$\bar{x}$	Average
ε	Molar absorptivity
ϕ	Quantum yield

1 INTRODUCTION

1.1 The Discovery of Fluorescence

In 1565, Nicolás Monardes published a book on New World medicines. Within this text, he detailed the medicinal properties of the Mexican Kidneywood tree, including a footnote about a strange bluish iridescence appearing in aqueous infusions of its wood.[1] This minor descriptive detail is thought to have been the very first written account of fluorescence. Continued observations of this puzzling optical phenomenon in various natural materials sparked the imagination of scientists in the centuries to follow.

In 1845, John Herschel observed the fluorescence of quinine sulfate, an important antimalarial medicine also extracted from the wood of a new world tree (Cinchona).[2] Seven years later, George Gabriel Stokes published *On the Change of Refrangibility of Light*. Within this publication, Stokes coined the term "fluorescence" to describe the light emitted by quinine upon illumination. Stokes repeated Herschel's observation using sunlight separated into its component spectrum by a prism, and made the observation that the blue fluorescence only occurred when the ultraviolet region of the spectrum was incident upon the sample.[3] He deduced from this that the emitted fluorescence occurs at a longer wavelength than that of the exciting light, a phenomenon that would later be called the Stokes shift in his honor. Years later, in his 1864 lecture "*On the Application of the Optical Properties of Bodies to the Detection and Discrimination of Organic Substances*," Stokes would also be the first to suggest that fluorescence could be useful as an analytical tool.[4]

1.2 Modern Fluorescence Techniques in Bioanalytical Chemistry

Today, fluorescence is the basis for many techniques in analytical chemistry and particularly within the subdiscipline of bioanalytical chemistry, where it finds a multitude of applications in DNA sequencing, microarrays, immunoassays, fiber optic biosensors, capillary electrophoresis-based biomolecule detection, and imaging of biological systems *in vivo* and *in vitro*, among others.[5-10] While radioisotopes were the original reporting groups used in applications such as immunoassays and DNA sequencing, these approaches suffered from a number of substantial disadvantages including short half-lives, the generation of radioactive waste, the need for specialized facilities, and the substantial health risks posed by radiation exposure.[11] Accordingly, it is unsurprising that as safe and reliable spectroscopic methods became available, they mostly replaced those approaches involving radioactive labels. The majority of modern reporter-based bioanalytical techniques rely on optical spectroscopy, making use of either absorption or fluorescence. While absorption-based assays are widespread and quite useful in many applications, fluorescence-based techniques boast the advantages of intrinsic high sensitivity and specificity.

The advantages of fluorescence over absorption come about in part because of the differences in measurement approaches. Fluorescence of a sample is measured directly against a dark background without a reference beam, whereas absorption is measured as a difference in the amount of light transmitted through a sample versus that passing through a reference. Because absorption measurements are relative and based on changes in light intensity for a bright reference beam, noise becomes an issue due to such variables as cuvette surface reflection and transmission. Fluorescence is more sensitive due to the dark background (promoting greater ease in signal deconvolution) and lack of confounding variability from reference measurements; there

is far less noise. Furthermore, fluorescence-based detection methods offer greater specificity than those reliant on absorption, as molecules that absorb light at similar wavelengths are abundant, whereas naturally-occurring fluorophores are less common. (REF: Lakowicz) The importance of these advantages to applications in complex biological matrices and *in vivo* imaging cannot be stressed enough.

Fluorescence-based bioanalytical techniques were historically based on the use of dyes as fluorescent labels. However, recent advances in technology have allowed for the use of fluorescent nanomaterials, including intrinsically fluorescent quantum dots, gold nanoparticles, and nanorods, as well as fluorescent dye-doped organic polymer nanoparticles, micelles, dendrimers, and silica nanoparticles. There are a number of advantages to using these novel materials in fluorescent tagging applications, including improved signal intensity, photostability, and robustness in challenging biological environments.[12]

1.3 Fluorescent dyes

1.3.1 UV-visible dyes

Dyes with absorption and fluorescence spectra in the UV-visible range were the first fluorophores applied in bioanalytical chemistry. Fluorescein was one of the very first synthetic fluorescent dyes, created in 1871 by Adolf van Baeyer.[13] Eleven years later, Paul Ehrlich applied this dye to determine the secretion pathway of aqueous humor in the eye in very first *in vivo* application of fluorescence.[13] In doing so, he both paved the way for the modern field of ophthalmic fluorescein angiography and helped initiate the long and fruitful relationship between fluorescence and bioanalytical chemistry. Fluorescein remains one of the most widely used

fluorescent dyes in bioanalytical applications, along with additional applications in search and rescue operations, groundwater tracing, and leak detection in underwater oil and gas pipelines.[14]

Fluorescein is a substituted xanthene with a pH-dependent green fluorescence. The fluorescence of the deprotonated dianion form is very intense ($\Phi_F = 0.93$) and that of the monoanion form is high ($\Phi_F = 0.37$), whereas in the neutral and protonated forms the compound is nonfluorescent ($\Phi_F = 0$).[15] An illustration of the different forms of fluorescein and the corresponding pK_a and quantum yield values is provided in Figure 1.1.

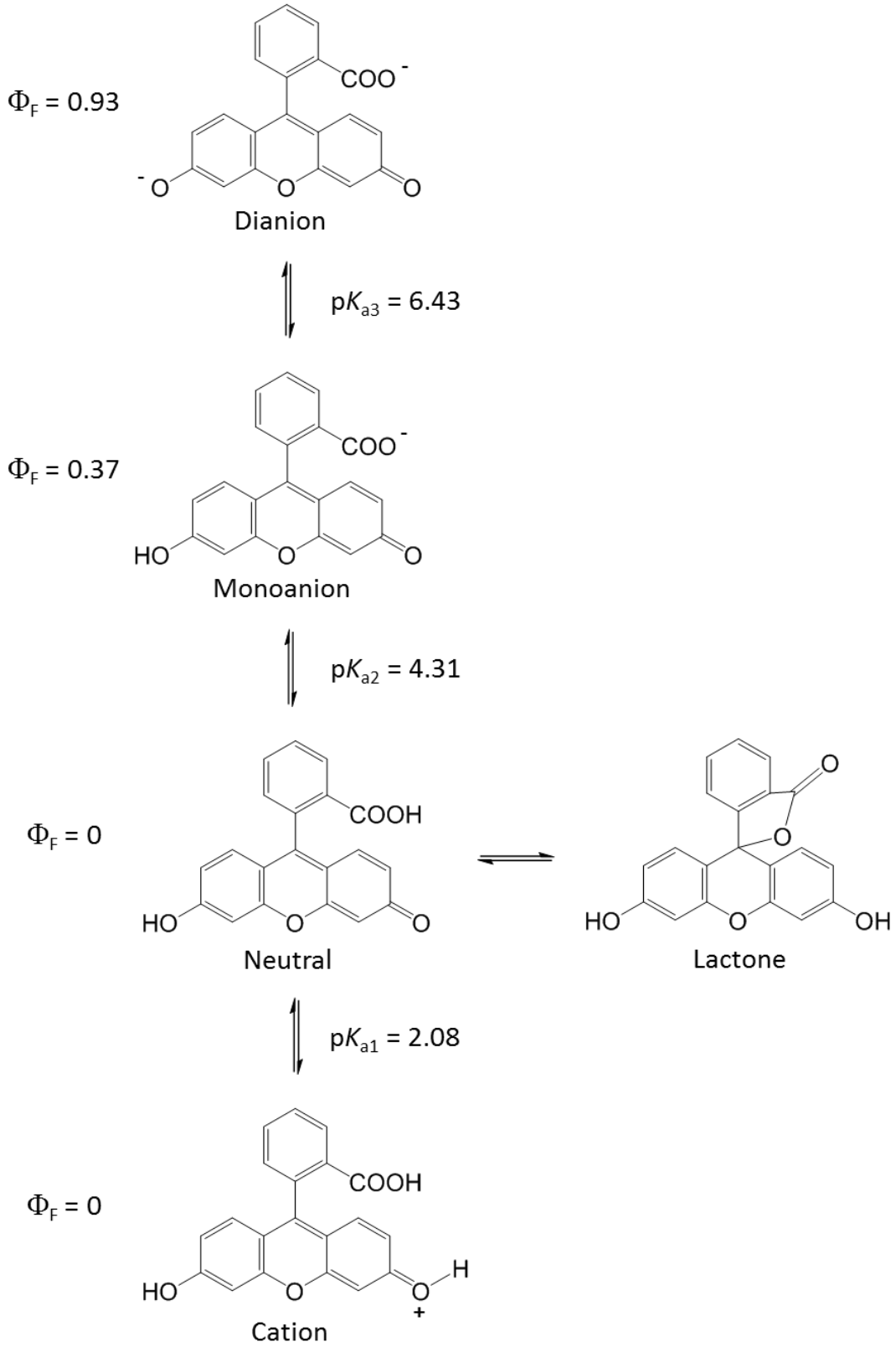

Figure 1.1: Ionization equilibria of fluorescein: quantum yields and pKa values[15, 16]

The predominant forms at physiological pH are the fluorescent monoanion and dianion forms (pK_a 6.43), making this a useful fluorescent probe for bioanalytical applications around pH 7.4. However, the pH dependence can be a drawback for certain uses, particularly those involving more acidic media. In response to this potential issue, several fluorinated analogs of fluorescein have been prepared, such as the dyes Oregon Green 488 and Oregon Green 514. Fluorination of the conjugated xanthene backbone substantially increases the acidity of fluorescein via strong inductive electron-withdrawing effects, lowering the pK_{a3} from 6.43 to 4.7.[17] This results in a high fluorescence intensity that is unaffected by pH in the physiological range and is still reasonably high even at more acidic pH values.

Several other important dye types are also based upon the xanthene backbone, including eosin, erythrosine, and the family of dyes known as rhodamines. Structures of the xanthene-based dyes are summarized in Figure 1.2.

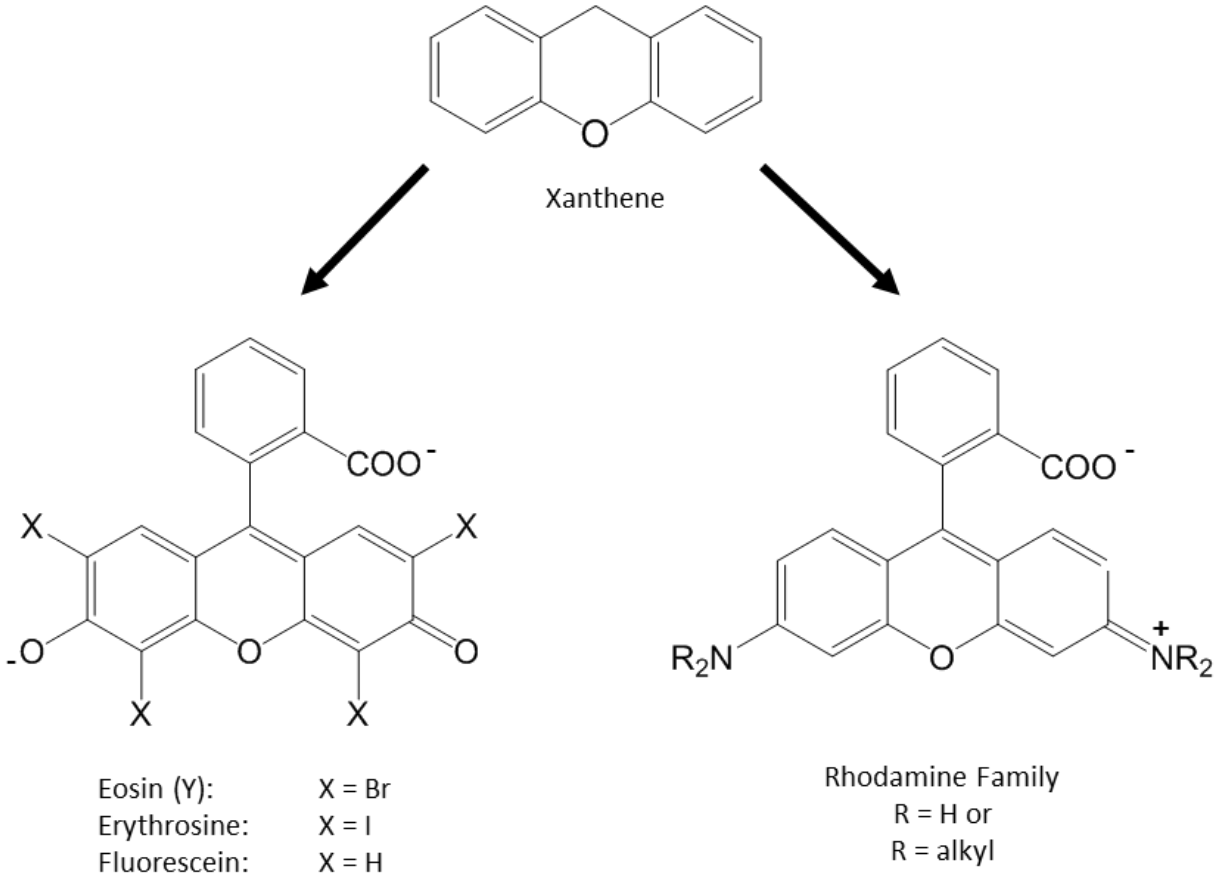

Figure 1.2: General structures of xanthene dyes

The most common bioanalytical applications of eosin and erythrosine are as staining agents in histology,[18-20] although both are also useful as phosphorescence probes and fluorescence quenchers.[21-24] On the other hand, rhodamines, like fluorescein, are applied in a wide variety of bioanalytical applications beyond cell staining, most commonly as fluorescent labels of biomolecules for use in immunoassays, nucleic acid microarrays, DNA sequencing, and other related applications.[25-30] Rhodamine fluorescence spectra are generally less pH-sensitive than those of fluorescein. However, for some rhodamine dyes, there is a potentially undesirable dependence of the quantum efficiency on both the solvent viscosity and the temperature. For rhodamines disubstituted with alkyl groups at the nitrogen atoms, (e.g. Rhodamine B, Figure

1.3a), this dependence of quantum yield on temperature and solvent is very strong.[31] This is thought to be due to nonradiative loss of the excitation energy as a result of N-alkyl group mobility; both increased temperature and decreased viscosity result in greater rates of internal conversion in this case.[32] For rhodamines monosubstituted with alkyl groups at the nitrogen atoms (e.g. Rhodamine 6G, Figure 1.3b), this dependence of quantum yield on solvent and temperature is substantially less pronounced, presumably due at least in part to the reduction in wobbly N-alkyl groups. The suboptimal fluorescence behavior of rhodamines due to temperature and solvent effects may be more fully addressed by rigidizing the amino and alkyl groups via cyclization, thereby incorporating them into a greater part of the xanthene heterocycle (e.g. Rhodamine 101, Figure 1.3c). For rigidized rhodamine structures, quantum yields are nearly perfect ($\Phi_F \approx 1$) and fluorescence intensities become nearly impervious to solvent and temperature effects.[31]

In general, most fluorescent dyes are poorly water soluble due to their structures. Dye chromophores tend to be large, heavily conjugated systems often involving polycyclic aromatic components. A major potential drawback of this hydrophobicity is that it tends to promote the formation of nonfluorescent aggregates in the aqueous solutions required for many bioanalytical applications. However, this property can also be valuable, and in fact, the principal applications for some classes of UV-visible fluorescent dyes rely specifically on their spectroscopic properties as pertaining to hydrophobicity. For example, phenanthridine dyes such as ethidium bromide and propidium iodide are used primarily as intercalating nucleic acid stains. These compounds possess hydrophobic polycyclic chromophores that stack and aggregate in aqueous solution, possessing low quantum efficiencies in this environment.[33] However, in the presence of DNA, these dyes will preferentially dissociate and intercalate in the interstitial space between

base pairs, as shown in Figure 1.4. When the aggregates dissociate and slide between the base pairs into the hydrophobic helix interior, the chromophore also becomes both conformationally restrained and protected from potential quenching effects of surrounding solvent molecules. The result of this is a blue shift in the excitation spectrum, a concomitant red shift in the emission profile (indicative of the conformational change), and a massive increase in the quantum yield. This substantial fluorescence enhancement enables the facile visualization of nucleic acids during agarose gel electrophoresis separations.[34] However, nucleic acid staining with phenanthridine dyes necessitates the use of UV transilluminators for visualization, which results in UV-induced damage to the DNA fragments if protective measures are not taken.[35]

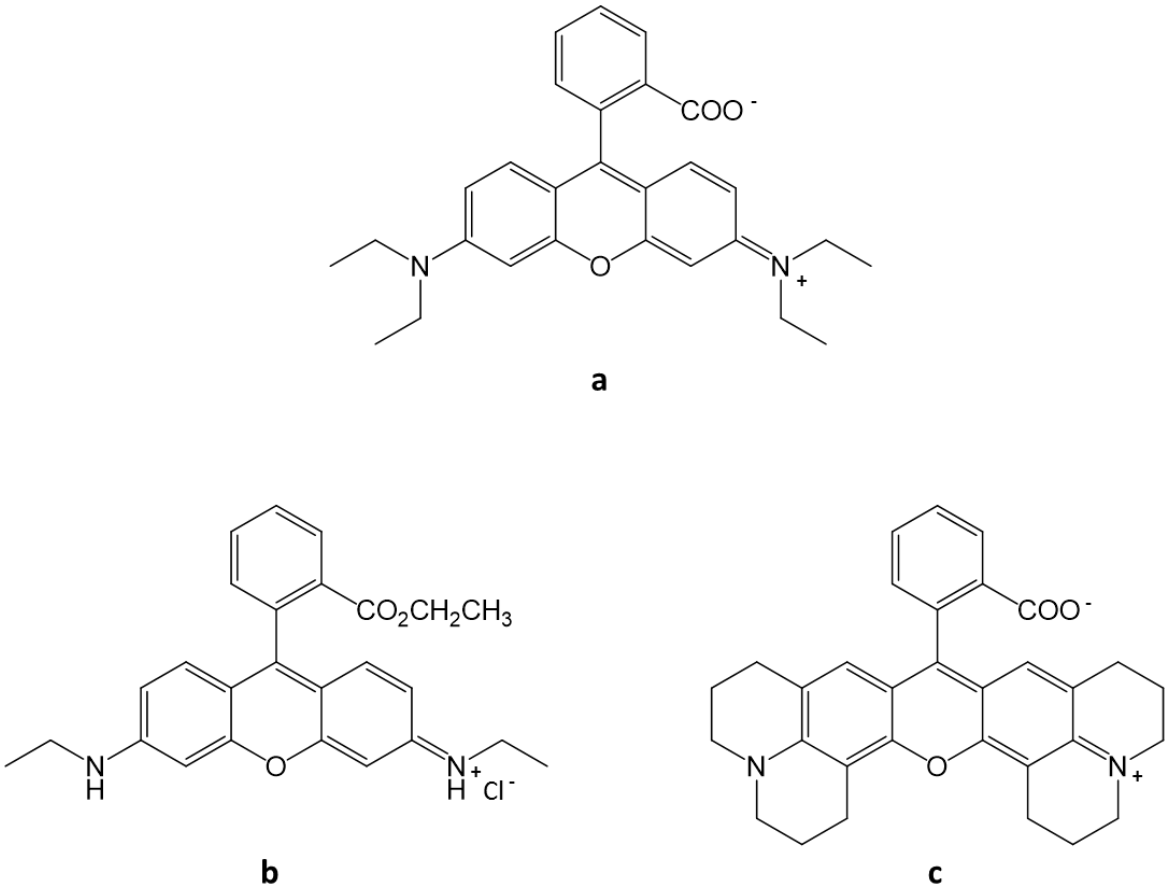

Figure 1.3: Structures of (a) Rhodamine B, (b) Rhodamine 6G, and (c) Rhodamine 101

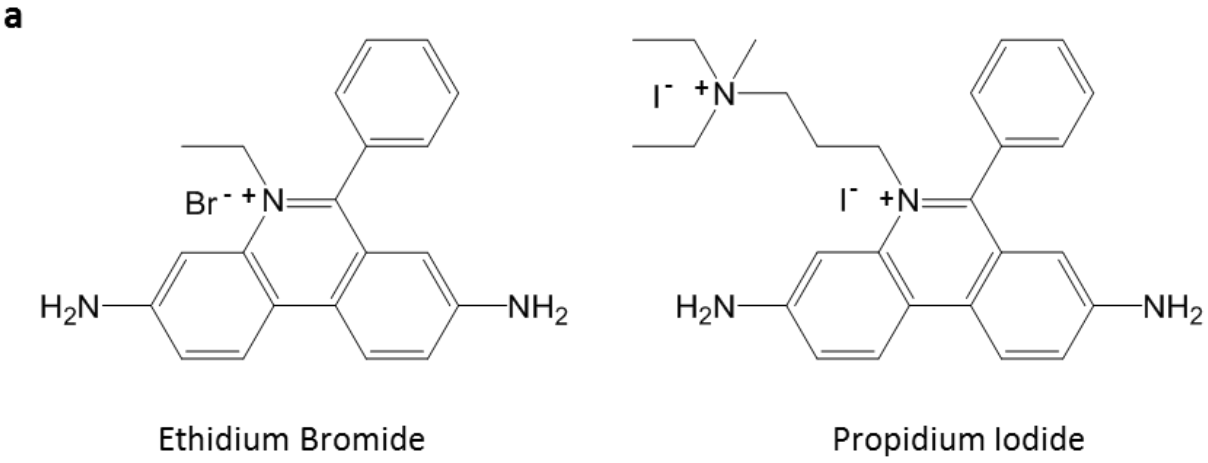

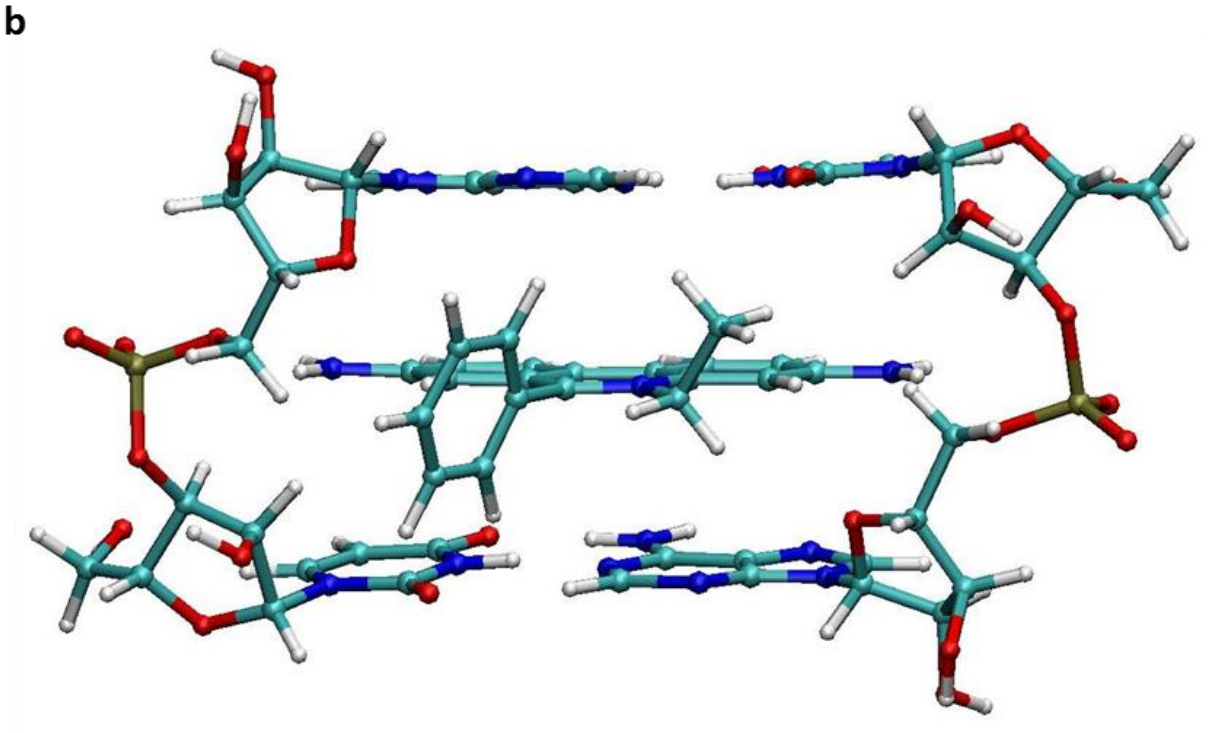

Figure 1.4: (a) Structures of phenanthridine dyes ethidium bromide and propidium iodide, (b) illustration of ethidium bromide intercalated into duplex DNA

The oxazine dyes are another class of UV-vis fluorophores used principally for their hydrophobic interactions. Oxazine dyes, like the xanthene dyes, are based on an anthracene backbone; however where the xanthene dyes have only oxygen incorporated as a heteroatom in the conjugated structure, the oxazine dyes possess both a nitrogen and an oxygen atom. The general structure of the oxazine center, phenoxazine backbone, and representative dye structures of oxazine dyes Nile Red and Nile Blue are provided in Figure 1.5.

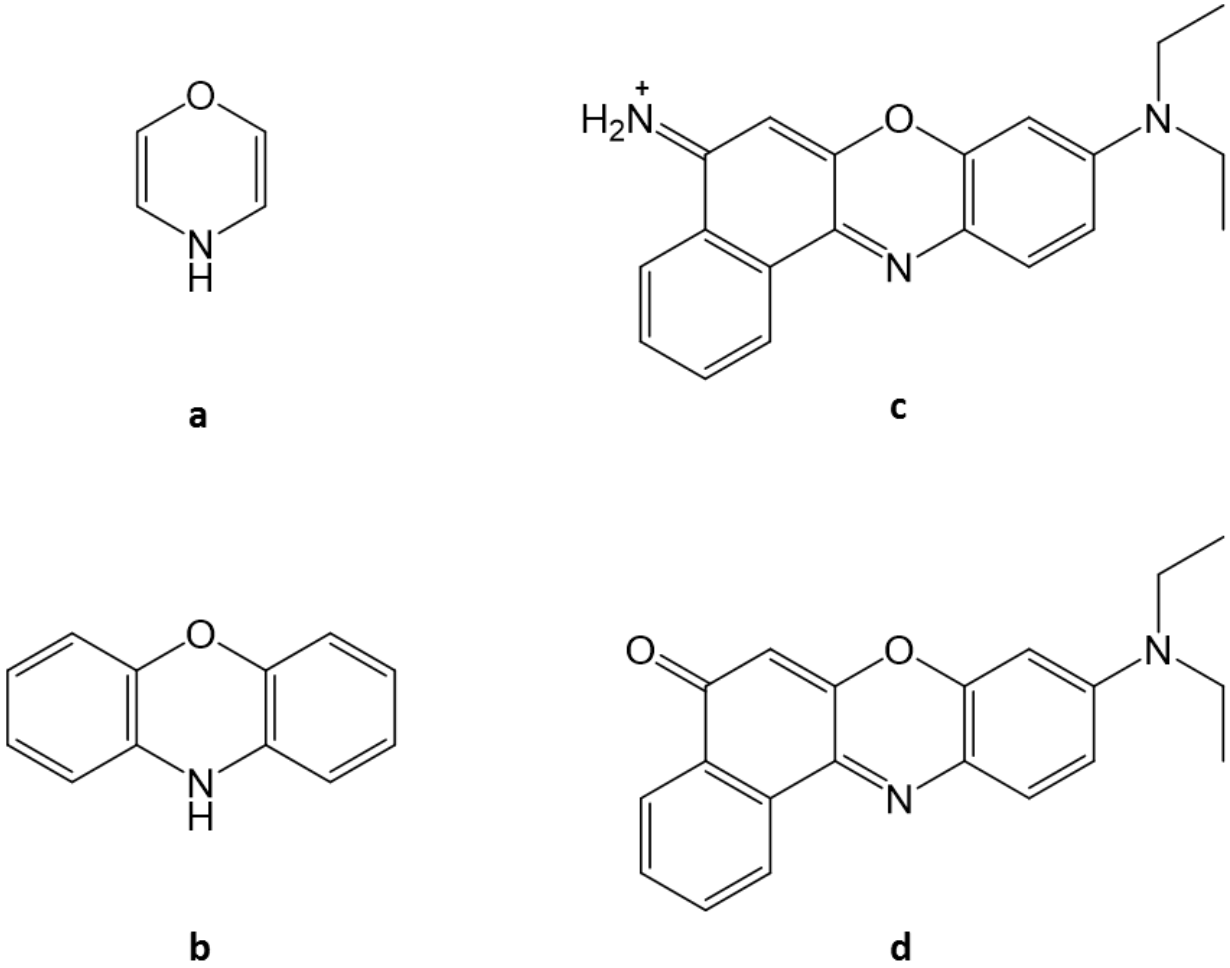

Figure 1.5: Structures of (a) 4H-1,4-oxazine, (b) phenoxazine backbone, and representative structures of oxazine dyes (c) Nile Blue and (d) Nile Red

The oxazine dyes Nile Red and Nile Blue exhibit a strong solvatochromism, with widely varying colors and fluorescence intensities. More specifically, in highly polar media (e.g. water), Nile Red and Nile Blue absorb and fluoresce at longer wavelengths and exhibit substantially lower fluorescence quantum yields. As the polarity of the media decreases, absorption and fluorescence wavelengths exhibit a hypsochromic (blue) shift and both dyes become substantially more fluorescent. The basis for the strong solvatochromism originates with the dyes undergoing an intramolecular charge transfer upon excitation, which results in a large change in dipole moment. The highly polar excited states of these molecules are better stabilized by polar solvents than nonpolar ones due to the preexisting solvent dipoles; solvent molecules readily reorganize around and stabilize the excited state, resulting in a red-shifted (lower energy) absorption wavelength.[36-38] The solvatochromism, polarity-dependent quantum yield, and hydrophobicity of these dyes makes them extremely useful in applications as lipophilic stains. Nile Red and Nile Blue are frequently used in lipid quantification and visualization, adipocyte staining, and cell membrane staining, with both *in vitro* and *in vivo* applications.[39-49] Nile Blue, like the phenanthridine dyes, also efficiently intercalates DNA and is accordingly used in both nucleic acid assays and in gel electrophoresis separations. Unlike the traditional phenanthridine dyes, Nile Blue requires no UV transillumination in its applications as a nucleic acid stain; this substantially reduces the chance of photodamage to DNA fragments.[35, 50] However, for both the phenanthridine and oxazine dyes, applications are mostly limited to those making direct use of their lipophilic natures.

1.3.2 NIR dyes

While materials absorbing and fluorescing in the ultraviolet to visible band of the electromagnetic spectrum have traditionally been the most heavily used in bioanalytical techniques, there has been a recent trend toward utilization of the near-infrared (NIR) region of the electromagnetic spectrum, which encompasses wavelengths from 700 to 1400 nm. Using reporter materials that absorb and fluoresce in the NIR is advantageous for many reasons, most notably the lack of interfering autofluorescence from biomolecules in this region, the greater transparency of tissues, and the reduced likelihood of radiative damage to tissues, biomolecules, or the fluorophores themselves due to the lower energy of longer-wavelength light.[51] Additional benefits of using the NIR region include decreased scattering noise at longer wavelengths and the increased availability of inexpensive, reasonably sized excitation light sources emitting in this range (in particular diode lasers and light emitting diodes) and detectors sensitive in this range (such as avalanche photodiodes).[52]

One class of NIR-fluorescent dyes are the macrocyclic phthalocyanines and naphthalocyanines. These compounds are similar to the ubiquitous and biologically-relevant porphyrins in terms of structure and behavior. The basal structures of phthalocyanine, naphthalocyanine, amd porphyrin are provided in Figure 1.6. Like porphyrins, the "free base" forms of both phthalocyanine and naphthalocyanine are ideally suited to complexation of electrophilic atoms, including many metals and some nonmetal atoms in compounds. Complexation with metal atoms modulates the spectroscopic behavior of these dyes. Naphthalocyanines generally exhibit longer wavelength absorption and fluorescence than phthalocyanines due to the additional benzene rings present along the exterior of the macrocycle. These dyes are commonly used as photosensitizers, with the potential for applications ranging

from solar cells to electrochromic devices to photodynamic therapy for cancer.[53-56] Both the phthalocyanines and naphthalocyanines are generally extremely hydrophobic, which limits their bioanalytical applicability. The (relative) few existing bioanalytical uses primarily hinge upon their binding to DNA.[57-59]

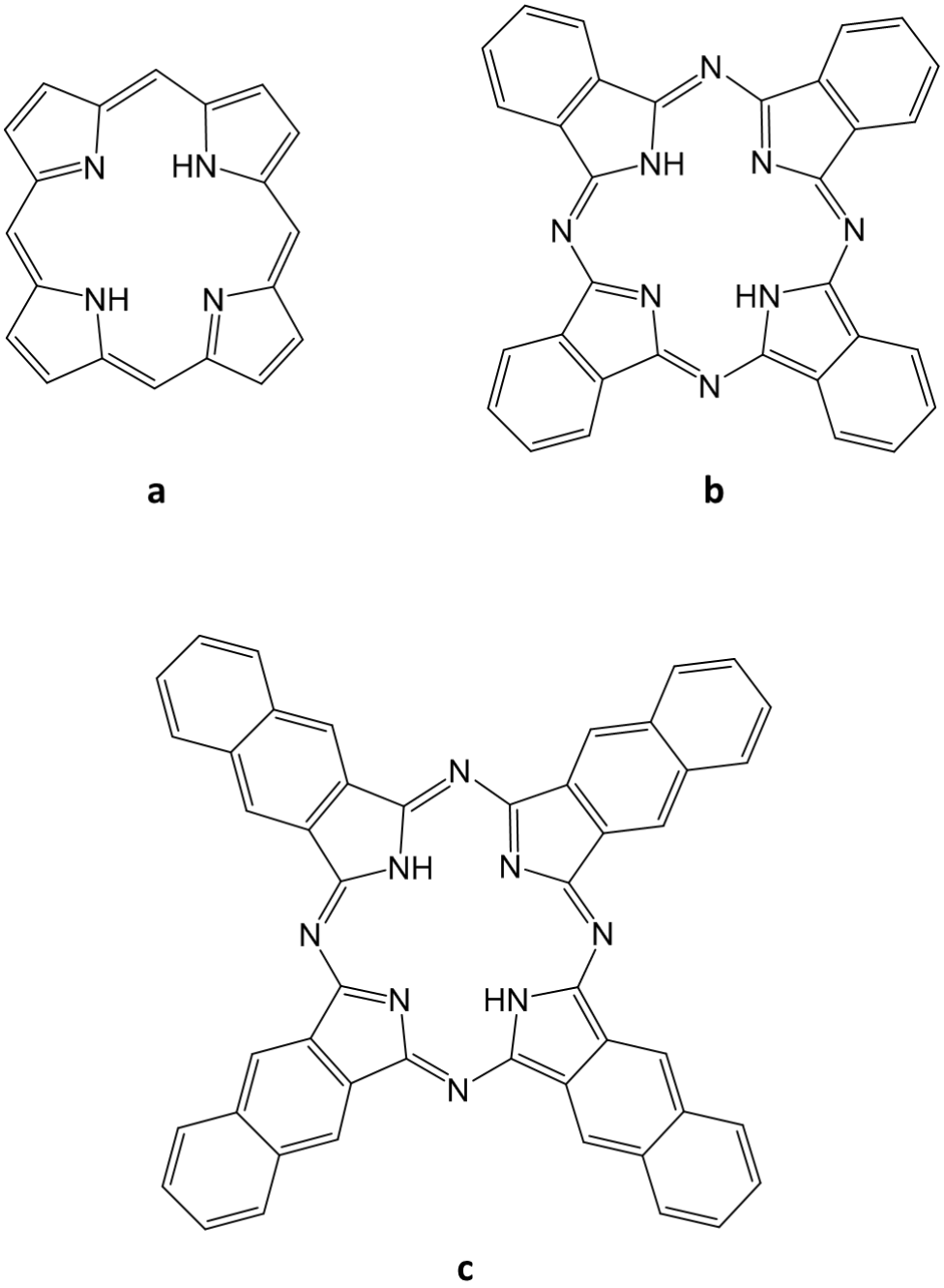

Figure 1.6: Basal structures of (a) porphyrins, (b) phthalocyanines, (c) naphthalocyanines

The other major class of dyes absorbing and fluorescing in the NIR region of the electromagnetic spectrum are based on the cyanine backbone. The general cyanine dye structure involves a tertiary amine and a quaternary amine moiety connected by a polymethine chromophore comprising an odd number of carbon atoms. The unusually long wavelength absorption and fluorescence of these dyes stems from the delocalization of the positive charge of the quaternary ammonium moiety across the entire polymethine chromophore. There are three general types of cyanine chromophore: streptocyanines, hemicyanines, and closed chain cyanines. Streptocyanines involve two alkyl amino terminal groups, hemicyanines involve one alkyl amine terminus and one aryl amine terminus, and closed-chain cyanines involve two aryl amine termini, as illustrated in Figure 1.7.

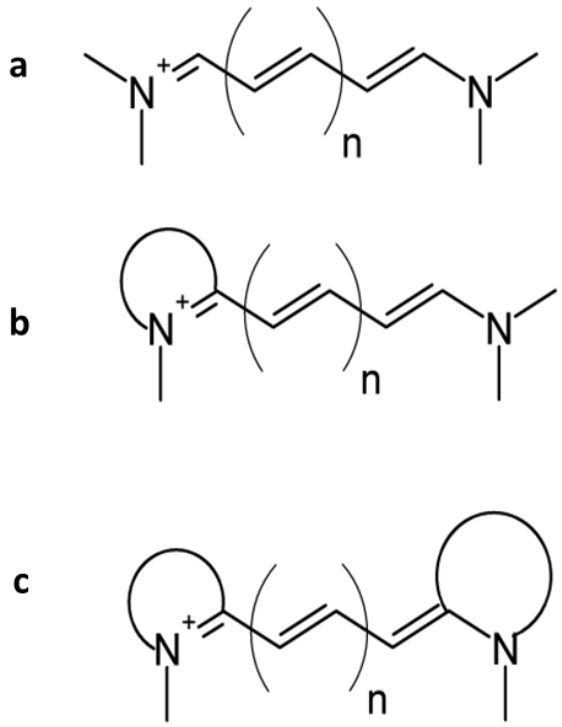

Figure 1.7: Basic structures of different cyanine dye classes: (a) streptocyanines, (b) hemicyanines, (c) closed-chain cyanines

Cyanine dyes are further classified by the number of repeating methine units in the chromophore; trimethine cyanine dyes (n = 1) possess a total of three carbon atoms, pentamethine cyanine dyes (n = 2) possess a total of five carbon atoms, and heptamethine cyanine dyes (n = 3) possess a total of seven carbon atoms in the polymethine bridge. For a series of otherwise identical cyanine dyes, each increase in n yields a red shift of approximately 100 nm to the absorption maximum. Cyanine dyes with a very wide range of absorption maxima stretching from the visible to the NIR may be synthesized by making simple changes to the chain length, substitution, and end groups.

Cyanine dyes may also be grouped by their terminal moieties. Closed-chain cyanine dyes utilizing a variety of different heterocycles have been synthesized, many of which are based on the six-membered pyridine backbone or the five-membered pyrrole, oxazole, and thiazole backbones.[60-63] Structures of some of the common heterocycles and heterocycle backbones found in cyanine dyes are provided in Figure 1.8.

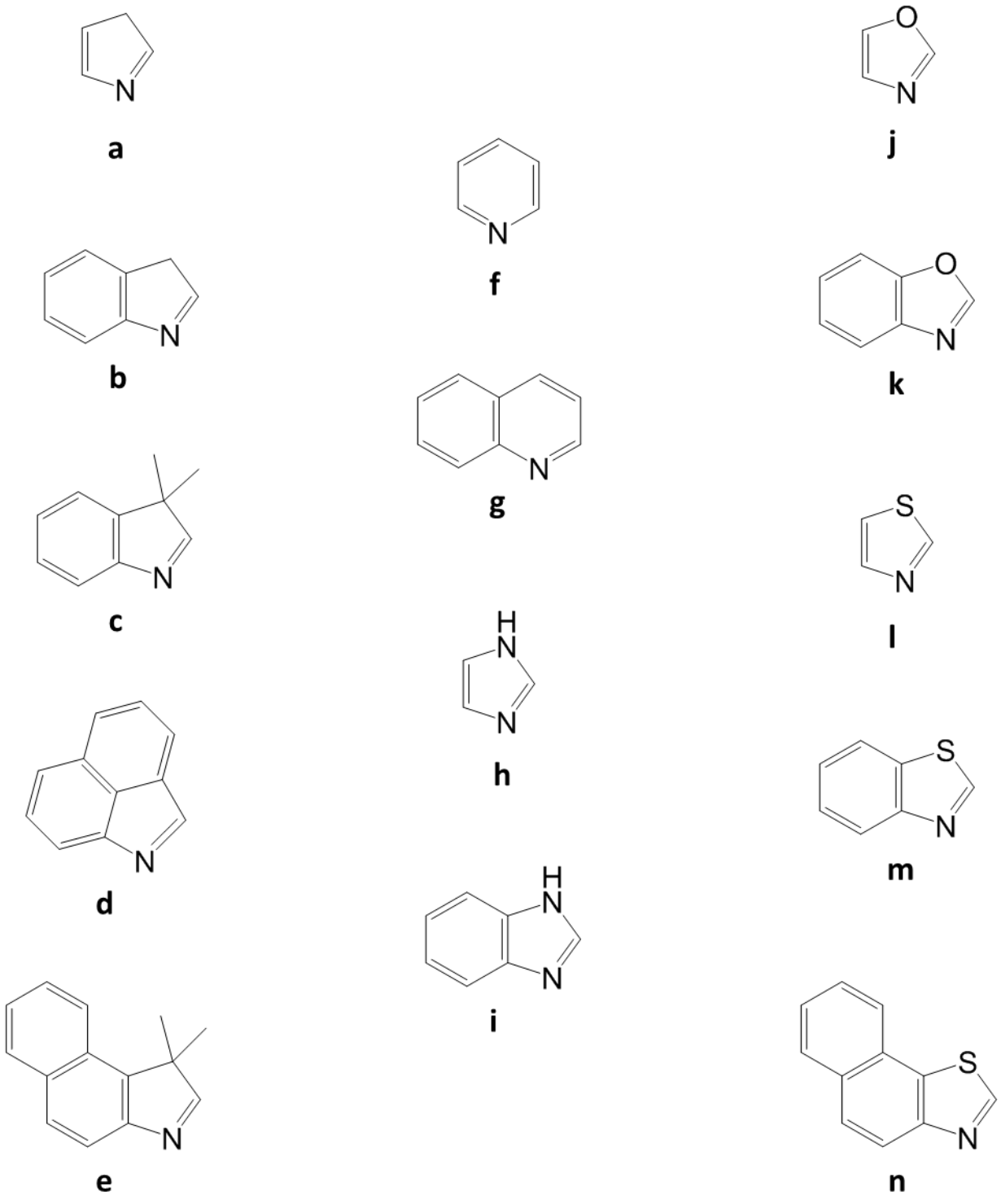

Figure 1.8: Heterocyclic backbones and common derivatives used as termini in closed-chain cyanines: pyrroles (a-e), pyridines (f-g), imidazoles (h-i), oxazoles (j-k), and thiazoles (l-n)

In 1856, Greville Williams distilled the alkaloid extracts of Cinchona with caustic alkali and treated the products with silver oxide; the result was a beautiful reddish-blue dye, which he called "cyanine" for its color. Early on, this dye and others found applications as spectral sensitizing agents in photographic emulsions, which in turn promoted greater scientific interest in the synthesis and characterization of a variety of related dyes. By 1910, hundreds of different related dyes had been synthesized, providing sensitivity throughout the entire visible spectrum.[64] Since their first applications in photographic emulsions, cyanine dyes have found many additional uses in lasing media, dye-sensitized solar cells, and coatings for optical recording media such as CDs and DVDs, among others. There are a tremendous number of bioanalytical uses for cyanine dyes as well, with frequent applications as fluorescent tags in flow cytometry and in ELISA, microarray-based, chromatography-based, and capillary electrophoresis-based assays for DNA, RNA, proteins, viruses, and single-celled organisms. There are also *in-vivo* applications of cyanine dyes for imaging organs and tumors in small animals. Indocyanine green, a heptamethine cyanine dye, has even been approved for fluorescence angiography in humans; the only other dyes approved to date by the FDA for human *in vivo* use are fluorescein and methylene blue.[13, 65] Still other cyanine dyes show promise as photosensitizers for use in photodynamic therapy for cancer.[66] The wide array of applications for these compounds is attributable in large part to the facile introduction of different functional groups to various positions along the cyanine backbone.

Two other cyanine-like dye classes are the squaryllium and croconium dyes. These dyes are structurally similar to cyanine dyes, and are frequently functionalized with similar heterocycilic termini. Unlike the cyanine dyes, squaryllium and croconium dyes possess a carbon ring functionalized with oxygen atoms at their chromophoric centers. Squaryllium dyes are

derived from squaric acid, possessing a four-membered carbon ring and two oxygen atoms, whereas croconium dyes (derived from croconic acid) possess a five-membered carbon ring and three oxygen atoms. Cyclization along the chromophore in cyanine-type dyes has the effect of increasing the photostability of the compound, and the introduction of electron-withdrawing carbonyl groups into these positions on the chromophore also has the effect of increasing the absorption wavelength. An illustration of the structures of cyanine, squaryllium, and croconium dyes are provided in Figure 1.9.

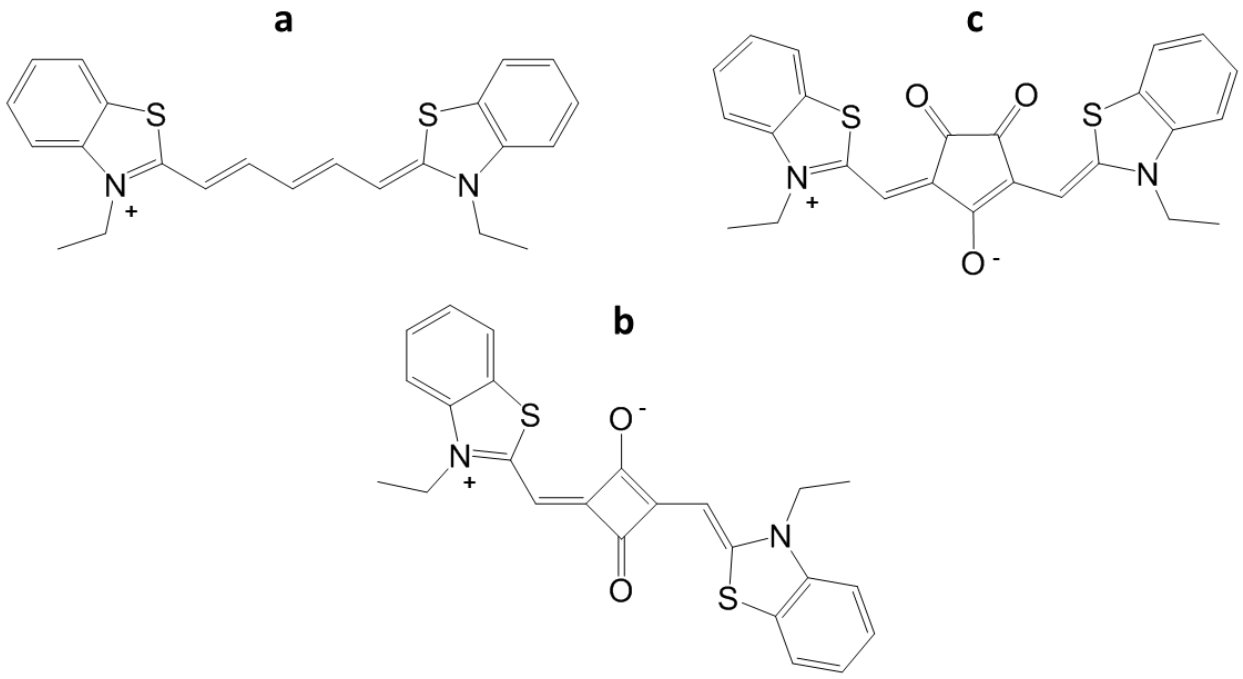

Figure 1.9: Representative structures of equivalent (a) cyanine, (b) squaryllium and (c) croconium dyes

Squaryllium dyes typically exhibit high quantum yields and good photostability; both of these characteristics make them attractive for a multitude of applications. These compounds are particularly well-suited for use in electronic and photonic devices, including optical recording

media, photodetectors, and solar cells. Squaryllium dyes have also been used in bioanalysis in much the same manner as cyanine dyes, with frequent applications as noncovalent fluorescent tags for biomolecules, viruses, and single celled organisms.[67-69] Unfortunately, the unique structure of these compounds imparts a substantial limitation to their applications in some biological media, as the electron-withdrawing oxygen substituents leave the cyclobutene core of the chromophore extremely susceptible to nucleophilic attack. One way around this is to incorporate squaryllium dyes into a rotaxane structure. Rotaxanes are dumbbell-shaped mechanically interlocked molecular architectures in which a long, thin molecule with two large ends sits in the center of a macrocycle. The inner diameter of the macrocycle is typically smaller than that of the two ends of the long molecule in order to prevent the dissociation of the complex. In squaraine rotaxanes, the electron-deficient cyclobutene ring is effectively protected by the macrocycle, resulting in greater chemical stability, photostability, and biological applicability.[70]

1.3.3 Functionalization of dyes for solubility and bioconjugation

Basal NIR dyes of all types suffer the same aqueous solubility issues discussed previously for the UV-vis dyes, namely the formation of nonfluorescent aggregates in aqueous solution. As with the UV-vis dyes and particularly the oxazine and phenanthridine dyes, there are applications for NIR dyes that capitalize on this aggregation behavior. Specifically, cyanine, squaraine, phthalocyanine, and naphthalocyanine dyes are frequently applied as probes in noncovalent binding interactions with hydrophobic portions of biomolecules, in which the substantial fluorescence enhancement upon binding is used as the basis for differentiating the biomolecular signal from the background. Despite the great utility of this characteristic in these

types of applications, it is also a significant limitation in cases where the target lacks suitable hydrophobic regions or in cases where a covalent labeling linkage with a surface region of a biomolecular target is desired instead.

Fortunately, the hydrophobicity issue can be circumvented through substitution with hydrophilic or charged groups. Common solubility promoters include uncharged hydrophilic substituents such as polyethylene glycol, substituents possessing charges at physiological pH such as amino and carboxylate groups, and substituents possessing pH-independent charges such as quaternary ammonium and sulfonate groups. The advantages conferred by hydrophilic substitution of fluorescent dye tags are the basis for the success and popularity of the "Alexa Fluor" dye family made by Invitrogen. These dyes are produced through sulfonation of existing UV-visible and NIR dye classes, including many xanthene, rhodamine, and cyanine dyes. In particular, substitution with polyethylene glycol, sulfonates, or quaternary ammonium salts can significantly reduce or eliminate the pH dependence of fluorescence for many dye structures, yielding a reliably bright label under many different conditions. Additionally, it has been shown that substitution with sulfonate groups can improve photostability in many cases.[71] Substitution of dyes with pH-independent charged groups can also be used to furnish hydrophilic zwitterionic (zero net charge) dyes, which have been shown to demonstrate reduced nonspecific binding and improved clearance *in vivo* for applications as imaging and contrast agents.[72, 73]

In order for dyes to be useful as covalent fluorescent tags, dye structures must be further functionalized with appropriate reactive substituents. To this end, many UV-visible and NIR dyes are now commercially available with *N*-hydroxysuccinimide ester, isothiocyanate, isocyanate sulfonyl chloride, halide, maleimide, and azide moieties for facile conjugation to

various native and modified biochemical functionalities (e.g. native amino groups, carboxyl groups, thiols, and alcohols, and biochemical-derived aldehydes and alkynes).

1.4 Particle-based fluorescent tags

Fluorescence-based bioanalytical assays have historically relied on fluorescent dyes as reporters. However, there are a few disadvantages to this approach. Many fluorescent dyes suffer from poor photostability, poor hydrolytic stability, nonspecific binding, a tendency toward nonfluorescent aggregation, and vastly different optical properties in biological media when compared to buffer, resulting in reduced sensitivity and robustness of methods relying on the incorporation or application of individual dye molecules. Additionally, fluorescence assays are often limited to one or a few dye molecule tags incorporated per biomolecule target, which potentially limits the sensitivity of methods reliant on this approach. Finally, many fluorescent dyes are toxic, which limits their *in vivo* applications. It is for these reasons that recent trends in fluorescent labeling technologies have been moving towards particle-based fluorescent tags. Some of the major classes of particles useful for bioanalytical fluorescence applications are noble metal nanoparticles, nanorods, quantum dots (QDs), organic polymer nanoparticles, dendrimers, micelles and vesicles, and silica nanoparticles (SiNPs).[74] Particle-based fluorescent tags may either exhibit intrinsic fluorescence resulting from the structural matrix (as in the case of noble metal nanoparticles, nanorods, and QDs) or they may serve as vessels encapsulating fluorescent dye molecules (as in the case of organic polymer nanoparticles, dendrimers, micelles and vesicles, and silica nanoparticles).

1.4.1 Noble metal nanoparticles and nanoclusters

A variety of different fluorescent metal nanoparticles have been synthesized, most of which are based on intrinsically fluorescent noble metal cores coated with a surface layer of organic ligands. The most common materials for core synthesis are gold and silver, and ligands are typically alkanethiols or arenethiols. For metal nanoparticles, size is inversely correlated with fluorescence yield, and recent studies have demonstrated that the observed fluorescence primarily originates from the mixed electronic states at the inorganic-organic interface, with metal core fluorescence playing a substantially smaller role.[75, 76] Advances in synthetic methods have allowed for the synthesis of even smaller metal particles, comprised of several atoms to tens of atoms of the core metal (stabilized with ligand). These small nanoparticles, known as nanoclusters, possess an upper size limit of approximately two nanometers. Due to their small size, nanoclusters do not display plasmonic behavior, instead possessing more discrete energy levels than the bands exhibited by larger nanoparticles; thus it can be said that nanocluster behavior straddles the line between atomic behavior and nanoparticle behavior. As expected given their small size, nanoclusters are more fluorescent than their larger counterparts, with quantum yields up to around 15% reported in the literature.[76]

There is a recent uptick of scientific interest in mixed-metal nanoparticles, specifically core-shell nanoparticles, in which the particle is made of distinct layers of two (or more) metals. Core-shell nanoparticles can be advantageous over single-metal nanoparticles in several regards. For example, the use of an appropriate outer shell can improve stability in difficult matrices, facilitate bioconjugation, and reduce expense if a less expensive core "carrier" is used. Additionally, due to the distinct plasmonic properties of different metals, core-shell combinations of varying thicknesses within a single nanoparticle can improve the tunability of

the optical properties. Alternatively, synthesis of core-shell nanoparticles with metal cores and nonmetal shell coatings such as organic polymers or silica can reduce toxicity and improve the biocompatibility of nanoparticles for *in vivo* applications.[77, 78]

The benefits of using noble metal nanoparticles and nanoclusters in bioanalytical applications include their large Stokes shifts and their visible to NIR fluorescence, which enables ready differentiation of fluorescence signals from the excitation light and bypasses the wavelengths at which interfering biological fluorescence may be observed.[79] These materials can be directly functionalized with nucleic acids and proteins for use as fluorescent reporters in biomolecular assays. Additionally, gold nanoparticles in particular have shown promise in some *in vivo* applications, particularly as theranostic agents in photodynamic cancer therapy, enabling concomitant fluorescent imaging and destruction of cancer cells.[80]

Noble metal nanoparticles and nanoclusters are also electrochemically active and may be utilized in electrochemical bioanalytical assays. For example, Hamidi-Asl et al. used silver-core gold-shell nanoparticles as aptasensors for *Escherichia coli* bacteria. The group modified these core-shell nanoparticles with aptamers specific to *E. coli*, then used the modified nanoparticles as an electrode coating in order to develop an electrochemical assay for the bacterial strain. Use of gold as the outer shell was found to facilitate aptamer bioconjugation and improve the stability of the constructed nanoparticles. Furthermore, the use of these nanoparticle-coated electrodes was found to improve the sensitivity fourfold relative to the use of planar gold electrode surfaces coated with the same aptamer.[78]

1.4.2 Nanorods

Nanorods are a unique morphology of inorganic particles. Unlike many other classes of nanoparticles, which are roughly spherical or spheroid, nanorods are longer in one dimension (Figure 1.10). These particles are typically generated from intrinsically fluorescent metals or semiconductors via specialty synthetic techniques. Nanorods have a few unique applications stemming from their morphology, specifically in nanoscale electronic and photonic devices and in anisotropic optical materials such as "stretchable" holograms.[81-83] Gold nanorods also share some characteristics of gold nanoparticles, with possible applications as theranostic agents for use in simultaneous *in vivo* fluorescence imaging and photodynamic treatment of cancer.[84, 85] Zinc oxide nanorods possess some bioanalytical utility as well, with applications as photoluminescent or fluorescence-enhancing scaffolds for recognition groups.[86, 87]

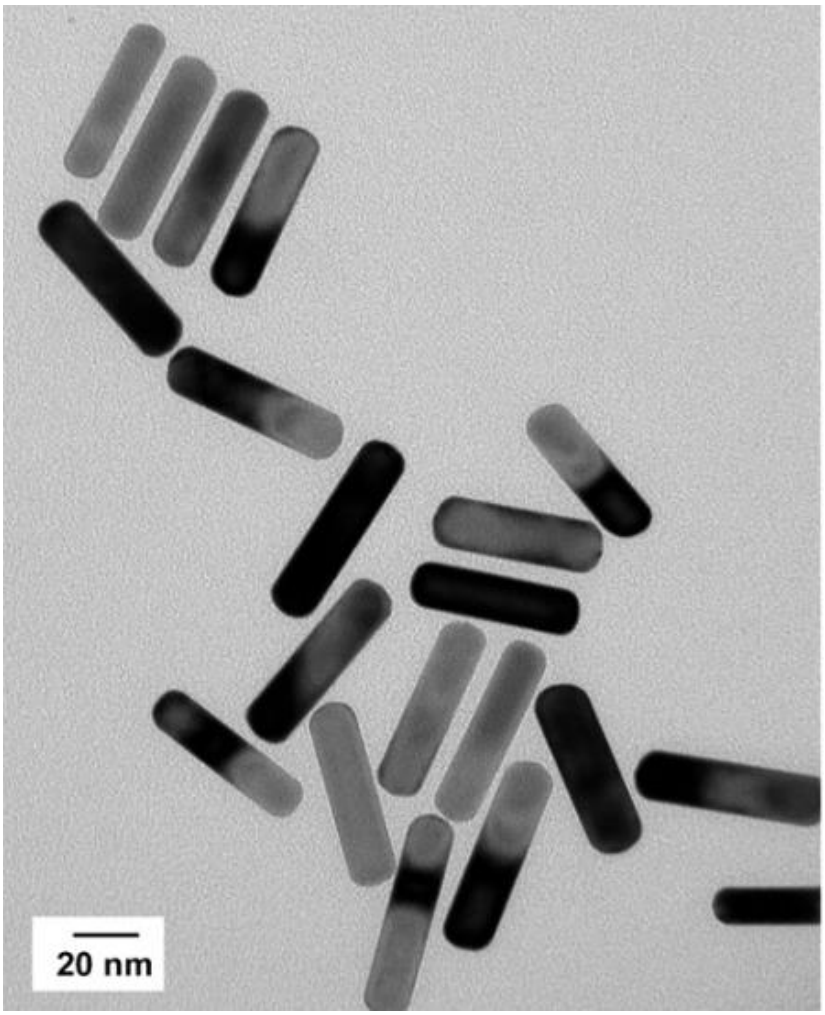

Figure 1.10: TEM image of gold nanorods illustrating approximate size and morphology[85]

1.4.3 Quantum dots

Quantum dots (QDs) are extremely small (2-6 nm) particles made of semiconducting materials, with unusual optoelectronic properties. Like the noble metal nanoclusters described previously, the electronic structure of these intrinsically fluorescent nanocrystals straddles the line between that of atoms and that of larger nanoparticles; due to the discrete electronic transitions exhibited by these materials, they have sometimes been referred to as “artificial

atoms." The spectroscopic characteristics of QDs are dependent on their shape and their size, with larger QDs absorbing and emitting at longer wavelengths than smaller ones.[88] This property is due to the quantum confinement effect, in which the nanocrystal size dictates the spatial confinement of the electrons and holes in the semiconductor material following photoexcitation; the larger the dot, the less confined the charge carriers, the smaller the bandgap, the lower the energy, and the longer the wavelength of absorption and emission.[89] This relationship is illustrated in Figure 1.11.

Quantum dots exhibit good photostability and chemical resistance as well as narrow, symmetric emission spectra which may be tuned from the UV to the NIR. These properties make QDs attractive for bioimaging purposes. Quantum dots are typically binary mixtures of cadmium, indium, lead, mercury, or zinc with sulfur, selenium, or tellurium, although core-shell structures containing layers of different components are common as well. For bioanalytical applications, zinc sulfide shells are frequently applied to cores composed of other mixtures (e.g. CdSe). The ZnS layer serves to enhance the quantum yield, prevent oxidation, passivate the surface, and reduce leaching of the substantially more toxic core constituents into the surrounding biological media.[90] QDs have demonstrated their utility in DNA sequencing, cell labeling, and in a number of *in vitro* assays for various types of biomolecules.[90, 91] Larger, long wavelength-emitting QDs are also particularly attractive for *in vivo* deep tissue imaging. However, the larger NIR-emitting QDs tend to have low quantum yields, leading to low signals and poor sensitivity.[92] Additionally, when QDs are used *in vivo*, leaching of the toxic, teratogenic core components is not entirely precluded under all conditions, even with relatively thick layers of ZnS, and furthermore, mechanisms of excretion are unknown and most likely limited.[90] In one

study, persistent fluorescence was observed in mice injected with quantum dots two years prior.[93] Accordingly, *in vivo* applications of these nanostructures remain problematic.

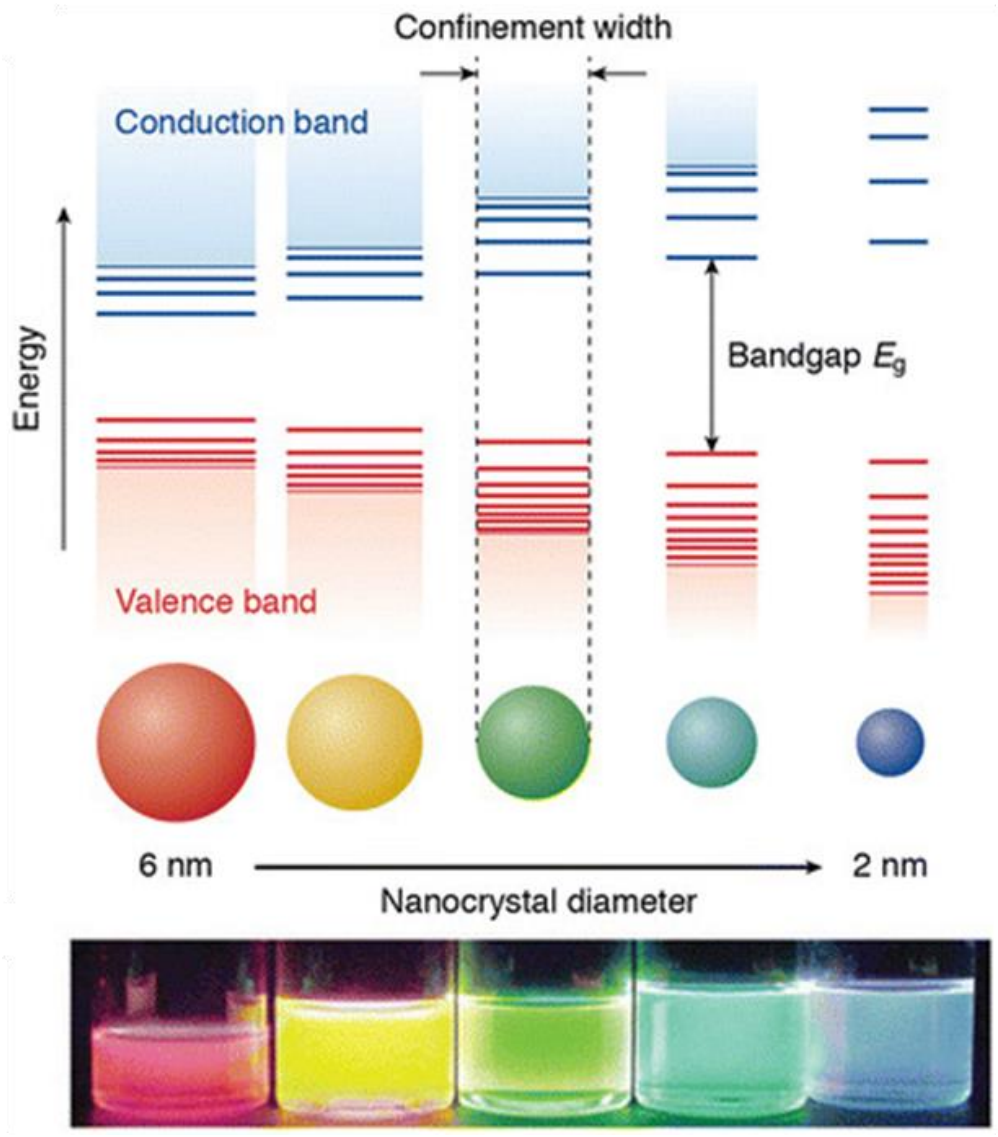

Figure 1.11: Illustration of the quantum confinement effect in QDs with respect to size, bandgap separation, and emission color[89]

One additional challenge to the application of quantum dots is their propensity towards photoblinking, or fluorescence intermittency upon continuous exposure to the excitation light source.[90, 94] It is now posited that QDs actually undergo two distinct types of photoblinking,

known as A-type and B-type. A-type photoblinking is attributed to a phenomenon known as Auger electron emission, in which the QDs relax from the excited state via electron ejection rather than photon emission, whereas B-type photoblinking is attributed to charge fluctuations on the QD surfaces. Concerted scientific efforts are currently being made at both understanding and controlling these phenomena.[95]

1.4.4 Organic polymer nanoparticles

Organic polymer nanoparticles can be synthesized from either hydrophobic or hydrophilic starting materials. These materials are produced via carefully controlled chemical polymerization or copolymerization reactions between appropriate monomers, resulting in a network of covalent bonds comprising the structure. While these structures are not typically produced from materials exhibiting native fluorescence, they do possess great utility as nanocontainers and delivery vessels for fluorescent dyes.

Organic polymer nanoparticles may be synthesized from hydrophobic or hydrophilic materials. Hydrophobic polymer nanoparticles are commonly made from polystyrene (PS), polyacrylonitrile (PAN), or poly(decyl methacrylate) (PDMA), although other compositions are possible. Particle synthesis is typically achieved through emulsion polymerization in or precipitation from organic solvents, and particle dyeing is more frequently accomplished through noncovalent means either by soaking particles in a dye solution or by simultaneous coprecipitation with dyes during particle synthesis.[96] Because dye incorporation is typically noncovalent, in most cases hydrophobic nanoparticles must be doped with hydrophobic dyes in order to ensure reasonable retention of fluorophores. However, even with the use of hydrophobic fluorophores, dye leaching is still a common issue.[97]

Many hydrophobic nanoparticles, including those listed above, exhibit reasonable biocompatibility for *in vivo* applications, with low toxicities, reasonable rates of excretion, low immunogenicities, good cell wall permeabilities, and a relatively slow rates of coating by intracellular proteins. However, *in vitro* applications as surface-modified fluorescent scaffolds are somewhat hindered by the relative chemical inertness of the nanoparticle surfaces. Introduction of reactive functional groups must be done during the particle synthesis step rather than as a post-synthetic modification in most cases, and available functional groups for these surface modifications are limited.[74]

Hydrophilic organic nanoparticles are commonly made from various types of natural or synthetic hydrogels, including cellulose, polyethylene glycols, polyacrylamide (PAA), poly(hydroxyethyl methacrylamide) (pHEMA), and polyurethanes. These nanoparticles are soft and water-soluble, and although they do not aggregate in water they display a tendency to swell in aqueous solution which is dependent on both compositional variables such as polymer composition and extent of crosslinking and environmental variables such as temperature, ionic strength, pH, and light.[74, 98] Incorporation of fluorescent dyes into hydrophilic organic nanoparticles may be achieved via covalent or noncovalent means, but if noncovalent dye incorporation is applied, the dye of choice must possess strong electrostatic interactions with the polymer matrix in order to reduce leaching.[74]

Like hydrophobic organic nanoparticles, hydrophilic organic nanoparticles display excellent biocompatibility, as they are nontoxic and may be excreted. However, unlike their hydrophobic counterparts, these nanostructures tend to be fairly immunogenic. Types of hydrophilic organic nanoparticles that are capable of permeating cell walls tend to become covered by intracellular proteins and degraded by intracellular enzymes quite rapidly; this

characteristic may limit the types of *in vivo* applications available for these materials.[74] Additional similarities to hydrophobic organic nanoparticles may be drawn in terms of the limited variety of surface functionalization available. Generally, surface functionalities cannot be easily added following particle synthesis; reactive functional groups are instead better introduced to the monomers prior to nanoparticle synthesis, and this step can change the overall composition and properties of the resulting polymeric structures.[74] As in the case of their hydrophobic counterparts, this restricted possibility for surface functionalization limits the applicability of these structures as *in vitro* fluorescent tags.

1.4.5 Dendrimers

One distinct class of organic polymer nanoparticles are the dendritic polymers, which are repetitively branched molecules exhibiting symmetric, spherical structures with excellent monodispersity. Dendrimer backbones are frequently based on poly(amidoamine), which is synthesized via copolymerization of diamines with methyl acrylate, although other types of dendrimers have been described. The first dendrimers were synthesized via divergent synthesis, which involves a series of reactions building upon the dendrimer core; this approach leads to structural inconsistencies and incorporation of impurities, which limited the utility and potential applications.[99, 100] However, in 1990, Hawker and Fréchet introduced a new convergent synthetic method for dendrimers. The convergent synthetic approach involves building the dendrimer from the outside in, which results in greater monodispersity and purity of the final product.[101] Introduction of the convergent synthesis led to an explosion in scientific interest in dendrimers and their applications. Dendrimers are grouped by "generations:" a dendrimer core, made up of 1-2 of each of the dendrimer components, is deemed generation 0 or G-0, and further increases in

component numbers lead to incremental increases in the generation number. Low dendrimer generations are better characterized as elastic polymers rather than nanoparticles, but as the generations and branching increase, the structures begin to take form until finally (at G-7 and above for PAMAM) they effectively become solid particles due to the density of branches making up the surface. At this stage, dendrimers become useful nanocontainers for small molecules, including fluorescent dyes.[100]

The surface groups of dendrimers play a strong role in their biocompatibility; common "naked" dendrimers are cell wall permeable but cytotoxic. This toxicity can be substantially decreased via functionalization with carboxyl, hydroxyl, lauroyl, pyrrolidone, or poly(ethylene glycol) groups, which makes these structures more suitable for bioimaging and particularly for cell imaging via direct incorporation.[102-105] Dye-doped dendrimers may be applied in bioimaging as carriers of fluorescent dyes. Benefits of using dendrimers as nanocontainers are much the same as using other types of nanoparticles for the same purposes, namely: improved solubility, biocompatibility, target binding, and enhanced fluorescence due to the segregation of the fluorophore from the surrounding environent.[103] It is interesting to note that some dendrimers (including PAMAM-based dendrimers) exhibit intrinsic fluorescence despite lacking a typical fluorophore structure. Biswal et al. used both the intrinsic fluorescence and nanocontainer properties of PAMAM dendrimers in an *in vitro* theranostic simulation, simultaneously collecting fluorescence images of HeLa cancer cells while delivering the anticancer drugs doxorubicin and methotrexate to the cells.[104]

1.4.6 Micelles and vesicles

Like the organic polymer nanoparticles discussed previously, micelles and vesicles are assembled from organic starting materials. However, unlike organic polymer nanoparticles, which are typically synthesized from either hydrophobic or hydrophilic starting materials, these structures are produced from amphiphilic surfactants. In addition, while organic polymer nanoparticles are typically produced via chemical polymerization reactions resulting in the formation of covalent bonds, micelles and vesicles self-assemble spontaneously via noncovalent interactions.

Micelle self-assembly is primarily driven by the hydrophobic effect. In aqueous solutions, the hydrophobic "tails" of the surfactant crowd together in a monolayer, orienting the polar "head" groups toward the solution. However, it is also possible to form reverse micelles in nonpolar solutions; in this case the polar "head" groups are oriented inward and the hydrophobic tails point outward into solution. Some surfactants are also capable forming bilayer structures such as flat bilayer sheets and ellipsoid vesicles; in these cases, the polar headgroups on both sides of the lipid bilayer orient outward and aqueous solution is present on either side of the bilayer. The factors governing the self-assembly properties of amphiphiles can include environmental factors such as ionic strength, pH, and temperature, however, the strongest indication of whether a particular surfactant will form micelles or bilayers is the surfactant structure: surfactants with single hydrophobic tails preferentially form micelles, whereas those with multiple hydrophobic tails tend to form bilayers.[106] Surfactants used for micelles and vesicles may also be categorized as non-ionic, cationic, anionic, or zwitterionic depending on the characteristics and composition of their head groups.[107, 108]

Micelles are frequently employed in analytical chemistry as a mobile phase modifier in chromatographic separations, specifically in micellar liquid chromatography (MLC) and in a variant of capillary electrophoresis known as micellar electrokinetic chromatography (MEKC). Micellar liquid chromatography is typically used under reversed-phase conditions and can improve separations of complex mixtures by adding an additional solute-micelle partitioning interaction to the preexisting partitioning interactions between solute and the stationary and mobile phases. In MEKC, micelles act as a pseudo-stationary phase in the electrophoretic separation, assisting in separations by introducing partitioning interactions between solutes and micelles in addition to the existing separation based on electrophoretic mobility; incorporation of micelles makes it possible to separate neutral compounds via electrophoresis. Although both MLC and MEKC are general analytical techniques, both have been applied to the separation of biological mixtures.[107, 109]

Outside of chromatography, both micelles and vesicles can be versatile vessels for the delivery of fluorophores to cells both *in vitro* and *in vivo*. Dye doping is most commonly noncovalent and therefore the rule of "like dissolves like" applies in these cases. Micelles may be used for the delivery of hydrophobic fluorophores via encapsulation within the hydrophobic interior, whereas vesicles may carry either hydrophobic fluorophores within the bilayer membrane or hydrophilic fluorophores within the aqueous interior.[110-112] Both micelles and vesicles suffer from some drawbacks in terms of stability, particularly in biological matrices. Liposomes are further limited by difficulties with batch reproducibility and polydispersity; micelles are further limited especially in terms of *in vivo* applicability due to toxicity and difficulties in controlling payload release.[113]

1.4.7 Silica nanoparticles

Silica nanoparticles were one of the earliest nanomaterials to be applied as carriers of fluorescent dyes for use as bioanalytical probes. While this technology is more mature than those previously mentioned, silica nanoparticles remain a hot topic in nanomaterials. Silica nanoparticles are particularly useful both as fluorescent tags and as biomolecule scaffolds, with a wide range of bioanalytical applications in ultrasensitive immunoassays, oligonucleotide microarrays, cell staining, and *in vivo* and *in vitro* tumor imaging, among others.[114-118]

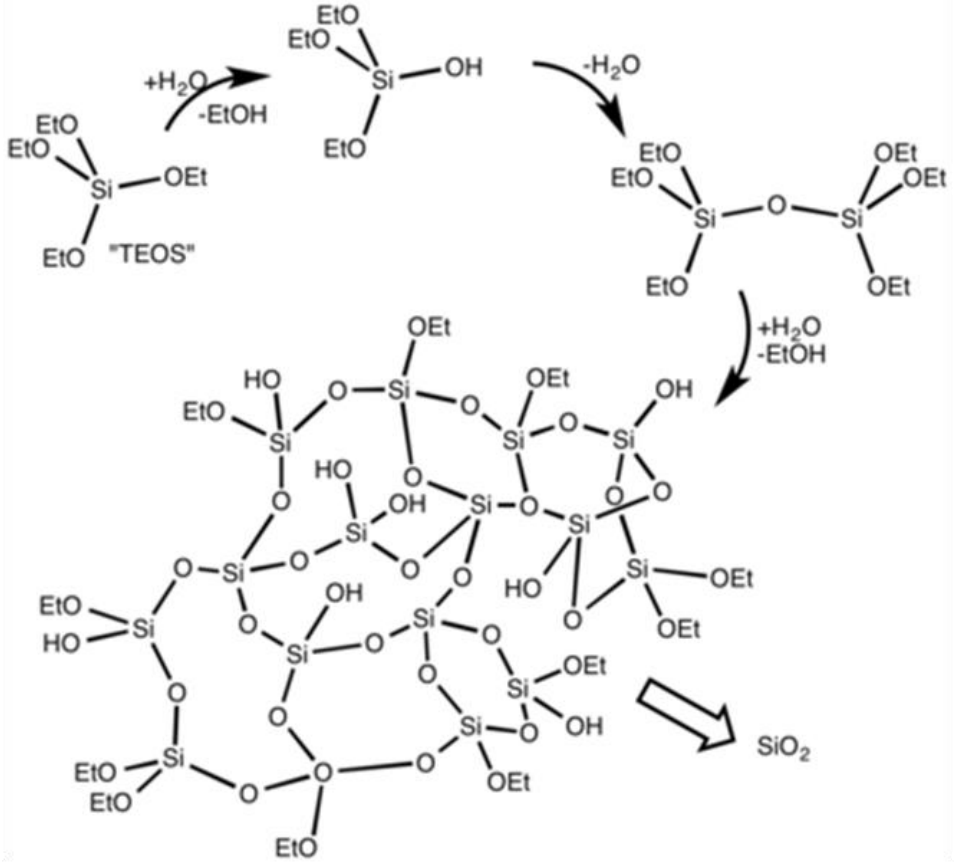

Figure 1.12: Sol-gel condensation of tetraethyl orthosilicate (TEOS)

Silica nanoparticles are synthesized via a sol-gel process involving the (typically base-catalyzed) condensation of silicate esters into a siloxane polymer network (Figure 1.12). As with organic polymer nanoparticles, the synthetic conditions of the sol-gel polymerization process used to produce silica nanoparticles require careful control in order to produce monodisperse, discrete particles of the desired size and shape. A variety of different synthetic approaches have been developed in order to produce nanoparticles of differing size, shape, surface morphology, and surface chemistry. In 1968, Stöber and Fink were the first to document the synthesis of silica nanoparticles, which they achieved via the controlled addition of tetraethyl orthosilicate (TEOS) to an ethanolic solution containing ammonia.[119] Particles resulting from this process are monodisperse, and the particle size is readily altered by changes in the solution chemistry.[120, 121] More recent techniques for synthesizing silica nanoparticles rely instead on biphasic systems containing immiscible organic and aqueous layers, into which TEOS is added in a single delivery and diffusion from the organic layer into the aqueous layer controls the particle growth. One of these newer methods is the reverse microemulsion method, which is based on a primarily organic reaction mixture into which a surfactant and cosurfactant are introduced along with a small amount of water and base; nanoparticle formation and growth occur inside the reverse micelles that form in these conditions.[115] Another biphasic reaction system is the arginine method, in which a biphasic reaction mixture is created and the rate of nanoparticle synthesis is moderated by arginine or lysine, which act as phase transfer catalysts.[122, 123]

Dye molecules can be covalently or noncovalently incorporated into these nanoparticles. Covalent attachment of dye molecules requires the formation of a conjugate between a silicate ester and a dye, which is then hydrolyzed and incorporated into the nanoparticle matrix. This is frequently done by reacting a dye functionalized with either an NHS ester or isothiocyanate

group with an amine-linked silicate ester to form the conjugate. This conjugate is then incorporated into the nanoparticle reaction mixture. Dyes may either be bound within the silica matrix or attached to the surface; however, encapsulation shields the dye molecules from their environment, substantially increasing photostability, reducing solvent effects, limiting exposure to quenchers and oxidizers, and reducing lability relative to surface functionalization.[115] Covalent attachment of any type of dye can be accomplished in any of the aforementioned nanoparticle synthetic processes, but noncovalent incorporation via simple addition of dye to the nanoparticle reaction mixture can only be accomplished using the reverse microemulsion or arginine methods, and will work only for hydrophilic dyes that will adequately partition into the aqueous phase.[124] Covalent dye attachment is generally preferred over noncovalent attachment due to a greater tendency towards leaching and limitations in dye choices in the latter case.[125]

The previously discussed synthetic processes typically produce nonporous silica nanoparticles, however, mesoporous particles may also be synthesized using different reaction conditions. These materials may also be doped with fluorescent dyes via covalent or noncovalent means in order to produce fluorescent labels.[126] Mesoporous silica has other applications in catalysis and in desiccants,[127] but fluorescent mesoporous nanoparticles, like their nonporous counterparts, also have bioanalytical applications.[128, 129] The porous channels in these materials are useful for loading fluorophores, drugs, and biomolecules for targeted delivery. Additionally, for applications where surface conjugation of dyes is preferred over encapsulation, the presence of the porous channels within the mesoporous particles greatly increases the surface area available for surface conjugation of dyes, allowing for heavier dye loading relative to nonporous particles.[126]

Dye-doped silica nanoparticles have some clear advantages over traditional labeling approaches involving the use of single dye labels: they exhibit improved photostability, reduced environmental quenching and degradation, greater hydrophilicity than most dyes, and substantially increased per-label fluorescence intensity and assay sensitivity due to the possibility of incorporating tens to thousands of dye molecules per particle.[115, 130] Silica nanoparticles also possess some advantages over other nanomaterials. Unlike some of the previously discussed nanomaterials (e.g. dendrimers, QDs, and micelles) silica nanoparticles tend to be reasonably nontoxic, biocompatible, and excretable.[130-132] They are more amenable to surface modification, and (in the case of covalently doped silica particles) less prone to dye leaching than organic polymer nanoparticles.[74] Dye-doped silica particles do not exhibit the fluorescence blinking observed in quantum dots, and their fluorescence maxima and quantum yields are not dependent on their size.[120] Additionally, high quantum yields can be easier to obtain with dye-doped nanoparticles than with gold nanoparticles when high intensity dyes are chosen as dopants.[133] Furthermore, unlike liposomes, silica nanoparticles encapsulating dyes exhibit good monodispersity and reproducibility when proper and consistent synthetic conditions are observed.[113]

Dye-doped silica nanoparticles have a few weaknesses as well. Some drawbacks are related to the silica matrix itself. Silica nanoparticles display a tendency to irreversibly agglomerate when dried under certain conditions, when suspended in aqueous solutions at pH values close to the isoelectric point, or in the presence of certain ions at critical concentrations.[134-137] Additionally, nonspecific binding, protein unfolding, and binding site blockage can sometimes occur in biomolecular binding interactions, particularly when larger silica nanoparticles are employed as tags.[130, 134, 138] Other drawbacks are related to the limitations

of the dyes incorporated into the particles: few fluorophores can compete with the narrow emission spectra exhibited by quantum dots or the inherent large Stokes shifts exhibited by gold nanoparticles.[79, 130]

Some of the limitations of dye-doped silica nanoparticles can be overcome through the addition of surface coatings. Nanoparticle surfaces can be modified with anionic, zwitterionic, or hydrophilic surface coatings in order to reduce aggregation in aqueous solutions and to shield biomolecules interacting with those nanoparticles from undesirable surface interactions.[134, 139-142] Additionally, the smaller Stokes shifts exhibited in dye-doped nanoparticles may be overcome through the incorporation of multiple different fluorophores into the nanoparticle matrix in order to introduce FRET interactions between the immobilized dye molecules; in this way, a much larger pseudo-Stokes shift between FRET paired dyes may be attained. These multidye nanoparticles show great promise as multiplexing or barcoding tags: by doping with different concentrations of dyes or different dye combinations, many different tags with unique signatures can be produced from just a few starting dyes.[143]

Herein we discuss the development and functionalization of a variety of single and multidye doped silica nanoparticles for use as fluorescent tags in bioanalytical applications. Some of the multidye doped nanoparticles possess a very long pseudo-Stokes shift and show promise in a variety of potential multiplexing applications, some have very high fluorescence intensities and may be used in high sensitivity detection, and one of the single dye-doped nanoparticles possesses a large Stokes shift, a good quantum yield, and NIR fluorescence, with possible applications to low background detection of biomolecule targets in complex biological media. In this dissertation, the design, synthesis and characterization of a novel NIR dye will be described, along with the optimization of synthetic parameters for dye-doped silica

nanoparticles, the optimization of doping ratios and concentrations of single and multiple dyes in silica nanoparticles, the optimization of biocompatible and bioconjugatable surface coatings, biocompatibility studies of surface modified particles for *in vivo* applications, and a proof of concept for *in vitro* assay applications. Additionally, dye-doped nanoparticles will be characterized in terms of yields, morphology, spectroscopic properties, dye distribution, signal enhancements, and resonance energy transfer characteristics of the incorporated dye species.

1.5 References

1. Monardes, N., *Primera y segunda y tercera partes de la Historia medicinal, de las cosas que se traen de nuestras Indias Occidentales, que siruen en Medicina: Tratado de la Piedra Bezaar y de la yerua escuerçonera; Dialogo de las grandezas del hierro y de sus virtudes medicinales; Tratado de la nieue y del beuer frio*. en casa de Alonso Escriuano: 1574.

2. Herschel, J. F. W., On a Case of Superficial Colour Presented by a Homogeneous Liquid Internally Colourless. *Phil. Trans. R. Soc.* **1845,** *135*, 143-145.

3. Stokes, G. G., On the Change of Refrangibility of Light. *Phil. Trans. R. Soc.* **1852,** *142*, 463-562.

4. Stokes, G. G., XXXIV.-On the application of the optical properties of bodies to the detection and discrimination of organic substances. *J. Chem. Soc.* **1864,** *17* (0), 304-318.

5. Shealy, D. B.; Lohrmann, R.; Ruth, J. R.; Narayanan, N.; Sutter, S. L.; Casay, G. A.; Evans, L.; Patonay, G., Spectral Characterization and Evaluation of Modified Near-Infrared Laser Dyes for DNA Sequencing. *Appl. Spectrosc.* **1995,** *49* (12), 1815-1820.

6. Williams, R. J.; Peralta, J. M.; Tsang, V. C. W.; Narayanan, N.; Casay, G. A.; Lipowska, M.; Strekowski, L.; Patonay, G., Near-Infrared Heptamethine Cyanine Dyes: A New Tracer for Solid-Phase Immunoassays. *Appl. Spectrosc.* **1997,** *51* (6), 836-843.

7. Shriver-Lake, L. C.; Golden, J. P.; Patonay, G.; Narayanan, N.; Ligler, F. S., Use of three longer-wavelength fluorophores with the fiber-optic biosensor. *Sens. Actuators B Chem.* **1995,** *29* (1-3), 25-30.

8. Daneshvar, M. I.; Peralta, J. M.; Casay, G. A.; Narayanan, N.; Evans, L., 3rd; Patonay, G.; Strekowski, L., Detection of biomolecules in the near-infrared spectral region via a fiber-optic immunosensor. *J. Immunol. Methods* **1999,** *226* (1-2), 119-28.

9. Sowell, J.; Parihar, R.; Patonay, G., Capillary electrophoresis-based immunoassay for insulin antibodies with near-infrared laser induced fluorescence detection. *J. Chromatogr. B Biomed. Sci. Appl.* **2001,** *752* (1), 1-8.

10. Baars, M. J.; Patonay, G., Ultrasensitive detection of closely related angiotensin I peptides using capillary electrophoresis with near-infrared laser-induced fluorescence detection. *Anal. Chem.* **1999,** *71* (3), 667-71.

11. *Antibodies Applications and New Developments*. Bentham Science Sharjah, 2012.

12. Ow, H.; Larson, D. R.; Srivastava, M.; Baird, B. A.; Webb, W. W.; Wiesner, U., Bright and Stable Core−Shell Fluorescent Silica Nanoparticles. *Nano Lett.* **2005,** *5* (1), 113-117.

13. *Retinal Vascular Disease*. Springer-Verlag: Heidelberg, 2010.

14. Bennett, T. J. Fundamentals of Fluorescein Angiography. http://www.opsweb.org/?page=FA (accessed 3 May 2017).

15. Sjöback, R.; Nygren, J.; Kubista, M., Absorption and fluorescence properties of fluorescein. *Spectrochim. Acta A* **1995,** *51* (6), L7-L21.

16. Ferrari, L.; Rovati, L.; Fabbri, P.; Pilati, F., Disposable Fluorescence Optical pH Sensor for Near Neutral Solutions. *Sensors* **2013,** *13* (1), 484.

17. Sabnis, R. W., *Handbook of Fluorescent Dyes and Probes*. John Wiley & Sons, Inc.: Hoboken, 2015.

18. Letuta, S. N.; Pashkevich, S. N.; Ishemgulov, A. T.; Lantukh, Y. D.; Alidzhanov, E. K.; Sokabaeva, S. S.; Bryukhanov, V. V., Delayed luminescence of erythrosine in biological tissue and photodynamic therapy dosimetry. *J. Photochem. Photobiol. B* **2016,** *163*, 232-236.

19. Gurav, S.; Tilloo, S.; Burade, K., Histological and Histochemical Staining Techniques. In *Indian Herbal Drug Microscopy*, Gurav, S. S.; Gurav, N. S., Eds. Springer New York: New York, NY, 2014; pp 9-14.

20. Bancroft, J. D., *Theory and Practice of Histological Techniques*. Elsevier Health Sciences: Philadelphia, 2008.

21. Skou, J. C.; Esmann, M., Eosin, a fluorescent probe of ATP binding to the (Na+ + K+)-ATPase. *Biochim. Biophys. Acta Biomembr.* **1981,** *647* (2), 232-240.

22. Pravdin, A. B.; Kochubey, V. I.; Mel'nikov, A. G., Fluorescent eosin probe in investigations of structural changes in glycated proteins. *Opt. Spectrosc.* **2010,** *109* (2), 193-196.

23. Garland, P. B.; Moore, C. H., Phosphorescence of protein-bound eosin and erythrosin. A possible probe for measurements of slow rotational mobility. *Biochem. J.* **1979,** *183* (3), 561-572.

24. Ma, C. Q.; Li, K. A.; Tong, S. Y., Determination of proteins by fluorescence quenching of erythrosin B. *Anal. Chim. Acta* **1996,** *333* (1), 83-88.

25. Yang, W.-C.; Schmerr, M. J.; Jackman, R.; Bodemer, W.; Yeung, E. S., Capillary Electrophoresis-Based Noncompetitive Immunoassay for the Prion Protein Using Fluorescein-Labeled Protein A as a Fluorescent Probe. *Anal. Chem.* **2005,** *77* (14), 4489-4494.

26. Lee, L. G.; Connell, C. R.; Woo, S. L.; Cheng, R. D.; McArdle, B. F.; Fuller, C. W.; Halloran, N. D.; Wilson, R. K., DNA sequencing with dye-labeled terminators and T7 DNA polymerase: effect of dyes and dNTPs on incorporation of dye-terminators and probability analysis of termination fragments. *Nucleic Acids Res.* **1992,** *20* (10), 2471-2483.

27. Shalon, D.; Smith, S. J.; Brown, P. O., A DNA microarray system for analyzing complex DNA samples using two-color fluorescent probe hybridization. *Genome Res.* **1996,** *6* (7), 639-645.

28. Li, F.; Ambrosini, G.; Chu, E. Y.; Plescia, J.; Tognin, S.; Marchisio, P. C.; Altieri, D. C., Control of apoptosis and mitotic spindle checkpoint by survivin. *Nature* **1998,** *396* (6711), 580-584.

29. Pinkel, D.; Segraves, R.; Sudar, D.; Clark, S.; Poole, I.; Kowbel, D.; Collins, C.; Kuo, W.-L.; Chen, C.; Zhai, Y.; Dairkee, S. H.; Ljung, B.-m.; Gray, J. W.; Albertson, D. G., High resolution analysis of DNA copy number variation using comparative genomic hybridization to microarrays. *Nat. Genet.* **1998,** *20* (2), 207-211.

30. Rosenblum, B. B.; Lee, L. G.; Spurgeon, S. L.; Khan, S. H.; Menchen, S. M.; Heiner, C. R.; Chen, S. M., New dye-labeled terminators for improved DNA sequencing patterns. *Nucleic Acids Res.* **1997,** *25* (22), 4500-4504.

31. Drexhage, K. H., Fluorescence Efficiency of Laser Dyes. *J. Res. Natl. Bur. Stand. A* **1976,** *80A* (3), 421-428.

32. Lopez Arbeloa, I.; Rohatgi-Mukherjee, K. K., Solvent effects on the photophysics of the molecular forms of rhodamine B. Internal conversion mechanism. *Chem. Phys. Lett.* **1986,** *129* (6), 607-614.

33. Löber, G.; Koudelka, J.; Smékal, E., Stacking interactions of ethidium bromide bound to a polyphosphate and phage DNA in situ. *Biophys. Chem.* **1974,** *2* (2), 158-163.

34. Olmsted, J.; Kearns, D. R., Mechanism of ethidium bromide fluorescence enhancement on binding to nucleic acids. *Biochemistry* **1977,** *16* (16), 3647-3654.

35. Grundemann, D.; Schomig, E., Protection of DNA during preparative agarose gel electrophoresis against damage induced by ultraviolet light. *Biotechniques* **1996,** *21* (5), 898-903.

36. Martinez, V.; Henary, M., Nile Red and Nile Blue: Applications and Syntheses of Structural Analogues. *Chem. Eur. J.* **2016,** *22* (39), 13764-13782.

37. Murugan, N. A.; Rinkevicius, Z.; Ågren, H., Modeling solvatochromism of Nile red in water. *Int. J. Quantum Chem.* **2011,** *111* (7-8), 1521-1530.

38. Ghanadzadeh Gilani, A.; Moghadam, M.; Zakerhamidi, M. S., Solvatochromism of Nile red in anisotropic media. *Dyes Pigm.* **2012,** *92* (3), 1052-1057.

39. Fowler, S. D.; Greenspan, P., Application of Nile red, a fluorescent hydrophobic probe, for the detection of neutral lipid deposits in tissue sections: comparison with oil red O. *J. Histochem. Cytochem.* **1985,** *33* (8), 833-836.

40. Krishna, M. M. G., Excited-State Kinetics of the Hydrophobic Probe Nile Red in Membranes and Micelles. *J. Phys. Chem. A* **1999,** *103* (19), 3589-3595.

41. Prifti, E.; Reymond, L.; Umebayashi, M.; Hovius, R.; Riezman, H.; Johnsson, K., A Fluorogenic Probe for SNAP-Tagged Plasma Membrane Proteins Based on the Solvatochromic Molecule Nile Red. *ACS Chem. Biol.* **2014,** *9* (3), 606-612.

42. Chen, W.; Sommerfeld, M.; Hu, Q., Microwave-assisted Nile red method for in vivo quantification of neutral lipids in microalgae. *Bioresour. Technol.* **2011,** *102* (1), 135-141.

43. Montalbo-Lomboy, M.; Kantekin, M. N.; Wang, T., Lipid Estimation of Surfactant-Extracted Microalgae Oil Using Nile Red. *J. Am. Oil Chem. Soc.* **2014,** *91* (4), 665-680.

44. Genicot, G.; Leroy, J. L. M. R.; Soom, A. V.; Donnay, I., The use of a fluorescent dye, Nile red, to evaluate the lipid content of single mammalian oocytes. *Theriogenology* **2005,** *63* (4), 1181-1194.

45. Bonilla, E.; Prelle, A., Application of nile blue and nile red, two fluorescent probes, for detection of lipid droplets in human skeletal muscle. *J. Histochem. Cytochem.* **1987,** *35* (5), 619-621.

46. Vijayalakshmi, S.; Karthika, T. N.; Mishra, A. K.; Chandra, T. S., Spectrofluorimetric method for the estimation of total lipids in Eremothecium ashbyii fungal filaments using Nile blue and avoiding interference of autofluorescent riboflavin. *J. Microbiol. Methods* **2003,** *55* (1), 99-103.

47. Slater, R. S.; Smith, E. B., The microdissection of large atherosclerotic plaques to give morphologically and topographically defined fractions for analysis. *Atherosclerosis* **1972,** *15* (1), 57-69.

48. Braasch, K.; de la Hunty, M.; Deppe, J.; Spindler, X.; Cantu, A. A.; Maynard, P.; Lennard, C.; Roux, C., Nile red: Alternative to physical developer for the detection of latent fingermarks on wet porous surfaces? *Forensic Sci. Int.* **2013,** *230* (1–3), 74-80.

49. Castelló, A.; Alvarez-Seguí, M.; Verdú, F., Luminous lip-prints as criminal evidence. *Forensic Sci. Int.* **2005,** *155* (2–3), 185-187.

50. Yang, Y.-I.; Hong, H.-Y.; Lee, I.-S.; Bai, D.-G.; Yoo, G.-S.; Choi, J.-K., Detection of DNA Using a Visible Dye, Nile Blue, in Electrophoresed Gels. *Anal. Biochem.* **2000,** *2* (280), 322-324.

51. Lakowicz, J. R., *Principles of Fluorescence Spectroscopy*. 2nd ed.; Kluwer Academic: New York, 1999.

52. Legendre, B. L.; Moberg, D. L.; Williams, D. C.; Soper, S. A., Ultrasensitive near-infrared laser-induced fluorescence detection in capillary electrophoresis using a diode laser and avalanche photodiode. *J. Chromatogr. A* **1997,** *779* (1), 185-194.

53. Li, X.; Long, N. J.; Clifford, J. N.; Campbell, C. J.; Durrant, J. R., New peripherally-substituted naphthalocyanines: synthesis, characterisation and evaluation in dye-sensitised photoelectrochemical solar cells. *New J. Chem.* **2002,** *26* (8), 1076-1080.

54. Kouzeki, T.; Tatezono, S.; Yanagi, H., Electrochromism of Orientation-Controlled Naphthalocyanine Thin Films. *J. Phys. Chem.* **1996,** *100* (51), 20097-20102.

55. Biolo, R.; Jori, G.; Soncin, M.; Pratesi, R.; Vanni, U.; Rihter, B.; Kenney, M. E.; Rodgers, M. A. J., PHOTODYNAMIC THERAPY OF B16 PIGMENTED MELANOMA WITH LIPOSOME-DELIVERED Si(IV)-NAPHTHALOCYANINE. *Photochem. Photobiol.* **1994,** *59* (3), 362-365.

56. Luo, Y.; Kessel, D., Initiation of Apoptosis versus Necrosis by Photodynamic Therapy with Chloroaluminum Phthalocyanine. *Photochem. Photobiol.* **1997,** *66* (4), 479-483.

57. Uslan, C.; Şebnem Sesalan, B., Synthesis of novel DNA-interacting phthalocyanines. *Dyes Pigm.* **2012,** *94* (1), 127-135.

58. John, D. C. A.; Rosamund, J.; Douglas, K. T., Tight binding of a copper (II) phthalocyanine (Cuprolinic Blue) to DNA. *Biochem. Biophys. Res. Commun.* **1989,** *159* (3), 1256-1262.

59. Mehrgardi, M. A.; Daneshtalab, R., Electrochemical detection of different types of single-base mismatches in DNA using copper-phthalocyanine tetrasulfonic acid. *J. Electroanal. Chem.* **2011,** *650* (2), 214-218.

60. Wang, L.; Xiang, J.; Sun, H.; Yang, Q.; Yu, L.; Li, Q.; Guan, A.; Tang, Y., Controllable cy3-MTC-dye aggregates and its applications served as a chemosensor. *Dyes Pigm.* **2015,** *122*, 382-388.

61. Jeffreys, R. A., 675. Oxazole cyanine and merocyanine dyes, and intermediates. Part II. Intermediates derived from desylamines (1 : 2-diaryl-2-oxoethylamines). *J. Chem. Soc.* **1957,** (0), 3396-3402.

62. He, L.; Lin, W.; Xu, Q.; Wei, H., A Unique Type of Pyrrole-Based Cyanine Fluorophores with Turn-on and Ratiometric Fluorescence Signals at Different pH Regions for Sensing pH in Enzymes and Living Cells. *ACS Appl. Mater. Interfaces* **2014,** *6* (24), 22326-22333.

63. Pardal, A. C. R., S.S.; Santos, P.F.; Reis, L.V.; Almeida, P., Synthesis and Spectroscopic Characterisation of N-Alkyl Quaternary Ammonium Salts Typical Precursors of Cyanines. *Molecules* **2002,** *7*, 320-330.

64. *The Complete Technology Book On Dyes & Dye Intermediates*. National Institute of Industrial Research: Delhi, 2003.

65. Gibbs, S. L., Near infrared fluorescence for image-guided surgery. *Quant. Imaging Med. Surg.* **2012,** *2* (3), 177-187.

66. Delaey, E.; van Laar, F.; De Vos, D.; Kamuhabwa, A.; Jacobs, P.; de Witte, P., A comparative study of the photosensitizing characteristics of some cyanine dyes. *J. Photochem. Photobiol. B* **2000,** *55* (1), 27-36.

67. Rockett, S. E. Characteristics and performance of novel squarylium dyes as fluorescent probes for the analysis of proteins and viruses by CE-LIF. Wake Forest University, Winston-Salem, NC, 2012.

68. Saito, S.; Massie, T. L.; Maeda, T.; Nakazumi, H.; Colyer, C. L., On-Column Labeling of Gram-Positive Bacteria with a Boronic Acid Functionalized Squarylium Cyanine Dye for Analysis by Polymer-Enhanced Capillary Transient Isotachophoresis. *Anal. Chem.* **2012,** *84* (5), 2452-2458.

69. Chen, Y.; Yan, S.; Yuan, L.; Zhou, Y.; Song, Y.; Xiao, H.; Weng, X.; Zhou, X., Nonlinear optical dye TSQ1 as an efficiently selective fluorescent probe for G-quadruplex DNA. *Org. Chem. Front.* **2014,** *1* (3), 267-270.

70. Arunkumar, E.; Forbes, C. C.; Noll, B. C.; Smith, B. D., Squaraine-Derived Rotaxanes: Sterically Protected Fluorescent Near-IR Dyes. *J. Am. Chem. Soc.* **2005,** *127* (10), 3288-3289.

71. Panchuk-Voloshina, N.; Haugland, R. P.; Bishop-Stewart, J.; Bhalgat, M. K.; Millard, P. J.; Mao, F.; Leung, W.-Y.; Haugland, R. P., Alexa Dyes, a Series of New Fluorescent Dyes that Yield Exceptionally Bright, Photostable Conjugates. *J. Histochem. Cytochem.* **1999,** *47* (9), 1179-1188.

72. Njiojob, C. N.; Owens, E. A.; Narayana, L.; Hyun, H.; Choi, H. S.; Henary, M., Tailored Near-Infrared Contrast Agents for Image Guided Surgery. *J. Med. Chem.* **2015,** *58* (6), 2845-2854.

73. Jee, J.-E.; Lim, J.; Hyun, H.; Oon, J.; Ong, Y. S.; Massif, C.; Chang, Y.-T.; Choi, H. S.; Lee, S. S., Investigating fluorescent dyes in fluorescence-assisted screenings. *Chem. Commun.* **2014,** *50* (96), 15220-15223.

74. Wolfbeis, O. S., An overview of nanoparticles commonly used in fluorescent bioimaging. *Chem. Soc. Rev.* **2015,** *44* (14), 4743-4768.

75. Ashenfelter, B. A.; Desireddy, A.; Yau, S. H.; Goodson, T.; Bigioni, T. P., Fluorescence from Molecular Silver Nanoparticles. *J. Phys. Chem. C* **2015,** *119* (35), 20728-20734.

76. Luo, Z.; Yuan, X.; Yu, Y.; Zhang, Q.; Leong, D. T.; Lee, J. Y.; Xie, J., From Aggregation-Induced Emission of Au(I)–Thiolate Complexes to Ultrabright Au(0)@Au(I)–Thiolate Core–Shell Nanoclusters. *J. Am. Chem. Soc.* **2012,** *134* (40), 16662-16670.

77. Li, J.-F.; Zhang, Y.-J.; Ding, S.-Y.; Panneerselvam, R.; Tian, Z.-Q., Core–Shell Nanoparticle-Enhanced Raman Spectroscopy. *Chem. Rev.* **2017,** *117* (7), 5002-5069.

78. Hamidi-Asl, E.; Dardenne, F.; Pilehvar, S.; Blust, R.; De Wael, K., Unique properties of core shell Ag@ Au nanoparticles for the aptasensing of bacterial cells. *Chemosensors* **2016,** *4* (3), 16.

79. Zheng, J.; Zhou, C.; Yu, M.; Liu, J., Different Sized Luminescent Gold Nanoparticles. *Nanoscale* **2012,** *4* (14), 4073-4083.

80. Singh, M.; Harris-Birtill, D. C.; Markar, S. R.; Hanna, G. B.; Elson, D. S., Application of gold nanoparticles for gastrointestinal cancer theranostics: A systematic review. *Nanomedicine* **2015,** *11* (8), 2083-2098.

81. Malek, S. C.; Ee, H.-S.; Agarwal, R., Strain Multiplexed Metasurface Holograms on a Stretchable Substrate. *Nano Lett.* **2017,** *17* (6), 3641-3645.

82. Burrows, N. D.; Vartanian, A. M.; Abadeer, N. S.; Grzincic, E. M.; Jacob, L. M.; Lin, W.; Li, J.; Dennison, J. M.; Hinman, J. G.; Murphy, C. J., Anisotropic Nanoparticles and Anisotropic Surface Chemistry. *J. Phys. Chem. Lett.* **2016,** *7* (4), 632-641.

83. Kim, J.; Mohd Nasir, S. N. F.; Mat Teridi, M. A.; bin Mohd Yusoff, A. R.; Jang, J., Zinc oxide nanorod doped graphene for high efficiency organic photovoltaic devices. *RSC Adv.* **2016,** *6* (90), 87319-87324.

84. Jang, B.; Choi, Y., Photosensitizer-Conjugated Gold Nanorods for Enzyme-Activatable Fluorescence Imaging and Photodynamic Therapy. *Theranostics* **2012,** *2* (2), 190-197.

85. von Maltzahn, G.; Park, J.-H.; Agrawal, A.; Bandaru, N. K.; Das, S. K.; Sailor, M. J.; Bhatia, S. N., Computationally Guided Photothermal Tumor Therapy Using Long-Circulating Gold Nanorod Antennas. *Cancer Res.* **2009,** *69* (9), 3892-3900.

86. Viter, R.; Jekabsons, K.; Kalnina, Z.; Poletaev, N.; Hsu, S. H.; Riekstina, U., Bioanalytical system for detection of cancer cells with photoluminescent ZnO nanorods. *Nanotechnology* **2016,** *27* (46), 465101.

87. Singh, M.; Alabanza, A.; Gonzalez, L. E.; Wang, W.; Reeves, W. B.; Hahm, J.-i., Ultratrace level determination and quantitative analysis of kidney injury biomarkers in patient samples attained by zinc oxide nanorods. *Nanoscale* **2016,** *8* (8), 4613-4622.

88. Bratschitsch, R.; Leitenstorfer, A., Quantum dots: Artificial atoms for quantum optics. *Nat. Mater.* **2006,** *5* (11), 855-856.

89. Rabouw, F. T.; de Mello Donega, C., Excited-State Dynamics in Colloidal Semiconductor Nanocrystals. *Top. Curr. Chem.* **2016,** *374* (5), 58.

90. Medintz, I. L.; Uyeda, H. T.; Goldman, E. R.; Mattoussi, H., Quantum dot bioconjugates for imaging, labelling and sensing. *Nat. Mater.* **2005,** *4* (6), 435-446.

91. Thompson, J. F.; Milos, P. M., The properties and applications of single-molecule DNA sequencing. *Genome Biol.* **2011,** *12* (2), 217.

92. Yu, W. W.; Qu, L.; Guo, W.; Peng, X., Experimental Determination of the Extinction Coefficient of CdTe, CdSe, and CdS Nanocrystals. *Chem. Mater* **2003,** *15* (14), 2854-2860.

93. Fitzpatrick, J. A. J.; Andreko, S. K.; Ernst, L. A.; Waggoner, A. S.; Ballou, B.; Bruchez, M. P., Long-term Persistence and Spectral Blue Shifting of Quantum Dots in Vivo. *Nano Lett.* **2009,** *9* (7), 2736-2741.

94. Krauss, T. D.; Peterson, J. J., Quantum dots: A charge for blinking. *Nat. Mater.* **2012,** *11* (1), 14-16.

95. Galland, C.; Ghosh, Y.; Steinbrück, A.; Sykora, M.; Hollingsworth, J. A.; Klimov, V. I.; Htoon, H., Two types of luminescence blinking revealed by spectroelectrochemistry of single quantum dots. *Nature* **2011,** *479* (7372), 203-207.

96. Berberan-Santos, M. N., *Fluorescence of Supermolecules, Polymers, and Nanosystems*. Springer-Verlag: Berlin Heidelberg, 2008; Vol. 4.

97. Reisch, A.; Klymchenko, A. S., Fluorescent Polymer Nanoparticles Based on Dyes: Seeking Brighter Tools for Bioimaging. *Small* **2016,** *12* (15), 1968-1992.

98. Ahmed, E. M., Hydrogel: Preparation, characterization, and applications: A review. *J. Adv. Res.* **2015,** *6* (2), 105-121.

99. Tomalia, D. A.; Baker, H.; Dewald, J.; Hall, M.; Kallos, G.; Martin, S.; Roeck, J.; Ryder, J.; Smith, P., A New Class of Polymers: Starburst-Dendritic Macromolecules. *Polym. J* **1985,** *17* (1), 117-132.

100. Vashist, S. K., Dendrimers: Prospects for Bioanalytical Sciences. *J. Nanomed. Nanotechnol.* **2013,** *4* (5), e131.

101. Hawker, C. J.; Frechet, J. M. J., Preparation of polymers with controlled molecular architecture. A new convergent approach to dendritic macromolecules. *J. Am. Chem. Soc.* **1990,** *112* (21), 7638-7647.

102. Kono, K., Dendrimer-based bionanomaterials produced by surface modification, assembly and hybrid formation. *Polym. J* **2012,** *44* (6), 531-540.

103. Trzepiński, P.; Klajnert-Maculewicz, B., Dendrimers for fluorescence-based bioimaging. *J. Chem. Technol. Biotechnol.* **2017,** *92* (6), 1157-1166.

104. Biswal, B. K.; Kavitha, M.; Verma, R. S.; Prasad, E., Tumor cell imaging using the intrinsic emission from PAMAM dendrimer: a case study with HeLa cells. *Cytotechnology* **2009,** *61* (1), 17-24.

105. Kolhatkar, R. B.; Kitchens, K. M.; Swaan, P. W.; Ghandehari, H., Surface acetylation of polyamidoamine (PAMAM) dendrimers decreases cytotoxicity while maintaining membrane permeability. *Bioconjugate Chem.* **2007,** *18* (6), 2054-2060.

106. Tanford, C., *The hydrophobic effect: Formation of micelles and biological membranes*. 2nd ed.; Wiley-Interscience: New York, 1980; Vol. 18, p 687-687.

107. Romero, J. E.; Broch, S. C.; Alegre, M. R., Micellar liquid cromatography in bioanalytical chemistry. *Contrib. Sci.* **2010**, 105-114.

108. Müller, L. K.; Landfester, K., Natural liposomes and synthetic polymeric structures for biomedical applications. *Biochem. Biophys. Res. Commun.* **2015,** *468* (3), 411-418.

109. Olędzka, I.; Plenis, A.; Konieczna, L.; Kowalski, P.; Bączek, T., Micellar electrokinetic chromatography for the determination of cortisol in urine samples in view of biomedical studies. *Electrophoresis* **2010,** *31* (14), 2356-2364.

110. Perry, D. G.; Martin, W. J., Fluorescent liposomes as quantitative markers of phagocytosis by alveolar macrophages. *J. Immunol. Methods* **1995,** *181* (2), 269-285.

111. Deissler, V.; Rüger, R.; Frank, W.; Fahr, A.; Kaiser, W. A.; Hilger, I., Fluorescent Liposomes as Contrast Agents for In Vivo Optical Imaging of Edemas in Mice. *Small* **2008,** *4* (8), 1240-1246.

112. Sun, M.; Yin, W.; Dong, X.; Yang, W.; Zhao, Y.; Yin, M., Fluorescent supramolecular micelles for imaging-guided cancer therapy. *Nanoscale* **2016,** *8* (9), 5302-5312.

113. *Advanced Drug Delivery*. John Wiley & Sons, Inc.: Hoboken, 2014.

114. Yang, W.; Zhang, C. G.; Qu, H. Y.; Yang, H. H.; Xu, J. G., Novel fluorescent silica nanoparticle probe for ultrasensitive immunoassays. *Anal. Chim. Acta* **2004,** *503* (2), 163-169.

115. Liu, A.; Wu, L.; He, Z.; Zhou, J., Development of highly fluorescent silica nanoparticles chemically doped with organic dye for sensitive DNA microarray detection. *Anal. Bioanal. Chem.* **2011,** *401* (6), 2003-11.

116. Zhou, W.-J.; Chen, Y.; Corn, R. M., Ultrasensitive Microarray Detection of Short RNA Sequences with Enzymatically Modified Nanoparticles and Surface Plasmon Resonance Imaging Measurements. *Anal. Chem.* **2011,** *83* (10), 3897-3902.

117. Qhobosheane, M.; Santra, S.; Zhang, P.; Tan, W., Biochemically functionalized silica nanoparticles. *Analyst* **2001,** *126* (8), 1274-1278.

118. Rampazzo, E.; Boschi, F.; Bonacchi, S.; Juris, R.; Montalti, M.; Zaccheroni, N.; Prodi, L.; Calderan, L.; Rossi, B.; Becchi, S.; Sbarbati, A., Multicolor core/shell silica nanoparticles for in vivo and ex vivo imaging. *Nanoscale* **2012,** *4* (3), 824-830.

119. Stöber, W.; Fink, A.; Bohn, E., Controlled growth of monodisperse silica spheres in the micron size range. *J. Colloid Interface Sci.* **1968,** *26* (1), 62-69.

120. Bringley, J. F.; Penner, T. L.; Wang, R.; Harder, J. F.; Harrison, W. J.; Buonemani, L., Silica nanoparticles encapsulating near-infrared emissive cyanine dyes. *J. Colloid Interface Sci.* **2008,** *320* (1), 132-9.

121. Chou, K.-S.; Chen, C.-C., The critical conditions for secondary nucleation of silica colloids in a batch Stöber growth process. *Ceram. Int.* **2008,** *34* (7), 1623-1627.

122. Hristov, D. R.; Mahon, E.; Dawson, K. A., Controlling aqueous silica nanoparticle synthesis in the 10–100 nm range. *Chem. Commun.* **2015,** *51* (98), 17420-17423.

123. Mahon, E.; Hristov, D. R.; Dawson, K. A., Stabilising fluorescent silica nanoparticles against dissolution effects for biological studies. *Chem. Commun.* **2012,** *48* (64), 7970-7972.

124. Auger, A.; Samuel, J.; Poncelet, O.; Raccurt, O., A comparative study of non-covalent encapsulation methods for organic dyes into silica nanoparticles. *Nanoscale Res Lett* **2011,** *6* (1), 328.

125. Labéguerie-Egéa, J.; McEvoy, H. M.; McDonagh, C., Synthesis, characterisation and functionalisation of luminescent silica nanoparticles. *J. Nanopart. Res.* **2011,** *13* (12), 6455-6465.

126. Cho, E. B.; Volkov, D. O.; Sokolov, I., Ultrabright fluorescent mesoporous silica nanoparticles. *Small* **2010,** *6* (20), 2314-2319.

127. Huirache-Acuña, R.; Nava, R.; Peza-Ledesma, C. L.; Lara-Romero, J.; Alonso-Núez, G.; Pawelec, B.; Rivera-Muñoz, E. M., SBA-15 mesoporous silica as catalytic support for hydrodesulfurization catalysts. *Materials* **2013,** *6* (9), 4139-4167.

128. Ispas, C.; Sokolov, I.; Andreescu, S., Enzyme-functionalized mesoporous silica for bioanalytical applications. *Anal. Bioanal. Chem.* **2009,** *393* (2), 543-554.

129. Aznar, E.; Mondragón, L.; Ros-Lis, J. V.; Sancenón, F.; Marcos, M. D.; Martínez-Máñez, R.; Soto, J.; Pérez-Payá, E.; Amorós, P., Finely Tuned Temperature-Controlled Cargo Release Using Paraffin-Capped Mesoporous Silica Nanoparticles. *Angew. Chem. Int. Ed.* **2011,** *50* (47), 11172-11175.

130. Wang, L.; Wang, K.; Santra, S.; Zhao, X.; Hilliard, L. R.; Smith, J. E.; Wu, Y.; Tan, W., Watching Silica Nanoparticles Glow in the Biological World. *Anal. Chem.* **2006,** *78* (3), 646-654.

131. Ivanov, S.; Zhuravsky, S.; Yukina, G.; Tomson, V.; Korolev, D.; Galagudza, M., In vivo toxicity of intravenously administered silica and silicon nanoparticles. *Materials* **2012,** *5* (10), 1873-1889.

132. Yu, T.; Hubbard, D.; Ray, A.; Ghandehari, H., In Vivo Biodistribution and Pharmacokinetics of Silica Nanoparticles as a Function of Geometry, Porosity and Surface Characteristics. *J. Control. Release* **2012,** *163* (1), 46-54.

133. Rogers, N. J. The Development of Gold Nanoparticles Labelled with Transition Metal Complexes for Imaging Applications. Ph.D. Dissertation, University of Birmingham, Edgbaston, Birmingham, 2014.

134. Bagwe, R. P.; Hilliard, L. R.; Tan, W., Surface Modification of Silica Nanoparticles to Reduce Aggregation and Nonspecific Binding. *Langmuir* **2006,** *22* (9), 4357-4362.

135. Metin, C. O.; Lake, L. W.; Miranda, C. R.; Nguyen, Q. P., Stability of aqueous silica nanoparticle dispersions. *J. Nanopart. Res.* **2011,** *13* (2), 839-850.

136. Honary, S.; Zahir, F., Effect of Zeta Potential on the Properties of Nano-Drug Delivery Systems - A Review (Part 2). *Trop. J. Pharm. Res.* **2013,** *12* (2), 265-273.

137. Sameti, M.; Bohr, G.; Ravi Kumar, M. N. V.; Kneuer, C.; Bakowsky, U.; Nacken, M.; Schmidt, H.; Lehr, C. M., Stabilisation by freeze-drying of cationically modified silica nanoparticles for gene delivery. *Int. J. Pharm.* **2003,** *266* (1–2), 51-60.

138. Satzer, P.; Svec, F.; Sekot, G.; Jungbauer, A., Protein adsorption onto nanoparticles induces conformational changes: Particle size dependency, kinetics, and mechanisms. *Eng. Life Sci.* **2016,** *16* (3), 238-246.

139. Hwang, Y.-J.; Lee, Y.-H.; Oh, C.; Jun, Y.-D.; Oh, S.-G., Preparation and Characterization of PEG-Grafted Silica Particles Using Emulsion. *J. Ind. Eng. Chem.* **2006,** *12* (3), 380-386.

140. Schulz, A.; Woolley, R.; Tabarin, T.; McDonagh, C., Dextran-coated silica nanoparticles for calcium-sensing. *Analyst* **2011,** *136* (8), 1722-1727.

141. Huang, C.-J.; Chang, Y.-C., *In Situ* Surface Tailoring with Zwitterionic Carboxybetaine Moieties on Self-Assembled Thin Film for Antifouling Biointerfaces. *Materials* **2014,** *7*, 130-142.

142. Nooney, R. I.; McCahey, C. M. N.; Stranik, O.; Le Guevel, X.; McDonagh, C.; MacCraith, B. D., Experimental and theoretical studies of the optimisation of fluorescence from near-infrared dye-doped silica nanoparticles. *Anal. Bioanal. Chem.* **2009,** *393* (4), 1143-1149.

143. Wang, L.; Yang, C.; Tan, W., Dual-Luminophore-Doped Silica Nanoparticles for Multiplexed Signaling. *Nano Lett.* **2005,** *5* (1), 37-43.

2 DESIGN, SYNTHESIS, AND CHARACTERIZATION OF A NOVEL NIR DYE:

2.1 Introduction

2.1.1 Chemical interactions with light

Biomolecules are complex systems best characterized by nondisruptive means; accordingly, optical detection methods such as spectroscopy are ideal choices. These methods primarily make use of the characteristic absorption and emission of light by molecular and atomic species. These processes may be conveniently illustrated using a Jablonski diagram, as exemplified in Figure 2.1.

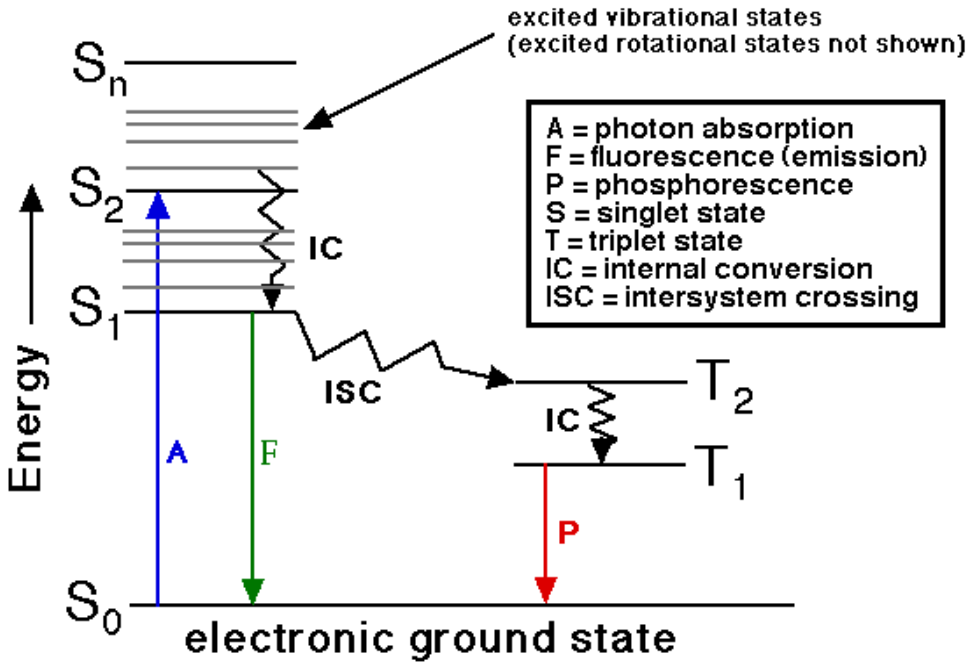

Figure 2.1: A representative Jablonski diagram[1]

Absorption occurs when an incident photon of appropriate frequency interacts with a molecule in such a way that the energy of the photon is absorbed and an electron is promoted from the low-energy singlet "ground" state (S_0) to a higher energy "excited" singlet state

(typically S_1 or S_2). In order for the absorption to occur, the energy of the absorbed photon must equal the energy difference between the ground and excited electronic states.[2, 3]

Absorption typically involves excitation of the electron to one of the upper vibrational states of the first or second excited singlet states (S_1 or S_2), but once the electron is present in one of these upper states it tends to quickly undergo internal conversion, relaxing into the lowest vibronic level of S_1 and giving off the excess energy as heat. Once the electron has relaxed to the lowest vibrational state of S_1, it may return from there to one of the higher vibronic levels of the ground state (S_0), shedding the remaining photon energy as fluorescence. As a result of the energy loss during internal conversion, the energy of the photon emitted during fluorescence is lower than that of the absorbed photon, and the fluorescence occurs at a longer wavelength; this is the origin of the Stokes shift. Internal conversion may also result in full nonradiative decay back to the ground state.

An excited state electron may alternatively undergo a spin flip via a process known as intersystem crossing, entering a lower energy triplet state (T). From there, the electron returns to the singlet ground state through a separate radiative process known as phosphorescence. Phosphorescence occurs much more slowly due to the energetic barrier to the additional spin conversion required for full relaxation, and it tends to occur at longer wavelengths than fluorescence due to the energetic requirements of these spin transitions.[2, 3]

Some compounds are capable of utilizing excited state energy to undergo isomerization reactions (frequently ring closures and *trans-cis* conversions); these are collectively known as photoisomerization reactions. An example of vital biological importance is the photoisomerization of retinal; this reaction forms the chemical basis for both vision in animals and photosynthesis in archaebacteria. Other materials exhibiting these properties are applied

commercially in optical recording media, molecular devices, and photochromic sunglass lenses.[4-7]

The absorbed photon energy of an excited state electron may also be shed by many other nonradiative means; such nonradiative means can collectively be defined as fluorescence quenching. For example collisional (or dynamic) quenching may occur, in which collisions with certain solutes (particularly halides, oxygen, and heavy atoms) facilitate nonradiative energy loss. A similar phenomenon is external conversion (also known as solvent relaxation), in which the molecule returns to a lower energy state by means of collisions with the surrounding solvent molecules; this is the basis for some of the solvent effects observed in spectroscopy (notably the cause of higher fluorescence quantum yields observed in more viscous solvents). Static quenching may also occur, which is typically a result of compounds forming close-knit complexes in the ground state (e.g. dye aggregation), or alternatively, excimers (dimers occurring only in the excited state) may form. Other related mechanisms of fluorescence quenching include Förster resonance energy transfer (FRET), electron exchange quenching (or Dexter interactions), and photoinduced electron transfer (PET). Resonance energy transfer occurs when a molecular species with a larger energy gap (the "donor") between S_0 and S_1 is excited, and upon returning to ground state the emitted energy serves to excite a nearby second molecular species with a smaller energy gap between S_0 and S_1 (the "acceptor"). In these cases, the fluorescence of the donor is quenched because the emitted energy of the donor is funneled into the excitation of the acceptor, which may or may not emit that absorbed energy as fluorescence (depending on its own spectroscopic characteristics). Dexter interactions are similar to FRET in that they involve both a donor and acceptor, but in these cases there is an actual electron exchange that occurs between the donor and acceptor rather than an excitation of

the acceptor; the interaction requires a wavefunction overlap and close proximity ($\leq$10 Å) between the donor and acceptor and involves a nonradiative path for energy dispersal that is associated with quenching only. Following the excited state electron transfer to the acceptor, the acceptor transfers a ground state electron back to the donor, thus no net redox is carried out between the donor-acceptor pair. Photoinduced electron transfer is related to Dexter interactions in that it also involves an excited state electron transfer, but in this case a net redox reaction does occur with the donor acting as a reducing agent. Materials exhibiting photoinduced electron transfer have practical applications ranging from biological systems (e.g. chlorophyll-based photosynthesis) to materials science (e.g. solar cells).[2, 7, 8]

2.1.2 Molecular orbital theory

Another useful model for understanding the energetic transitions that occur in absorption and fluorescence is molecular orbital theory. According to this theory, single bonds are designated as sigma (σ) bonds, and their strength is attributed to the fact that they are formed by the head on overlap of atomic electron orbitals. Higher order (double and triple) bonds are known as pi (π) bonds, and they are weaker than sigma bonds as they are formed via the overlap of parallel atomic orbitals (rather than the head on overlap found in σ bonds). The σ and π bonds formed from the atomic orbitals correspond to σ and π molecular orbitals formed by the merging of the atomic orbitals, and for each of these molecular orbitals there exist corresponding higher energy antibonding molecular orbitals (known as σ^* and π^*, respectively). Unlike bonding orbitals, antibonding orbitals have nodes in the bonding region between nuclei, possessing less electron density than would exist if the bond was not present at all; these create mutual repulsion between atoms. A third type of molecular orbital known as a nonbonding (n) orbital also exists

when the molecule possesses an atom with unbound lone pairs of electrons; the energy of this type of orbital is intermediate between the π and π* orbitals.

For the most part, electrons in the ground state occupy the bonding σ and π orbitals and the nonbonding n orbitals. The occupied orbital of highest energy (corresponding to the ground state "S_0" in the Jablonski diagram) is deemed the highest occupied molecular orbital, or HOMO; the nearest (unoccupied) molecular orbital is deemed the lowest unoccupied molecular orbital, or LUMO (corresponding to the first excited state "S_1" in the Jablonski diagram). During the excitation process, electrons are typically promoted from the HOMO to the LUMO. A comparison of the different types of molecular orbitals, their energy levels, and allowed electronic transitions involved in the excitation process is illustrated in Figure 2.2.

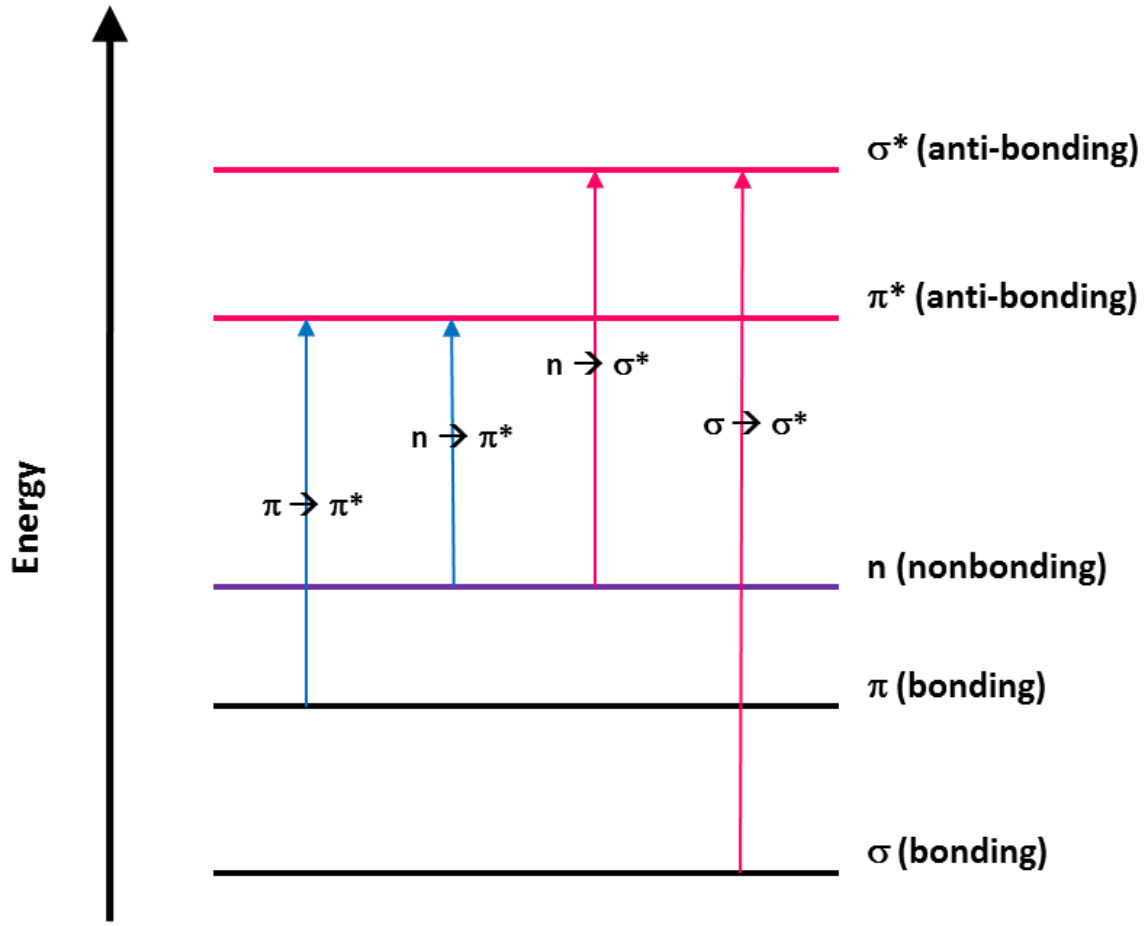

Figure 2.2: Relative energy levels of molecular orbitals and allowed electronic transitions

In spectrophotometry, excitation typically involves π or n electrons (as excitation of σ electrons generally results in bond breakage), and the typical transitions observed are the lower energy π → π* and n → π* transitions. The corresponding photons required for these energetic transitions fall between the ultraviolet and infrared regions of the electromagnetic spectrum. Dye chromophores absorbing in the UV-visible range typically involve conjugated systems of alternating single and double carbon-carbon bonds. As the extent of conjugation increases, the energy gap between the HOMO and the LUMO decreases, resulting in the absorption of lower

energy (longer wavelength) photons. A simple case is illustrated in Figure 2.3 for ethene, 1,3-butadiene, and 1,3,5-hexatriene; for clarity, only the π orbitals are shown in this figure.

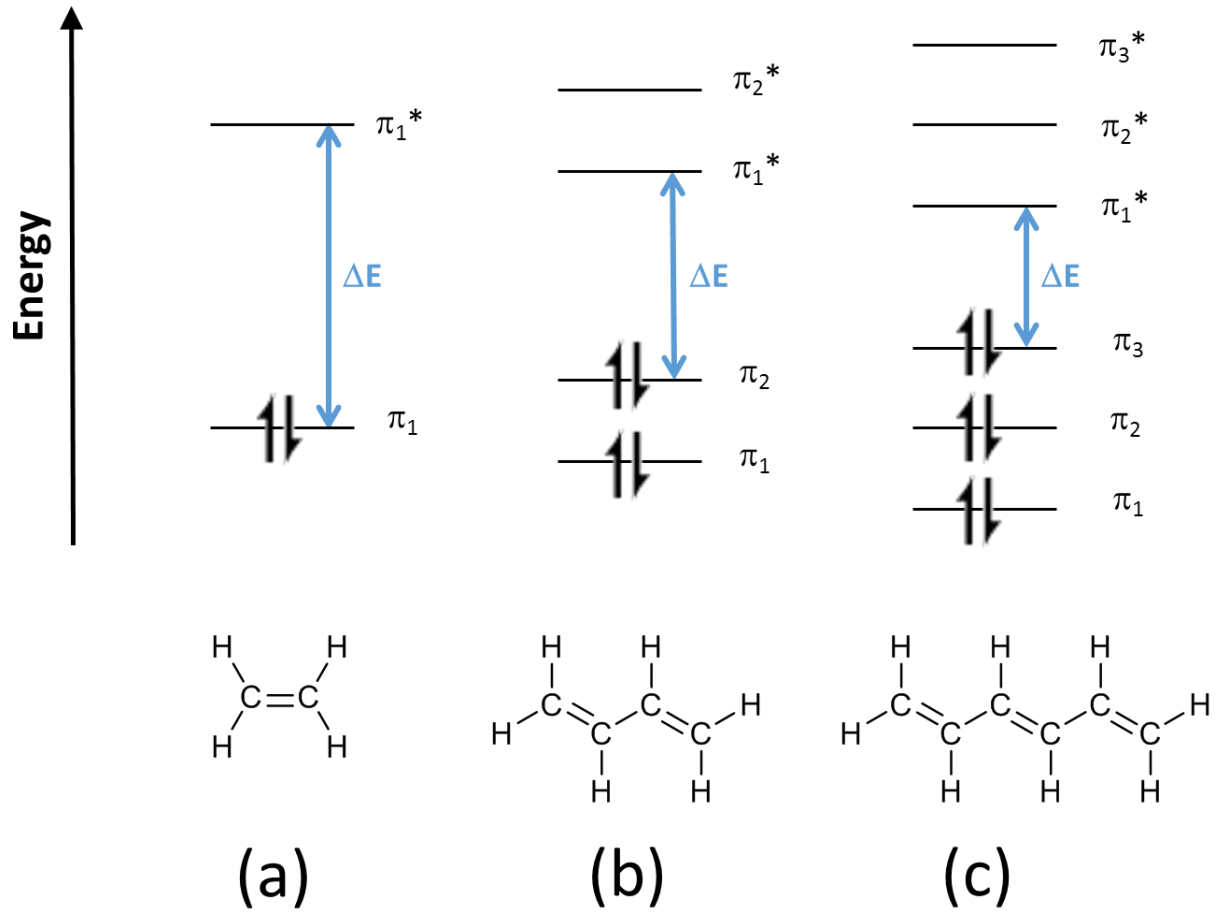

Figure 2.3: Relative HOMO and LUMO energy differentials (ΔE) for (a) ethene, (b) 1,3-butadiene, and (c) 1,3,5-hexatriene; ground state electronic configurations indicated

2.1.3 Absorbance and molar absorptivity

During the absorption process, a photon of a particular energy (matching the difference in energy between the ground state and excited state or HOMO and LUMO) is absorbed. The energy of the photon is related to the frequency by Planck's equation (Equation 2.1), where h is Planck's constant (6.63×10^{-34} J s^{-1}). Absorption spectra are typically acquired relative to

wavelength (λ), which is related to frequency by Equation 2.2, in which c is the speed of light (3×10^8 m s^{-1}). Substituting Equation 2.2 into Equation 2.1 gives the relationship between photon energy and wavelength (Equation 2.3).

$$E = h\nu \quad (2.1)$$

$$\nu = c / \lambda \quad (2.2)$$

$$E = hc / \lambda \quad (2.3)$$

The transmittance of light (T) through a sample at a given wavelength is given by the ratio of the intensity of the light leaving the sample (I) to the intensity of the light incident upon the sample (I_0), as per Equation 2.4. The absorbance of that sample at a given wavelength is defined as the negative logarithm of the transmittance as per Equation 2.5.

$$T = I/I_0 \quad (2.4)$$

$$A = -\log_{10}T \quad (2.5)$$

Because absorption is based on the ratio of incident and transmitted light, absorption values at a given wavelength for a sample of a particular concentration (C) in a container with a specified pathlength of light (b) are constant regardless of instrumentation and light source intensity. The relationship between absorption, concentration, and light pathlength is given by Beer's law (Equation 2.6).

$$A = \varepsilon bC \quad (2.6)$$

In this equation, ε is the molar absorptivity, which is constant for a given material at a given wavelength. Absorption generally has a linear relationship with concentration up to values of 2 arbitrary units (A.U.), at which point only 1% of the incident light is transmitted; absorption values higher than this approach the limit of detection due to decreasing signal-to-noise ratios for the remaining transmitted light.[2]

2.1.4 Fluorescence spectra and quantum yield

For molecular species, absorption and emission spectra encompass a range of wavelengths rather than the sharp and narrow absorption and emission bands present in atomic spectra. The reason for this is the continuum of vibrational and rotational energy levels available within both the ground state and excited states for molecular species; this continuum correlates with the energetic possibilities of bond vibration and rotation and results in spectral band broadening.

Fluorescence emission has a substantially lower intensity than the incident light, and thus fluorescence spectra are acquired at an angle (typically 90°) to the incident excitation light using a filter that blocks scattered excitation light from reaching the detector. Unlike absorption spectra, fluorescence spectra are acquired without any correction for the incident light, thus fluorescence intensity readings are largely meaningless unless compared to a standard; intensities can vary greatly from instrument to instrument, and instrument response from a single instrument may vary over time. Another caveat of fluorescence spectral acquisition is that fluorescence readings must be taken from fairly dilute solutions, with absorbance values at the excitation

wavelength $\leq$ 0.1, corresponding to an absorbance $\leq$ 0.05 and a percent transmission $\geq$ 89% at the cuvette midpoint where fluorescence intensities are read. If fluorescence readings are taken of solutions with A > 0.1, the intensity of incident light will not be adequate to fully permeate and excite the sample at the cuvette midpoint and the observed fluorescence intensities will be lower than expected; this is known as the inner filter effect. If fluorescence readings must be acquired for samples with higher optical densities, this effect can be circumvented using different cuvette and illumination geometries (e.g. front face fluorescence) to reduce the pathlength of light traveling through the samples.[2]

According to the Franck-Condon principle, the electronic transitions associated with absorption occur so rapidly (10^{-15} s) that no substantial nuclear displacement (and therefore no rearrangement of energy levels) occurs. Accordingly, fluorescence spectra are often mirror images of the $S_0 - S_1$ transition of absorption spectra; this is known as the mirror image rule. A related property of fluorescence emission is that emission spectra are almost always independent of excitation wavelength; this is known as Kasha's rule. The intensity of the emission is a function of the amount of light absorbed (i.e. where the excitation wavelength falls on the excitation spectrum), but the emission spectrum itself remains constant. An illustration of this property is provided in Figure 2.4. Good adherence to the mirror image rule is also apparent in this figure. It's important to note that both Kasha's rule and the mirror image rule are predicated on the assumption that the primary absorption corresponds to a single electron $S_0 \rightarrow S_1$ transition; this is the case for the vast majority of fluorophores.[2]

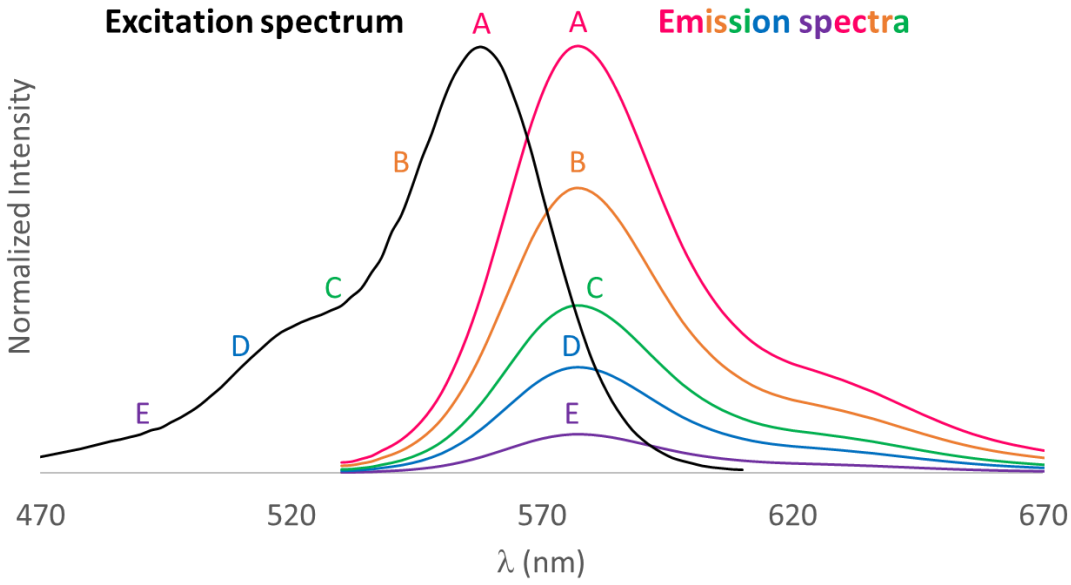

Figure 2.4: Effect of chosen excitation wavelengths (points A-E) on the emission spectra (corresponding spectra A-E); emission spectral intensity changes but the spectrum itself does not

One consequence of Kasha's rule is that the quantum yields of the vast majority of fluorophores are independent of the excitation wavelength; this property greatly eases the measurement of quantum yield for unknown fluorophores. Quantum yield may be defined as the ratio of the intensity of the emitted fluorescence to the intensity of the absorbed light, and it is an important characteristic of fluorophores in terms of their utility as fluorescent probes. The fluorescence quantum yield of an unknown fluorophore may be calculated relative to a standard of known quantum yield from the areas under the fluorescence curves (F), the absorbance readings at the excitation wavelength, (A), the known quantum yield of the standard (ϕ_S) and the refractive indices (n) of the solvents used, as per Equation 2.7. In this equation, the indices S and U refer to the standard and the unknown, respectively. This calculation assumes negligible

variation in instrument response within the range of emission wavelengths exhibited by the unknowns with respect to the standard emission wavelengths.[2]

$$\phi = \phi_S \left(\frac{FA_S}{F_S A}\right)\left(\frac{n^2}{n_S^2}\right) \quad (2.7)$$

2.1.5 Cyanine dye spectral characteristics

Cyanine dyes are a common type of visible to NIR dyes with attractive spectral characteristics for applications as fluorescence probes, including large molar absorptivities (on the order of 10^6 M^{-1} cm^{-1}) and greater likelihoods of return to the ground state via the fluorescence pathway due to short fluorescence lifetimes (τ). However, cyanine dyes also decay to the ground state via three other major nonradiative pathways, as illustrated in the polymethine-specific Jablonski diagram (Figure 2.5); in order from most to least significant in terms of energy loss the pathways are: photoisomerization, internal conversion, and intersystem crossing.[9, 10]

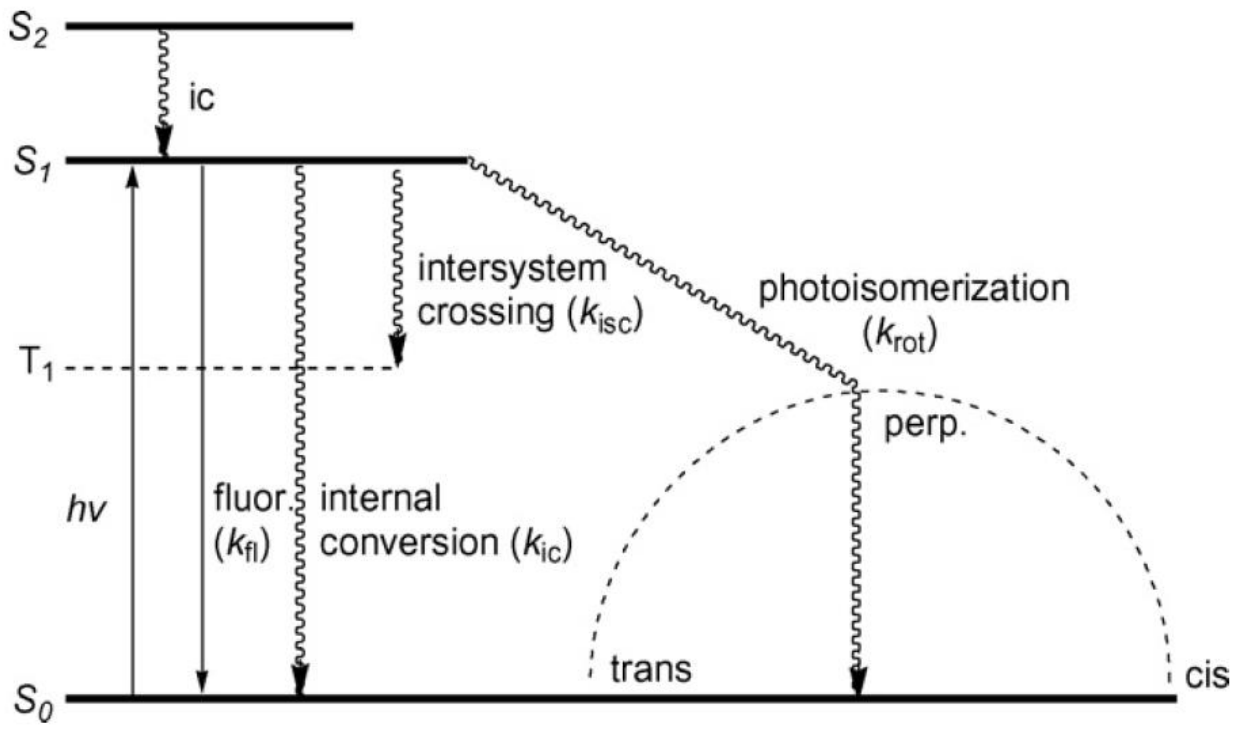

Figure 2.5: Typical Jablonski diagram for a polymethine dye[11]

Dye rigidity has been found to have a strong influence on both photoisomerization and photostability; generally speaking, the less rigid the dye, the worse the photostability and the higher the propensity for photoisomerization. The introduction of rigidifying moieties such as cyclic structures along the chromophore has been shown to improve both photostability and fluorescence quantum yields, particularly in dyes with longer polymethine chains, and this is presumably due in part to sterically driven reductions in photoisomerization reactions.[12-17]

Like many fluorophores, unsubstituted cyanine dyes have a tendency to form concentration-dependent nonfluorescent aggregates in aqueous solutions, but this tendency can be reduced or eliminated by substitution with polar or charged moieties. Cyanine dyes may also experience self-quenching via photodimerization, but this is typically observed in solid state and

monolayer assemblies of these dyes on surfaces.[18] In addition, unsubstituted cyanine dyes tend to display small Stokes shifts, which can limit their utility as fluorescence probes, but this characteristic may also be modulated by changing the functional groups attached to the dye. Substitution is capable of having strong effects on the spectroscopic characteristics of cyanine dyes, particularly when electron-withdrawing or electron-donating groups are conjugated directly to the primary chromophore.[19] Spectroscopic substitution effects on cyanine dyes may be predicted as per the Dewar-Knott rule. For clarity, illustration of this rule as it applies to a heptamethine cyanine dye is provided in Figure 2.6.

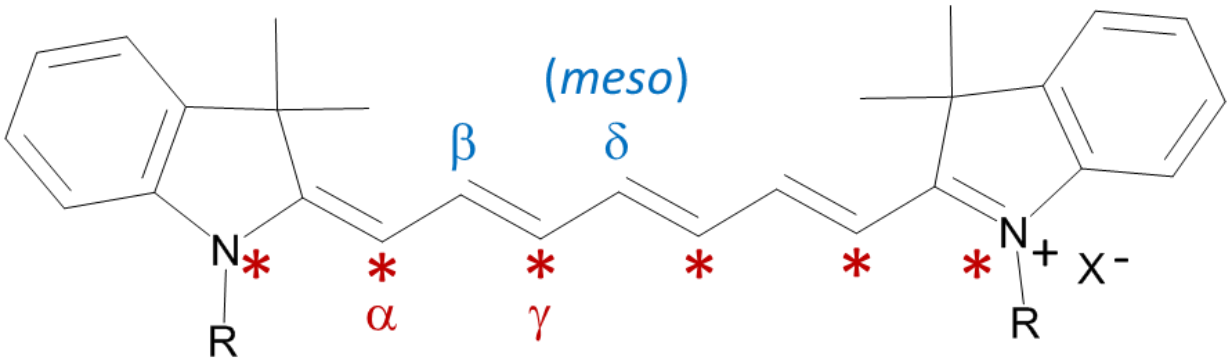

Figure 2.6: Dewar-Knott substitution positions for a heptamethine cyanine dye

According to the Dewar-Knott rule, substitution with electron-withdrawing substituents at the starred (α and γ) carbons or nitrogen termini of the polymethine chain result in a hypsochromic (blue) shift in the absorption spectrum. A similar blue shift is observed when the unstarred (β and δ) carbons are substituted with electron-donating substituents. The converse is also true; a red (bathochromic) shift is observed when electron-withdrawing moieties are introduced to the unstarred carbons or when electron-donating substituents are introduced at the starred positions.

The Dewar-Knott rule may be explained in terms of molecular orbital theory. If an electron-donating substituent is introduced at one of the starred positions, it has a destabilizing effect on the HOMO, bringing its energy level closer to that of the LUMO and resulting in a red shift; the same occurs when an electron-withdrawing substituent is introduced at one of the unstarred positions. If an electron-withdrawing substituent is introduced at one of the starred positions, it has a stabilizing effect on the HOMO, resulting in a lower energy relative to the LUMO, increasing the energy gap between the two orbitals, and resulting in a blue shift; the same occurs when an electron-donating substituent is introduced at one of the unstarred positions.[20-22] Through application of the Dewar-Knott rule and structural modifications such as rigidifying structures, solubilizing or aggregation-promoting groups, and reactive moeities for covalent and noncovalent bonding, the rational design of cyanine dyes with a wide variety of different spectroscopic and functional properties becomes possible.

2.1.6 Aminocyanine dyes

One purpose of this project is to develop a NIR-fluorescing fluorophore with a large Stokes shift suitable for incorporation into silica nanoparticles bound for bioanalytical applications. The benefits of NIR fluorescence have been discussed previously, and the long Stokes shift serves multiple purposes: it allows for easy deconvolution of the excitation light from the emission spectrum, and it strongly reduces the likelihood of fluorescence self-quenching (homo-quenching). Homo-quenching results from resonance energy transfer between dye molecules of the same species, and its likelihood increases in molecules with small Stokes shifts as the energy difference between the absorption and fluorescence bands is small; fluorescence from one dye molecule (the donor) excites another (the acceptor) rather than being

emitted as light. Resonance energy transfer is a distance-dependent process; the greater the spectral overlap, the more efficient this process is over greater distances. Efficient homo-quenching reduces the concentration of dye molecules that can be incorporated within a given space, as the fluorescence intensity begins to suffer when dyes are sufficiently close to allow resonance energy transfer amongst themselves. This property can become a significant handicap in applications requiring multiple dye molecules in close proximity, such as biomolecular labeling and construction of dye-doped nanoparticles, but it is readily avoidable through the use of fluorophores with larger Stokes shifts.[23, 24]

Heptamethine cyanine dyes possessing a central chlorocyclohexene ring along the polymethine chain were developed by Patonay, Strekowski, and Lipowska in 1992.[13] This class of dyes is typified by the structure of IR-786 iodide given in Figure 2.7. This represented a major advance in cyanine dye technology, as the stabilizing ring structure improved the photostability and quantum yield relative to equivalent acyclic heptamethine chromophores, and the nucleofugal chlorine at the *meso* (or δ) carbon provides a very useful reactive site for derivatization of the dye molecule along the chromophore, allowing for further tuning of the spectroscopic properties. Following this development, many different *meso*-substituted heptamethine cyanine dyes have been synthesized and characterized.[14, 15, 24-28]

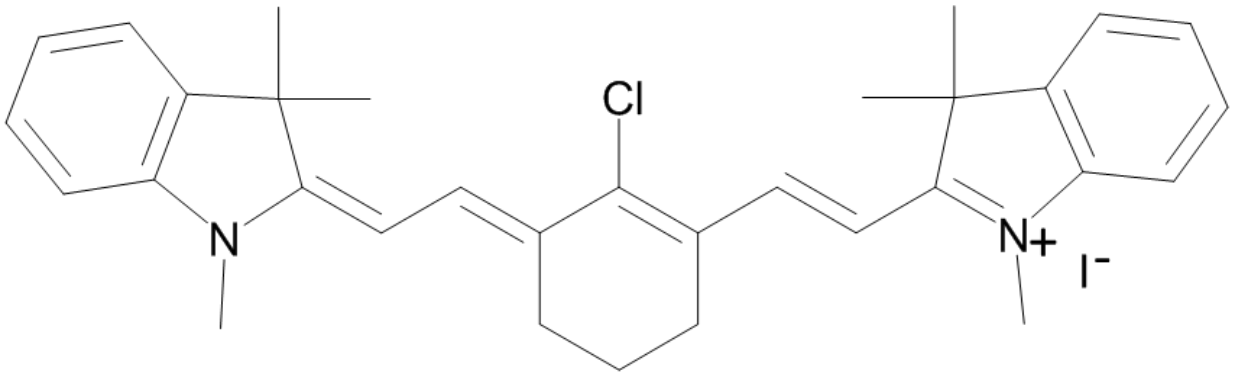

Figure 2.7: Example of a chlorocyclohexenyl ring-stabilized heptamethine dye (IR-786 iodide)

Aminocyanine dyes represent one important group of dye derivatives arising from substitution of the cyanine chromophore with amino compounds. Substitution with an amino group at an unstarred position such as the *meso* carbon results in substantial increases in both the fluorescence quantum yield and the Stokes shift.[24, 29] Amino groups possess a strong net electron-donating character via resonance effects (which is slightly attenuated by a weaker electron-withdrawing inductive effect). The spectroscopic effects of this substitution are in line with those predicted using the Dewar-Knott rule; amino substitution at unstarred positions (such as the *meso* chloro group in IR-786) is correlated with a strong hypsochromic shift in the absorption spectrum of these dyes. However, the fluorescence spectrum does not undergo a comparably strong hypsochromic shift, thus one of the net results of the amino substitution is a substantially increased Stokes shift (from ~20 nm in unsubstituted heptamethine cyanine dyes to >100 nm in aminocyanine dyes). Additional spectroscopic features of aminocyanine dyes include a featureless and broad fluorescence spectrum and a departure from the mirror image rule. These spectroscopic characteristics can suggest either proton transfer or an intramolecular charge transfer (ICT) is occurring in the excited state; the strong solvatochromic shifts observed in the

absorption spectra of aminocyanine dyes implicate the latter process.[24, 29] There are thought to be two processes involved in excited state ICT involving amino groups: the formation of a locally excited (LE) state in which the pyramidal geometry of the amino group is retained, followed by a flattening of the pyramidal geometry into a planar configuration in the ICT state; this excited state change in molecular configuration explains both the large Stokes shift and the departure from the mirror image rule. The planar ICT state promotes the delocalization of the lone pair electron density into the chromophore due to increased orbital overlap between the nitrogen and the *meso* carbon.[24] The charge transfer characteristic of aminocyanine dyes lends itself to their applications as metal ion sensors and ratiometric pH probes owing to their lone-pair electron interactions with Lewis acids, which affects their spectroscopic properties as a result of the decreased availability of the nitrogen lone pair electrons to the chromophore.[26, 30] The larger Stokes shift exhibited by these compounds also lends itself to incorporation of higher dye concentrations into silica nanoparticles while reducing the likelihood of homo-quenching occurring between neighboring dye molecules.

2.1.7 Overview

In this chapter, we discuss the synthesis and characterization of a NIR-fluorescent aminocyanine dye GC-1-23 designed for incorporation into silica nanoparticles. Due to its low cost and ready availability, the four carbon diamino linker putrescine (1,4-diaminobutane) was chosen as the spectral modulator for the novel cyanine dye to be synthesized. Once this diamine is linked with the cyanine chromophore, the terminal primary amine allows for covalent incorporation into silica nanoparticles via reaction with the isocyanate-functionalized alkoxysilane ICPTES; as mentioned previously, covalent attachment is generally preferred both

to reduce the likelihood of dye leaching and to allow for the incorporation of a wider variety of dye molecules regardless of polarity.[31, 32]. Because long wavelength fluorescence, good stability, and the presence of a nucleofugal group was desired, the heptamethine dye IR-786 was chosen as the cyanine backbone. The intended structure of the dye to be synthesized is provided in Figure 2.8. Intermediates in each of the synthetic steps were characterized using ^{1}H and ^{13}C NMR spectroscopy, and the final dye product was characterized using high resolution mass spectrometry and ^{1}H and ^{13}C NMR spectroscopy. The synthesized dye was further characterized in terms of its spectroscopic properties, specifically its molar absorptivity, Stokes shift, and fluorescence quantum yield.

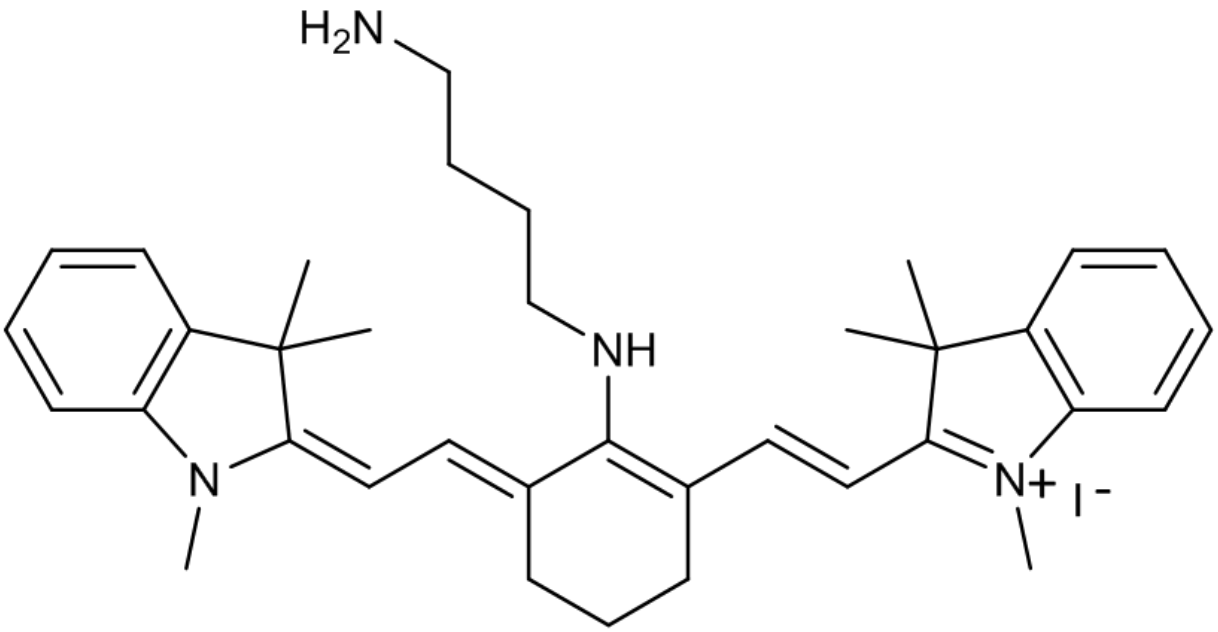

Figure 2.8: Structure of the designed NIR aminocyanine dye (GC-1-23)

2.2 Experimental

2.2.1 Reagents, materials, and instrumentation

Acetic anhydride (Ac_2O, 99.5%), acetonitrile (CH_3CN, CHROMASOLV® Plus, for HPLC, ≥99.9%), aniline (ACS reagent, ≥99.5%), cyclohexanone (ACS reagent, ≥99%), 1,4-diaminobutane (99%), *N*,*N*-dimethylformamide (DMF, 99.8%), hydrochloric acid (HCl; ACS reagent, 37%), indocyanine green (ICG; cardiogreen polymethine dye, ~90%), phosphorus (V) oxychloride ($POCl_3$, ReagentPlus, 99%), 1,2,3,3-tetramethyl-3*H*-indolium iodide (98%), and triethylamine (Et_3N, ≥99%) were obtained from Sigma Aldrich (St. Louis, MO). Diethyl ether (ACS reagent, anhydrous), hexanes (technical grade), methanol (MeOH; certified ACS, ≥99.8%), methylene chloride (CH_2Cl_2, certified ACS, ≥99.5%), and sodium chloride (certified ACS, >99.9%) were obtained from Thermo Fisher Scientific (Hudson, NH). Absolute 200 proof ethanol (EtOH) was obtained from Greenfield Ethanol, Inc. (Toronto, ON). Triply deionized water was obtained from a Barnstead Nanopure water purification system (Thermo Fisher Scientific, West Palm Beach, FL).

All volumetric glassware (pipets used to deliver volumes greater than 1 mL and volumetric flasks) was categorized as class A. Volumes less than 1 mL were delivered using either a 10-100 μL or a 100-1000 μL adjustable volume Eppendorf pipette (Eppendorf, Hauppauge, NY.). Absorption spectra were measured using a Cary 3G UV-visible absorption spectrophotometer (Agilent Technologies, Santa Clara, CA.). Fluorescence spectra were measured using an ISS-K2 fluorimeter (ISS Inc., Champaign, IL) fitted with a 650 nm class IIIb laser as an excitation source (Lasermax, Inc., Rochester, NY). Nuclear magnetic resonance (NMR) spectra were measured on a 400 MHz Bruker Avance NMR spectrometer (Bruker Biospin Corporation, Billerica, MA) operated using Bruker TopSpin Software (v.3.1). High-

resolution mass spectra (HRMS) of novel dye GC-1-23 was obtained at the Georgia State University Mass Spectrometry Facility using a Waters Q-TOF micro (ESI-Q-TOF) mass spectrometer.

2.2.2 Synthesis of novel dye GC-1-23

The heptamethine dye IR-786 was synthesized via a modified Strekowski approach.[33] Dye IR-786 was then reacted with 1,4-diaminobutane (putrescine) via an $S_{RN}1$ pathway[13] to produce the diamino linker at the *meso* position, forming novel dye GC-1-23. An outline of the synthetic pathway is provided in Scheme 2.1.

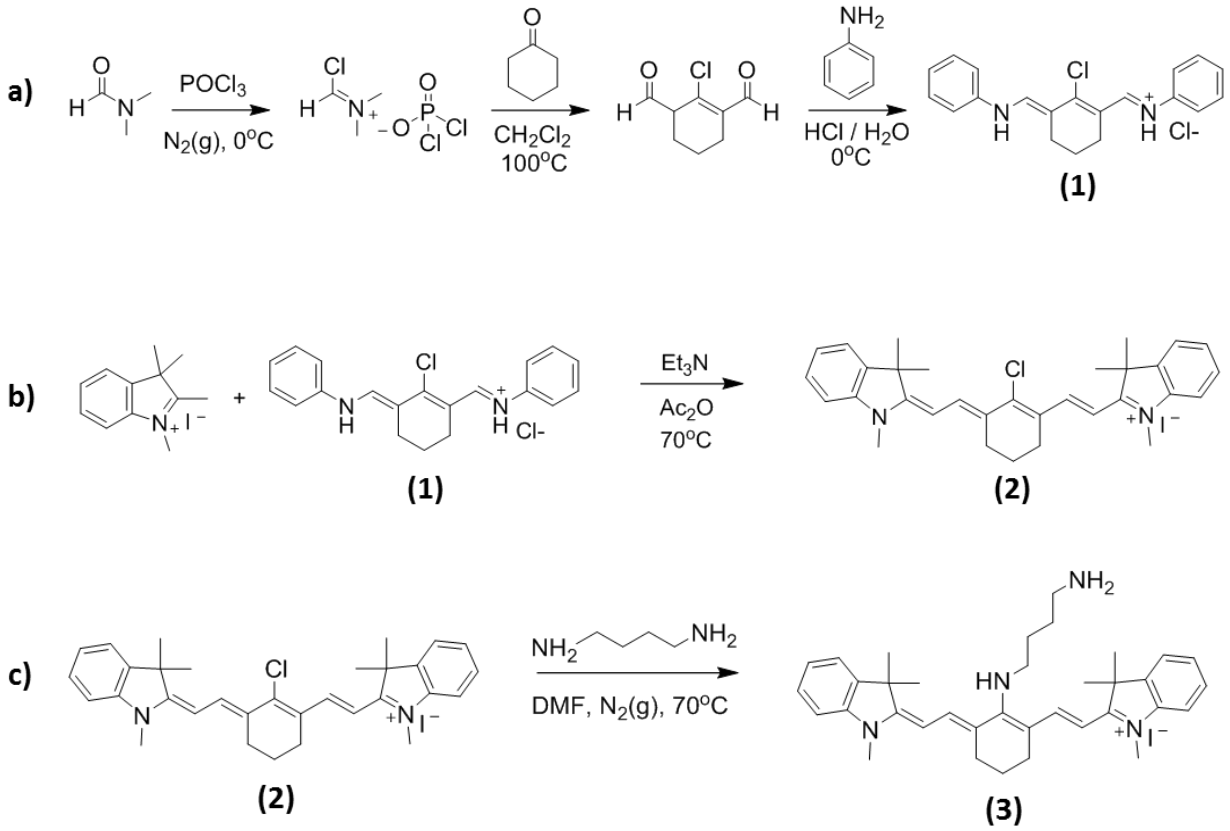

Scheme 2.1: Synthetic pathway to aminocyanine dye GC-1-23

(a) Synthesis of *N*-([(3E)-3-(anilinomethylene)-2-chlorocyclohex-1-en-1-yl]methylene)benzene-aminium chloride [Vilsmeier-Haack-Arnold reagent (1)]

A 250 mL 3-necked round bottom flask equipped with a magnetic stir bar, pressure-equalized addition funnel, and reflux condenser was flushed with N_2(g) and placed in an ice bath containing sodium chloride to maintain a temperature lower than 0° C. The flushed reaction flask was charged with DMF (99.8%, 50 mL, 644 mmol). The addition funnel was charged with $POCl_3$ (99%, 42 mL, 446 mmol) and added dropwise to the reaction vessel at such a rate that the temperature was maintained at or below 0° C, forming the chloroiminium Vilsmeier reagent. A mixture of methylene chloride (20 mL) and cyclohexanone (99%, 10 mL, 95.5 mmol) was then added to the addition funnel, and the mixture was added dropwise to the reaction mixture with continued stirring, maintaining the temperature at or below 0° C. Once all of this mixture was added, the solution turned yellow. At this point, the ice bath was removed and replaced with an oil bath, then the reaction was heated to 100° C and held at that temperature for 2 hours. The oil bath was then removed, the reaction flask was opened to the air, and the mixture was cooled to 0° C with the aid of another ice bath. The addition funnel was then charged with a mixture of aniline (36 mL) and ethanol (36 mL; 395 mmol) and added dropwise to the reaction flask with shaking while the temperature was maintained at or below 0° C. Once reagent addition was completed, shaking and stirring of the flask contents was continued until the reaction was complete, as evidenced by stabilization of the temperature in the reaction vessel. A hydrochloric acid solution in ice water was prepared by adding HCl (37%, 37 mL, 444 mmol) to 300 mL of ice in a beaker and filling to the 400 mL mark with triple deionized water. The contents of the reaction vessel were poured into the cold acid solution and stirred, and the resultant solid was collected by vacuum filtration. This crude product was dissolved in methanol (150 mL), the

resultant solution was added to a mixture of hexane (500 mL) and diethyl ether (500 mL), and then the reprecipitated product, consisting of dark purple-black crystals, was collected by vacuum filtration. The reprecipitation step was repeated once to improve product purity and the crystals were collected via vacuum filtration and washed three times with a 1:1 mixture of hexane and diethyl ether. Yield 15.9 g (46%). ^{1}H NMR (400 MHz, DMSO-d_6): δ = 1.84 (p, 2H, *J* = 6.0 Hz), 2.78 (t, 4H, *J* = 6.0 Hz), 7.26 (t, 2H, *J* = 7.4 Hz), 7.44-7.48 (m, 4H), 7.66 (d, 4H, *J* = 7.8 Hz), 8.53 (s, 2H), 8.70-9.30 ppm (br); ^{13}C NMR (400 MHz, DMSO-d_6): δ = 19.4, 24.9, 115.0, 118.9, 126.2, 129.5, 139.4, 148.6, 155.7 ppm.

(b) Synthesis of 2-(2-[2-chloro-3-(1,3-dihydro-1,3,3-trimethyl-2*H*-indol-2-ylidine]ethylidine)-1-cyclohexen-1-yl]ethenyl)-1,3,3-trimethylindolium iodide [IR-786 (2)]

A 250 mL round bottomed flask was charged with 1,2,3,3-tetramethyl-3H-indolium iodide (7.00 g, 23.24 mmol), Vilsmeier-Haack-Arnold reagent (1) (4.18 g, 11.62 mmol), acetic anhydride (60 mL), and triethylamine (6.00 mL, 42.59 mmol), fitted with a condenser, and heated to 70° C on an oil bath with stirring. The reaction was carried to completion as indicated by TLC and UV-visible spectrophotometry. Less than half an hour at temperature was typically required for completion, at which point the reaction mixture was cooled to room temperature and the resultant golden-green precipitate was collected by vacuum filtration and washed three times with acetic anhydride, three times with water, and three times with diethyl ether. The crude product was reprecipitated from methanol and diethyl ether (1:4 v/v ratio) to yield iridescent golden-green crystals. The precipitate was collected again by vacuum filtration, washed three times with diethyl ether, then dried for 24 hours in a 130° C oven. Yield 4.18 g (59%). ^{1}H NMR

(400 MHz, DMSO-d_6): δ = 1.67 (s, 12H), 1.86 (br, 2H), 2.72 (t, 4H, *J* = 6.0 Hz), 3.69 (s, 6H), 6.31 (d, 2H, *J* = 14.3 Hz), 7.27-7.31 (m, 2H), 7.42-7.47 (m, 4H), 7.63 (d, 2H, *J* = 7.4 Hz), 8.25 ppm (d, 2H, *J* = 14.2 Hz); ^{13}C NMR (400 MHz, DMSO-d_6): δ = 20.9, 26.4, 27.8, 32.0, 49.3, 102.4, 111.9, 122.9, 125.6, 126.5, 129.0, 141.5, 143.1, 143.3, 148.1, 173.1 ppm.

(c) Synthesis of 2-(2-[2-(1,4-diaminobutyl)-3-(1,3-dihydro-1,3,3-trimethyl-2*H*-indol-2-ylidine]ethylidine)-1-cyclohexen-1-yl]ethenyl)-1,3,3-trimethylindolium iodide [GC-1-23; (3)]

A three-necked round bottom flask was fitted with a condenser, pressure-equalized addition funnel, and magnetic stir bar and flushed with nitrogen gas. To this flask was added a solution of putrescine (0.577 g; 6.5 mmol; 4 equivalents) in DMF (10 mL), and the vessel was heated to 70° C. The addition funnel was charged with a solution of IR-786 (3) (1.00 g; 1.6 mmol; 1 equivalent) in DMF (10 mL). This solution was added dropwise to the reaction vessel. Putrescine is homobifunctional reagent and therefore a side reaction resulting in the formation of the bis-cyanine dye shown in Figure 2.9 competes with the monocyanine dye formation. The intent behind both the slow addition of dye and the use of four equivalents of amine was to promote formation of the mono-cyanine dye product GC-1-23 through favorable stoichiometry and promotion of homogeneous mixing prior to reaction.[34]

The reaction was carried to completion, as indicated by UV-visible spectrophotometry; as the reaction progresses, the IR-786 peak around 780 nm decreases and a new peak around 630 nm appears and increases in intensity, accompanied by a visible color change from green to blue in the reaction flask. Approximately one hour at 70° C was required for full reaction following completion of the addition, at which point the reaction mixture was stripped of solvent under

reduced pressure using a rotary evaporator. The crude residue was scraped and washed with ether in an ultrasonic bath, and the ether washings were discarded. The iridescent fuchsia residue was then resuspended in methylene chloride and the dye was purified by normal phase silica gel chromatography using a methylene chloride and methanol mixture as eluent. Column chromatography was exceedingly slow due to the presence of primary and secondary amines on the compound and due to the necessity of separating the mono-cyanine and bis-cyanine products; both of these products appeared as blue bands on the column and eluted with some separation. The pure fractions of each compound (as indicated by TLC on silica gel plates) were combined separately and stripped of solvent under reduced pressure, yielding iridescent fuchsia amorphous solids. Samples from each fraction were submitted for HRMS analysis; HRMS results indicated that the early eluting blue fraction contained the bis-cyanine and the later eluting fraction contained the intended mono-cyanine product; this is the expected elution order given the presence of the primary amine on the mono-cyanine product, which interacts more strongly with the somewhat acidic silica stationary phase. Yield 0.3587 g (33%). ^{1}H NMR (400 MHz, DMSO-d_6): δ = 1.59 (s, 12H), 1.74 (m, 4H), 2.80 (br, 2H), 3.43 (s, 6H), 3.69 (br, 2H), 5.72 (d, 2H, J = 13.1 Hz), 7.06 (t, 2H, J = 7.4 Hz), 7.16 (d, 2H, J = 7.9 Hz), 7.30 (t, 2H, J = 7.7 Hz), 7.45 (d, 2H, J = 7.3 Hz), 7.59 (d, 2H, J = 13.1 Hz), 7.65 (br, 3H), 8.86 (br); ^{13}C NMR (400 MHz, DMSO-d_6): δ = 21.2, 24.3, 24.9, 27.3, 28.2, 38.5, 47.0, 49.1, 54.9, 94.2, 108.9, 119.8, 121.9, 122.4, 128.1, 137.6, 139.6, 143.5, 167.5, 169.1 ppm; HRMS (ESI^{+}): *m/z*: calcd for $C_{36}H_{48}N_4$, z =2: 268.1939; found: 268.1937; *m* calcd for $C_{36}H_{48}N_4$: 536.3879; found: 536.3874.

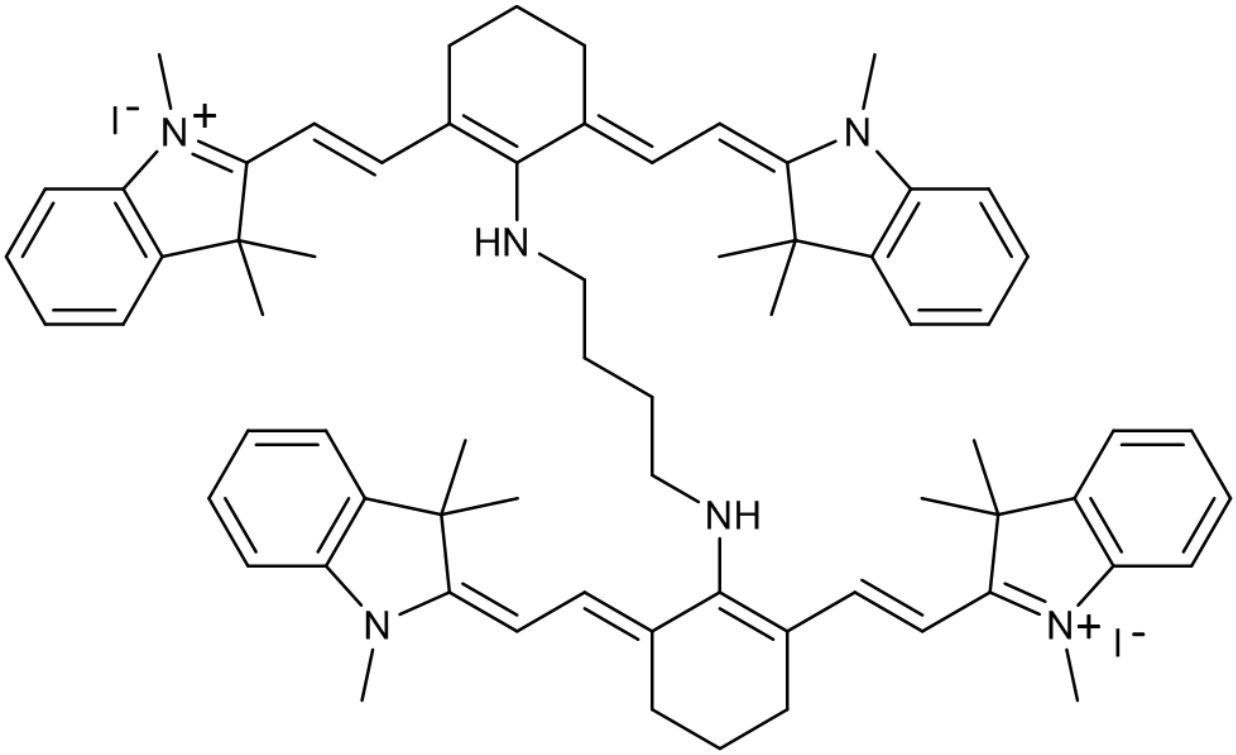

Figure 2.9: Structure of bis-cyanine side product resulting from reaction of IR-786 with putrescine

2.2.3 Spectroscopic characterization of novel dye GC-1-23

The molar absorptivity was determined from the slope of a plot of absorbance versus concentration. Stock solutions were prepared in methanol and used to prepare working solutions (also in methanol) with concentrations ranging from 5 - 20 μM. The absorbance spectrum of each working solution was measured, and the absorption at the wavelength of maximum absorbance (λ_{MAX}^{AB}) was determined. The absorption values [A(λ)] at λ_{MAX}^{AB} were plotted as a function of dye concentration (C). Molar absorptivity [ε(λ)] at the wavelength of maximum absorption was calculated from the least squares slope of the data set, as per Beer's law (Equation 2.6). Molar absorptivity was determined from the average of five separate datasets.

The fluorescence quantum yield of GC-1-23 was calculated relative to indocyanine green (ICG). This standard was chosen as its maximum emission wavelength (~800 nm) is relatively close to that determined for the dye (~745 nm), thereby reducing errors resulting from wavelength dependent variation in detector response. A series of working solutions of both the dye and their respective standards were prepared for absorption measurements and each absorption sample was subjected to a 1:50 dilution to prepare the corresponding fluorescence sample. Fluorescence sample concentrations were selected to ensure an absorption of less than 0.1 at the excitation wavelength (λ_{EXC} = 650 nm) in order to prevent the inner filter effect.

The absorption and fluorescence spectra of each "set" of working solutions (dye and standard) were obtained concurrently to minimize experimental error from photobleaching. The emission spectra of the dyes were measured in triplicate using the ISS-K2 fluorimeter (at the invariable 650 nm excitation wavelength). For both sets of dyes, the area under each fluorescence curve was calculated and corrected for the Rayleigh peak area (if necessary). The average fluorescence peak areas were then calculated for each sample.

Quantum yield may be calculated according to Equation 2.7. As methanol was used as the solvent for both the standard and the unknown, the quotient n_U^2 / n_S^2 is unity, so Equation 2.7 simplifies to Equation 2.8.

$$\phi = \phi_S \left(\frac{FA_S}{F_S A}\right) \qquad 2.8$$

Quantum yield calculations may be carried out from either single point measurements of absorption and fluorescence or via plotting such measurements from serial dilutions. To carry out the quantum yield calculations for the novel dye, the latter approach was used. Fluorescence

peak areas (Int) of the fluorescence samples were plotted as a function of the absorption readings at λ_{EXC} [A(λ_{EXC})] for the absorption samples. The least squares lines were drawn for both the standard data set and the unknown data set, and the ratio of the slopes of the least squares lines for the unknown data set (m_U) and the standard data (m_S) set was used to calculate quantum yield, as shown in Equation 2.9.

$$\phi = \phi_S \left(\frac{m}{m_S}\right) \qquad 2.9$$

Equation 2.9 is obtained by rearranging Equation 2.8, given that slope $m = \Delta F/\Delta A$. Note also that as the dilution factor between the fluorescence and absorption samples remains constant and the equation for calculating quantum yield is a ratio, this dilution cancels without having to be factored into the equation.

2.3 Results and discussion

2.3.1 Determination of molar absorptivity and quantum yield of GC-1-23

Molar absorptivity of the dye GC-1-23 was determined in methanol. A representative plot of absorption as a function of concentration is provided in Figure 2.10, along with the least squares slope and correlation coefficient.

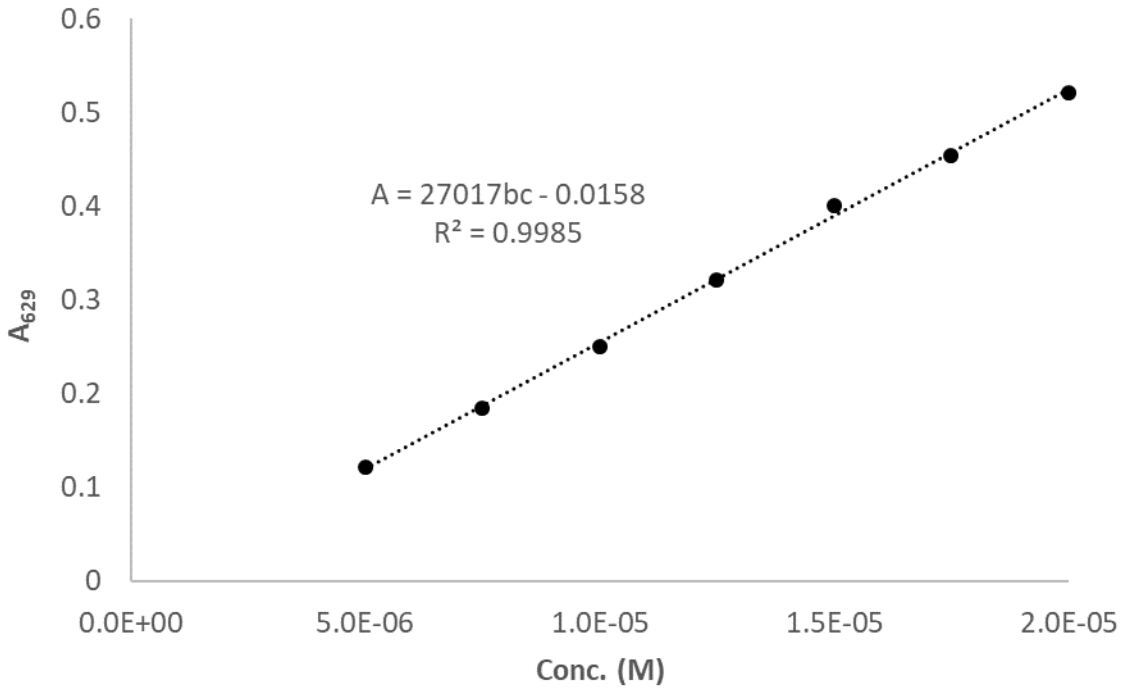

Figure 2.10: Absorption at 629 nm as a function of concentration for GC-1-23 in methanol

The wavelength of maximum absorption was determined to be 629 nm, and the average absorptivity from five separate measurements was calculated to be $2.6_9(\pm\ 0.16_6)*10^4$ M^{-1} cm^{-1}; the percent relative standard deviation of the five measurements was 6.2%. For similar *meso*-aminocyanine dyes; absorptivity values in methanol may range between 4000 – 40,000 M^{-1} cm^{-1} and absorption maxima fall between 613-638 nm.[29] This reduced absorptivity may be a consequence of the electron-donating nature of the amino group.

2.3.2 Spectroscopic characterization and Stokes shift of GC-1-23

Preliminary measurements of fluorescence were carried out to determine the Stokes shift and for the purpose of choosing a standard and excitation wavelength for the quantum yield studies. A comparison of the absorption and fluorescence spectra for dye GC-1-23 and parent cyanine IR-

786 is provided in Figure 2.11. The 118 nm (312 meV) Stokes shift demonstrated by aminocyanine dye GC-1-23 is massive compared to observed shifts in unfunctionalized cyanine dyes such as the parent compound IR-786 (22 nm; 46 meV). This increase in Stokes shift is attributable to a strong hypsochromic shift in the absorption spectrum; in accordance with the Dewar-Knott rule, *meso* substitution with an electron-donating amino group stabilizes the HOMO relative to the LUMO, thereby increasing the energy gap.[20-22] Additional differences between the electronic structures of the two dyes are manifested in the band broadening and disappearance of the Soret band ($S_0 – S_2$ transition, evident at ~700 nm in Figure 2.11.a) observed in the GC-1-23 spectra. These changes may both be attributable to the increased ICT character of the aminocyanine dye as discussed in Section 2.1.6; broad and featureless spectra are characteristic of ICT states and are typically observed for aminocyanines.[24, 29]

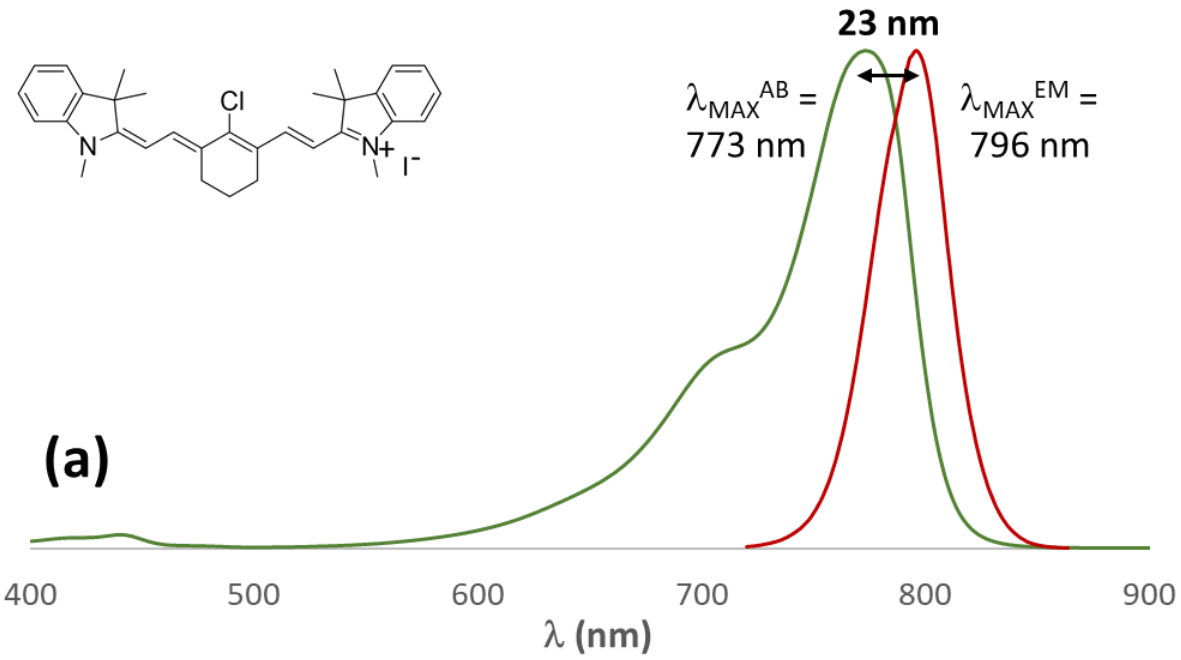

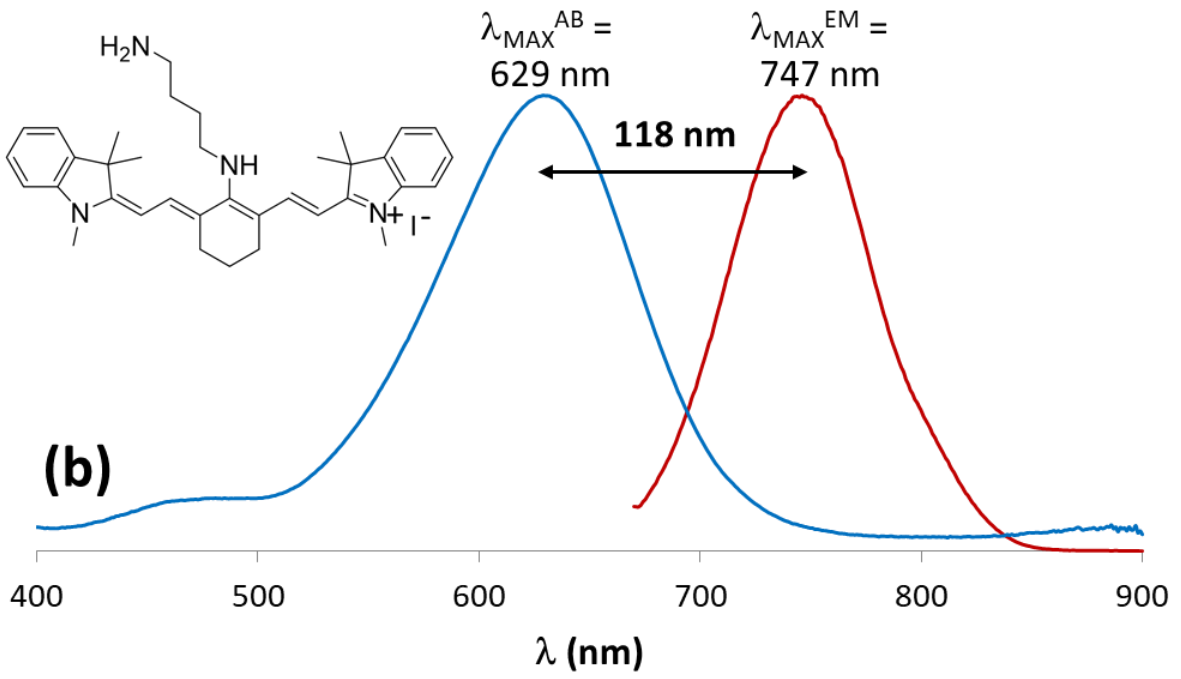

Figure 2.11: Normalized absorption and fluorescence spectra of (a) parent dye IR-786 and (b) aminocyanine derivative GC-1-23, with labeled Stokes shifts

2.3.3 Quantum yield of GC-1-23

While the exceptionally large Stokes' shift observed for dye GC-1-23 was intentionally created through dye functionalization and is considered highly desirable for the application, it did create a problem with respect to quantum yield standard selection. Following a comprehensive search of preexisting characterized standards, it was found that those possessing a wavelength of maximum excitation close to that of GC-1-23 tended to have a much lower wavelength of maximum emission, and those possessing a wavelength of maximum emission close to that of GC-1-23 had a wavelength of maximum excitation at a much longer wavelength. Moreover, fewer well-studied standards are available for dyes in the NIR region than those in the visible to UV region. Accordingly, indocyanine green (ICG) was chosen as it is a well-characterized fluorescence standard possessing an emission wavelength (~800 nm) relatively close to that determined for the dye (~745 nm), thereby reducing errors resulting from wavelength dependent variation in detector response. An excitation wavelength of 650 nm (slightly longer than the λ_{MAX} of GC-1-23) was chosen as a "compromise" so that the absorption of the standard would still be detectable while the energy of the photon would not be too low to excite the unknown dye as well.

The quantum yield of dye GC-1-23 was determined relative to ICG, as described in the experimental section. Quantum yield was calculated by taking the quotient of the slope of the dataset for the unknown and that of the standard and multiplying by the published quantum yield of the standard ICG (7.8%),[35] as per Equation 2.9. The average quantum yield from three iterations was found to be 21.0($\pm$0.9)%; the 4.7% percent relative standard deviation demonstrates adequate reproducibility. This calculated quantum yield is substantially higher than that of the parent cyanine IR-786 (7.6%),[19] higher than that of ICG, and higher than that of many

other compounds that fluoresce in this range. However, the calculated value appears reasonable as it falls within the range of published quantum yields for *meso*-aminocyanines (3%-47%).[24, 29, 30, 36]

2.4 Conclusions

Novel aminocyanine dye GC-1-23 was designed and synthesized in 33% yield. The structure and molecular weight of the dye was verified by NMR and HRMS, respectively. The dye exhibited a large Stokes shift of 118 nm. A molar absorptivity of 27,000 M^{-1} cm^{-1} and a quantum yield of 21% were determined for the synthesized compound. The large Stokes shift, high fluorescence quantum yield, and long wavelength absorption and fluorescence exhibited by dye GC-1-23 are promising features for the potential application of this dye in nanoparticle-based bioanalytical labeling applications.

2.5 References

1. Chasteen, T. G. Jablonski Diagram: Relaxation mechanism for excited state molecules. http://www.tissuegroup.chem.vt.edu/chem-ed/quantum/jablonsk.html (accessed November 27, 2017).

2. Lakowicz, J. R., *Principles of Fluorescence Spectroscopy*. 3rd ed.; Springer Science+Business Media, LLC: New York, 2006.

3. Skoog, D.; Holler, J.; Crouch, S., *Principles of Instrumental Analysis*. 6th ed. ed.; Thomson Brooks/Cole: Australia, 2007.

4. Hasson, K. C.; Gai, F.; Anfinrud, P. A., The photoisomerization of retinal in bacteriorhodopsin: Experimental evidence for a three-state model. *Proc. Natl. Acad. Sci. U.S.A* **1996,** *93* (26), 15124-15129.

5. Wald, G., The Molecular Basis of Visual Excitation. *Nature* **1968,** *219*, 800.

6. *Photochromism: Molecules and Systems*. Elsevier: Amsterdam, 2003.

7. Wasielewski, M. R., Photoinduced electron transfer in supramolecular systems for artificial photosynthesis. *Chem. Rev.* **1992,** *92* (3), 435-461.

8. Park, S. H.; Roy, A.; Beaupré, S.; Cho, S.; Coates, N.; Moon, J. S.; Moses, D.; Leclerc, M.; Lee, K.; Heeger, A. J., Bulk heterojunction solar cells with internal quantum efficiency approaching 100%. *Nat. Photonics* **2009,** *3*, 297.

9. Murphy, S.; Schuster, G. B., Electronic Relaxation in a Series of Cyanine Dyes: Evidence for Electronic and Steric Control of the Rotational Rate. *J. Phys. Chem.* **1995,** *99* (21), 8516-8518.

10. Soper, S. A.; Mattingly, Q. L., Steady-State and Picosecond Laser Fluorescence Studies of Nonradiative Pathways in Tricarbocyanine Dyes: Implications to the Design of Near-IR Fluorochromes with High Fluorescence Efficiencies. *J. Am. Chem. Soc.* **1994,** *116* (9), 3744-3752.

11. Fernando, N. T. Novel Near-Infrared Cyanine Dyes for Fluorescence Imaging in Biological Systems. Ph.D. Dissertation, Georgia State University, Atlanta, GA, 2011.

12. Ranjit, S.; Gurunathan, K.; Levitus, M., Photophysics of Backbone Fluorescent DNA Modifications: Reducing Uncertainties in FRET. *J. Phys. Chem. B* **2009,** *113* (22), 7861-7866.

13. Strekowski, L.; Lipowska, M.; Patonay, G., Substitution reactions of a nucleofugal group in heptamethine cyanine dyes. Synthesis of an isothiocyanato derivative for labeling of proteins with a near-infrared chromophore. *J. Org. Chem.* **1992,** *57* (17), 4578-4580.

14. Strekowski, L.; Lipowska, M.; Patonay, G., Facile Derivatizations of Heptamethine Cyanine Dyes. *Synth. Commun.* **1992,** *22* (17), 2593-2598.

15. Zhang, Z.; Achilefu, S., Synthesis and Evaluation of Polyhydroxylated Near-Infrared Carbocyanine Molecular Probes. *Org. Lett.* **2004,** *6* (12), 2067-2070.

16. Cooper, M.; Ebner, A.; Briggs, M.; Burrows, M.; Gardner, N.; Richardson, R.; West, R., Cy3B™: Improving the Performance of Cyanine Dyes. *J. Fluoresc.* **2004,** *14* (2), 145-150.

17. Tyutyulkov, N.; Fabian, J.; Mehlhorn, A.; Dietz, F.; Tadjer, A., *Polymethine Dyes: Structure and Properties*. St. Kliment Ohridski University Press: Sofia, 1991.

18. Mishra, A.; Behera, R. K.; Behera, P. K.; Mishra, B. K.; Behera, G. B., Cyanines during the 1990s: A Review. *Chem. Rev.* **2000,** *100* (6), 1973-2012.

19. Chapman, G.; Henary, M.; Patonay, G., The Effect of Varying Short-Chain Alkyl Substitution on the Molar Absorptivity and Quantum Yield of Cyanine Dyes. *Anal. Chem. Insights* **2011,** *6*, 29-36.

20. Matichak, J. D.; Hales, J. M.; Barlow, S.; Perry, J. W.; Marder, S. R., Dioxaborine- and Indole-Terminated Polymethines: Effects of Bridge Substitution on Absorption Spectra and Third-Order Polarizabilities. *J. Phys. Chem. A* **2011,** *115* (11), 2160-2168.

21. Knott, E. B., 227. The colour of organic compounds. Part I. A general colour rule. *J. Chem. Soc.* **1951,** (0), 1024-1028.

22. Dewar, M. J. S., 478. Colour and constitution. Part I. Basic dyes. *J. Chem. Soc.* **1950,** (0), 2329-2334.

23. Lakowicz, J. R.; Malicka, J.; D'Auria, S.; Gryczynski, I., Release of the self-quenching of fluorescence near silver metallic surfaces. *Anal. Biochem.* **2003,** *320* (1), 13-20.

24. Peng, X.; Song, F.; Lu, E.; Wang, Y.; Zhou, W.; Fan, J.; Gao, Y., Heptamethine Cyanine Dyes with a Large Stokes Shift and Strong Fluorescence: A Paradigm for Excited-State Intramolecular Charge Transfer. *J. Am. Chem. Soc.* **2005,** *127* (12), 4170-4171.

25. Levitz, A.; Marmarchi, F.; Henary, M., Synthesis and Optical Properties of Near-Infrared meso-Phenyl-Substituted Symmetric Heptamethine Cyanine Dyes. *Molecules* **2018,** *23* (2), 226.

26. Descalzo, A. B.; Rurack, K., On the Signalling Pathways and CuII-Mediated Anion Indication of N-meso-Substituted Heptamethine Cyanine Dyes. *Chem. Eur. J.* **2009,** *15* (13), 3173-3185.

27. Matsui, M.; Hashimoto, Y.; Funabiki, K.; Jin, J.-Y.; Yoshida, T.; Minoura, H., Application of near-infrared absorbing heptamethine cyanine dyes as sensitizers for zinc oxide solar cell. *Synth. Met.* **2005,** *148* (2), 147-153.

28. Lee, H.; Mason, J. C.; Achilefu, S., Synthesis and Spectral Properties of Near-Infrared Aminophenyl-, Hydroxyphenyl-, and Phenyl-Substituted Heptamethine Cyanines. *J. Org. Chem.* **2008,** *73* (2), 723-725.

29. Ornelas, C. L., R.; Durandin, A.; Canary, J. W.; Pennell, R.; Liebes, L. F.; Weck, M., Combining Aminocyanine Dyes with Polyamide Dendrons: A Promising Strategy for Imaging in the Near-Infrared Region. *Chem Eur. J.* **2011,** *17*, 3619-3629.

30. Myochin, T.; Kiyose, K.; Hanaoka, K.; Kojima, H.; Terai, T.; Nagano, T., Rational Design of Ratiometric Near-Infrared Fluorescent pH Probes with Various pKa Values, Based on Aminocyanine. *J. Am. Chem. Soc.* **2011,** *133* (10), 3401-3409.

31. Labéguerie-Egéa, J.; McEvoy, H. M.; McDonagh, C., Synthesis, characterisation and functionalisation of luminescent silica nanoparticles. *J. Nanopart. Res.* **2011,** *13* (12), 6455-6465.

32. Liu, A.; Wu, L.; He, Z.; Zhou, J., Development of highly fluorescent silica nanoparticles chemically doped with organic dye for sensitive DNA microarray detection. *Anal. Bioanal. Chem.* **2011,** *401* (6), 2003-11.

33. Lipowska, M.; Patonay, G.; Strekowski, L., New Near-Infrared Cyanine Dyes for Labelling of Proteins. *Synth. Commun.* **1993,** *23* (21), 3087-3094.

34. Simons, D. M., Spacers, Probability, and Yields. *Bioconjugate Chem.* **1999,** *10* (1), 3-8.

35. Benson, R. A.; Kues, H. A., Fluorescence properties of indocyanine green as related to angiography. *Phys. Med. Biol.* **1978,** *23* (1), 159-163.

36. Kiyose, K.; Aizawa, S.; Sasaki, E.; Kojima, H.; Hanaoka, K.; Terai, T.; Urano, Y.; Nagano, T., Molecular Design Strategies for Near-Infrared Ratiometric Fluorescent Probes Based on the Unique Spectral Properties of Aminocyanines. *Chem. Eur. J.* **2009,** *15* (36), 9191-9200.

3 SILICA NANOPARTICLE SYNTHESIS AND CHARACTERIZATION

3.1 Introduction

3.1.1 Importance of silica nanoparticles

Silica nanoparticles remain an important and growing interest to the fields of materials science, medicine, and bioanalytical chemistry due to their straightforward synthesis and versatility. These nanostructures serve as excellent scaffolds with a wide and tunable variety of sizes and morphologies, and their chemistry allows for surface modifications and covalent or noncovalent incorporation of a nearly endless variety of other compounds and materials. Accordingly, there are diverse potential applications of silica nanoparticles ranging from water purification and solar cells to catalysis and drug delivery systems.[1-8] As discussed in Section 1.4.7, silica nanoparticles are characterized by porosity; both mesoporous and nonporous silica nanoparticles possess useful attributes for different biomedical and bioanalytical applications. Mesoporous silica nanoparticles possess porous channels; the large surface areas of these structures allow for either dense surface modification or noncovalent assimilation of payloads (e.g. drug delivery).[9] On the other hand, nonporous dye-doped silica nanoparticles are of particular interest as fluorescent labels, as they provide significantly enhanced per-label fluorescence intensities, greater photostabilities, and improved shielding from environmental effects relative to labeling techniques based on the use of individual dye molecules.[10, 11] The following discussion concerns only the nonporous variety of silica particles, as these were the focus of this project.

3.1.2 Synthesis of silica nanoparticles

Silica nanoparticles may be synthesized via sol-gel condensation of orthosilicate esters such as TEOS under either monophasic reaction conditions (such as the Stöber process, Figure 3.1.a) or biphasic reaction conditions (such as the reverse microemulsion process, Figure 3.1.b).

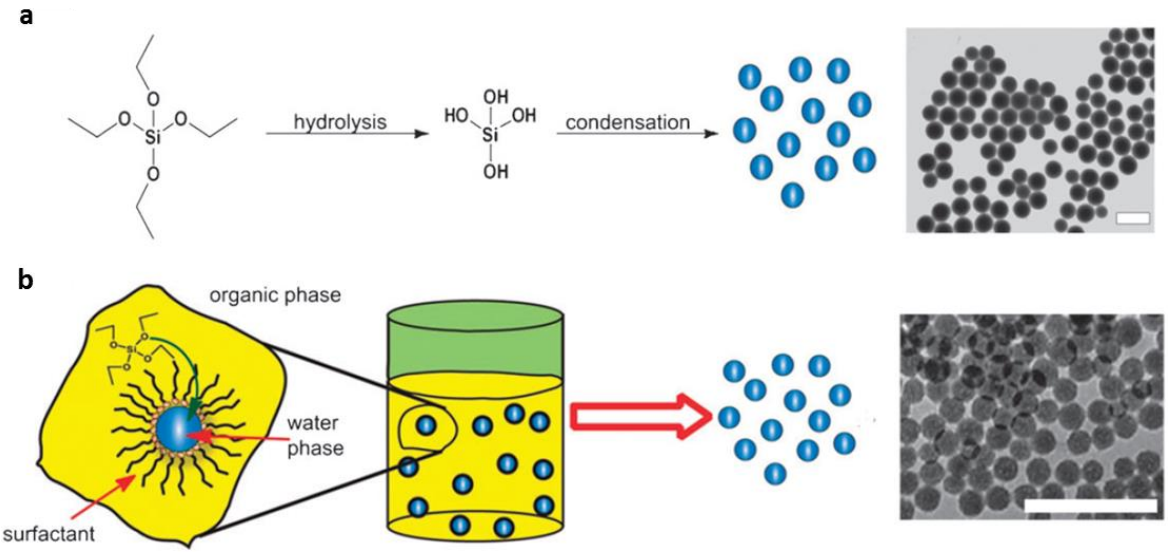

Figure 3.1: Representative nanoparticle synthetic approaches: (a) monophasic Stöber process; (b) biphasic reverse microemulsion process[12]

Dye molecules may be noncovalently or covalently incorporated into the silica matrix in order to create fluorescent nanoparticles. Noncovalent incorporation is only possible using biphasic reaction conditions and dyes with sufficient hydrophilicity to partition into the aqueous phase (Figure 3.2.a); as previously discussed in Section 1.4.7, noncovalent incorporation both predisposes the dyes to leaching and limits the options for dye incorporation.[13, 14] Covalent dye incorporation (Figure 3.2.b) is the preferred approach for probe stability and flexibility of fluorophore choice. This is accomplished through the formation of a dye-silane conjugate via

covalent coupling of the desired fluorophore with an appropriately functionalized trialkoxysilane, followed by copolymerization of the dye-silane conjugate with TEOS or another orthosilicate ester. This covalent coupling approach is highly versatile; a wide variety of different alkoxysilanes are commercially available to facilitate the covalent incorporation of nearly any dye bearing reactive moieties.

The distribution of copolymerized dye molecules within the silica matrix may be controlled by the timing and order of reagent addition. When dye-silane conjugates are added to the reaction solution and allowed to prehydrolyze prior to TEOS addition (Figure 3.2.b), the dye molecules will be distributed throughout the nanoparticle matrix, whereas if TEOS is added prior to the dye-silane conjugates, the fluorophores will reside on the nanoparticle exterior. If desired, stepwise additions of TEOS and dye-silane conjugates can even be made to reaction solutions in order to furnish discrete layers of fluorophore and matrix.[15, 16] For applications requiring stable fluorescent probes with high fluorescence intensities, low environmental sensitivities, and minimal dye leaching, covalent incorporation of dyes distributed throughout the nanoparticle interior is generally preferable.[10, 13, 14] Dyes encapsulated within silica nanoparticles have repeatedly been shown to exhibit higher quantum yields than free dye molecules in solution.[17, 18] This has been attributed to a restriction in dye mobility within the solid silica matrix, leading to a decrease in the rate of nonradiative energy loss for excited-state molecules.[15] Similarly, encapsulated dye molecules demonstrate substantially enhanced photostability relative to free dyes in solution as a posited result of being both conformationally restrained and isolated from solvent interactions.[19]

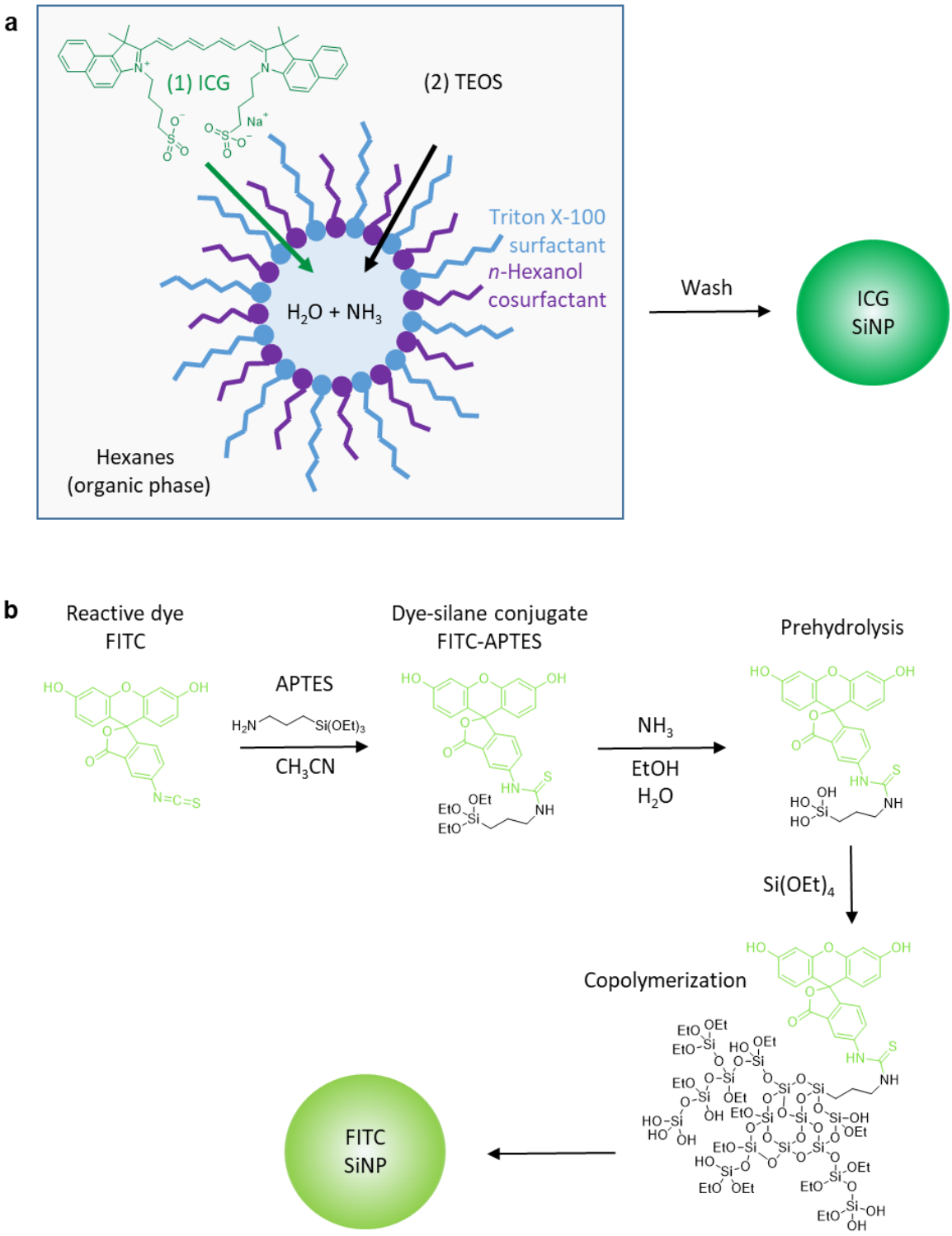

Figure 3.2: Examples of different approaches for dye incorporation into silica nanoparticles: (a) noncovalent incorporation of hydrophilic dye indocyanine green (ICG) via biphasic reverse microemulsion synthesis; (b) covalent incorporation of isothiocyanate-modified fluorescein (FITC) via formation of silane conjugate (FITC-APTES) followed by monophasic Stöber synthesis

3.1.3 Surface modification of nanoparticles for biocompatibility and bioconjugation

While silica nanoparticles encapsulating fluorescent dyes display numerous advantages as fluorescent probes, nanoparticle surfaces must be suitably functionalized in order to be useful for bioanalysis. A number of reports indicate bare silica nanoparticles cause both *in vivo* and *in vitro* toxicity via a number of putative mechanisms, including membrane disruption and generation of reactive oxygen species.[20] Furthermore, bare nanoparticles possess very large surface-area-to-volume ratios and high surface charge densities; as a consequence, these materials have a strong tendency to adsorb proteins *in vivo* via combinations of steric, Van der Waals, and electrostatic interactions. This tendency, known as the protein corona effect, can significantly and unpredictably alter the biological outcome of nanoparticle introduction into a living system.[21, 22] Furthermore, the adsorption or covalent linkage of proteins directly onto nanoparticle surfaces can often lead to conformational changes and denaturation of the involved proteins; this tendency results in additional challenges associated with functionalizing nanoparticles for *in vitro* applications.[23-25] Furthermore, silica nanoparticles display a tendency to irreversibly coagulate in electrolyte solutions and at pH values approaching the isoelectric point.[26, 27]

The unfavorable tendencies of nanoparticles towards coagulation, toxicity, and nonspecific adsorption and denaturation of proteins may be addressed via carefully chosen surface modifiers. Surface modification approaches for addressing coagulation generally fall into one of two categories: modifiers that change the charge distribution in order to increase electrostatic repulsion between particles (typically zwitterionic or negatively-charged moieties)[28-33] and modifiers that improve solubility in water via improved hydrophilic interactions (such as polyethylene glycol and dextran).[34-38] While zwitterionic and negatively charged surface

modifiers are quite effective in preventing flocculation, surface modifiers must also address the issues of toxicity and nonspecific adsorption and denaturation of either the capture biomolecules to be used (for *in vitro* assay applications) or the biomolecules present in the living system (in the case of *in vivo* applications); introduction of highly charged and zwitterionic moieties can in some cases actually strengthen these undesired interactions through electrostatic forces. On the other hand, the introduction of PEG or dextran can be effective in improving nanoparticle dispersity in aqueous solutions, reducing nanoparticle toxicity in vivo, and blocking interactions with the nanoparticle surface through steric shielding.[39-42] Furthermore, for applications requiring further bioconjugation of nanomaterials, derivatives of PEG and dextran containing common terminal functionalities (such as biotin) are already commercially available.

Targeted bioanalytical applications of nanomaterials requires a linkage between the signaling probe (nanoparticle) and the affinity reagent (antibody or aptamer). This linkage is often accomplished through t[41]he use of the avidin-biotin system due to the uniquely high affinity (Kd = 0.6 x 10^{-15} M) and specificity of the protein-ligand bond.[43-45] Biotin (Figure 3.3.a) is a key coenzyme used in a variety of metabolic processes by both prokaryotes and eukaryotes. Avidin is a 66 kDa tetrameric protein found in the egg whites of amphibians, reptiles, and birds; this protein is postulated to function as a bacteriostatic agent in eggs via sequestration of biotin needed for bacterial growth.[46-48] The original avidin-biotin system has been exploited in biotechnology applications for more than 40 years; however, the application of unprocessed egg white avidin does present a few challenges. Egg white avidin is a glycosylated protein possessing a strongly negative charge at physiologic pH (pI ≈ 10); the consequence of these characteristics is the possibility of nonspecific binding with certain nontarget interferents when this protein is applied, particularly at physiological pH.[47, 49] More recently, a bacterial form of avidin (known as

streptavidin, Figure 3.3.b) was isolated from *Streptomyces avidinii*; this 53 kDa tetrameric protein shares a similar binding affinity for biotin (Kd = 4 x 10^{-14} M), but it demonstrates substantially less nonspecific binding than egg white avidin due to its lack of glycosylation and its nearer-to-neutral isoelectric point (pI = 6.8-7.5).[45, 47] More recently still, a modified deglycosylated form of egg white avidin (deemed NeutrAvidin), has been prepared. NeutrAvidin possesses a reduced mass (60 kDa) and a near neutral isoelectric point (pI = 6.3) while still maintaining the same biotin binding efficiency as unmodified avidin; furthermore, this derivative exhibits the highest specificity of any of the three commercially important forms of avidin.[47]

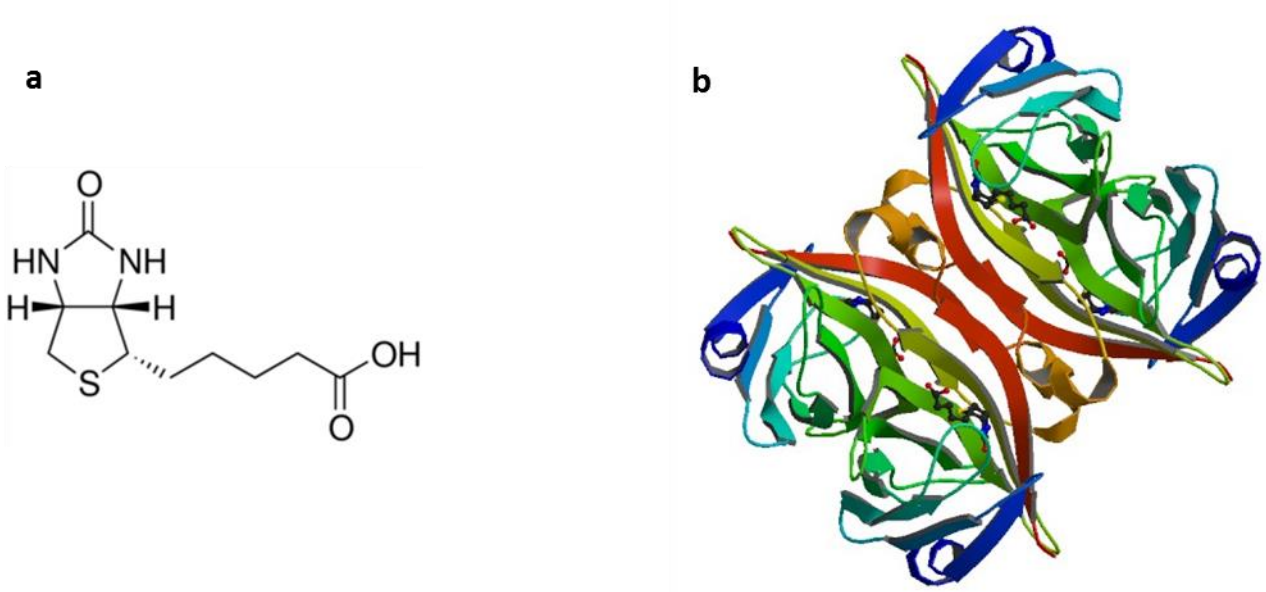

Figure 3.3: Structures of (a) free biotin and (b) streptavidin bound to biotin[50]

Regardless of the form of avidin used, the avidin-biotin system is a crucial component of countless bioconjugation schemes. While direct linkage of an affinity probe may be accomplished by covalent or noncovalent binding to NP surfaces, this can result in reduced activity through either denaturing or blocking of the probe's active site (Figure 3.4.a). Avidin-biotin linkages may involve binding biotin to the affinity reagent and avidin to the signaling

probe (Figure 3.4.b), or vice versa.[51, 52] Alternatively, both the signaling probe and the affinity reagent may first be biotinylated, and avidin may be introduced in order to link the two together (Figure 3.4.c).[51]

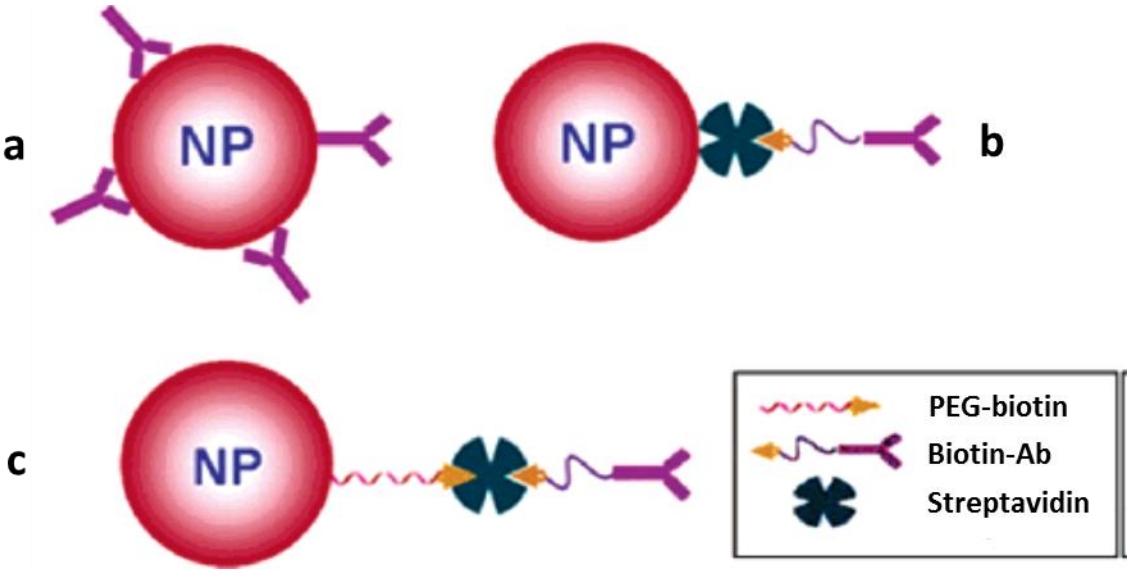

Figure 3.4: Bioconjugation of antibodies (Ab) to NPs: (a) direct conjugation of Ab to surface; (b) direct binding of streptavidin to NP surface and conjugation using biotinylated Ab; (c) use of streptavidin as a "bridge" to link PEG-biotin bound NPs to biotinylated Ab[51]

3.1.4 Overview

In the present chapter, the synthesis, characterization, surface functionalization, and proofs of concept for bioanalytical applications of dye-encapsulated silica nanoparticles (NPs) are explored. Preliminary work was focused on the investigation and optimization of NP synthetic techniques, molar ratios of dye-silane conjugates, and surface coating densities for NPs encapsulating various dye-silane conjugates. Following the optimization of techniques, NPs containing single or multiple (FRET-paired) dye species were synthesized in order to produce a series of NPs with large Stokes shifts and readily differentiable fluorescence signals. These NPs were characterized with respect to size, synthesis yield, reproducibility of relative dye doping

ratios, extent of dye leaching, quantum yield, and fluorescence enhancement. Suitability for *in vitro* use was demonstrated through binding to streptavidin microbeads and imaging using fluorescence microscopy, and *in vivo* suitability was demonstrated through nonspecific protein binding studies and a hemolysis assay.

3.2 Preliminary work

3.2.1 Introduction

Preliminary studies were focused primarily on the optimization of methods for preparing dye-copolymerized NPs and the optimization of surface coatings for bioanalytical applications. Dye-silane conjugates used as the building blocks for fluorescent NPs were prepared from three different dyes: fluorescein isothiocyanate (FITC), Texas Red (TR; sulforhodamine 101 acid chloride), and the novel aminocyanine GC-1-23 described in Chapter 2. Of the three dyes, FITC possesses the shortest wavelength excitation and emission, GC-1-23 exhibits the longest, and TR falls in between; optical absorption and fluorescence properties of the three dyes combined span from the blue to the near infrared regions of the electromagnetic spectrum. These dyes were chosen for their reactive functionalities, high quantum yields, and the significant overlap of their absorption and emission spectra; the three can either be used separately to prepare single dye copolymerized NPs or together as multidye copolymerized resonance energy transfer paired NPs. Alkoxysilane conjugates of FITC and TR were furnished via reaction with (3-aminopropyl)triethoxysilane (APTES), whereas the alkoxysilane conjugate of GC-1-23 was furnished via reaction with 3-(triethoxysilyl)propyl isocyanate (ICPTES).

Several nanoparticle synthetic routes were explored, including the biphasic reverse microemulsion process and the monophasic Stöber process (using both uncontrolled and

controlled addition of TEOS). Dye molar ratios were optimized for per-particle fluorescence intensity, and the distribution of copolymerized dye molecules within the nanoparticle matrix was probed using relative fluorescence experiments in different solvents. Nanoparticle surfaces were modified with polyethylene glycol-silane derivatives and biotin for efficient biological "stealthing;" both the total surface coverages and the relative surface coating ratios were optimized.

3.2.2 Experimental

3.2.2.1 Reagents, materials, and instrumentation

Acetic acid (AcOH, glacial, >99%), acetonitrile (CH_3CN, CHROMASOLV® Plus, for HPLC, ≥99.9%), (3-aminopropyl)triethoxysilane (APTES, > 98%), N,N-dimethylformamide (DMF, 99.8%), fluorescein isothiocyanate (FITC, 98%), 1-hexanol (98%), tetraethyl orthosilicate (TEOS, 99.999%), and 3-(triethoxysilyl)propyl isocyanate (ICPTES, 95%) were obtained from Sigma Aldrich (St. Louis, MO). Aqueous ammonia (certified ACS plus, 29.6%), methanol (MeOH, certified ACS, >99.8%), neutravidin coated high capacity microplates, sodium phosphate monobasic monohydrate (certified, >98%), and sodium phosphate dibasic dodecahydrate (99%) were obtained from Thermo Fisher Scientific (Waltham, MA). Absolute 200 proof ethanol (EtOH) was obtained from Greenfield Ethanol, Inc. (Toronto, ON). Biotin-polyethylene glycol-silane (Bio-PEG-Sil, MW 3400) and methoxypolyethylene glycol-silane (mPEG-Sil, MW 1000) were obtained from Laysan Bio (Arab, AL). Sulforhodamine 101 acid chloride (Texas Red/TR, 96.5%) was purchased from Chemodex (St. Gallen, Switzerland). Dye GC-1-23 was synthesized as detailed in 2.2.2. Triply deionized water was obtained from a

Barnstead Nanopure water purification system (Thermo Fisher Scientific, West Palm Beach, FL).

All volumetric glassware (pipets used to deliver volumes greater than 1 mL and volumetric flasks) was categorized as class A. Volumes less than 1 mL were delivered using either a 10-100 μL or a 100-1000 μL adjustable volume Eppendorf pipette, and in cases where volumetric pipets or flasks were unavailable in the desired volume, volumes larger than 1 mL were delivered via a positive-displacement Eppendorf repeating pipette (Eppendorf, Hauppauge, NY.). UV-visible and fluorescence spectroscopic measurements were carried out on Biotek Synergy H1 and Synergy H4 Microplate Readers (Biotek, Winooski, VT) and results were generated using Biotek Gen5 Software (v.2.04.11). Additional calculations, spectral processing, and spectral deconvolutions were carried out using Microsoft Excel (2016, Microsoft Corporation, Redmond, WA) and a|e - UV-Vis-IR Spectral Software (v.2.2, FluorTools, www.fluortools.com). Transmission electron microscopy (TEM) was carried out using a ZEISS Leo 906E Transmission Electron Microscope (ZEISS, Jena, Germany).

3.2.2.2 Formation of FITC-APTES conjugate

Fluorescein isothiocyanate (FITC) was combined with (3-aminopropyl)triethoxysilane (APTES) to prepare the silane conjugate FITC-APTES for covalent encapsulation into NPs. The FITC dye reagent was quickly transferred into a closed, preweighed vial and the mass measured by difference, then FITC was dissolved in an appropriate volume of acetonitrile (or 1-hexanol) with stirring to produce a 1 mM dye solution. Following 30 minutes of stirring to fully dissolve the dye, a 1.5-10 fold excess of APTES was added to the flask and the mixture was stirred in the dark for 16 hours to promote complete formation of the thiourea linkage between the amino

group and the isothiocyanate moiety. This reaction is detailed in Equation 3.1. Note that while acetonitrile is an excellent solvent for this reaction when the conjugate is used in Stöber nanoparticle syntheses, it is important to prepare dye-silane conjugates in 1-hexanol for use in the reverse microemulsion nanoparticle synthesis in order to avoid disrupting the micellar structures that control the ingress of reactants and serve as structural templates in the reaction.

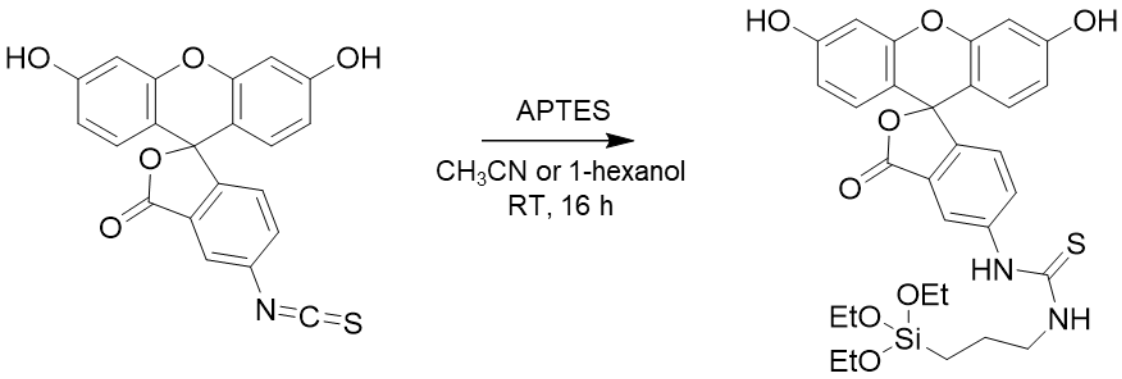

Equation 3.1: Formation of FITC-APTES conjugate

3.2.2.3 Formation of TR-APTES conjugate

Texas Red Sulfonyl Chloride (TR) was combined with (3-aminopropyl)triethoxysilane (APTES) to prepare the silane conjugate TR-APTES for covalent encapsulation into NPs. The TR dye reagent was quickly transferred into a closed, preweighed vial and the mass measured by difference, then the dye was dissolved in an appropriate volume of dry, fresh DMF with stirring to produce a 1 mM dye solution. Following brief stirring to fully dissolve the dye, a 1.5-fold excess of APTES was added to the vial and the mixture was stirred in the dark for 3 hours to

promote complete formation of the sulfonamide linkage between the amino group and the isothiocyanate moiety. This reaction is detailed in Equation 3.2.

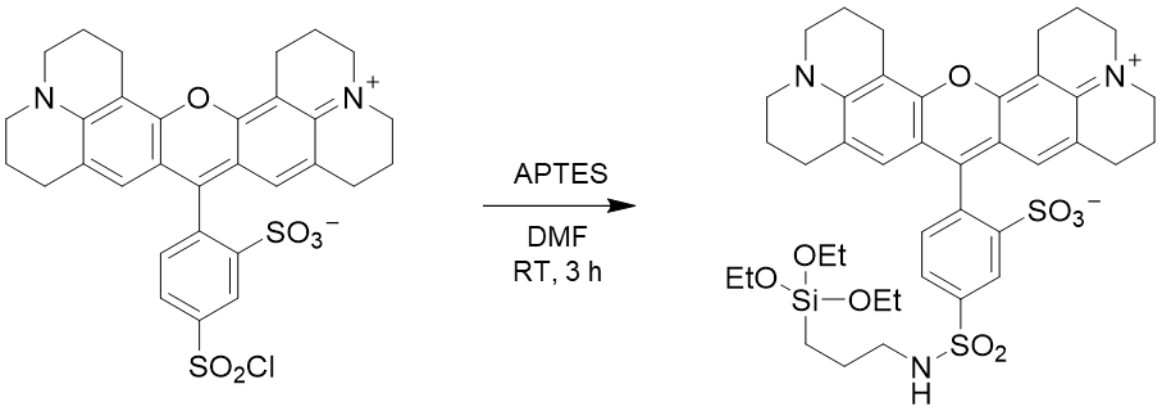

Equation 3.2: Formation of TR-APTES conjugate

3.2.2.4 Formation of GC-1-23-ICPTES conjugate

Aminocyanine dye GC-1-23 was combined with 3-(triethoxysilyl)propyl isocyanate (ICPTES) to produce dye-silane conjugate GC-1-23-ICPTES. A sample of GC-1-23 was transferred quickly into a closed, weighed vial and the mass was measured by difference. The GC-1-23 sample was dissolved directly in the weighing vial in a small volume of acetonitrile with stirring, resulting in a 2 mM solution. The reaction vial was protected from light using aluminum foil. Following 30 minutes of stirring to fully dissolve the dye, a 1.5-10 fold excess of ICPTES was added to the flask and the mixture was stirred in the dark for 16 hours to allow complete formation of the urea linkage between the amino group and the isocyanate moiety. This reaction is detailed in Equation 3.3.

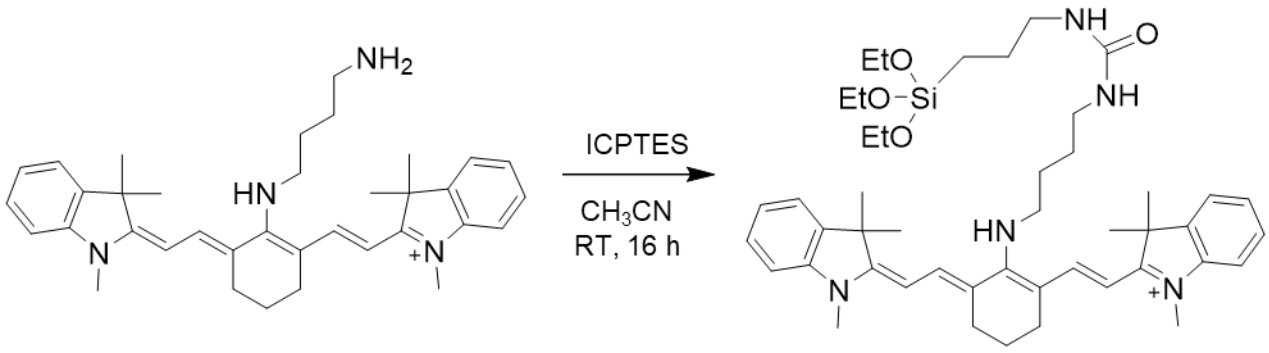

Equation 3.3: Formation of GC-1-23-ICPTES conjugate

3.2.2.5 Reverse microemulsion NP synthesis

A reverse microemulsion was prepared by combining 15 mL cyclohexane, 1.125 mL deionized water, 3.550 mL of Triton X-100 (as surfactant), and 2.60 mL of 1-hexanol (as co-surfactant) and stirring vigorously until the cloudy mixture became clear (approximately 15 minutes). At this point, 1.0 mL of FITC-APTES conjugate in 1-hexanol was introduced to the reaction vessel and vigorous stirring was continued for 30 minutes to allow partitioning of the conjugate into the reverse micelles and prehydrolysis. After 30 minutes, 0.20 mL of tetraethyl orthosilicate (TEOS) was introduced into the reaction mixture, followed by 0.14 mL of 28% aqueous ammonia (NH_3) to catalyze the polymerization reaction. The reaction was left to stir in the dark at room temperature for 18-21 hours, after which the NPs were separated from the reaction mixture by centrifuging at 10,397 g for 30 minutes. The supernatant was separated from the pellet, the pellet was resuspended in ethanol via sonication, and the centrifugation was repeated as a washing step. Washing was carried out in this manner three times with ethanol and three times with deionized water, then NPs were resuspended in 15 mL ethanol.

3.2.2.6 Stöber synthesis of silica NPs using uncontrolled addition of TEOS

Stöber synthesis of dye-doped NPs was carried out following a published synthetic procedure.[53] Changes to the synthesis were the following: the total reaction volume was adjusted to 20 mL (from an original volume of 49 mL) and reagent volumes were scaled down accordingly, and the initial concentration of FITC-APTES conjugate (in EtOH) was 3.71 mM (versus the published concentration of 5.09 mM); the volume of FITC-APTES was scaled accordingly to produce an equivalent final FITC-APTES concentration. Despite the reduction in reaction volume, all final reactant concentrations were equal to those published. Briefly, our adapted synthetic parameters were as follows: in a closed reaction vessel protected from light, 17.90 mL ethanol, 55 μL deionized water, and 0.742 mL of 29.6% NH_3 were combined with stirring for 5 minutes. Following this, 0.549 mL FITC-APTES conjugate (3.71 mM in EtOH) was added to the mixture, and the conjugate was allowed to hydrolyze for 1 minute (in an alternate approach, this time was increased to 12 hours). Following hydrolysis, 0.759 mL TEOS was added to the reaction mixture quickly and all at once, and the reaction was allowed to continue for an additional 20 hours. The NPs were separated from the reaction mixture by centrifuging at 10,397 g for 30 minutes. Without undue delay, the supernatant was separated from the pellet, the pellet was resuspended in ethanol via sonication, and the centrifugation was repeated as a washing step. In all cases, the supernatant was removed and the pellet was resuspended as quickly as possible following centrifugation in order to prevent aggregation of the synthesized NPs. Washing was carried out three times with ethanol and the final NP solution was resuspended in 15 mL ethanol.

3.2.2.7 Stöber synthesis of silica NPs using controlled addition of TEOS

In a closed reaction vessel protected from light, 15.75 mL ethanol, 0.780 mL deionized water, and 0.500 mL of 29.6% NH_3 were combined with stirring for 5 minutes. Following this, the desired volume of dye-silane conjugate was added to the mixture, and the conjugate was allowed to hydrolyze for 30 minutes prior to addition of TEOS. In a separate vial, 10.00 mL of 50 mM TEOS solution was prepared in absolute ethanol. A total of 5.00 mL of TEOS solution was added slowly by syringe pump at a flow rate of approximately 0.29 mL/h. The syringe was connected to the closed reaction vessel via a piece of Tygon tubing and a custom glass fitting (inserted through the stopper). Following addition of all TEOS, the reaction was allowed to proceed for an additional 2 hours, then NPs were separated from the reaction mixture and cleaned up using the same procedure detailed in 3.2.1.6.

3.2.2.8 Surface modification of Stöber silica NPs with biotin and polyethylene glycol

Silica NPs were surface functionalized with Bio-PEG-Sil and mPEG-Sil in order to both passivate the NP surfaces and prepare them for further bioconjugation applications. Following reaction cleanup, ethanol solutions of NPs at concentrations of ~0.9 mg/mL were pipetted into centrifuge tubes containing stir bars and set to stir at 320 rpm. Separately, Bio-PEG-Sil was dissolved in 1 mM AcOH(aq) at a concentration of 50 mg/mL, and mPEG-Sil was dissolved in 1 mM AcOH(aq) at a concentration of 70 mg/mL. Polyethylene glycol surface modifiers were prehydrolyzed in their respective acid solutions for 10 min, then appropriate volumes of Bio-PEG-Sil and mPEG-Sil solutions were introduced to the NP samples with continued stirring in order to furnish the desired surface coverage densities. Specific surface areas (SSA) of NPs were

determined using Equation 3.4. In this equation, d is the NP diameter (in nm) and ρ is the density of silica (2.2 g/cm^3).[54-56]

$$\text{SSA } (m^2/g) = \frac{6000}{d\rho} \quad 3.4$$

The volumes of PEG-silane reagent to be added were then calculated based on NP mass, the desired surface coverage density of PEG-silane (μmol/m^2), and the initial concentrations of PEG-silane reagents in 1 mM AcOH solutions. Surface functionalization reactions were carried out for 2 hours at room temperature, then surface passivated NPs were centrifuge washed three times using a 50% EtOH/H_2O mixture. Resuspension was carried out carefully using brief sonication steps in an ice bath. As-prepared PNPs (NPs functionalized only with mPEG-Sil) and BPNPs (NPs functionalized with both mPEG-Sil and Bio-PEG-Sil) were stored in 50% EtOH/H_2O mixtures at 4 °C until further use.

3.2.2.9 Optimization of NP surface modifier coverage: microplate binding studies

Apparent avidin binding efficiency was tested by determining postwash fluorescence intensity of biotinylated and PEGylated FITC-NPs relative to that of fluorescein-PEG-biotin (BPF) on neutravidin-coated microplates. The apparent binding efficiency was first assessed as a function of the total PEG surface coverage, then as a function of the ratio of Bio-PEG-Sil:mPEG-Sil. All BPNPs and PNPs (with varying total surface coverages and surface coverage ratios) were prepared from a single batch of FITC-NPs in order to ensure no inherent variation in fluorescence intensity between samples with varying surface coatings. The prepared BPNPs were centrifuged and resuspended in syringe-filtered phosphate buffer (PB, 11.8 mM, pH 7.4) twice,

with resuspension carried out via brief sonication in an ice bath. For the neutravidin conjugation reactions, 100 uL of surface-modified NP solution or BPF solution (also in PB) was introduced to each microplate well. The NP and BPF solutions were made up in such a manner that the introduced concentration was in substantial excess (>60x) of that needed for saturation in order to ensure complete binding site occupancy. The biotinylated fluorophores were incubated in the microplate wells for two hours at room temperature with gentle agitation on a laboratory rocker, then microplate wells were each thoroughly washed a total of five times with PB in order to reduce the likelihood of nonspecific binding. Following plate washing, microplates were gently tapped on an absorbent tissue to remove excess liquid from microplate wells and surfaces. Nonspecific binding was assessed via concurrent analysis of biotin-free FITC-NPs modified with only mPEG-Sil.

3.2.2.10 Determination of solvent-accessible dye residues

In order to determine whether the dye molecules were actually encapsulated and distributed within the NPs or just linked to the NP surface, the solvent-dependent fluorescence changes of dye-copolymerized NPs were determined relative to those of their respective "free" dye-silane conjugates (FITC-APTES, TR-APTES, and GC-1-23-ICPTES). The solvent systems compared for these purposes were EtOH and PB (phosphate buffer, 11.8 mM, pH 7.4) since these were the two primary solvent systems used in most of the NP characterization and bioconjugation steps. Fluorescence intensities (I_F) were calculated for each sample in each solvent, then the percentage change (%Change) was calculated as per Equation 3.5. Absorption values at excitation wavelengths (450, 510, and 650 nm for FITC, TR, and GC-1-23,

respectively) were acquired for all samples and verified to be < 0.1 in order to ensure minimal contributions from the inner filter effect.

$$\%\text{Change} = \frac{|F_{PB} - F_{EtOH}|}{F_{EtOH}} \times 100 \quad (3.5)$$

In order to draw a comparison between the fluorescence change of dye-copolymerized NPs relative to that observed for free dyes in solution and determine the number of surface (i.e. solvent-accessible) dye residues, the percentage of surface dyes were calculated according to Equation 3.6.

$$\%\text{Surface}_{DYE} = \frac{\%\text{Change}_{NP}}{\%\text{Change}_{DYE}} \times 100 \quad (3.6)$$

3.2.3 Results and Discussion

3.2.3.1 Comparison of NP synthetic techniques

Preliminary NP syntheses were primarily conducted using the FITC-APTES conjugate as a representative fluorophore; synthesized NPs using this dye conjugate are designated FITC-NPs. Later syntheses incorporated additional dye conjugates TR-APTES and GC-1-23-ICPTES, forming TR-NPs and GC-1-23-NPs, respectively.

The first successful NP synthesis conducted was based on the reverse microemulsion approach. A representative TEM image of the NPs isolated from this synthesis is provided in

Figure 3.5. The prepared FITC-NPs were spherical and monodisperse, with an average radius of 33.3 ± 1.7 nm; (n = 30, 5.1% RSD). However, despite the consistent size and morphology of NPs prepared using this approach, there are significant drawbacks. Foremost, the reaction makes use of rather toxic solvents and harshly basic conditions within the reverse micelles, which was found to result in significant decomposition of aminocyanine GC-1-23 even during the prehydrolysis step, precluding the formation of a silica NP enclosure to protect the dye molecules from their environment. Furthermore, complete removal of microemulsion components by centrifuge washing was found to be exceedingly difficult. Accordingly, the reverse microemulsion approach was discontinued following preliminary studies.

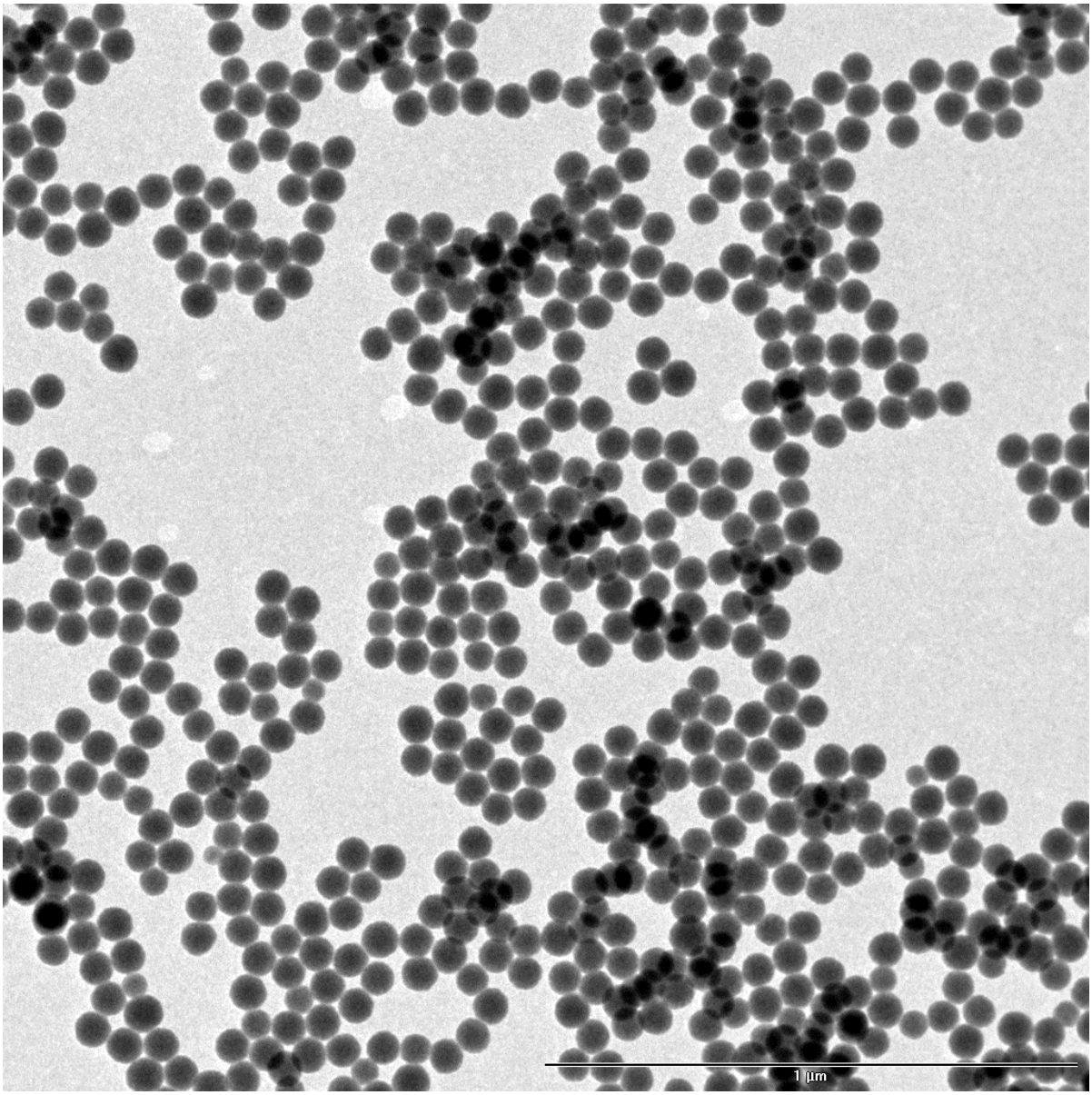

Figure 3.5: Representative TEM image of reverse microemulsion NPs (scale bar: 1 μm)

Subsequent NP syntheses focused on the Stöber approach. Stöber synthesis was initially carried out using a published method involving uncontrolled addition of TEOS.[53] During the initial synthesis of these particles, the published prehydrolysis period (1 minute) was used. A TEM image of the resultant particles is provided in Figure 3.6; the Stöber FITC-NPs demonstrated irregular morphology and some polydispersity, with an average radius of 23.5 ±

5.3 nm; (22.6% RSD). The prepared particles were observed to leach significant (visible) amounts of dye following thorough cleanup. In the hopes of addressing this issue, a subsequent synthesis was attempted, with a sole modification of a longer prehydrolysis time (12 hours) and all other parameters equal. A similar size distribution and morphology was observed following this synthesis. Furthermore, while the leaching was no longer visible to the naked eye, spectroscopic analysis of the "clean" supernatant obtained following resuspension of NPs in EtOH and cold (4℃) storage for a period of 5 days indicated leaching continued to occur despite the significantly longer prehydrolysis provision.

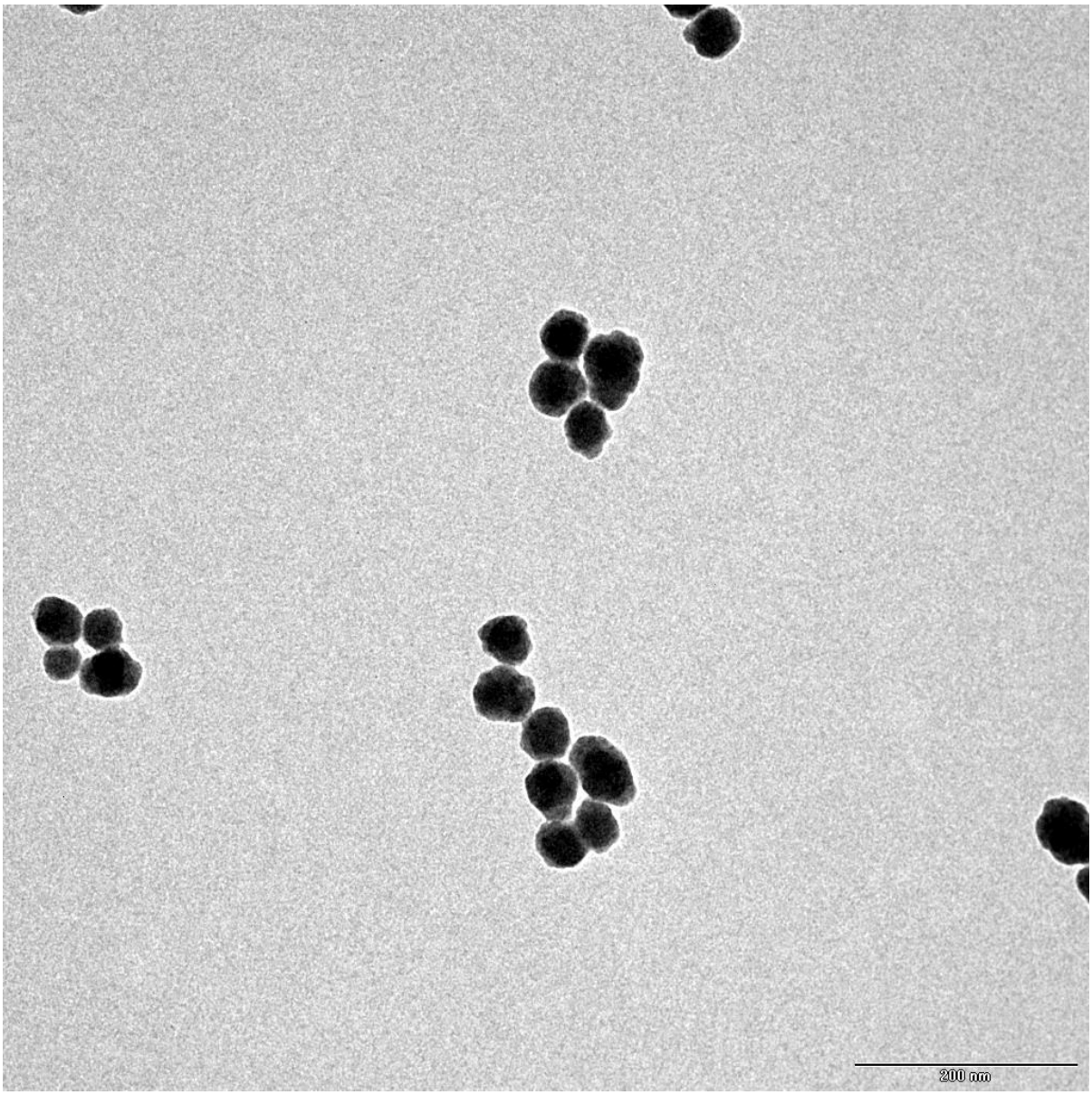

Figure 3.6: Representative TEM image of Stober NPs prepared using uncontrolled addition of TEOS and a prehydrolysis time of 1 minute (scale bar: 200 nm)

Due to the irregular particle shape and the ongoing issues with dye leaching, the "uncontrolled addition" approach was discontinued in favor of an alternate Stöber synthetic approach involving controlled, metered addition of TEOS, the rationale being that slowing the rate of NP formation and growth should lead to better morphological outcomes and better distribution of dye-silane throughout the NP structure (therefore hopefully less leaching). In

these reactions, a combination of ethanol, water, ammonia, and dye-silane conjugate were combined and allowed to prehydrolyze prior to the beginning of TEOS addition. Following the prehydrolysis perioed, an ethanolic solution of TEOS was added gradually using a syringe pump. The rate of addition requires careful control in order to strike an optimal balance between the rate of hydrolysis and the rate of nucleation, as these two factors ultimately control the monodispersity of particles.[57] The syringe pump was calibrated gravimetrically using deionized water at an ambient temperature of 22 °C in order to accurately determine the actual flow rate associated with syringe pump settings. Preliminary Stöber synthesis experiments involving the syringe pump (as detailed in 3.2.1.7) indicated that a flow rate of 0.29 mL/h was sufficient to produce spherical, relatively monodisperse particles from a 50 mM solution of TEOS (5 mL total volume; 250 μmol TEOS total added at a rate of 14.5 μmol/h). Due to the slower rate of TEOS addition in this "controlled" synthesis, a 30 minute dye-silane prehydrolysis time was employed instead of the 12 hour "head start" used when TEOS was added all at once. A TEM image of one of the first batches of NPs resulting from this "controlled addition" approach is depicted in Figure 3.7; these NPs were copolymerized with a total of 5 umol FITC-APTES conjugate, and the average radius was found to be 72.4 ± 6.8 nm. Importantly, these NPs were found to be substantially more stable against dye leakage than Stöber NPs prepared using uncontrolled addition of TEOS; no measurable fluorescence was observed in the supernatant after a month of storage in ethanol.

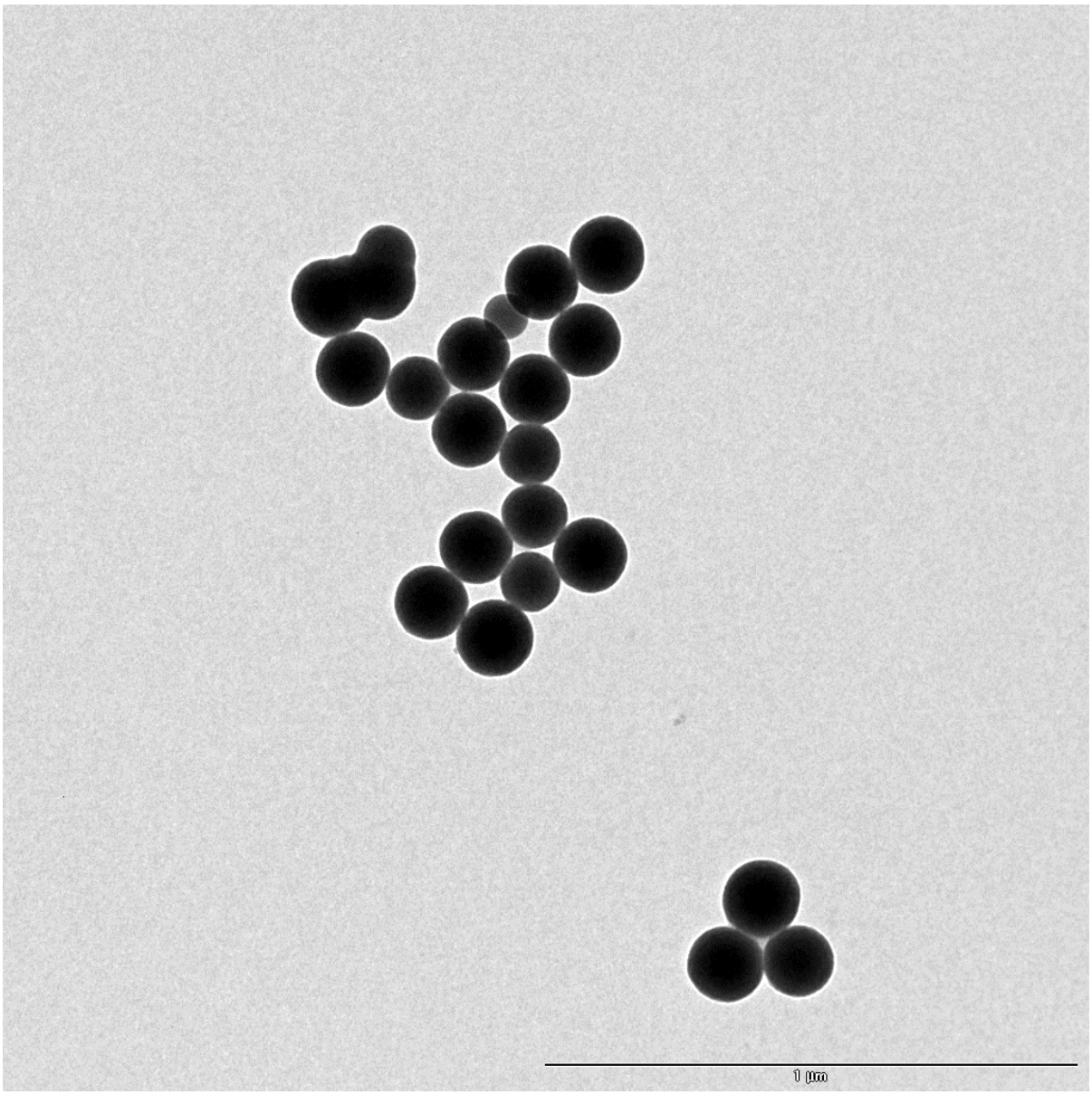

Figure 3.7: Representative TEM image of Stöber NPs copolymerized with 5 µmol FITC-APTES prepared using controlled addition of TEOS (0.29 mL/h; 14.5 µmol/h; scale bar: 1 µm)

The size of Stöber NPs can be affected by a number of different factors, including ammonia concentration, total water concentration, alcohol choice, and choice of orthosilicate ester.[58, 59] Previous studies on NPs have also indicated that NP size can be affected by the choice of fluorescent dye incorporated therein.[60] This was tested by preparing Stöber NPs under identical reaction conditions to those described in the preceding paragraph except NPs were

copolymerized with 5 μmol GC-1-23-ICPTES conjugate. The resultant NPs (Figure 3.8) were found to be substantially smaller (average radius 13.0 ± 2.8 nm) and somewhat rougher in appearance than those prepared using FITC-APTES.

In order to further test the origin of this substantial dependence of NP size on reaction components, a similar batch of "blank" NPs were prepared in which the same concentration of ICPTES was incorporated (without any dye conjugation); reaction conditions were otherwise identical. It was observed that the NP size was unchanged relative to the NPs containing GC-1-23-ICPTES conjugate; the average radius was found to be 12.6 ± 1.59 nm. Accordingly, the choice of reactive trialkoxysilane may also play a role in the modification of NP size.

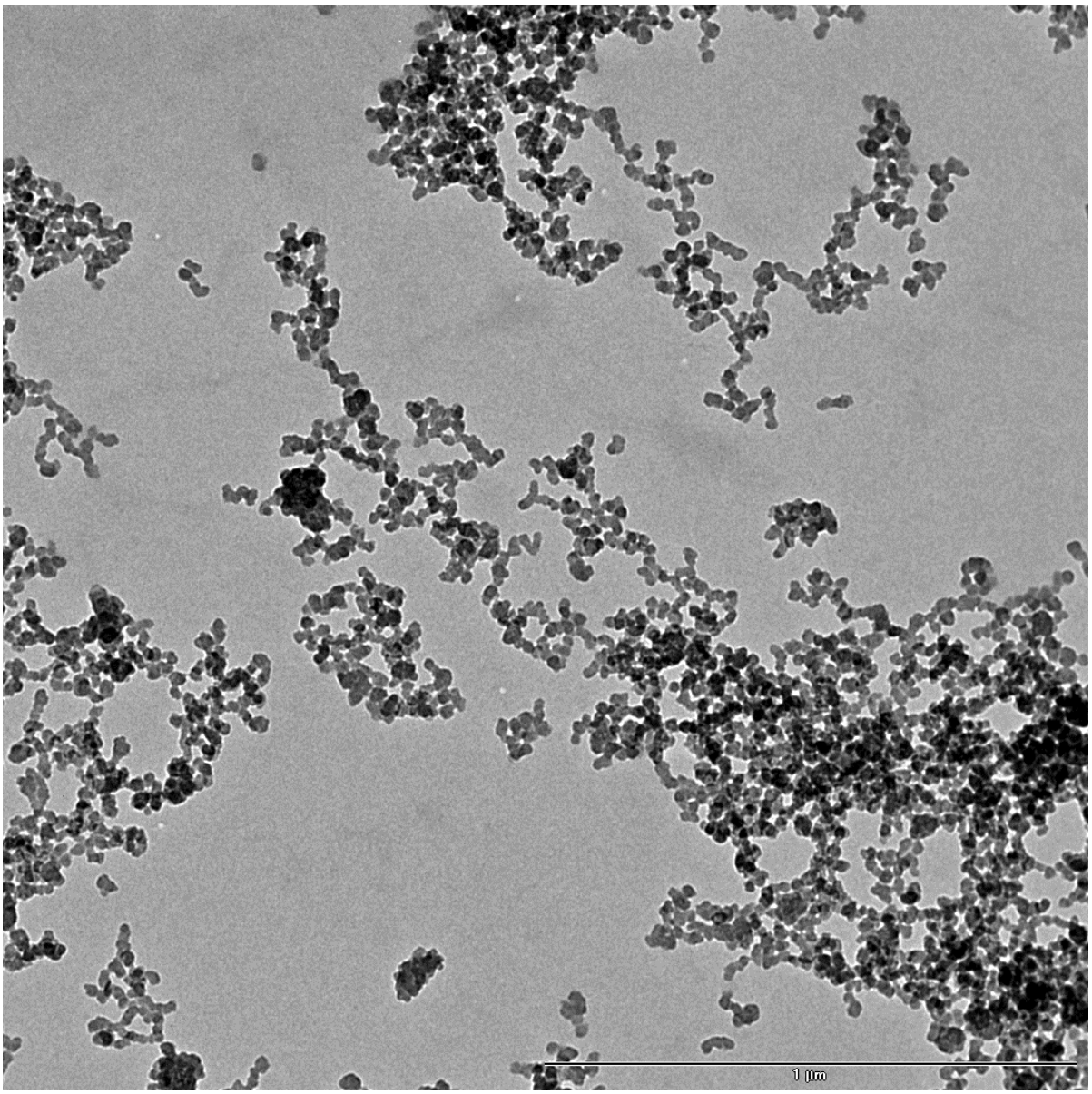

Figure 3.8: Representative TEM image of Stöber NPs copolymerized with 5 µmol GC-1-23-ICPTES prepared using controlled addition of TEOS (0.29 mL/h; 14.5 µmol/h; scale bar: 1 µm)

While the dependence of NP size on choices of dye and reactive trialkoxysilane is an interesting observation, it could also potentially present some challenges in applications requiring NPs containing multiple different dye types (e.g. multiplexed assays). However, results from later experiments involving the optimization of fluorescence signals (Section 3.2.2.4) indicated that much lower dye-silane concentrations were required in order to maximize the per-

particle fluorescence intensity and prevent self-quenching within the confines of individual NPs. The optimized concentrations for each of the considered dye-silane conjugates were 62.5 nmol FITC-APTES (0.0249 mol% of TEOS), 62.5 nmol TR-APTES (0.0249 mol% of TEOS), or 127 nmol GC-1-23-ICPTES (0.508 mol% of TEOS); these concentrations are 40 to 80 fold lower than the concentrations used in the NP syntheses depicted in Figures 3.7 and 3.8. It was determined that as dye-silane concentrations were decreased to these levels, NPs copolymerized with these dye concentrations (and combinations of dyes with these same individual concentrations) converged towards an average size of 38 ± 2 nm regardless of their dye content. The average radius in this case was obtained by averaging NP radii from 6 different dye syntheses with different dye contents, as discussed further in Section 3.3.4.3. Accordingly, the observed dependence of NP size on dye and trialkoxysilane content is (fortunately) also concentration-dependent. A representative TEM image from one of these NP syntheses (copolymerized with 62.5 nmol each of FITC-APTES and TR-APTES and 127 nmol GC-1-23-ICPTES) is provided in Figure 3.9; the NP morphology was smooth and spherical, intermediate in both dispersity and size (average radius 36.2 ± 5.8 nm) between the previous syntheses depicted in Figures 3.7 and 3.8. A comparison of synthetic techniques, dye loadings as mole percent (mol %) of TEOS, and radii (r, determined by TEM) for NPs discussed in this section is provided in Table 3.1.

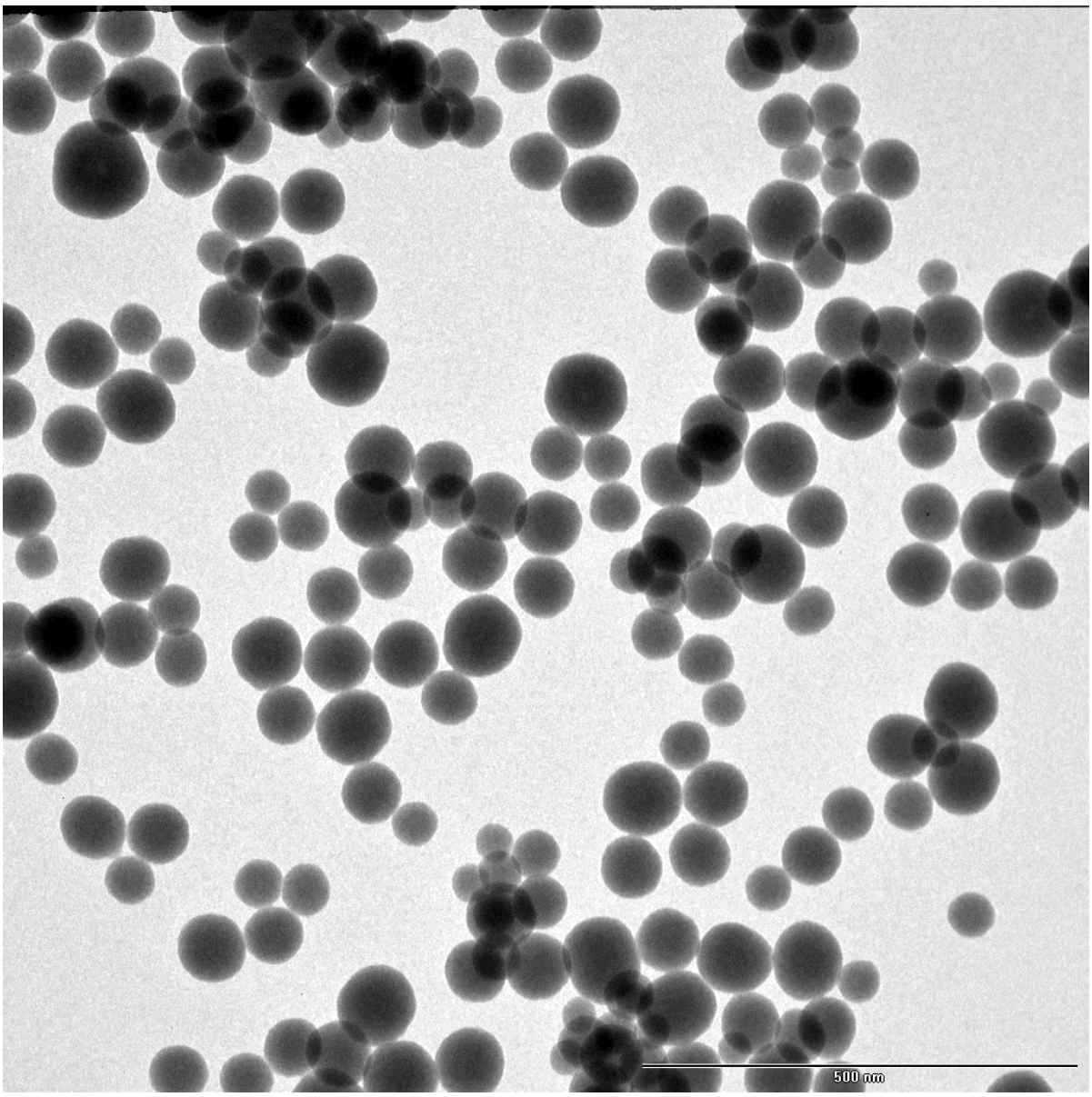

Figure 3.9: Representative TEM image of Stöber NPs copolymerized with 62.5 nmol FITC-APTES, 62.5 nmol TR-APTES, and 127 nmol GC-1-23-ICPTES; prepared using controlled addition of TEOS (0.29 mL/h; 14.5 μmol/h; scale bar: 500 nm)

Table 3.1: Mole percentages of dye-silane conjugates as a function of TEOS, synthetic approaches, and TEM radii for NP syntheses discussed in this section

Nanoparticle Category	mol % of Indicated Dye-Silane Conjugate(s) Relative to TEOS				Avg r (nm)	RSD r (%)	Dye species incorporated; Molar Ratio[a]; Synthetic Technique[b]
	FITC-APTES	TR-APTES	GC-1-23-ICPTES	Total Dye-Silane			
Preliminary Syntheses	0.112	0	0	0.112	33.3 ± 1.7	5.1	FITC; Reverse Microemulsion
	0.147	0	0	0.147	23.5 ± 5.3	22.6	FITC; Uncontrolled Stöber
	0.422	0	0	0.422	72.4 ± 6.8	9.4	FITC; Stöber
	0	0	1.95	1.95	13.0 ± 2.8	21.5	GC-1-23; Stöber
Optimized Syntheses	0.0249	0	0	0.0249	38.1 ± 6.2	16.3	FITC; 1:0:0; Stöber
	0	0	0.0254	0.0254	35.3 ± 5.5	15.6	GC-1-23; 0:0:2; Stöber
	0	0.0249	0	0.0249	41.4 ± 6.8	16.4	TR; 0:1:0; Stöber
	0.0249	0	0.0254	0.0503	39.0 ± 5.6	14.4	FITC + GC-1-23; 1:0:2; Stöber
	0.0249	0.0249	0	0.0498	38.5 ± 3.9	10.1	FITC + TR; 1:1:0; Stöber
	0.0249	0.0249	0.0254	0.0753	36.2 ± 5.8	16.0	All dyes; 1:1:2; Stöber

[a] Applies only to optimized syntheses
[b] Uncontrolled Stöber: all TEOS added at once; Stöber: TEOS added via syringe pump at rate of 14.5 μmol TEOS/h

3.2.3.2 Optimization of NP surface modifier coverage: microplate binding studies

The avidin-biotin system was chosen for bioconjugation purposes due to the high affinity and specificity of this protein-ligand pair (detailed in 3.1.3) as well as the availability of a commercial biotin-polyethylene glycol-silane reagent for straightforward surface functionalization. Surface modifiers based on polyethylene glycol were chosen based on their effectiveness in reducing NP flocculation in aqueous solutions and shielding NP surfaces from unwanted nonspecific surface interactions with proteins, as discussed in 3.1.3. Preliminary studies involved binding excess biotin-PEGylated NPs to neutravidin-coated microplates and measuring postwash fluorescence intensities; the results of these studies indicated greater extent of binding efficiency (higher fluorescence intensity) when a mixture of mPEG-silane and biotin-PEG-silane was used (relative to Bio-PEG-Sil alone). While the reason for this observation is not entirely clear, it may be that the reduced number of reactive surface groups reduces the chances

of single NPs binding multiple avidin groups on the microplate surface. Subsequent syntheses of biotinylated and PEGylated NPs made use of a mixture of the two surface modifiers.[51]

The surface coating coverage (total PEG-silane) and relative ratios of surface coatings (Bio-PEG-Sil and mPEG-Sil) were optimized for apparent binding efficiency to neutravidin by a comparison of the relative postwash fluorescence signals of biotin-PEGylated NPs bound to neutravidin coated microplates. A series of NPs with varying Bio-PEG-Sil and mPEG-Sil surface coverages (BPNPs and PNPs) were synthesized from a single batch of FITC-NPs. The apparent binding efficiency was first assessed as a function of the total PEG surface coverage, then as a function of the ratio of Bio-PEG-Sil:mPEG-Sil, as detailed in Tables 3.2.a and 3.2.b.

Table 3.2.a: Optimization of total PEG-silane coverage (as specific surface area/SSA) by calculation of fluorescence intensity as a percentage of that of the maximum fluorescence intensity observed (%I_F^{MAX})

SSA (μmol/m^2)			% Bio-PEG-Sil	% I_F^{MAX}
Bio-PEG-Sil	mPEG-Sil	Total PEG		
1.00	19.0	20.0	5.0	35%
1.50	28.5	30.0	5.0	51%
2.00	38.0	40.0	5.0	66%
2.50	47.5	50.0	5.0	34%

Table 3.2.b: Optimization of percent Bio-PEG-Sil coverage by calculation of fluorescence intensity as a percentage of the maximum observed fluorescence intensity (%I_F^{MAX})

SSA (μmol/m^2)			% Bio-PEG-Sil	% I_F^{MAX}
Bio-PEG-Sil	mPEG-Sil	Total PEG		
0	40.0	40.0	0	0%
1.60	38.4	40.0	4.0	46%
2.00	38.0	40.0	5.0	66%
3.20	36.8	40.0	8.0	73%
4.00	36.0	40.0	10.0	100%
4.80	35.2	40.0	12.0	95%
5.60	34.4	40.0	14.0	75%
6.40	33.6	40.0	16.0	71%

The overall results of the study indicate a significant relationship between the apparent binding efficiency and both the total PEG coverage and relative ratio of added Bio-PEG-Sil:mPEG-Sil, with a nearly threefold increase in the apparent binding efficiency upon optimization. In particular, the results from the optimization of total [PEG-silane] provided in Table 3.2.a indicate that the ideal total PEG surface coverage is 40 μmol/m^2, and the results from the optimization of Bio-PEG-Sil:mPEG-Sil coverage provided in Table 3.2.b indicate that the optimal added Bio-PEG-Sil surface coverage is 4 μmol/m^2 (10% of the total PEG-silane

concentration). The reasons for the dependence of binding efficiency on total PEG coverage are not entirely clear, but they may involve a combination of issues such as limited NP surface areas resulting in saturation and preferential binding of one PEG-silane reagent over another at higher total concentrations versus inadequate surface coverage (leading to flocculation and/or reduced binding probability) at lower concentrations. The reasons for the dependence of binding efficiency on the relative percentage of Bio-PEG-Sil are similarly unclear, but may involve a combination of factors such as reduced binding probability at low [Bio-PEG-Sil] versus increased probability of NPs binding multiple avidin sites at high [Bio-PEG-Sil], as previously conjectured. These observations warrant further study. Nonspecific binding was assessed against FITC-NPs coated only with mPEG-Sil (Table 3.2.b); no background fluorescence was observed for this sample after plate washing, indicating that any NP fluorescence observed following washing steps in biotinylated samples is specific to the avidin-biotin interaction.

3.2.3.3 Optimization of dye molar ratio

A series of NP syntheses was carried out in which equimolar amounts of dye conjugates were incorporated into NPs; the added concentration of each dye was held constant in each batch but dye concentrations were increased incrementally from batch to batch. Dye ratios and the corresponding added (theoretical) dye mole percentages (mol %) of dye-silane conjugates in NPs are provided relative to TEOS in Table 3.3; percentages are theoretical because the conjugation reaction between the dyes and their respective reactive silanes are not 100% efficient.[32] The NP samples were diluted identically such that the total absorption at the excitation wavelengths (λ_{EXC}) for each dye was <0.1, then fluorescence intensities (I_F) of the individual dyes at the wavelengths of maximum emission (λ_{EM}) were collected. Results indicated highest per-particle

fluorescence intensities for 0.025 mol% FITC, 0.025% TR, and 0.050% GC-1-23 (Figure 3.10); the optimal molar dye ratio (FITC:TR:GC-1-23) was estimated to be 1:1:2.

Table 3.3: Theoretical mol% of each dye in various dye molar ratios used in this text

Dye ratio (FITC:TR:GC-1-23)	Dye mol % (vs TEOS)
0.5:0.5:0.5	0.012
1:1:1	0.025
2:2:2	0.050
4:4:4	0.100
8:8:8	0.199
12:12:12	0.299

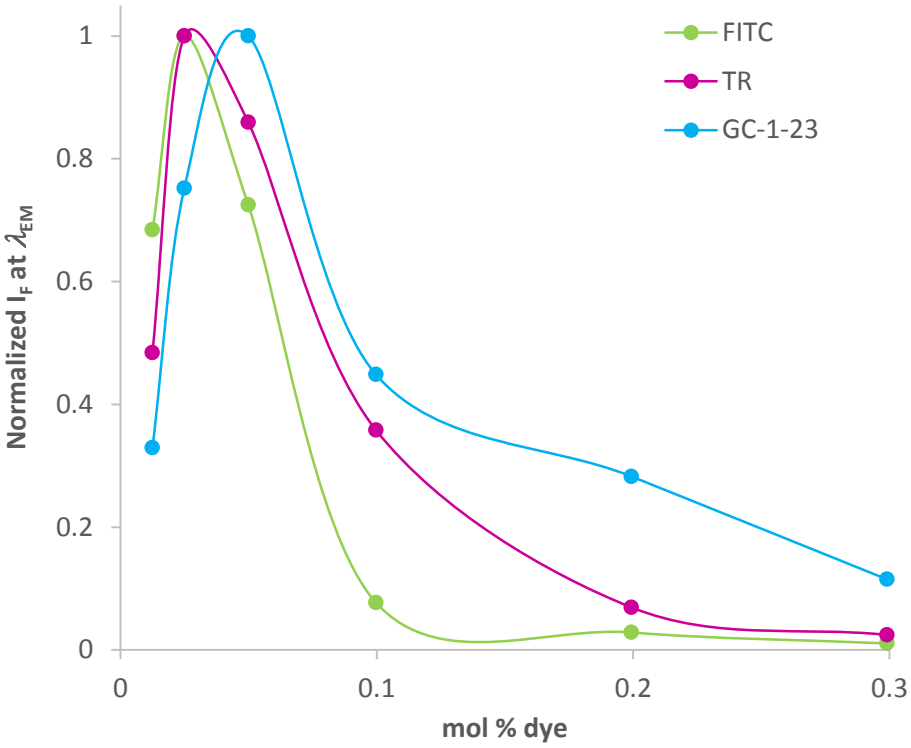

Figure 3.10: Normalized fluorescence intensities (I_F) at wavelengths of maximum emission (λ_{EM}) for individual dyes in multidye nanoparticles containing varying mole percentages (mol%) of dye relative to TEOS

3.2.3.4 Determination of solvent-accessible dye residues in NPs

The percentage of solvent-accessible dye residues was determined by comparing the solvent-dependent changes in fluorescence intensity for dyes copolymerized with NPs versus those free in solution, as discussed in detail in Section 3.2.2.10. The results of these studies are presented in Table 3.4. The calculated percentages of solvent-accessible dyes (%SurfaceDYE) in the dye-doped particles ranged from 2.0% for the FITC-NPs to 7.5% for GC-1-23-NPs, with an average of 5.3% solvent-accessible dyes (of the total number of dye molecules within each NP).

Table 3.4: Calculation of percentage of solvent-accessible dyes in dye-copolymerized NPs from relative fluorescence change in PB vs EtOH

NP Sample	Dye-Silane	$\lambda_{EXC}/\lambda_{EM}$ (nm)	$\%Change_{NP}$	$\%Change_{DYE}$	$\%Surface_{DYE}$	Average $\%Surface_{DYE}$
FITC-NPs (1:0:0)	FITC-APTES	450/512	20.1	983	2.0	
TR-NPs (0:1:0)	TR-APTES	510/589	3.92	60.4	6.5	5.3
GC-1-23-NPs (0:0:2)	GC-1-23-ICPTES	650/745	6.13	81.9	7.5	

The calculated percentage of surface dyes can be compared to the theoretical percentage of surface accessible dye molecules for dye-copolymerized NPs containing an even distribution of dye molecules using Equation 3.7.[61] In this equation, N is the calculated number of silica (SiO_2) units per particle and $\%Surface_{SILICA}$ is the percentage of the total silica units present on the surface. Assuming an even distribution of dyes throughout the NP, the theoretical percentage of surface dye molecules ($\%Surface_{DYE}^{THEOR}$) should be approximately equal to the percentage of surface silica units. The number of silica units per particle (N) may be calculated from the radius of the silica NP (r, determined to be an average of 3.8(±0.2) x 10^{-6} *cm* for all syntheses using TEM) and the density (ρ, 2.2 g/cm^3) and molecular weight (MW, 60.08 g/mol) of silica, as per Equation 3.8. This equation does not take into account the contribution from the dye-silane

conjugates to the NP radius; as dye-silane is present at 0.025 – 0.05 mol% of the total SiO_2, it is presumed that this contribution is relatively negligible.

$$\%\text{Surface}_{\text{DYE}}^{\text{THEOR}} = \%\text{Surface}_{\text{SILICA}} = 4\text{N}^{-\frac{1}{3}} \times 100 \quad (3.7)$$

$$\text{N} = \frac{4\pi r^3 \times \rho \times N_A}{3\text{MW}} = 5.1 \times 10^6 \quad (3.8)$$

Plugging the value of N from Equation 3.8 back into Equation 3.7, the theoretical percentage of surface dyes for a silica NP with a radius of 38 nm and a homogeneous distribution of dye molecules should be approximately 2.3%. While the actual (calculated) solvent accessibility averaged 5.3%, it is important to note that some superficially subsurface dye molecules encapsulated in NPs may still remain somewhat accessible to solvents. Overall, the general agreement between the theoretical and experimental results suggest that the dye-silane conjugate is distributed throughout the NP matrix rather than being concentrated at the surface. This is ostensibly due to the slow and controlled rate of TEOS addition, resulting in slow NP growth and ample opportunity for incorporation of dye-silane conjugates throughout the growth process. This observation is further supported by observations of dye quantum yield enhancements in NPs relative to free dye-silane in solution (as discussed later in Section 3.3.4.6), and by observations of the spectroscopic changes to the dyes following incorporation into NPs.

Spectroscopic changes are evident in dye spectra upon incorporation into NPs for all three of the dye species studied, as indicated in Figure 3.11. For all three dyes, band broadening occurs in the NP-bound absorption and emission spectra. Furthermore, a red shift is apparent in the absorption maximum of GC-1-23 and a blue shift is apparent in the absorption maximum of TR when these dye species are incorporated into NPs. Both the band broadening and shifts in the

absorption spectra are indicative of changes to the local environment of the fluorophores, indicating incorporation into the silica matrix. In making these observations, it's important to note that the linker groups are directly conjugated to the chromophore in the cases of fluorescein and Texas Red, thus the effects of incorporation into NPs cannot be directly deconvoluted from the effects of conjugation with APTES using the data presented in Figure 3.11 (this issue is addressed in greater detail in Section 3.3.4.6). However, GC-1-23 possesses a primary amine linker group that is offset from the chromophore via an insulating four carbon linker, thus in this case the spectroscopic differences between free dye in solution versus NP-bound dye molecules should be solely attributable to differences in the solvation environment (EtOH vs. silica matrix).

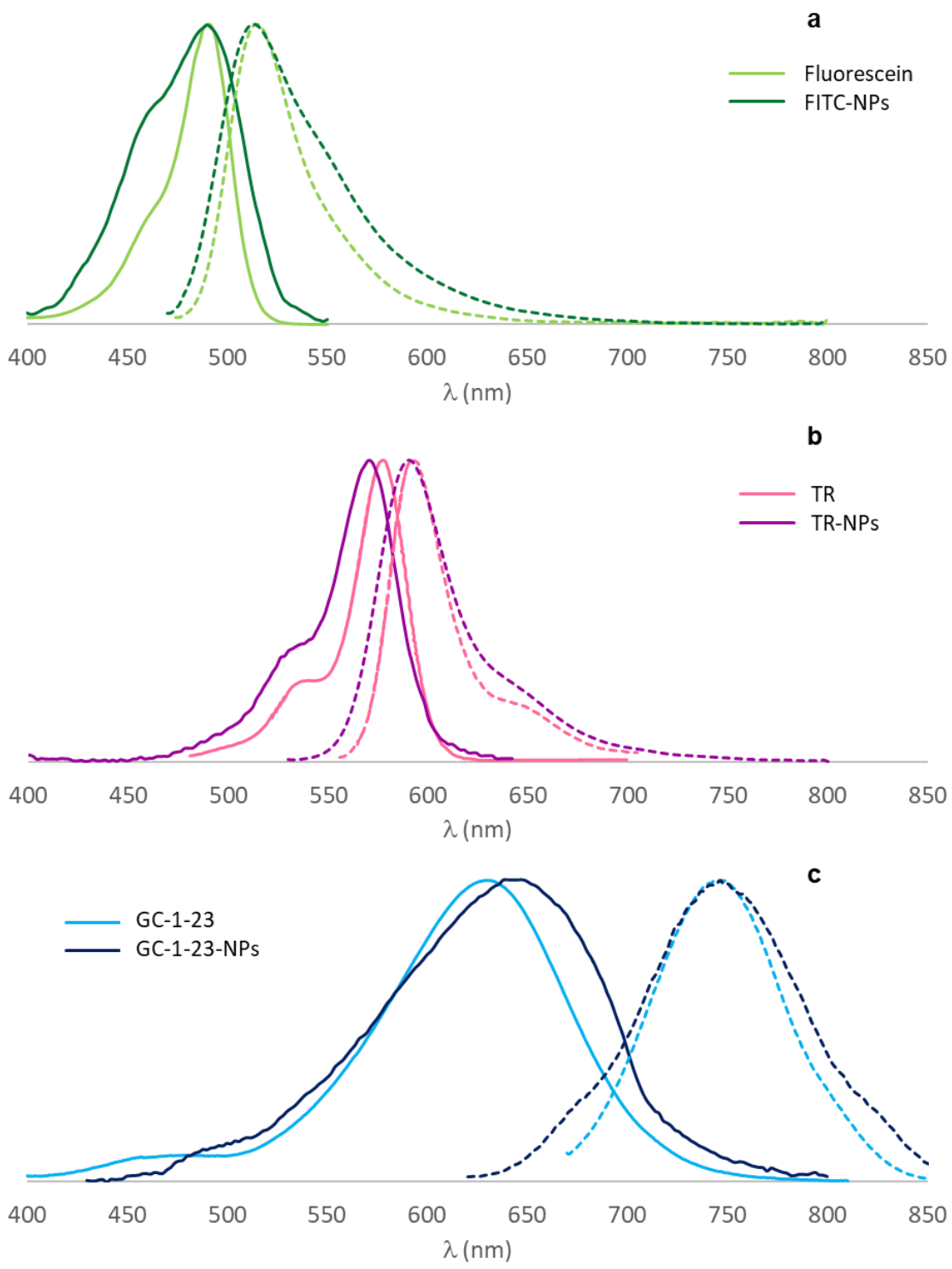

Figure 3.11: Comparison of dye spectra in solution to spectra in dye-copolymerized NPs: (a) fluorescein in 0.1 M NaOH vs. FITC-NPs in EtOH; (b) TR in EtOH vs. TR-NPs in EtOH; (c) GC-1-23 in EtOH vs GC-1-23-NPs in EtOH

3.2.4 Conclusions

Results of the preliminary studies indicated that use of the Stöber process with controlled addition of TEOS resulted in facile cleanup and optimal stability of dye-silane conjugates both during and after synthesis. Furthermore, it appears that dye-copolymerized NPs prepared using this route exhibit a relatively homogeneous distribution of dyes throughout the particle interior, as evidenced by the solvent accessibility studies. Optimal per-particle fluorescence was realized when the mol% of FITC-APTES and/or TR-APTES was 0.025% and the mol% of GC-1-23-ICPTES was 0.05% (relative to TEOS). Particle surfaces were surface functionalized with two polyethylene glycol and biotin derivatives; studies on relative and absolute concentrations of surface coatings for bioconjugation yielded optimal Bio-PEG-Sil and mPEG-Sil concentrations of 4 μmol/m^2 and 36 μmol/m^2, respectively (as evidenced by postwash fluorescence signals when NPs were bound to neutravidin microplate wells).

3.3 NIR-fluorescent multidye silica nanoparticles with large Stokes shifts for versatile biosensing applications

The content of Section 3.3 is a pre-print of an article "Chapman, G., Patonay, G. NIR-fluorescent multidye silica nanoparticles with large Stokes shifts for versatile biosensing applications" published in *Journal of Fluorescence*. The final authenticated version is available online at https://doi.org/10.1007/s10895-018-02339-z. Formatting changes to the submitted manuscript are as follows: tables and figures have been integrated into the text body, table and figure numbers have been changed to the style of this document, and references made to the

electronic supplementary material in the manuscript have been changed to reference the corresponding parts of this dissertation.

3.3.1 Abstract

We have synthesized and characterized of a series of single and multidye copolymerized nanoparticles with large to very large Stokes shifts (100 to 255 nm) for versatile applications as standalone or multiplexed probes in biological matrices. Nanoparticles were prepared via the Stöber method and covalently copolymerized with various combinations of three dyes, including one novel aminocyanine dye. Covalently encapsulated dyes exhibited no significant leakage from the nanoparticle matrix after more than 200 days of storage in ethanol. Across multiple batches of nanoparticles with varying dye content, the average yields and average radii were found to be highly reproducible. Furthermore, the batch to batch variability in the relative amounts of dye incorporated was small (relative standard deviations $\leq$ 2.3%). Quantum yields of dye copolymerized nanoparticles were increased 50% to 1000% relative to those of their respective dye-silane conjugates, and fluorescence intensities were enhanced by approximately three orders of magnitude. Prepared nanoparticles were surface modified with polyethylene glycol and biotin and bound to streptavidin microspheres as a proof of concept. Under single wavelength excitation, microsphere-bound nanoparticles displayed readily distinguishable fluorescence signals at three different emission wavelengths, indicating their potential applications to multicolor sensing. Furthermore, nanoparticles modified with polyethylene glycol and biotin demonstrated hematoprotective qualities and reduced nonspecific binding of serum proteins, indicating their potential suitability to *in vivo* imaging applications.

3.3.2 Introduction

Fluorescence-based techniques play a central and crucial role in the field of bioanalytical chemistry due to their intrinsic high sensitivity and excellent spatial and temporal resolution.[41, 62-67] Historically, these techniques have relied on the use of fluorescent dye molecules such as fluorescein, rhodamine, and cyanines as reporter tags. Near-infrared (NIR) fluorescent compounds such as heptamethine cyanine dyes are of particular utility to bioanalytical applications due to the reduced scattering and lack of interfering biomolecular autofluorescence at longer wavelengths.[68-72] However, the application of individual dye molecules has some drawbacks, including low fluorescence intensities due to limitations on the number of dye molecules that can be bound to targets, as well as the potential for undesirable environmental effects on the chemical stability and spectroscopic properties. In addition, many fluorescent dyes (particularly those with NIR fluorescence) exhibit small Stokes shifts, which hinders deconvolution of the incoming excitation light from the emission signal and predisposes the dyes to homo-quenching via resonance energy transfer between dyes of the same species.[73, 74]

Fortunately, the common issue of small Stokes shifts may be addressed through introduction of different functionalities at specific locations along the chromophore in order to modulate the spectroscopic properties.[75-79] The aminocyanine dyes are a particularly notable example of this; these compounds demonstrate strongly blue-shifted absorption in accordance with the Dewar-Knott rule, resulting in a large increase in the Stokes shift, (from ~20 nm in unsubstituted cyanine dyes to >100 nm in *meso*-substituted aminocyanines).[78-82] Issues with dye stability and environmental sensitivity may also be overcome; one straightforward approach is the incorporation of fluorophores into nanoparticles.[10, 83, 84] This approach also allows for substantially higher per-label fluorescence signals owing to both increased fluorescence quantum

yields and the possibility of incorporating hundreds or even thousands of dye molecules into a single fluorescent tag.[15, 41] An additional benefit of this approach is the ability to incorporate different dyes into a single label. If the incorporated dyes are capable of Förster resonance energy transfer (FRET), the effective Stokes shift of the prepared labels can be substantially increased. Furthermore, when FRET pairs are incorporated, series of nanoparticles containing different ratios and combinations of fluorescent dyes may be synthesized, resulting in a large variety of spectroscopically distinct tags from a relatively small number of starting materials. This approach produces fluorescent probes which allow for the simultaneous detection of multiple targets, thereby improving throughput capacity in multicolor sensing and imaging applications such as flow cytometry, multitarget assays, and *in vivo* labeling of various biological structures.[51, 60, 85, 86]

In this study, we have synthesized and characterized a series of single and multidye copolymerized silica nanoparticles possessing large to very large Stokes shifts with versatile potential applications either alone as individual fluorescence probes for biological matrices or together as a fluorescent probe series for simultaneous detection of multiple targets. Silica was chosen as the nanoparticle matrix due to the ease of both surface modification and covalent dye incorporation in order to impart maximum stability and minimize dye leaching.[10, 14, 87, 88] Aminocyanine dye GC-1-23 was designed, synthesized, and characterized, then incorporated into nanoparticles as either a lone fluorophore or as a FRET acceptor bearing a long Stokes shift. Fluorescein isothiocyanate and Texas Red were chosen as additional donor/acceptors based on their high quantum yields and spectral overlap with one another and with the aminocyanine acceptor. Fluorescent nanoparticles containing 1-3 different dyes were synthesized and characterized in terms of size, synthetic yield, quantum yield, signal enhancement,

reproducibility of dye incorporation, and dye leakage after extended storage. Nanoparticles were surface-modified with polyethylene glycol and biotin and bound to magnetic streptavidin microbeads as a proof of concept for the application of these nanomaterials as single excitation multiplexing tags. Hemocompatibility and protein nonspecific binding studies were also carried out in order to assess the suitability of the nanoparticles for *in vivo* use.

The present work provides a framework for the facile and low-cost synthesis of fluorescent silica nanoparticles with reproducible optical properties and sizes, tunable fluorescence characteristics, excellent stability against dye leaching, and substantial enhancements to fluorescence signals relative to the individual dyes. The method is widely applicable to any dye species with appropriate reactive moieties. Furthermore, the surface-functionalized NPs demonstrate hematoprotective properties, low nonspecific protein adsorption, and amenability to bioconjugation. These properties, in combination with the large Stokes shifts and NIR fluorescence indicate a wide range of potential *in vivo* and *in vitro* biosensing applications.

3.3.3 Experimental

3.3.3.1 Materials and instrumentation

Acetic acid (AcOH, glacial, ≥99%), acetonitrile (CH_3CN, CHROMASOLV® Plus, for HPLC, ≥99.9%), (3-aminopropyl)triethoxysilane (APTES, ≥ 98%), *N*,*N*-dimethylformamide (DMF, 99.8%), fluorescein isothiocyanate (FITC, 98%), human serum albumin (HSA, 97%), immunoglobulin G from human serum (IgG, 10 mg/mL in phosphate buffer), tetraethyl orthosilicate (TEOS, 99.999%), and 3-(triethoxysilyl)propyl isocyanate (ICPTES, 95%) were obtained from Sigma Aldrich (St. Louis, MO). Aqueous ammonia (certified ACS plus, 29.6%), methanol (MeOH, certified ACS, ≥99.8%), potassium chloride (USP), sodium chloride (certified

ACS, >99.9%), sodium hydroxide (Fisher Bioreagents, ≥97.0%) sodium phosphate monobasic monohydrate (certified, ≥98%), sodium phosphate dibasic dodecahydrate (99%), and Amicon Ultra centrifugal filter units (10 kDa) were obtained from Thermo Fisher Scientific (Waltham, MA). BcMag Streptavidin Magnetic Beads (1 μm) were obtained from Bioclone Inc. (San Diego, CA). Absolute 200 proof ethanol (EtOH) was obtained from Greenfield Ethanol, Inc. (Toronto, ON). Biotin-polyethylene glycol-silane (Bio-PEG-Sil, MW 3400) and methoxypolyethylene glycol-silane (mPEG-Sil, MW 1000) were obtained from Laysan Bio (Arab, AL). Sulforhodamine 101 acid chloride (Texas Red/TR, 96.5%) was purchased from Chemodex (St. Gallen, Switzerland). Dye GC-1-23 was synthesized as detailed in the supporting information. Triply deionized water was obtained from a Barnstead Nanopure water purification system (Thermo Fisher Scientific, West Palm Beach, FL). Human red blood cells (RBCs, stabilized with CPDA-1) were obtained from Tennessee Blood Services (Memphis, TN).

All volumetric glassware (pipets used to deliver volumes greater than 1 mL and volumetric flasks) was categorized as class A. Volumes less than 1 mL were delivered using either a 10-100 μL or a 100-1000 μL adjustable volume Eppendorf pipette, and in cases where volumetric pipets or flasks were unavailable in the desired volume, volumes larger than 1 mL were delivered via a positive-displacement Eppendorf repeating pipette (Eppendorf, Hauppauge, NY.). UV-visible and fluorescence spectroscopic measurements were carried out on Biotek Synergy H1 and Synergy H4 Microplate Readers (Biotek, Winooski, VT) and results were generated using Biotek Gen5 Software (v.2.04.11). Additional calculations, spectral processing, and spectral deconvolutions were carried out using Microsoft Excel (2016, Microsoft Corporation, Redmond, WA) and a|e - UV-Vis-IR Spectral Software (v.2.2, FluorTools, www.fluortools.com). Transmission electron microscopy (TEM) was carried out using a ZEISS Leo 906E Transmission

Electron Microscope (ZEISS, Jena, Germany). Fluorescence microscopy was carried out using an Olympus BX51WI fluorescence microscope fitted with an X-Cite Series 120 Q light source and an Infinity 3S-iUR 1.4 megapixel CCD camera; microscopy images were acquired using Micro-Manager (v.1.4.22).[89, 90] The excitation filter was a Chroma ET470/40x (470 nm/40 nm bandpass), the dichroic mirror was a Chroma T495lpxr (495 nm longpass), and the emission filters were a Chroma ET525/50 (525 nm/50 nm bandpass), an Omega EB00445B (607/45 nm bandpass), and an Omega 750DF50-0210 (750/50 nm bandpass). Microscopy images (TEM and fluorescence) were analyzed and processed using ImageJ software (v. 1.51j8) including the Align Slice and TransformJ plugins.[91, 92]

3.3.3.2 Nanoparticle Synthesis

Three dye-silane conjugates were prepared for covalent incorporation into silica nanoparticles (NPs) as illustrated in Scheme 3.1. Fluorescein isothiocyanate (FITC) was dissolved in dry CH_3CN and combined with an excess (1.5 equivalents) of APTES; the reaction was allowed to proceed for 16 hours. Texas Red (TR) was dissolved in dry DMF and combined with an excess (1.5 equivalents) of APTES; the reaction was allowed to proceed for 3 hours. Aminocyanine dye GC-1-23 was dissolved in dry CH_3CN and combined with an excess (1.5 equivalents) of ICPTES; the reaction was allowed to proceed for 16 hours. All reactions were conducted in closed, airtight containers at room temperature with stirring. Following conjugation reactions, dye conjugates FITC-APTES, TR-APTES, and GC-1-23-ICPTES were used “as is” and not subjected to further purification steps. Various ratios of these dye conjugates were employed in the synthesis of silica nanoparticles. Conjugates were stored at -20 °C under $N_2(g)$ when not in use.

Nanoparticles (NPs) were synthesized via an adaptation of the Stöber process utilizing controlled addition of TEOS.[93] Specifically, 15.75 mL absolute EtOH, 0.780 mL water, and 0.500 mL of NH_3(aq) were added to a clean round bottomed flask equipped with a stir bar and stopper. The desired amounts of dye conjugates were added to the reaction flasks and allowed to hydrolyze for 30 min. Separately, 0.112 mL TEOS was diluted to 10.00 mL with absolute EtOH in a volumetric flask and mixed thoroughly. This solution was transferred into a syringe attached to a calibrated syringe pump, and 5.00 mL of the TEOS solution was introduced into the solution at a flow rate of 0.29 mL/h. The mixture was stirred for a total of 20 hours (including TEOS addition), then the NPs were transferred to centrifuge tubes and separated from the reaction mixture by centrifugation (10,397 g for 30 min). The supernatant was removed, 15 mL EtOH was introduced into the tubes, then the centrifuge tubes were briefly placed in an ultrasonic bath to resuspend the NPs. The centrifugation/resuspension washing process was repeated three times using EtOH, and the final resuspension step was carried out into 15.00 mL EtOH delivered via a repeating pipette. Prepared NPs were stored in EtOH at 4 °C prior to further characterization.

3.3.3.3 Yields and radii of prepared NPs

Prepared NPs were characterized by transmission electron microscopy (TEM) in order to determine radii. Average NP sizes were used to calculate molecular weight (MW) following Equation 3.9, using the average radii determined from TEM images (r, in nm) and assuming the density of the particles is identical to the published density of silica (ρ = 2.2 g/cm^3).[32, 54] In this equation, N_A is Avogadro's number and 10^{-21} is a conversion factor from cm^3 to nm^3.

$$\text{MW NPs (g/mol)} = \frac{4}{3}\pi r^3 \rho N_A \times 10^{-21} \qquad 3.9$$

Gravimetric NP yields were determined as follows: exactly half of each NP solution (in EtOH) was transferred to a tared vial and dried using a controlled stream of dry N_2, then further dried in an oven at 110 °C. Oven-dried NP samples were brought to room temperature in a desiccator prior to weighing. Concentrations could then be determined for the remaining solution based on the known solution volume, calculated molecular weight, and yield.

3.3.3.4 Surface modification of NPs for biosensing applications

The prepared multifluorescent NPs appear to be excellent candidates for *in vitro* or *in vivo* biosensing applications due to their NIR fluorescence and long Stokes shifts. However, NP surfaces must be passivated to reduce issues with flocculation, toxicity, and nonspecific binding to biomolecules. Furthermore, appropriate functionalities must be introduced in order to promote bioconjugation for *in vitro* assay development. Bare silica nanoparticles were modified with polyethylene glycol derivatives for the purposes of both surface passivation and the introduction of biotin moieties for bioconjugation. Cleaned NPs in EtOH (~0.9 mg/mL) were aliquoted into centrifuge tubes fitted with stir bars. Separately, solutions containing 50 mg/mL Bio-PEG-Sil and 70 mg/mL mPEG-Sil were prepared in 1 mM AcOH(aq) and allowed to prehydrolyze for 10 min. Following the prehydrolysis time, appropriate volumes of Bio-PEG-Sil and mPEG-Sil solutions were introduced. To produce biotin- and PEG-functionalized particles (BPNPs) suitable for avidin binding, theoretical surface coverage densities of 4.0 μmol/m^2 Bio-PEG-Sil and 36 μmol/m^2 mPEG-Sil were introduced. For plain surface-passivated PEGylated particles lacking the biotin functionality (PNPs), a theoretical surface coverage density of 40 μmol/m^2 mPEG-Sil was introduced. Surface coverage densities were calculated using the specific surface

area (SSA), as given in Equation 3.4 (Section 3.2.2.8). In this equation, d is the NP diameter (in nm) and ρ is the density of silica (2.2 g/cm^3).[54-56]

The reactions were allowed to proceed at room temperature for 2 hours, then the surface modified nanoparticles (BPNPs and PNPs) were centrifuge washed three times with a 50% EtOH in water mixture to remove any excess unreacted silane, with resuspension sonication steps carried out in an ice bath to reduce the likelihood of PEG sonolysis.[94] The functionalized BPNPs were stored in 50% EtOH/water mixtures at 4 °C prior to characterization and application.

3.3.4 Results and discussion

3.3.4.1 Dye pair design

Heptamethine aminocyanine dye GC-1-23 was synthesized as detailed in Section 2.2.1. Spectroscopic characteristics (molar absorptivity, quantum yield, Stokes shift) of the native dye were assessed in MeOH (Section 2.3). The experimentally determined molar absorptivity (ε) of this dye was 2.7(±0.17)x10^4 M^{-1} cm^{-1} (n = 5), the quantum yield (ϕ) determined in triplicate relative to the standard indocyanine green[95] was 0.21(±0.099). Absorption and emission spectra for the dye are provided in Figure 2.11, highlighting a rather large Stokes shift of 118 nm. The experimentally determined quantum yield, molar absorptivity, and Stokes shift all fall within previously reported ranges for aminocyanines.[80-82]

GC-1-23 was designed as a NIR-fluorescent dye with both a *meso* secondary amino moiety imparting a long Stokes shift and a secondary reactive terminal primary amine for covalent incorporation into silica NPs via reaction with ICPTES (Scheme 3.1). The effective Stokes shift was further increased by co-functionalization of silica NPs with FITC and TR as FRET donors via their respective conjugates with APTES (Scheme 3.1). The neutral lactone tautomer of FITC

has been illustrated in this scheme due to the predominance of this form in aprotic solvents.[96] Normalized fluorescence spectra and absorption spectra (corrected for scattering) for each of the dye conjugates covalently incorporated into silica NPs are provided in Figure 3.12. The absorption spectra for both the primary and secondary acceptor dyes (TR and GC-1-23) exhibit significant overlap with the fluorescence spectrum of the primary donor (FITC).

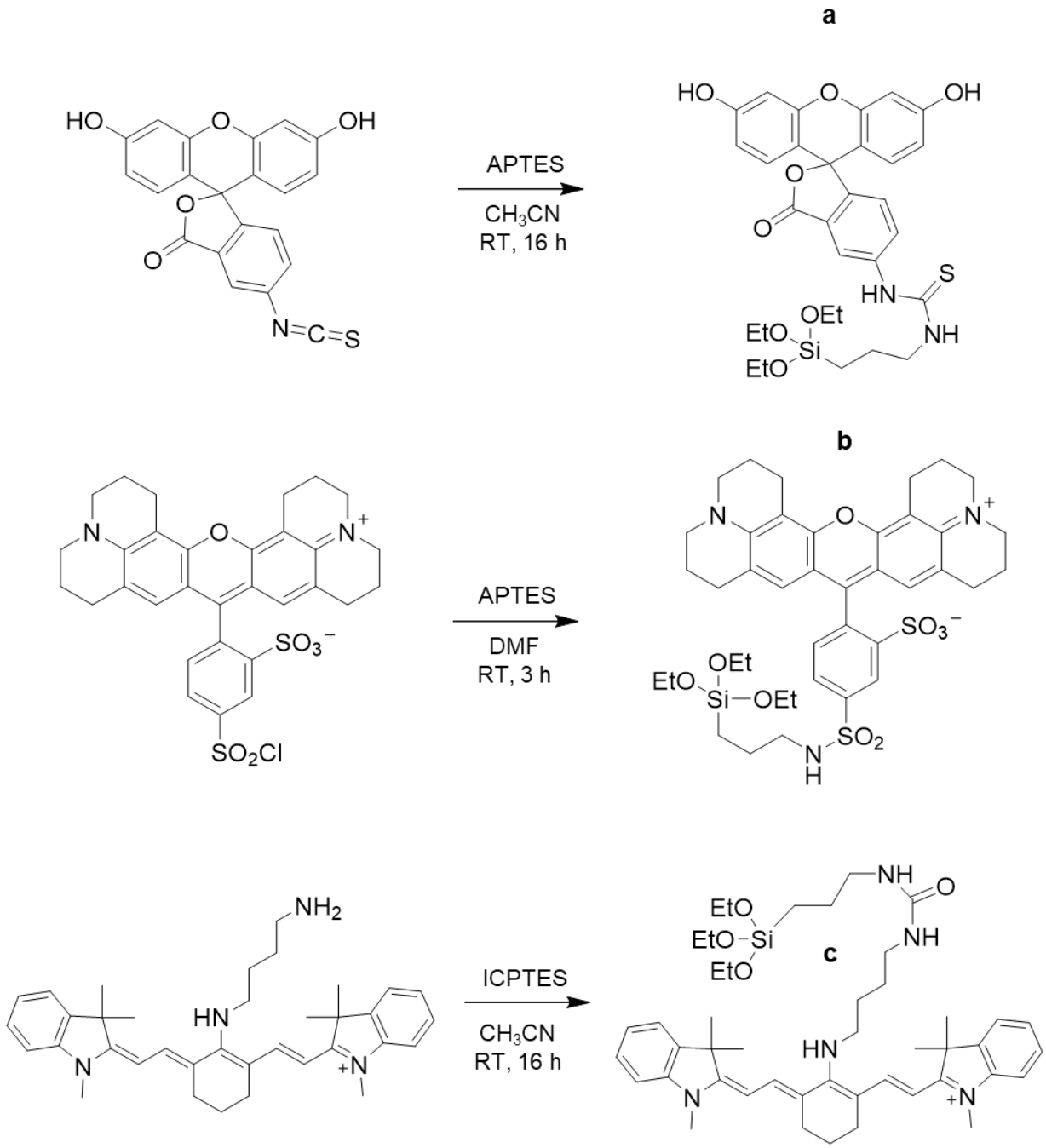

Scheme 3.1: Syntheses of dye-silane conjugates used in this study: (a) FITC-APTES, (b) TR-APTES, (c) GC-1-23-ICPTES

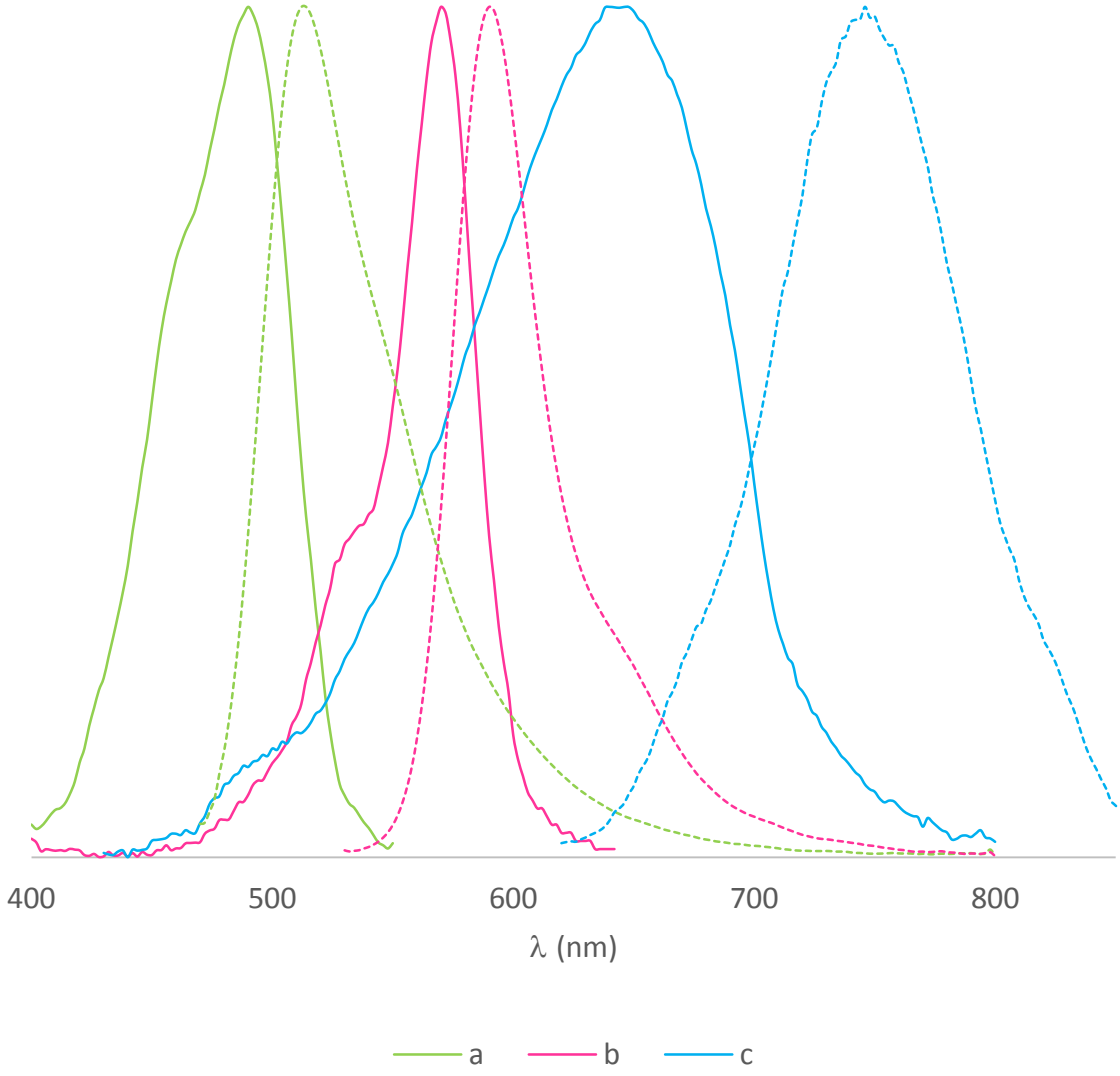

Figure 3.12: Normalized absorption (solid) and fluorescence (dashed) spectra from single dye copolymerized NPs: (a) FITC-NPs (1:0:0 dye ratio), (b) TR-NPs (0:1:0 dye ratio), (c) GC-1-23-NPs (0:0:2 dye ratio)

3.3.4.2 Optimization of dye ratios and fluorescence characterization of single and multidye NPs

Dye-silane concentrations were optimized for fluorescence intensities in preliminary studies (Section 3.2.3.3); the optimal molar dye ratio (FITC:TR:GC-1-23) was found to be 1:1:2 (in which one equivalent represents 0.025 mol% of dye-silane conjugate added relative to TEOS). Fluorescence intensities decreased for NPs incorporating higher dye-silane concentrations than this, presumably as a result of homo-FRET or possibly self-quenching interactions. A "family" of fluorescent NPs was then synthesized for the primary focus of this study. This group comprised all possible combinations of single and multiple dyes based on the optimized "1:1:2" molar ratio; ratios of FITC:TR:GC-1-23 in the synthesized NPs were as follows: 1:0:0, 0:1:0, 0:0:2, 1:1:0, 1:0:2, 0:1:2, and 1:1:2. Selected NPs from this family were chosen for further characterization. Photographs of these NPs in EtOH under ambient light and UV light are depicted in Figure 3.13. Under short-wavelength excitation (365 nm), the brightest visible fluorescence is observed for the 1:1:0 NPs, although bright fluorescence is also readily observed for the 1:0:0 and 0:1:0 NPs. Fluorescence spectra acquired for these three NP samples under a longer, more suitable excitation wavelength (λ_{EXC}) for donor FITC (450 nm) are provided in Figure 3.14. A comparison of the relative intensities of the fluorescence spectra of the 1:0:0, 0:1:0 and 1:1:0 NPs indicate an unexpectedly intense fluorescence enhancement for the 1:1:0 NPs upon excitation at 450 nm, with a net fluorescence intensity at the maximum emission wavelength 2.3 times that of NPs copolymerized with an equivalent amount of the donor alone (1:0:0) and more than 20 times that of the acceptor alone. This may be partially attributable to the very high quantum yield of the acceptor and the apparent high energy transfer efficiency between the donor and acceptor. These ultrabright particles are potentially very useful for high-

sensitivity imaging applications and feature a large Stokes shift of 100 nm. Stokes shifts were further increased to 255 nm through the addition of aminocyanine dye GC-1-23 at the expected trade-off of lower overall intensities than those exhibited by the 1:0:0 NPs and 1:1:0 NPs due to efficient energy transfer, the lower quantum yield of the aminocyanine acceptor, and the energy loss corresponding to the large Stokes shift of the acceptor. Fluorescence spectra for the 1:1:2 and 1:0:2 NPs (λ_{EXC} = 450 nm) containing this aminocyanine dye are provided in Figure 3.15. The NIR fluorescence and very large Stokes shifts exhibited by these materials are good indicators of suitability for applications as fluorescent tags in complex biological matrices. Also included in this figure are spectra for the 0:1:2 and 0:0:2 NPs under the same λ_{EXC} for comparison; observed fluorescence intensities for these materials were significantly lower given the absence of the donor (FITC).

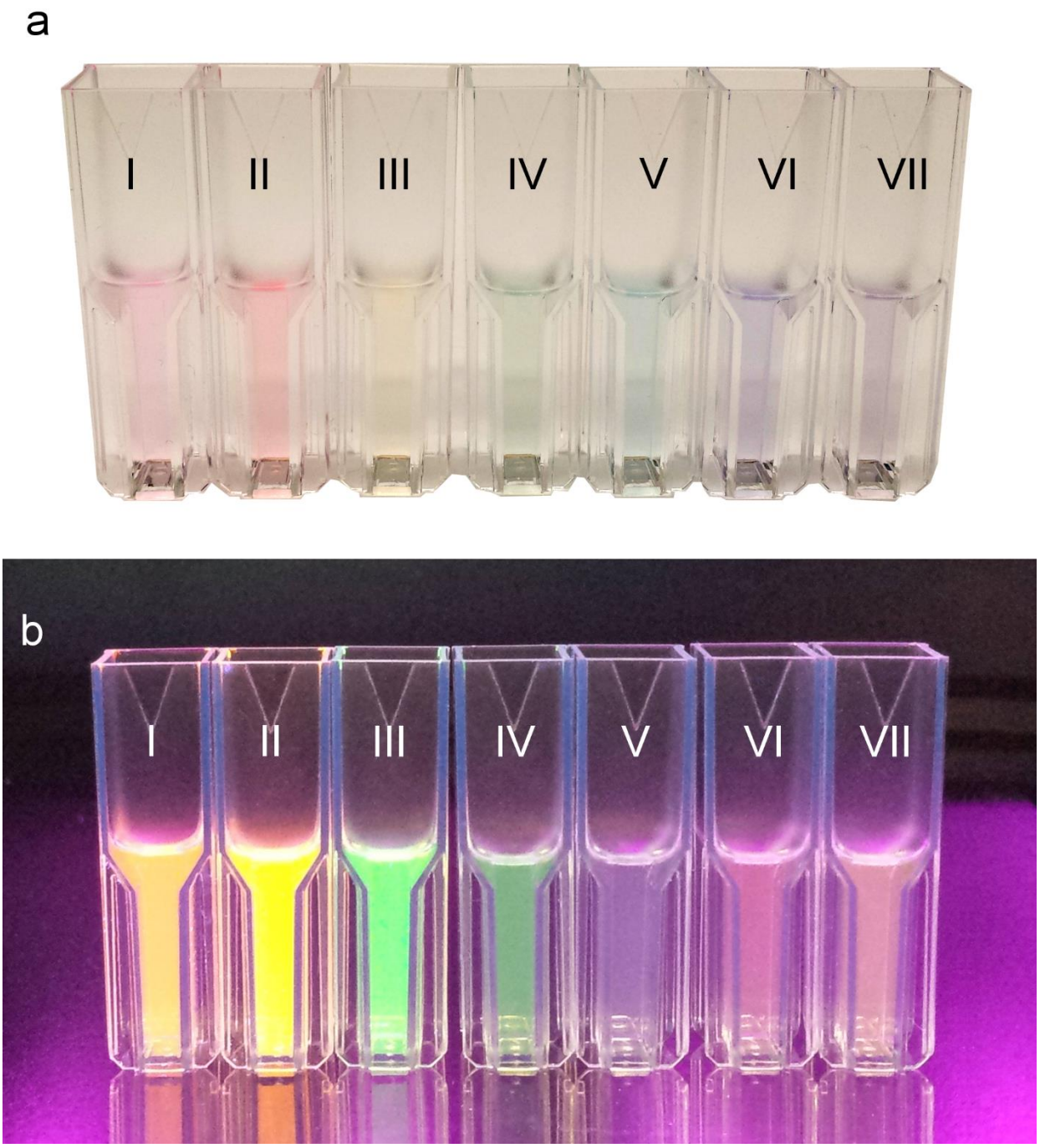

Figure 3.13: Comparison of single- and multidye-copolymerized NP samples under (a) ambient lighting and (b) ultraviolet lighting (365 nm). Dye molar ratios (FITC:TR:GC-1-23) for these samples were: (I) 0:1:0, (II) 1:1:0, (III) 1:0:0, (IV) 1:0:2, (V) 0:0:2, (VI) 0:1:2, and (VII) 1:1:2

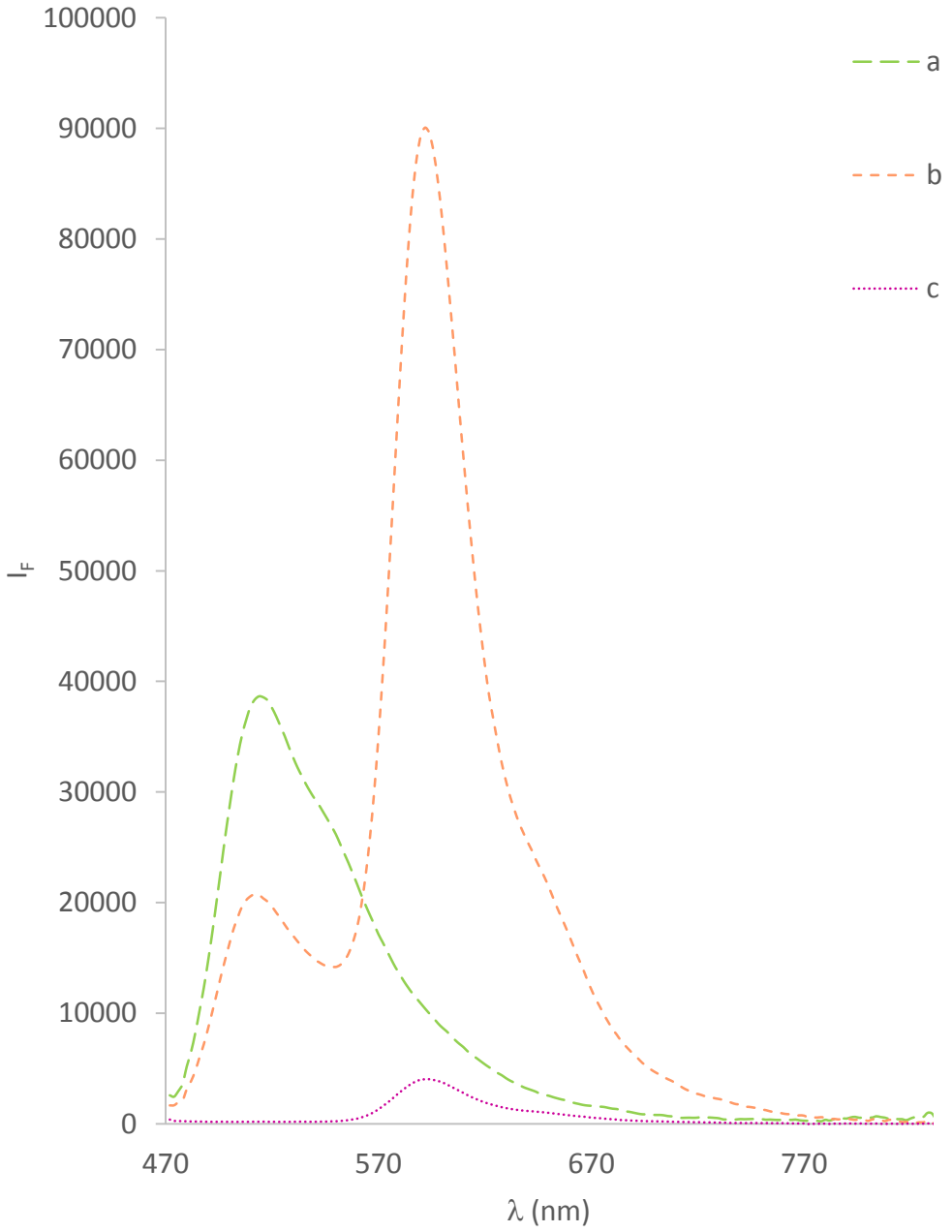

Figure 3.14: Fluorescence spectra for NPs copolymerized with FITC:TR:GC-1-23 in the ratios (a) 1:0:0, (b) 1:1:0, (c) 0:1:0 obtained using an excitation wavelength (λ_{EXC}) of 450 nm

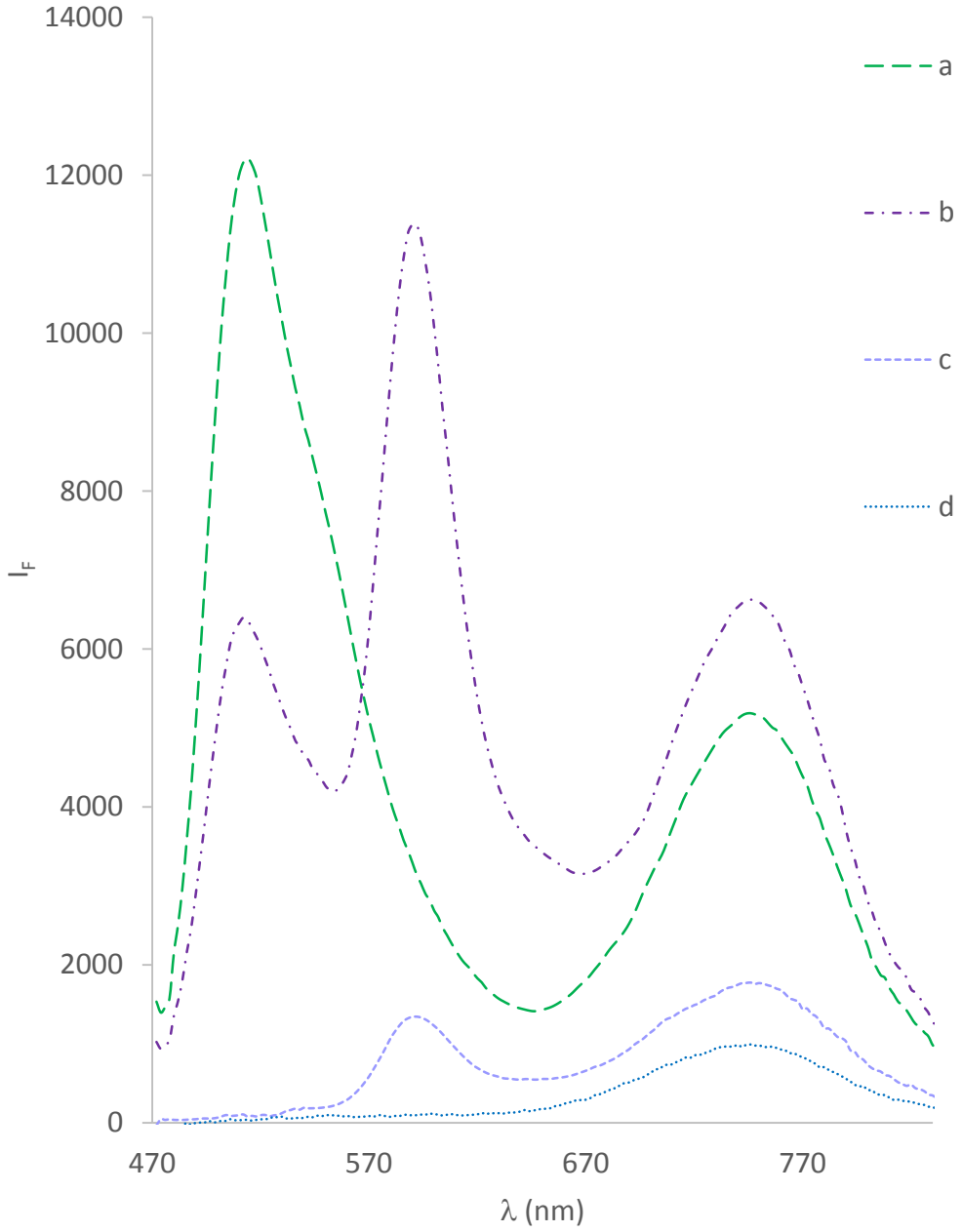

Figure 3.15: Fluorescence spectra for NPs copolymerized with FITC:TR:GC-1-23 in the ratios (a) 1:0:2, (b) 1:1:2, (c) 0:1:2, (d) 0:0:2 obtained using an excitation wavelength (λ_{EXC}) of 450 nm

3.3.4.3 NP yields and sizes

A summary of the experimentally determined NP yields and average radii (r, with included standard deviations, n = 30) for six separate samples of NPs containing different dye combinations is provided in Table 3.5. Also included in this table are averages ($\bar{x}$), standard deviations (s), and percent relative standard deviations (%RSD) of all the determined yields and radii across the six separate batches. A representative TEM image of prepared NPs is provided in Figure 3.16.

Table 3.5: Synthesis yields and TEM radii for NPs with different dye combinations

NP Sample	Yield (mg)	r (nm)
1:0:0	14.05	38 ± 6.2
0:1:0	13.4	41 ± 6.8
0:0:2	13.62	35 ± 5.5
1:1:0	12.45	38 ± 3.9
1:0:2	14	39 ± 5.6
1:1:2	12.83	36 ± 5.8
$\bar{x}$ (all)	13.4	38
s (all)	0.59	2
%RSD (all)	4.40%	5.30%

For NPs synthesized using the Stöber process, it has been shown that polydispersity increases with decreasing NP radius;[97] the prepared particles were on the smaller end of the Stöber size range and the measured radii displayed within-batch standard deviations ranging from 3.9 – 6.8 nm (10 – 17% RSD). The average radius among the six separate batches was 38 nm, and despite the different combinations and total amounts of dye-silane conjugates added to these different NP syntheses the batch-to-batch variation in average radius was small (±2 nm; 5.3% RSD) and not statistically significant. Average NP yields were also reproducible with a

batch-to-batch RSD of 4.4%. The apparent reproducibility of both the average radius (regardless of dye content and combination) and the average yield is particularly useful in downstream calculations requiring NP concentrations and surface areas, such as calculations for the surface coating and streptavidin-binding steps.

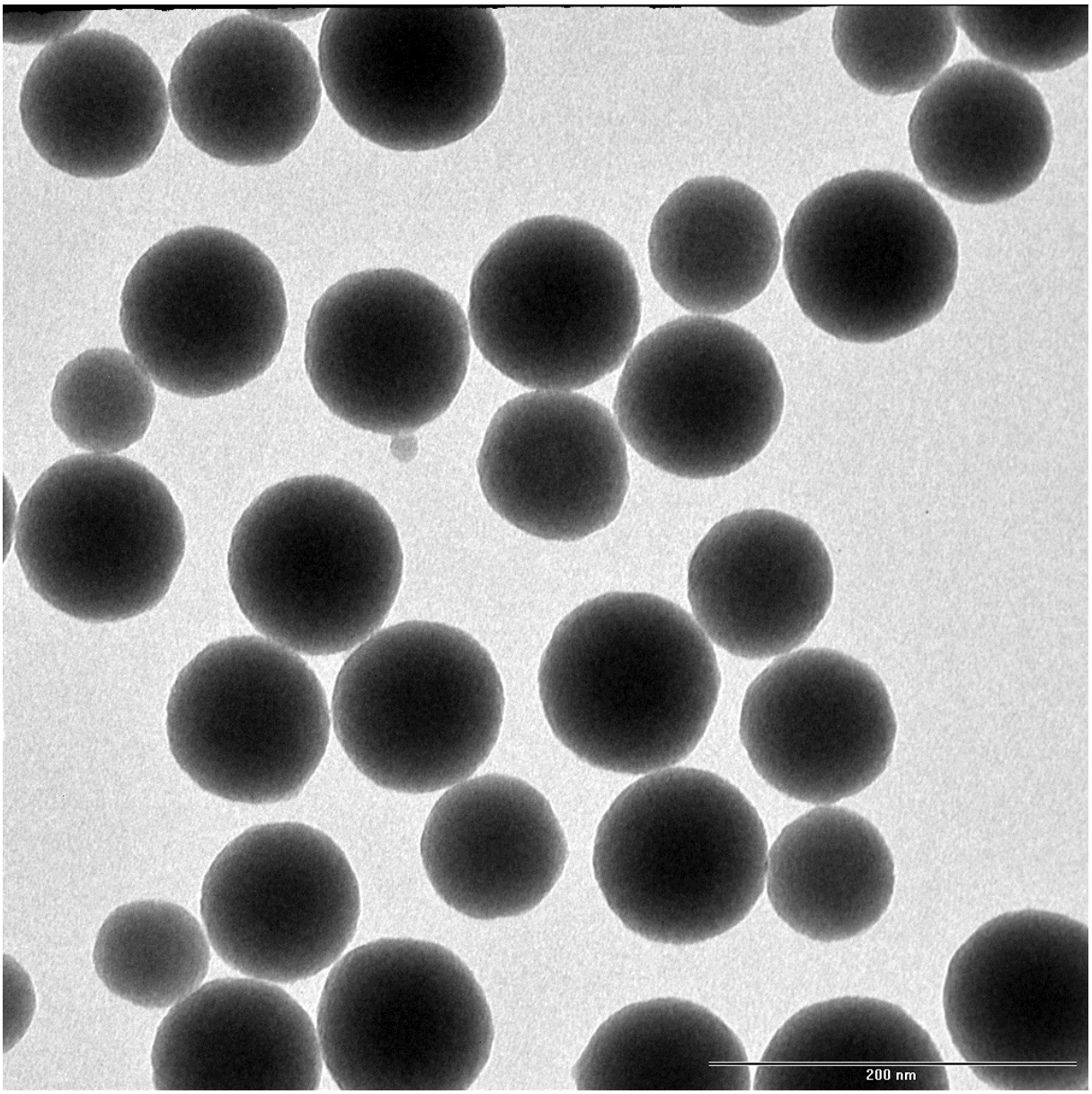

Figure 3.16: Representative TEM image of prepared NPs (scale bar: 200 nm)

3.3.4.4 Reproducibility of dye incorporation in NPs

Reproducibility of dye incorporation was determined using relative peak intensities determined from three separate syntheses of 1:1:2 NPs as detailed in Section B.1, Appendix B; results are provided in Table B.1. The incorporation rate appears to be very repeatable across multiple syntheses from a given dye-silane stock solution; the maximum observed batch-to-batch relative standard deviation for the calculated fluorescence ratios was 2.3%. This observed high batch-to-batch reproducibility of dye incorporation ratios, alongside the previously mentioned reproducibility of average radius and yield are promising indicators that these NPs may serve as reliable and consistent fluorescent labels regardless of the synthesis batch and choice of incorporated fluorophores. Additionally, the reproducibility of fluorescence ratios suggests that moderate adjustments to individual dye concentrations could produce additional fluorescent tags with readily distinguishable intensities at monitored wavelengths, further expanding the combinatorial possibilities for multicolor imaging.

3.3.4.5 Dye leaching

Dye leaching was assessed in EtOH solutions of NPs stored for 205 days by separating the supernatant from a batch of 1:1:2 NPs and assessing the fluorescence intensity as a percentage of that observed for the intact NP solution, as detailed in Section B.2, Appendix B; results are provided in Table B.2. The highest leaching percentage was observed for FITC; after 205 days, the percent relative fluorescence intensity of the supernatant was 1.5% of the total fluorescence. This good resistance to dye leaching both highlights the importance of covalent dye incorporation and indicates the long-term longevity of the prepared NPs.

3.3.4.6 Quantum yield

Quantum yields of dye-silane conjugates and single dye copolymerized nanoparticles were calculated as detailed in Section B.3, Appendix B. Quantum yields for FITC-APTES and FITC-NPs (1:0:0) were determined in EtOH relative to fluorescein (F) in 0.1 M NaOH, quantum yields for TR-APTES and TR-NPs (0:1:0) were determined in EtOH relative to rhodamine 6G (R6G) in EtOH, and quantum yields for GC-1-23-ICPTES and GC-1-23-NPs (0:0:2) were determined relative to the previously characterized value for GC-1-23 in MeOH. The standards were chosen for similarity of spectroscopic characteristics to those of the dyes and NPs in order to circumvent potential wavelength-dependent variations in detector response. Average quantum yields (ϕ, with included standard deviations, n = 3) for dye conjugates and their respective dye copolymerized NPs are provided in Table 3.6. Also provided in this table are the standards used (S) and the published quantum yields of the standards (ϕ_S).

Table 3.6: Quantum yields calculated for dye-silane conjugates and dye copolymerized NPs (n = 3)

Standard (S)	ϕ_S	λ_{EXC} (nm)	Sample	ϕ
F	0.925[a]	450	FITC-APTES	0.044 ± 0.0020
			1:0:0 NPs	0.49 ± 0.014
R6G	0.95[a]	510	TR-APTES	0.61 ± 0.020
			0:1:0 NPs	1.0 ± 0.021
GC-1-23	0.21[b]	650	GC-1-23 -ICPTES	0.25 ± 0.012
			0:0:2 NPs	0.39 ± 0.018

[a] Magde D, Wong R, Seybold PG (2002) Fluorescence Quantum Yields and Their Relation to Lifetimes of Rhodamine 6G and Fluorescein in Nine Solvents: Improved Absolute Standards for Quantum Yields. Photochem Photobiol 75(4): 327-334. https://doi.org/10.1562/0031-8655(2002)0750327FQYATR2.0.CO2

[b] Standardized relative to indocyanine green (Section 2.2.3).

Experimentally determined quantum yields were reproducible; relative standard deviations ranging from 2.0–4.8% were observed. Quantum yields of dyes in NPs increased substantially relative to those determined for the dye-silane conjugates in EtOH (50% to 1000%). Substantial enhancements in fluorophore quantum yield upon encapsulation into NPs have been previously documented in the literature and attributed to decreases in the nonradiative rate for dyes restricted within the NP polymeric matrix.[15, 17, 18, 98] The calculated 100% quantum yield of Texas Red NPs (0:1:0) likely contributes to the unexpectedly large fluorescence intensity enhancement observed in the acceptor emission for the 1:1:0 NPs. Interestingly, the calculated quantum yield of the TR-APTES conjugate in EtOH is substantially lower than that published for Texas Red in the same solvent ($\phi = 0.93$).[99] This is likely a substitution effect consequential to the direct conjugation of the reactive sulfonyl chloride group with the chromophore; in this case, conversion of this group to a sulfonamide via reaction with APTES (Scheme 3.1) modulates the fluorescence yield through an increase in the electron-donating properties.[100] No such strong effect is observed for the GC-1-23-ICPTES conjugate and only a minor change in quantum yield is measured upon reaction of GC-1-23 with ICPTES; this observation endorses the preferential reaction between isocyanate and the terminal primary amine due to the lack of conjugation between this amino group and the dye chromophore (Scheme 3.1).

Both the substantially larger relative increase in FITC-APTES quantum yield (1000%) upon incorporation into NPs relative to those increases observed for the other dye-silanes and the low observed quantum yield of FITC-APTES conjugate in EtOH may be attributable to the difference in protonation state of FITC-APTES in ethanol relative to that upon incorporation into silica nanoparticles. This supposition is supported by the normalized spectra included in Figure

3.17; the broad peaks exhibited by FITC-APTES in EtOH implies the majority of fluorescein is in its nonfluorescent neutral form, whereas the corresponding sets of spectra for both FITC NPs (1:0:0) and fluorescein standard in base solution (0.1 M NaOH) indicate relatively larger proportions of the fluorescent deprotonated forms of fluorescein.[101] The reduction in quantum yield and spectroscopic differences observed for both FITC-APTES and FITC 1:0:0 NPs relative to those of standard fluorescein in basic solution are likely attributable to a combination of differences in solvents and local environments resulting in differing protonation status as well as differences in dye substitution resulting in changes to the extent of photoinduced electron transfer. The isothiocyanate group present on FITC is conjugated with the xanthene chromophore in a manner analogous to the sulfonyl chloride group present on Texas red (Scheme 3.1); substitution at this moiety has previously been shown to result in changes to both quantum yield and spectra.[102, 103] Nonetheless, the experimentally determined quantum yield for the FITC NPs (1:0:0) was in close agreement with the value published previously by Hu et al. for FITC NPs prepared in their lab ($\phi = 0.52$).[104]

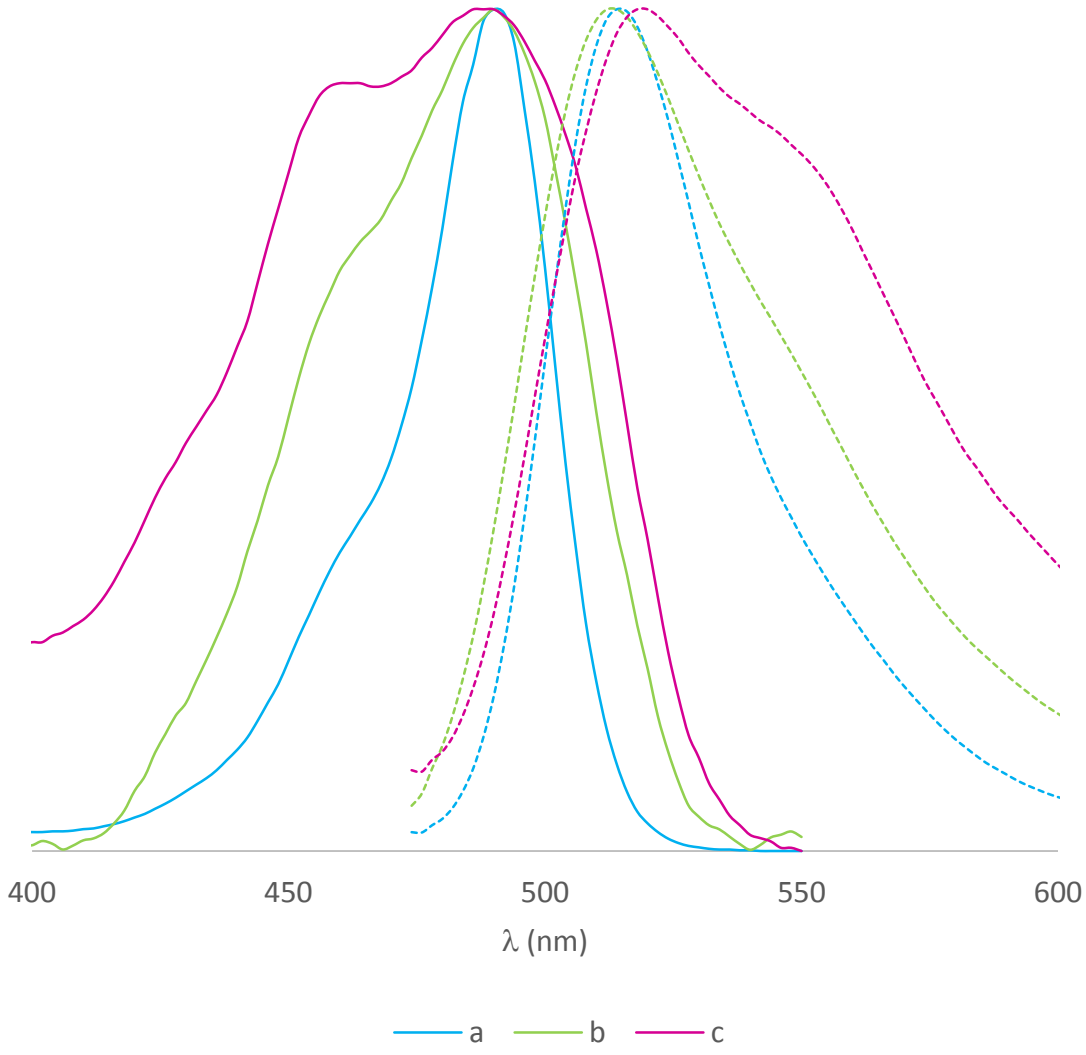

Figure 3.17: Normalized absorption (solid) and emission (dashed) spectra for fluorescein species in different environments: (a) fluorescein standard in base solution, (b) FITC-APTES copolymerized NPs in EtOH (1:0:0), and (c) FITC-APTES conjugate in EtOH

3.3.4.7 Fluorescence enhancement of dye copolymerized NPs

The fluorescence enhancement of the constituent dyes upon encapsulation into NPs was determined as the ratio of average limits of detection for the individual dye-silane conjugates (LOD_{DYE}) with those of their respective dye-containing NPs (LOD_{NP}). Experimental details are

provided in Section B.4, Appendix B. The calculated LOD values (as averages ± standard deviations) and ratios of average LOD values are presented in Table 3.7. Curves constructed for the calculation of LOD values all demonstrated coefficients of determination (R^2) greater than 0.99, indicating acceptable linearity. The calculated detection limit ratios reveal that the sensitivity is improved by approximately three orders of magnitude for the fluorescent NPs relative to their constituent dye-silane conjugates; this substantial enhancement in sensitivity may be attributed to both the large numbers of dye molecules encapsulated per NP and the substantial increases in quantum yield exhibited by the particle-bound dyes relative to their respective dye-silane conjugates.

Table 3.7: Calculated average LOD values for NPs and dye-silane conjugates (n = 3) and their ratios

NP Sample	Dye-Silane	LOD_{NP} (M)	LOD_{DYE} (M)	LOD_{DYE}/LOD_{NP}
1:0:0	FITC-APTES	1.38(+0.025)E-13	8.2(±0.12)E-10	5.90E+03
0:1:0	TR-APTES	6.5(±0.27)E-14	6.3(±0.17)E-11	9.80E+02
0:0:2	GC-1-23-ICPTES	3.2(±0.12)E-12	6.0(±0.25)E-09	1.90E+03

3.3.4.8 Demonstration of in vitro applicability to multitarget imaging

One major advantage of silica as a matrix for fluorescent dyes is its amenability to surface modification. Polyethylene glycol (PEG) is particularly useful for applications in biological matrices as it is effective in both reducing NP flocculation and shielding NP surfaces from unwanted nonspecific surface interactions with proteins.[39, 41] For bioconjugation purposes, the streptavidin-biotin system is of tremendous utility due to the binding specificity of streptavidin and the rapid formation, stability, and near-covalent strength of the bond ($K_d = 4 \times 10^{-14}$) between this protein and its target biotin.[44] Accordingly, the series of four NPs containing

donor FITC (1:0:0, 1:1:0, 1:0:2, and 1:1:2 NPs) were surface functionalized with a combination of silane derivatives of methoxy-PEG (mPEG-Sil) and biotin-PEG (Bio-PEG-Sil) to produce biotin-PEG-nanoparticles (BPNPs). These NPs were then conjugated to magnetic streptavidin microspheres and imaged with fluorescence microscopy as a proof of concept for these probes to *in vitro* multitarget assays; experimental details are provided in Section B.5, Appendix B. Fluorescence was measured using single wavelength excitation (470 nm) and emissions were imaged using three separate filters (with nominal wavelengths of 525 nm, 607 nm, and 750 nm). Fluorescence images obtained at each emission wavelength and corresponding brightfield overlays of the BPNP-microsphere conjugate samples are provided in Figure 3.18. The fluorescence colors chosen for the respective emission channels in this figure are representative of the nominal wavelengths of the emission filters used in this study.

The streptavidin microbeads demonstrated a tendency towards aggregation following slide spotting and drying regardless of whether they were functionalized with NPs. Blank particles exhibited no apparent intrinsic fluorescence at any of the monitored wavelengths. Upon single-wavelength excitation at 470 nm, the fluorescence images for tags with differing dye contents demonstrate markedly different filter-specific fluorescence from each dye in its corresponding channel, allowing ready differentiation even by simple visual inspection of the individual fluorescence channels. This characteristic greatly facilitates the distinction of targets in multicolor imaging applications. In future studies, these biotinylated NPs could readily be further functionalized with avidin and linked to biotinylated antibodies or oligonucleotides for applications in a variety of multicolor assays.

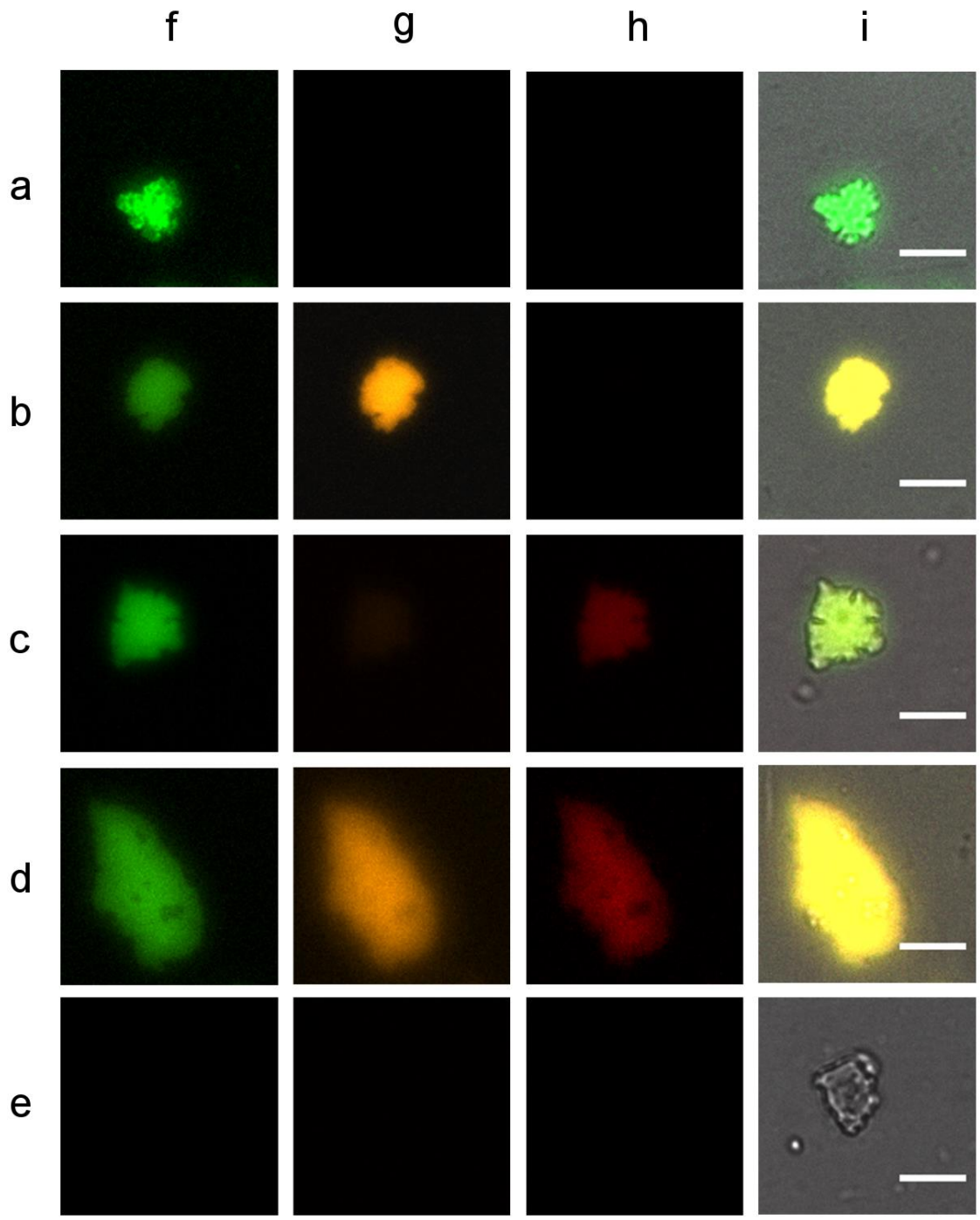

Figure 3.18: Fluorescence microscopy images of streptavidin microbeads conjugated with BPNPs with FITC:TR:GC-1-23 dye ratios of (a) 1:0:0, (b) 1:1:0, (c) 1:0:2, (d) 1:1:2; corresponding images of blank streptavidin microbeads are provided in (e). For all samples, the excitation filter nominal wavelength was 470 nm and the emission filter nominal wavelengths were (f) 525 nm, (g) 607 nm, (h) 750 nm. Combined emission spectra overlaid on brightfield images are provided in column (i); scale bar: 10 μm

3.3.4.9 Assessment of biocompatibility for in vivo applications

Fluorescent silica NPs are attractive probes for *in vivo* applications owing to their high fluorescence intensities and their reduced sensitivity to environmental conditions, and NIR-fluorescent NPs are particularly attractive candidates due to the lack of interfering fluorescence from biomolecules in this wavelength range. However, the surfaces of bare silica NPs tend to adsorb proteins *in vivo*; formation of these protein coronas alters the surface characteristics as well as the biological outcomes of interactions between NPs and living systems.[105] Additionally, bare silica NPs demonstrate significant hematotoxicity, which further limits their suitability to applications in biological systems.[106] Accordingly, NPs prepared with varying surface coating regimes were assessed for both hemolytic effects and extent of protein adsorption using slight modifications to methods described previously;[106, 107] details of the experimental approaches are provided in Sections B.6 and B.7, Appendix B. The representative NP samples for both studies all had a 1:1:2 dye ratio and differing surface modifications: bare 1:1:2 NPs, mPEG-only 1:1:2 PNPs, and 1:1:2 BPNPs with dual Bio-PEG-Sil and mPEG-Sil surface functionalization. Hemolysis experiments were conducted using human red blood cells (RBCs) and nonspecific binding was assessed using human serum albumin (HSA) and human immunoglobulin G (IgG) as model proteins. HSA was selected as it is a major constituent of blood as well as a key transport protein, and IgG was chosen due to the fact that it is the most common serum antibody and a major actor in immune response.

Bare silica NPs demonstrated substantial hematotoxicity (42% hemolysis) at a concentration of 1 mg/mL. However, following PEGylation of the NP surface, a dramatic reduction in hemolytic effects was observed; hemolysis percentages observed for equal

concentrations of PNPs and BPNPs were found to be -0.3% and -0.4%, respectively, as a result of hemoglobin absorption values below those of the negative control. The hematoprotective effects observed following PEGylation of NPs indicate effective surface passivation for these materials, shielding RBC membranes from destabilizing interactions with the highly charged surface silanol groups.[108] Efficient surface passivation may also explain the decrease in nonspecific adsorption of both HSA and IgG by the PEGylated particles relative to bare NPs, as illustrated in Figure 3.19. At nanoparticle concentrations of 2.5 mg/mL, the weight percent adsoption efficiency for IgG decreased from 4.8% for bare NPs to 1.0% for PNPs and 1.3% for BPNPs. Under the same conditions, weight percent adsorption efficiency for HSA decreased from 3.3% for bare NPs to 1.8% for PNPs and 2.4% for BPNPs. Protein-surface interactions occur as a result of a combination of electrostatic, Van der Waals, and steric interactions; introduction of PEG to the NP surface reduces both the strength and extent of these interactions through a combination of steric repulsion and charge shielding.[106] It is notable that, when comparing PEGylated PNPs and BPNPs, the BPNPs exhibited a somewhat higher percentage of protein adsorption than the PNPs for both proteins studied; the cause of this is not entirely clear but may be related to either the increased PEG chain length in Bio-PEG-Sil (MW 3400 vs MW 1000 for mPEG-Sil) or protein interactions with the terminal biotin moieties. This observation warrants further study. Nonetheless, the major improvement in hemocompatibility and the significant reduction in protein adsorption for the PEGylated PNPs and BPNPs indicates that NPs with these surface coating regimes are promising candidates for *in vivo* bioimaging applications. Nanoparticles containing either a combination of TR and GC-1-23 (0:1:2 NPs) or GC-1-23 only (0:0:2 NPs) should be well-suited to fluorescence imaging of sensitive biological tissues due to their lower energy excitation ranges. Moreover, for the clear, low-background

imaging of whole organisms, 0:0:2 NPs should be ideal probes due to the high quantum yield and large Stokes shift of this dye, the transparency of biological tissues at its excitation wavelength, and the negligible autofluorescence background at its emission. Furthermore, as previously demonstrated using streptavidin microspheres, the biotinylated BPNPs readily bind to avidin species, allowing further functionalization of NPs with biotinylated antibodies or aptamers for selective targeting of cell types and tissues. These applications will be the focus of future work.

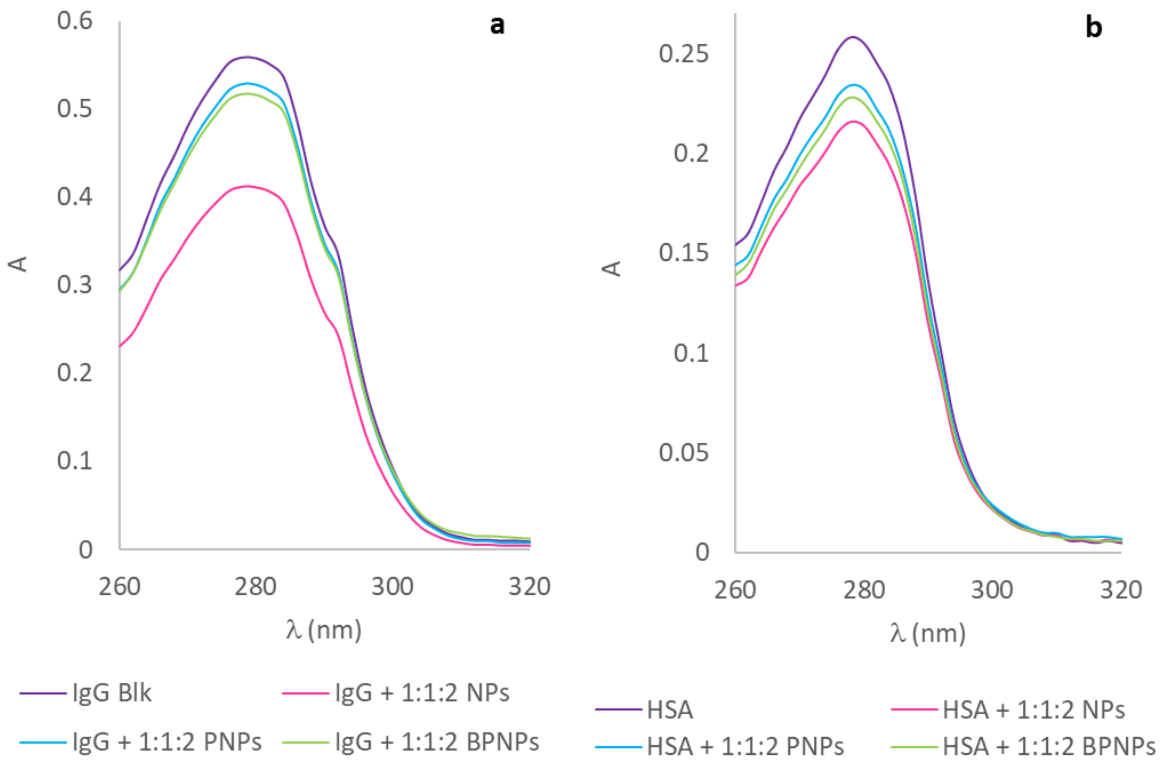

Figure 3.19: Absorption spectra of (a) IgG and (b) HSA solutions following incubation with bare 1:1:2 NPs, PEGylated 1:1:2 PNPs, and 1:1:2 BPNPs functionalized with both PEG and biotin

3.3.5 Conclusions

Aminocyanine dye GC-1-23 was synthesized and characterized; this dye exhibited a large Stokes shift and high quantum yield. A series of versatile, multifluorescent NPs with large Stokes shifts based on copolymerization with FITC, TR, and GC-1-23 was synthesized, characterized, and modified for bioconjugation. The prepared NPs exhibit minimal dye leaching even after more than 200 days of continuous storage in EtOH, and ratios of fluorescence intensities are reproducible from batch to batch. Regardless of dye content and the dyes used, both the average diameter and yield of the prepared NPs are reproducible. The independence of size on dye content and the low batch-to-batch variability in yield between individual syntheses eases calculations reliant on NP size and concentration, reduces the need for extensive characterizations of individual NP syntheses prior to application, and reduces the likelihood of size-dependent variations in interactions with biological targets.[24] The prepared NPs exhibited high quantum yields and substantial increases in fluorescence intensities relative to their constituent dye-silane conjugates. Following PEGylation and surface modification with biotin, proof of concept for these probes to *in vitro* multicolor assays was demonstrated through binding to magnetic streptavidin beads and fluorescence microscopy imaging. Furthermore, the reduced protein adsorption and hematoprotective properties demonstrated by PEGylated NPs indicate their promising potential for *in vivo* imaging.

The present study details an approach through which a variety of biocompatible NPs with readily distinguishable fluorescence signals and large Stokes shifts can be prepared using common laboratory equipment and a small number of relatively inexpensive starting materials. To the best of our knowledge, NPs containing FITC and GC-1-23 feature the largest Stokes shifts of any multidye NP tags produced to date. Of the NPs synthesized, the four NP

combinations with significant absorption at 450 nm (1:0:0, 1:1:0, 1:1:2, 1:0:2) could be applied as fluorescent barcodes for a single excitation multitarget assay, with individual fluorescence signals deconvoluted on the basis of fluorescence signals at characteristic wavelengths for each dye. The combinatorial possibilities could be expanded further by varying the relative dye ratios or incorporating additional dye species. Moreover, some of the individual synthesized NPs demonstrate particular strengths. For example, the brightly fluorescent FITC-TR 1:1:0 NPs in should make excellent labels for applications requiring high sensitivity, and particles encapsulating GC-1-23 (0:0:2 NPs) should lend themselves nicely to *in vivo* applications due to their longer wavelength absorption in the biological transparency window, NIR fluorescence, high quantum yield, and large Stokes shifts.

3.4 References

1. Slowing, I. I.; Vivero-Escoto, J. L.; Wu, C.-W.; Lin, V. S. Y., Mesoporous silica nanoparticles as controlled release drug delivery and gene transfection carriers. *Adv. Drug Deliv. Rev.* **2008,** *60* (11), 1278-1288.

2. Rahman, I. A.; Padavettan, V., Synthesis of silica nanoparticles by sol-gel: size-dependent properties, surface modification, and applications in silica-polymer nanocomposites — a review. *J. Nanomater.* **2012,** *2012,* 8-8.

3. Chen, A. M.; Zhang, M.; Wei, D.; Stueber, D.; Taratula, O.; Minko, T.; He, H., Co-delivery of Doxorubicin and Bcl-2 siRNA by Mesoporous Silica Nanoparticles Enhances the Efficacy of Chemotherapy in Multidrug-Resistant Cancer Cells. *Small* **2009,** *5* (23), 2673-2677.

4. Muhammad, F.; Guo, M.; Qi, W.; Sun, F.; Wang, A.; Guo, Y.; Zhu, G., pH-Triggered Controlled Drug Release from Mesoporous Silica Nanoparticles via Intracelluar Dissolution of ZnO Nanolids. *J. Am. Chem. Soc.* **2011,** *133* (23), 8778-8781.

5. Liu, Y.-L.; Hsu, C.-Y.; Hsu, K.-Y., Poly(methylmethacrylate)-silica nanocomposites films from surface-functionalized silica nanoparticles. *Polymer* **2005,** *46* (6), 1851-1856.

6. Yin, J.; Kim, E.-S.; Yang, J.; Deng, B., Fabrication of a novel thin-film nanocomposite (TFN) membrane containing MCM-41 silica nanoparticles (NPs) for water purification. *J. Membr. Sci.* **2012,** *423-424*, 238-246.

7. Wang, P.; Zakeeruddin, S. M.; Comte, P.; Exnar, I.; Grätzel, M., Gelation of Ionic Liquid-Based Electrolytes with Silica Nanoparticles for Quasi-Solid-State Dye-Sensitized Solar Cells. *J. Am. Chem. Soc.* **2003,** *125* (5), 1166-1167.

8. Banerjee, S.; Horn, A.; Khatri, H.; Sereda, G., A green one-pot multicomponent synthesis of 4H-pyrans and polysubstituted aniline derivatives of biological, pharmacological, and optical applications using silica nanoparticles as reusable catalyst. *Tetrahedron Lett.* **2011,** *52* (16), 1878-1881.

9. Bharti, C.; Nagaich, U.; Pal, A. K.; Gulati, N., Mesoporous silica nanoparticles in target drug delivery system: A review. *Int. J. Pharm. Investig.* **2015,** *5* (3), 124-133.

10. Liu, A.; Wu, L.; He, Z.; Zhou, J., Development of highly fluorescent silica nanoparticles chemically doped with organic dye for sensitive DNA microarray detection. *Anal. Bioanal. Chem.* **2011,** *401* (6), 2003-11.

11. Wang, L.; Wang, K.; Santra, S.; Zhao, X.; Hilliard, L. R.; Smith, J. E.; Wu, Y.; Tan, W., Watching Silica Nanoparticles Glow in the Biological World. *Anal. Chem.* **2006,** *78* (3), 646-654.

12. Taylor-Pashow, K. M. L.; Della Rocca, J.; Huxford, R. C.; Lin, W., Hybrid nanomaterials for biomedical applications. *Chem. Commun.* **2010,** *46* (32), 5832-5849.

13. Auger, A.; Samuel, J.; Poncelet, O.; Raccurt, O., A comparative study of non-covalent encapsulation methods for organic dyes into silica nanoparticles. *Nanoscale Res Lett* **2011,** *6* (1), 328.

14. Labéguerie-Egéa, J.; McEvoy, H. M.; McDonagh, C., Synthesis, characterisation and functionalisation of luminescent silica nanoparticles. *J. Nanopart. Res.* **2011,** *13* (12), 6455-6465.

15. Larson, D. R.; Ow, H.; Vishwasrao, H. D.; Heikal, A. A.; Wiesner, U.; Webb, W. W., Silica Nanoparticle Architecture Determines Radiative Properties of Encapsulated Fluorophores. *Chem. Mater* **2008,** *20* (8), 2677-2684.

16. Lessard-Viger, M.; Rioux, M.; Rainville, L.; Boudreau, D., FRET Enhancement in Multilayer Core−Shell Nanoparticles. *Nano Lett.* **2009,** *9* (8), 3066-3071.

17. Palantavida, S.; Tang, R.; Sudlow, G. P.; Akers, W. J.; Achilefu, S.; Sokolov, I., Ultrabright NIR fluorescent mesoporous silica nanoparticles. *J. Mater. Chem. B* **2014,** *2* (20), 3107-3114.

18. Bhattacharyya, S.; Prashanthi, S.; Bangal, P. R.; Patra, A., Photophysics and Dynamics of Dye-Doped Conjugated Polymer Nanoparticles by Time-Resolved and Fluorescence Correlation Spectroscopy. *J. Phys. Chem. C* **2013,** *117* (50), 26750-26759.

19. Altınoğlu, E. İ.; Adair, J. H., Near infrared imaging with nanoparticles. *Wiley Interdiscip. Rev. Nanomed. Nanobiotechnol.* **2010,** *2* (5), 461-477.

20. Murugadoss, S.; Lison, D.; Godderis, L.; Van Den Brule, S.; Mast, J.; Brassinne, F.; Sebaihi, N.; Hoet, P. H., Toxicology of silica nanoparticles: an update. *Arch. Toxicol.* **2017,** *91* (9), 2967-3010.

21. Saptarshi, S. R.; Duschl, A.; Lopata, A. L., Interaction of nanoparticles with proteins: relation to bio-reactivity of the nanoparticle. *J. Nanobiotechnology* **2013,** *11*, 26-26.

22. Treuel, L.; Docter, D.; Maskos, M.; Stauber, R. H., Protein corona - from molecular adsorption to physiological complexity. *Beilstein J. Nanotechnol.* **2015,** *6*, 857-873.

23. Satzer, P.; Svec, F.; Sekot, G.; Jungbauer, A., Protein adsorption onto nanoparticles induces conformational changes: Particle size dependency, kinetics, and mechanisms. *Eng. Life Sci.* **2016,** *16* (3), 238-246.

24. Lundqvist, M.; Sethson, I.; Jonsson, B.-H., Protein Adsorption onto Silica Nanoparticles: Conformational Changes Depend on the Particles' Curvature and the Protein Stability. *Langmuir* **2004,** *20* (24), 10639-10647.

25. Moulin, A. M.; O'Shea, S. J.; Badley, R. A.; Doyle, P.; Welland, M. E., Measuring Surface-Induced Conformational Changes in Proteins. *Langmuir* **1999,** *15* (26), 8776-8779.

26. Higashitani, K.; Nakamura, K.; Fukasawa, T.; Tsuchiya, K.; Mori, Y., Ionic Specificity in Rapid Coagulation of Silica Nanoparticles. *Langmuir* **2018,** *34* (7), 2505-2510.

27. Alves Júnior, J. A.; Baptista Baldo, J., The Behavior of Zeta Potential of Silica Suspensions. *NJGC* **2014,** *4*, 29-37.

28. Estephan, Z. G.; Jaber, J. A.; Schlenoff, J. B., Zwitterion-stabilized silica nanoparticles: toward nonstick nano. *Langmuir* **2010,** *26* (22), 16884-9.

29. Hu, F.; Chen, K.; Xu, H.; Gu, H., Functional short-chain zwitterion coated silica nanoparticles with antifouling property in protein solutions. *Colloids Surf., B* **2015,** *126* (0), 251-256.

30. Jia, G.; Cao, Z.; Xue, H.; Xu, Y.; Jiang, S., Novel Zwitterionic-Polymer-Coated Silica Nanoparticles. *Langmuir* **2009,** *25* (5), 3196-3199.

31. Huang, C.-J.; Chang, Y.-C., *In Situ* Surface Tailoring with Zwitterionic Carboxybetaine Moieties on Self-Assembled Thin Film for Antifouling Biointerfaces. *Materials* **2014,** *7*, 130-142.

32. Nooney, R. I.; McCahey, C. M. N.; Stranik, O.; Le Guevel, X.; McDonagh, C.; MacCraith, B. D., Experimental and theoretical studies of the optimisation of fluorescence from near-infrared dye-doped silica nanoparticles. *Anal. Bioanal. Chem.* **2009,** *393* (4), 1143-1149.

33. Bagwe, R. P.; Hilliard, L. R.; Tan, W., Surface Modification of Silica Nanoparticles to Reduce Aggregation and Nonspecific Binding. *Langmuir* **2006,** *22* (9), 4357-4362.

34. Xu, H.; Yan, F.; Monson, E. E.; Kopelman, R., Room-temperature preparation and characterization of poly (ethylene glycol)-coated silica nanoparticles for biomedical applications. *J. Biomed. Mater. Res. A* **2003,** *66A* (4), 870-879.

35. Hwang, Y.-J.; Lee, Y.-H.; Oh, C.; Jun, Y.-D.; Oh, S.-G., Preparation and Characterization of PEG-Grafted Silica Particles Using Emulsion. *J. Ind. Eng. Chem.* **2006,** *12* (3), 380-386.

36. Schulz, A.; Woolley, R.; Tabarin, T.; McDonagh, C., Dextran-coated silica nanoparticles for calcium-sensing. *Analyst* **2011,** *136* (8), 1722-1727.

37. Demircioglu, D. Surface Active Silica Sols: Effect of PEG-Silica Interactions. Masters, Chalmers University of Technology, Göteborg, Sweden, 2011.

38. Branda, F.; Silvestri, B.; Luciani, G.; Costantini, A.; Tescione, F., Synthesis structure and stability of amino functionalized PEGylated silica nanoparticles. *Colloids Surf., A* **2010,** *367* (1–3), 12-16.

39. Jokerst, J. V.; Lobovkina, T.; Zare, R. N.; Gambhir, S. S., Nanoparticle PEGylation for imaging and therapy. *Nanomedicine* **2011,** *6* (4), 715-728.

40. Yu, M.; Huang, S.; Yu, K. J.; Clyne, A. M., Dextran and polymer polyethylene glycol (PEG) coating reduce both 5 and 30 nm iron oxide nanoparticle cytotoxicity in 2D and 3D cell culture. *Int. J. Mol. Sci.* **2012,** *13* (5), 5554-5570.

41. Estévez, M. C.; O'Donoghue, M. B.; Chen, X.; Tan, W., Highly fluorescent dye-doped silica nanoparticles increase flow cytometry sensitivity for cancer cell monitoring. *Nano Res.* **2009,** *2* (6), 448-461.

42. Wei, Z.; Minyan, M.; Xiao-ai, Z.; Ze-yu, Z.; Sayed, M. S.; Xu-dong, W., Fluorescent proteins as efficient tools for evaluating the surface PEGylation of silica nanoparticles. *Methods Appl. Fluoresc.* **2017,** *5* (2), 024003.

43. Hirsch, J. D.; Eslamizar, L.; Filanoski, B. J.; Malekzadeh, N.; Haugland, R. P.; Beechem, J. M.; Haugland, R. P., Easily reversible desthiobiotin binding to streptavidin, avidin, and other biotin-binding proteins: uses for protein labeling, detection, and isolation. *Anal. Biochem.* **2002,** *308* (2), 343-357.

44. Wilchek, M.; Bayer, E. A., *Avidin-Biotin Technology*. Academic Press: San Diego, 1990.

45. Green, N. M., Avidin and Streptavidin. In *Methods in Enzymology: Avidin-Biotin Technology*, Wilchek, M.; Bayer, E. A., Eds. Academic Press: San Diego, 1990; Vol. 184.

46. Krkavcová, E.; Kreisinger, J.; Hyánková, L.; Hyršl, P.; Javůrková, V., The hidden function of egg white antimicrobials: egg weight-dependent effects of avidin on avian embryo survival and hatchling phenotype. *Biol. Open* **2018,** *7* (4).

47. Avidin-Biotin Technical Handbook. Thermo Scientific: 2014. https://www.thermofisher.com/us/en/home/life-science/protein-biology/protein-biology-learning-center/protein-biology-resource-library/pierce-protein-methods/avidin-biotin-interaction.html (accessed October 26, 2018).

48. Ternynck, T.; Avrameas, S., Avidin-Biotin System in Enzyme Immunoassays. In *Methods in Enzymology: Avidin-Biotin Technology*, Wilchek, M. B., E. A., Ed. Academic Press: San Diego, 1990; Vol. 184.

49. Duhamel, R. C.; Whitehead, J. S., Prevention of Nonspecific Binding of Avidin. In *Methods in Enzymology: Avidin-Biotin Technology*, Wilchek, M.; Bayer, E. A., Eds. Academic Press: San Diego, 1990; Vol. 184.

50. Weber, P.; Ohlendorf, D.; Wendoloski, J.; Salemme, F., Structural origins of high-affinity biotin binding to streptavidin. *Science* **1989,** *243* (4887), 85-88.

51. Wang, L.; Zhao, W.; O'Donoghu, M. B.; Tan, W., Fluorescent Nanoparticles for Multiplexed Bacteria Monitoring. *Bioconjugate Chem.* **2007,** *18* (2), 297-301.

52. Bayer, E. A.; Wilchek, M., Avidin and Streptavidin-Containing Probes. In *Methods in Enzymology: Avidin-Biotin Technology*, Wilchek, M.; Bayer, E. A., Eds. Academic Press: San Diego, 1990; Vol. 184.

53. Mahon, E.; Hristov, D. R.; Dawson, K. A., Stabilising fluorescent silica nanoparticles against dissolution effects for biological studies. *Chem. Commun.* **2012,** *48* (64), 7970-7972.

54. Jung, H.-S.; Moon, D.-S.; Lee, J.-K., Quantitative Analysis and Efficient Surface Modification of Silica Nanoparticles. *J. Nanomater.* **2012,** *2012*, 8.

55. Seminar on Adsorption. http://www.microtrac-bel.com/en/tech/bel/seminar06.html (accessed 26 March).

56. Zielinski, J. M.; Kettle, L. Physical Characterization: Surface Area and Porosity. www.intertek.com/chemical-physical-characterization-surface-area-and-porosity/ (accessed 19 August).

57. Green, D. L.; Lin, J. S.; Lam, Y.-F.; Hu, M. Z.-C.; Schaefer, D. W.; Harris, M. T., Size, volume fraction, and nucleation of Stober silica nanoparticles. *J. Colloid Interface Sci.* **2003,** *266* (2), 346-358.

58. Bringley, J. F.; Penner, T. L.; Wang, R.; Harder, J. F.; Harrison, W. J.; Buonemani, L., Silica nanoparticles encapsulating near-infrared emissive cyanine dyes. *J. Colloid Interface Sci.* **2008,** *320* (1), 132-9.

59. Yun, D. S.; Kim, H. J.; Yoo, J. W., Preparation of Silica Nanospheres: Effect of Silicon Alkoxide and Alcohol on Silica Nanospheres. *Bull. Korean Chem. Soc.* **2005,** *26* (12), 1927-1928.

60. Nakamura, M.; Shono, M.; Ishimura, K., Synthesis, Characterization, and Biological Applications of Multifluorescent Silica Nanoparticles. *Anal. Chem.* **2007,** *79* (17), 6507-6514.

61. Rao, C. N. R.; Thomas, P. J.; Kulkarni, G. U., *Nanocrystals: Synthesis, Properties and Applications*. Springer: Berlin, 2007.

62. *Fluorescence Microscopy and Fluorescent Probes*. Plenum Press: New York & London, 1998; Vol. 2.

63. Lakowicz, J. R., *Principles of Fluorescence Spectroscopy*. 3rd ed.; Springer Science+Business Media, LLC: New York, 2006.

64. Doré, K.; Leclerc, M.; Boudreau, D., Investigation of a Fluorescence Signal Amplification Mechanism Used for the Direct Molecular Detection of Nucleic Acids. *J. Fluoresc.* **2006,** *16* (259).

65. Weissleder, R.; Tung, C.-H.; Mahmood, U.; Bogdanov Jr, A., In vivo imaging of tumors with protease-activated near-infrared fluorescent probes. *Nat. Biotechnol.* **1999,** *17*, 375.

66. Shalon, D.; Smith, S. J.; Brown, P. O., A DNA microarray system for analyzing complex DNA samples using two-color fluorescent probe hybridization. *Genome Res.* **1996,** *6* (7), 639-645.

67. Lanz, E.; Gregor, M.; Slavík, J.; Kotyk, A., Use of FITC as a Fluorescent Probe for Intracellular pH Measurement. *J. Fluoresc.* **1997,** *7* (4), 317-319.

68. Dawson, P. L.; Acton, J. C., 22 - Impact of proteins on food color. In *Proteins in Food Processing (Second Edition)*, Yada, R. Y., Ed. Woodhead Publishing: Cambridge, 2018; pp 599-638.

69. Zipfel, W. R.; Williams, R. M.; Christie, R.; Nikitin, A. Y.; Hyman, B. T.; Webb, W. W., Live tissue intrinsic emission microscopy using multiphoton-excited native fluorescence and second harmonic generation. *Proc. Natl. Acad. Sci. U.S.A* **2003,** *100* (12), 7075-7080.

70. Pastrana, E., Near-infrared probes. *Nat. Methods* **2012,** *10*, 36.

71. Swamy, A.; Mason, J.; Lee, H.; Meadows, F.; Baars, M.; Strekowski, L.; Patonay, G., Near-infrared Absorption/Luminescence Measurements. In *Encyclopedia of Analytical Chemistry*, Meyers, R. A.; Warner, I. M., Eds. 2006.

72. Williams, A. T. R.; Winfield, S. A.; Miller, J. N., Relative fluorescence quantum yields using a computer-controlled luminescence spectrometer. *Analyst* **1983,** *108* (1290), 1067-1071.

73. Jares-Erijman, E. A.; Jovin, T. M., FRET imaging. *Nat. Biotechnol.* **2003,** *21*, 1387-1395.

74. Wu, X.; Sun, X.; Guo, Z.; Tang, J.; Shen, Y.; James, T. D.; Tian, H.; Zhu, W., In Vivo and in Situ Tracking Cancer Chemotherapy by Highly Photostable NIR Fluorescent Theranostic Prodrug. *J. Am. Chem. Soc.* **2014,** *136* (9), 3579-3588.

75. Lee, H.; Mason, J. C.; Achilefu, S., Synthesis and Spectral Properties of Near-Infrared Aminophenyl-, Hydroxyphenyl-, and Phenyl-Substituted Heptamethine Cyanines. *J. Org. Chem.* **2008,** *73* (2), 723-725.

76. Levitz, A.; Marmarchi, F.; Henary, M., Synthesis and Optical Properties of Near-Infrared meso-Phenyl-Substituted Symmetric Heptamethine Cyanine Dyes. *Molecules* **2018,** *23* (2).

77. Matichak, J. D.; Hales, J. M.; Barlow, S.; Perry, J. W.; Marder, S. R., Dioxaborine- and Indole-Terminated Polymethines: Effects of Bridge Substitution on Absorption Spectra and Third-Order Polarizabilities. *J. Phys. Chem. A* **2011,** *115* (11), 2160-2168.

78. Dewar, M. J. S., 478. Colour and constitution. Part I. Basic dyes. *J. Chem. Soc.* **1950,** (0), 2329-2334.

79. Knott, E. B., 227. The colour of organic compounds. Part I. A general colour rule. *J. Chem. Soc.* **1951,** (0), 1024-1028.

80. Peng, X.; Song, F.; Lu, E.; Wang, Y.; Zhou, W.; Fan, J.; Gao, Y., Heptamethine Cyanine Dyes with a Large Stokes Shift and Strong Fluorescence: A Paradigm for Excited-State Intramolecular Charge Transfer. *J. Am. Chem. Soc.* **2005,** *127* (12), 4170-4171.

81. Gorris, H. H.; Saleh, S. M.; Groegel, D. B. M.; Ernst, S.; Reiner, K.; Mustroph, H.; Wolfbeis, O. S., Long-Wavelength Absorbing and Fluorescent Chameleon Labels for Proteins, Peptides, and Amines. *Bioconjugate Chem.* **2011,** *22* (7), 1433-1437.

82. Menéndez, G. O.; Eva Pichel, M.; Spagnuolo, C. C.; Jares-Erijman, E. A., NIR fluorescent biotinylated cyanine dye: optical properties and combination with quantum dots as a potential sensing device. *Photochem. Photobiol. Sci.* **2013,** *12* (2), 236-240.

83. Zhang, W.-H.; Hu, X.-X.; Zhang, X.-B., Dye-Doped Fluorescent Silica Nanoparticles for Live Cell and In Vivo Bioimaging. *Nanomaterials* **2016,** *6* (81), 1-17.

84. Nooney, R. I.; McCormack, E.; McDonagh, C., Optimization of size, morphology and colloidal stability of fluorescein dye-doped silica NPs for application in immunoassays. *Anal. Bioanal. Chem.* **2012,** *404* (10), 2807-2818.

85. Wang, L.; Yang, C.; Tan, W., Dual-Luminophore-Doped Silica Nanoparticles for Multiplexed Signaling. *Nano Lett.* **2005,** *5* (1), 37-43.

86. Biffi, S.; Petrizza, L.; Rampazzo, E.; Voltan, R.; Sgarzi, M.; Garrovo, C.; Prodi, L.; Andolfi, L.; Agnoletto, C.; Zauli, G.; Secchiero, P., Multiple dye-doped NIR-emitting silica nanoparticles for both flow cytometry and in vivo imaging. *RSC Adv.* **2014,** *4* (35), 18278-18285.

87. Kumar, R.; Roy, I.; Ohulchanskyy, T. Y.; Goswami, L. N.; Bonoiu, A. C.; Bergey, E. J.; Tramposch, K. M.; Maitra, A.; Prasad, P. N., Covalently Dye-Linked, Surface-Controlled, and Bioconjugated Organically Modified Silica Nanoparticles as Targeted Probes for Optical Imaging. *ACS Nano* **2008,** *2* (3), 449-456.

88. Wang, Z.; Hong, X.; Zong, S.; Tang, C.; Cui, Y.; Zheng, Q., BODIPY-doped silica nanoparticles with reduced dye leakage and enhanced singlet oxygen generation. *Sci. Rep.* **2015,** *5*, 12602.

89. Edelstein, A.; Amodaj, N.; Hoover, K.; Vale, R.; Stuurman, N., Computer Control of Microscopes Using μManager. *Curr. Protoc. Mol. Biol.* **2010,** *92* (1), 14.20.1-14.20.17.

90. Edelstein, A. D.; Tsuchida, M. A.; Amodaj, N.; Pinkard, H.; Vale, R. D.; Stuurman, N., Advanced methods of microscope control using μManager software. *J. Biol. Methods* **2014,** *1* (2), e10.

91. Meijering, E. H. W.; Niessen, W. J.; Viergever, M. A., Quantitative evaluation of convolution-based methods for medical image interpolation. *Med. Image Anal.* **2001,** *5* (2), 111-126.

92. Landini, G. In *Advanced shape analysis with ImageJ*, Proceedings of the Second ImageJ User and Developer Conference, Luxembourg, 6-7 November; Luxembourg 2008; pp 116-121.

93. Stöber, W.; Fink, A.; Bohn, E., Controlled growth of monodisperse silica spheres in the micron size range. *J. Colloid Interface Sci.* **1968,** *26* (1), 62-69.

94. Murali, V. S.; Wang, R.; Mikoryak, C. A.; Pantano, P.; Draper, R., Rapid detection of polyethylene glycol sonolysis upon functionalization of carbon nanomaterials. *Exp. Biol. Med. (Maywood)* **2015,** *240* (9), 1147-51.

95. Benson, R. A.; Kues, H. A., Fluorescence properties of indocyanine green as related to angiography. *Phys. Med. Biol.* **1978,** *23* (1), 159-163.

96. Mchedlov-Petrossyan, N. O.; Kukhtik, V. I.; Bezugliy, V. D., Dissociation, tautomerism and electroreduction of xanthene and sulfonephthalein dyes in N,N-dimethylformamide and other solvents. *J. Phys. Org. Chem.* **2003,** *16* (7), 380-397.

97. Nyffenegger, R.; Quellet, C.; Ricka, J., Synthesis of Fluorescent, Monodisperse, Colloidal Silica Particles. *J. Colloid Interface Sci.* **1993,** *159* (1), 150-157.

98. Chen, X.; Zhang, X.; Xia, L.-Y.; Wang, H.-Y.; Chen, Z.; Wu, F.-G., One-Step Synthesis of Ultrasmall and Ultrabright Organosilica Nanodots with 100% Photoluminescence Quantum Yield: Long-Term Lysosome Imaging in Living, Fixed, and Permeabilized Cells. *Nano Lett.* **2018,** *18* (2), 1159-1167.

99. Soper, S. A.; Nutter, H. L.; Keller, R. A.; Davis, L. M.; Shera, E. B., The photophysical constants of several fluorescent dyes pertaining to ultrasensitive fluorescence spectroscopy. *Photochem. Photobiol.* **1993,** *57* (s1), 972-977.

100. Unruh, J. R.; Gokulrangan, G.; Wilson, G. S.; Johnson, C. K., Fluorescence Properties of Fluorescein, Tetramethylrhodamine and Texas Red Linked to a DNA Aptamer. *Photochem. Photobiol.* **2005,** *81* (3), 682-690.

101. Martin, M. M.; Lindqvist, L., The pH dependence of fluorescein fluorescence. *J. Lumin.* **1975,** *10* (6), 381-390.

102. Klonis, N.; Sawyer, W. H., The Thiourea Group Modulates the Fluorescence Emission Decay of Fluorescein-labeled Molecules *Photochem. Photobiol.* **2003,** *77* (5), 502-509.

103. Miura, T.; Urano, Y.; Tanaka, K.; Nagano, T.; Ohkubo, K.; Fukuzumi, S., Rational Design Principle for Modulating Fluorescence Properties of Fluorescein-Based Probes by Photoinduced Electron Transfer. *J. Am. Chem. Soc.* **2003,** *125* (28), 8666-8671.

104. Hu, Z.; Tan, J.; Lai, Z.; Zheng, R.; Zhong, J.; Wang, Y.; Li, X.; Yang, N.; Li, J.; Yang, W.; Huang, Y.; Zhao, Y.; Lu, X., Aptamer Combined with Fluorescent Silica Nanoparticles for Detection of Hepatoma Cells. *Nanoscale. Res. Lett.* **2017,** *12*, 96.

105. Lesniak, A.; Fenaroli, F.; Monopoli, M. P.; Åberg, C.; Dawson, K. A.; Salvati, A., Effects of the Presence or Absence of a Protein Corona on Silica Nanoparticle Uptake and Impact on Cells. *ACS Nano* **2012,** *6* (7), 5845-5857.

106. Zhou, G.; Li, L.; Xing, J.; Cai, J.; Chen, J.; Liu, P.; Gu, N.; Ji, M., Layer-by-layer construction of lipid bilayer on mesoporous silica nanoparticle to improve its water suspensibility and hemocompatibility. *J. Sol-Gel Sci. Technol.* **2017,** *82* (2), 490-499.

107. Abdelwahab, W. M.; Phillips, E.; Patonay, G., Preparation of fluorescently labeled silica nanoparticles using an amino acid-catalyzed seeds regrowth technique: Application to latent fingerprints detection and hemocompatibility studies. *J. Colloid Interface Sci.* **2018,** *512*, 801-811.

108. Slowing, I. I.; Wu, C.-W.; Vivero-Escoto, J. L.; Lin, V. S.-Y., Mesoporous Silica Nanoparticles for Reducing Hemolytic Activity Towards Mammalian Red Blood Cells. *Small* **2009,** *5* (1), 57-62.

4 RESONANCE ENERGY TRANSFER CHARACTERISTICS OF MULTIDYE-DOPED NANOPARTICLES

4.1 Introduction

4.1.1 Förster resonance energy transfer

Förster resonance energy transfer (FRET) is a phenomenon in which an excited-state fluorophore, known as a donor (D), transfers its excitation energy to a nearby fluorophore known as an acceptor (A) rather than directly emitting the energy as a photon, as discussed in 2.1.1. The process of FRET occurs through dipole-dipole interactions between the excited state donor and the ground state acceptor, and involves a quenching of the donor fluorescence due to the energy transfer. As the extent of energy transfer is dependent on distance but independent of environment, FRET can be a tremendously useful technique for probing spatial relationships, molecular dynamics, and interactions between biomolecules.[1] Furthermore, as discussed in some depth in Section 3.3., the use of FRET-paired dyes can also be extremely useful in the development of multiplexing tags due to the possibility of combining a limited number of different dyes in different ratios to generate a large variety of probes with readily distinguishable fluorescence signals.

4.1.2 Spectral overlap and the Förster distance

The resonance energy transfer process occurs through dipole-dipole interactions between the excited state donor and the ground state acceptor (Figure 4.1.a). In order for resonance to occur between the donor and acceptor, the emission energy of the donor must match the energy requirements for excitation of the acceptor (Figure 4.1.b); i.e. the donor emission spectrum must overlap with the acceptor excitation spectrum. The extent of resonance is dependent upon the area of overlap between the absorption spectrum of the donor and the emission spectrum of the acceptor, as illustrated in Figure 4.1.c.

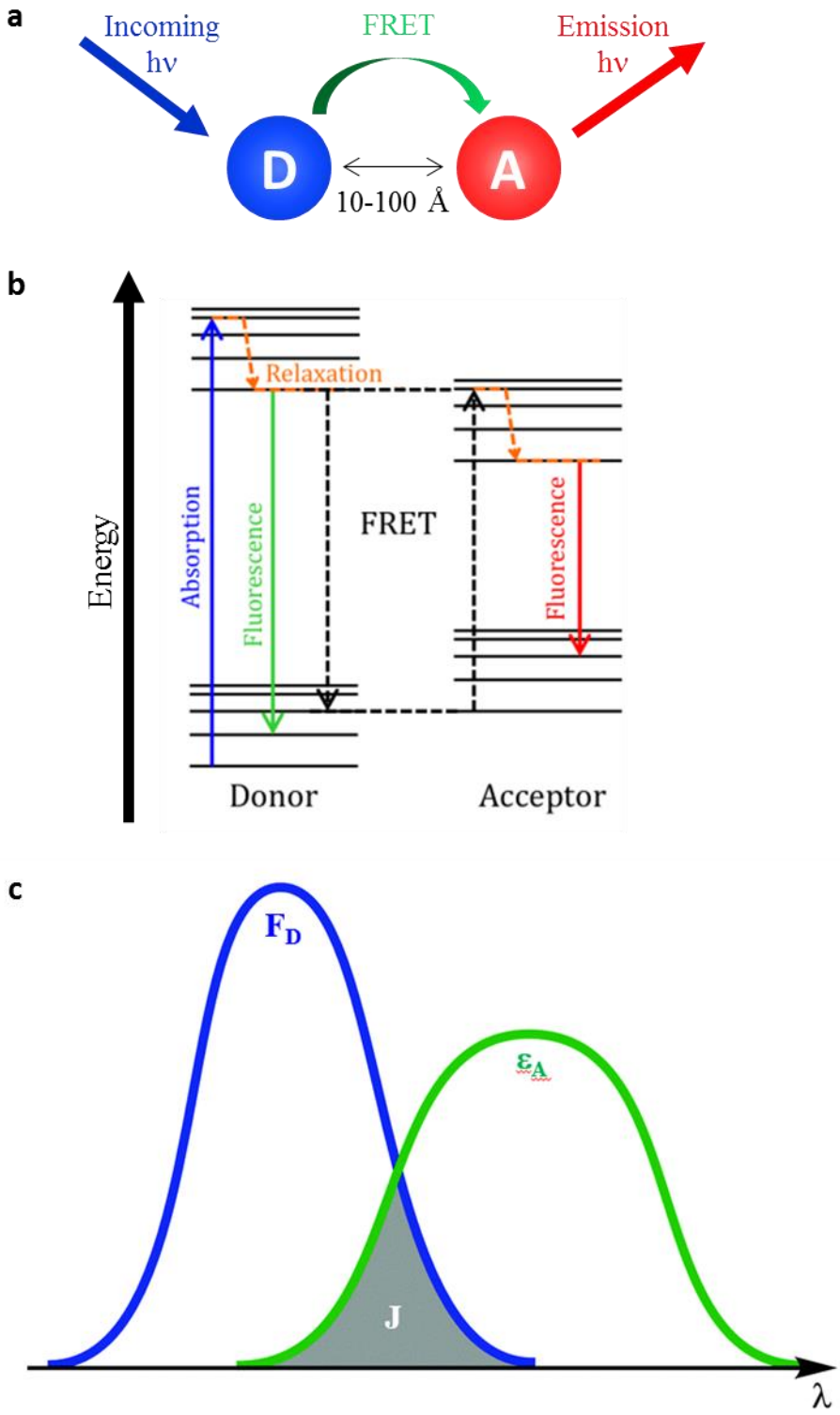

Figure 4.1: (a) Schematic illustration of resonance energy transfer between donor D and acceptor A; (b) Jablonski diagram of FRET; (c) adapted illustration of overlap integral (grey shaded area, J) between D fluorescence spectrum (blue, F_D) and A absorption spectrum (green, ε_A)[2]

The area of overlap between the donor emission and acceptor absorption (Figure 4.1.c) may be determined by calculating the overlap integral for the pair as per Equation 4.1. In this equation, $J(\lambda)$ is the overlap integral in M^{-1} cm^{-1}, $\varepsilon_A(\lambda)$ is the wavelength-dependent extinction coefficient of the acceptor in M^{-1} cm^{-1} and $F_D(\lambda)$ is the wavelength-dependent emission intensity of the donor.[3, 4] If the emission area is normalized to 1 [$F'_D(\lambda) = F_D(\lambda) / \int_0^\infty F_D(\lambda)d\lambda$], Equation 4.1 may be simplified to Equation 4.2.

$$J(\lambda) = \frac{\int_0^\infty F_D(\lambda)\varepsilon_A(\lambda)\lambda^4 d\lambda}{\int_0^\infty F_D(\lambda)d\lambda} \quad 4.1$$

$$J(\lambda) = \int_0^\infty F'_D(\lambda)\varepsilon_A(\lambda)\lambda^4 d\lambda \quad 4.2$$

Where $F'_D = \frac{F_D(\lambda)}{\int_0^\infty F_D(\lambda)d\lambda}$

In order for a successful dipole-dipole interaction to occur between molecules, the donor and acceptor must must be in relatively close proximity (generally 10-100 Å).[5] The actual distance for successful FRET between donor and acceptor varies by donor-acceptor pair and depends on a number of factors, including the overlap integral $J(\lambda)$, the quantum yield of the donor ϕ_D in the absence of acceptor, the refractive index of the medium (η), and the donor-acceptor orientation factor (κ^2). The Förster distance (R_0) for a FRET pair is defined as the distance at which the efficiency of resonance energy transfer is 50%; R_0 (in Å) may be calculated as per Equation 4.3.[3]

$$R_0 = 0.211 \left(\frac{\kappa^2 \phi_D J(\lambda)}{\eta^4} \right)^{1/6} \qquad 4.3$$

The orientation factor κ^2 describes the relative orientation of the donor and acceptor dipoles. Electronic excitation is dependent on the orientation of the electric field of the incoming excitation energy relative to the dipole of the accepting molecule. In the case of resonance energy transfer, the angular orientation of the excited state donor's dipole relative to that of the acceptor affects the efficiency of the energy transfer. Values of κ^2 range from 0 – 4; the value is 0 if the dipoles of the donor and acceptor are perpendicular, the value is 1 if the dipoles of the donor and acceptor are oriented side-by-side and parallel, and the value is 4 when the dipoles are oriented head to tail and parallel. In calculations of R_0 based on the overlap integral $J(\lambda)$, the value of κ^2 is typically taken to be 2/3; this approximation is based on relative probabilities of different donor-acceptor orientations with an assumption that the donor and acceptor are small molecules that rotate freely, isotropically, and independently of one another, with rotational diffusion occurring more quickly than the fluorescence lifetime of the donor. In instances where this is not the case (e.g. conformationally restricted fluorophores or large fluorescent proteins with slower rotational diffusion), more significant errors in the calculated values of R_0 may occur when Equation 4.3 is used.[6]

4.1.3 Energy transfer efficiency

The efficiency of energy transfer between fluorophores (E) is highly sensitive to distance, varying inversely with the sixth power of the distance (R) between the donor and acceptor, as illustrated in Equation 4.4 and Figure 4.2.[4]

$$E = \frac{1}{1+(\frac{R}{R_0})^6} = \frac{R_0^6}{R_0^6+R^6} \qquad 4.4$$

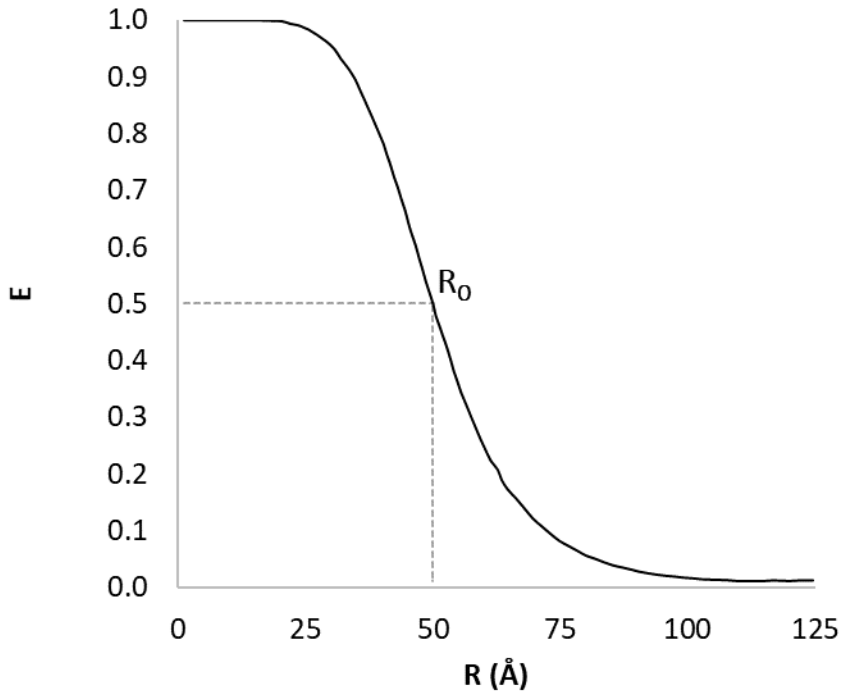

Figure 4.2: Variation of FRET efficiency (E) with radius (R) for a hypothetical donor-acceptor pair with a Förster radius (R_0) of 50 Å

Energy transfer from the donor to the acceptor necessitates an associated reduction in the fluorescence intensity of the donor; as the FRET efficiency (E) approaches 100%, the fluorescence intensity of the donor approaches zero. The extent of the reduction in fluorescence may be used to determine the energy transfer efficiency as per Equation 4.5. In this equation, F_D

is the fluorescence intensity of the donor on its own, and F_{DA} is the fluorescence intensity of an equal amount of the donor in the presence of the acceptor.[3]

$$E = 1 - \frac{F_{DA}}{F_D} \qquad 4.5$$

It's important to note that, in order for this equation to be meaningful, one must ensure equal concentrations of donor in both the samples with and without acceptor. In cases where this is not possible, a better means of comparison is by the quantum yield (ϕ) since this value is based on fluorescence-to-absorption ratios and is therefore insensitive to moderate variations in concentration; Equation 4.5 may therefore be rewritten as Equation 4.6.[4]

$$E = 1 - \frac{\phi_{DA}}{\phi_D} \qquad 4.6$$

4.1.4 Overview

In this chapter, the multidye-copolymerized NPs prepared as described in Chapter 3 are characterized in terms of their FRET-related parameters. In particular, the energy transfer efficiencies of donor-acceptor dye pairs, the number of dye molecules incorporated per particle, and the average distance between dye molecules will be calculated and compared with self-quenching parameters. The Förster distance will then be calculated two ways: by using the typical approach based on spectral overlap, and by using a more novel approach based on the relationship between energy transfer efficiency and distance.

4.2 Experimental

Reagents, materials, and instrumentation are listed in Section 3.2.2.1.

4.2.1 Determination of energy transfer efficiency

A series of NPs based on all possible combinations of dyes following the "1:1:2" ratio of FITC:TR:GC-1-23 were synthesized and quantum yields were determined in EtOH (n = 3). The relevant NP batches synthesized had FITC:TR:GC-1-23 ratios of 1:0:0, 0:1:0, 0:0:2, 1:1:0, 0:1:2, and 1:1:2. A series of NPs based following the "1:1:1" ratio of FITC:TR:GC-1-23 were also synthesized and quantum yields were determined in EtOH (n = 3). The additional NP batches synthesized had FITC:TR:GC-1-23 ratios of 0:0:1, 0:1:1, and 1:1:1; there was some overlap with the previous batch of NPs due to the similarity of the doping ratio. Donor quantum yields for relevant pairings of double and triple dye-doped NPs were determined in the same manner described previously for single dye-doped NPs (Section B.3, Appendix B). Specifically, the quantum yields of FITC-APTES in dye-doped NPs were determined relative to fluorescein in 0.1 M KOH (aq), quantum yields of TR-APTES in the dye-doped NPs were determined relative to Rhodamine 6G in EtOH, and quantum yields of GC-1-23-ICPTES in the dye-doped NPs were determined relative to the experimentally-determined quantum yield for GC-1-23 (Section 2.3.3). Dye-doped NP solutions were prepared such that the total absorption (dye plus particle scattering) was <0.1 at the excitation wavelength in order to reduce the inner filter effect in the fluorescence profiles. The dye absorption (rather than the total absorption) of the dye-doped particles was used to calculate the fluorescence quantum yields. The NP scattering profiles were determined using normalized absorption profiles of blank (dye-free) NPs synthesized separately. The normalized scattering profiles of these particles were subtracted from the total absorption to deconvolute the dye absorption. Fluorescence values for individual dyes in multidye

copolymerized particles were similarly deconvoluted in order to correct for spectral overlap. Dye quantum yields were determined from the "single-point" rather than the regression approach due to the extreme difficulty in generating multiple NP samples with total (dye + NP) absorption values < 0.1 which also had reliably measurable dye absorption values. The published refractive index for silica NPs ($\eta = 1.475 \pm 0.005$)[7] and the corresponding refractive index for the standard solvent were used in the calculation of all quantum yields involving dye-copolymerized NPs. Apparent FRET efficiencies (E) were then calculated from the change in donor quantum yields in NPs when an acceptor is introduced,[8] as per Equation 4.6.

4.2.2 Determination of number of dye molecules per NP

Because the molar absorptivity of dye-silane conjugates may change upon incorporation into NPs, the best way to determine the number of dyes incorporated into each particle is by difference. Specifically, the extent of dye incorporation can be determined indirectly by the change in absorption of the NP synthesis solution after the NPs have been removed by centrifugation, as illustrated using Equation 4.7. In this equation, ΔA_{tot} is the "equivalent" absorption for the total dye(s) incorporated into the NPs, as measured by the change in the absorption of the synthesis solution after removal of the NPs; A_I is the initial (pre-centrifugation) absorption of the NP synthesis solution and A_F is the final (post-centrifugation) absorption of the supernatant following removal of the NPs.

$$\Delta A_{tot} = A_I - A_F \qquad 4.7$$

In order to determine the concentration of dyes by absorption difference, molar absorptivities of dye-silane conjugates must first be determined in the synthesis solution using Beer's law (Equation 2.6). Molar absorptivities were determined in triplicate for all three dye-silane conjugates used in the multidye NP syntheses by linear regression. Serial dilutions of each dye-silane were made separately into a batch of Stöber NP synthesis solution (94.19% EtOH, 5.13% H_2O, 0.68% NH_3 (v/v) with no added TEOS). Dye-silane solutions were left to sit for 20h (the synthesis time of NPs from the time of dye addition until cleanup) to account for any possible base-catalyzed decomposition. Since some of the fluorescent NPs contained up to 3 dyes with partially overlapping absorption spectra, it was necessary to identify wavelengths at which absorption (and therefore the concentration) of each dye could be deconvoluted. Based on an examination of the absorption spectra for each dye species in the NP synthesis solution (Figure 4.3), appropriate wavelengths identified for this purpose were: 650 nm, 576 nm, and 502 nm.

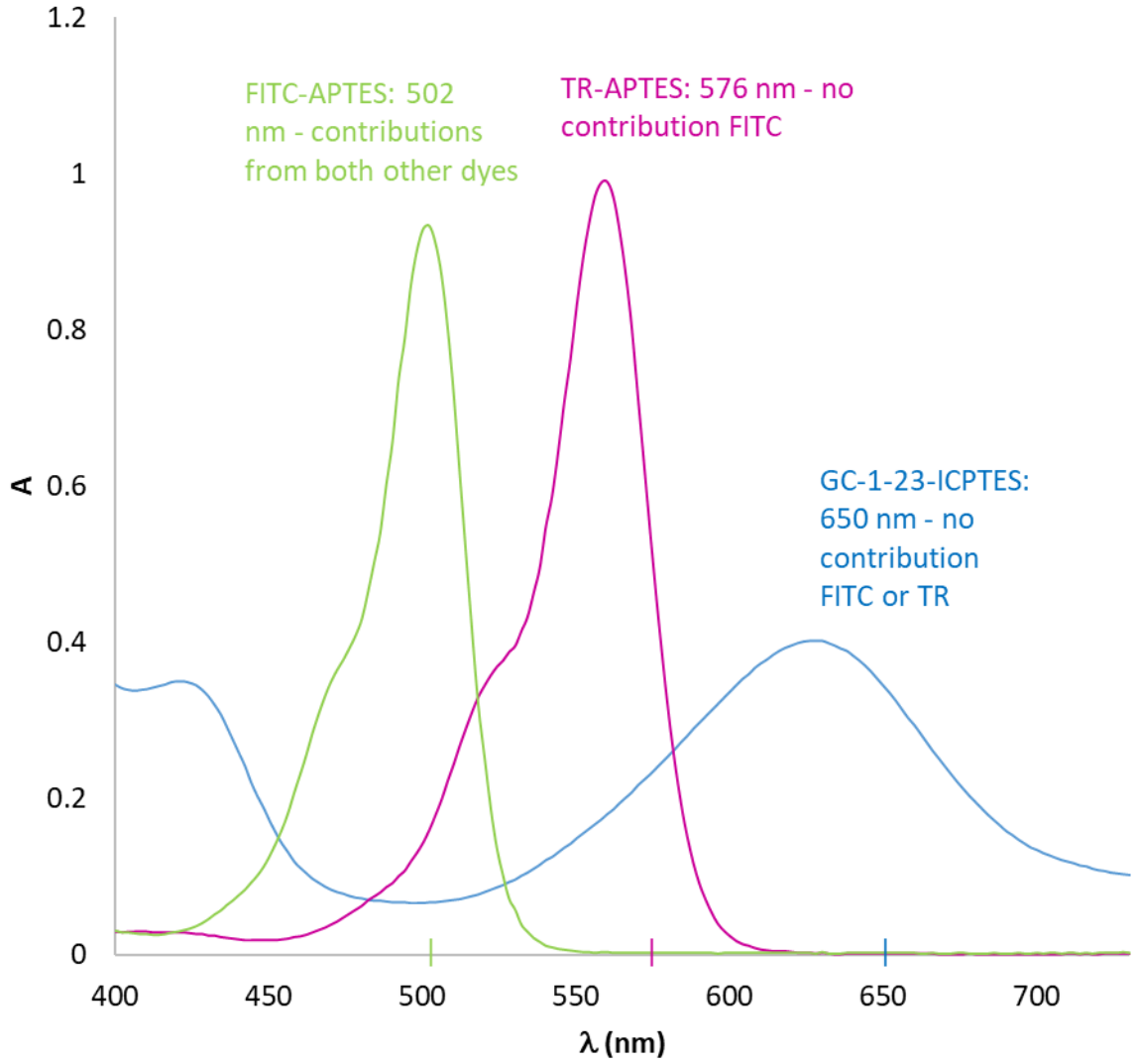

Figure 4.3: Representative absorption spectra of dye-silane conjugates in NP synthesis solution

Once the molar absorptivities of the dye-silane conjugates were determined in the NP synthesis solutions at the relevant wavelengths, a series of NP syntheses were set up using the usual method. Particular attention was paid to ensuring exact volumes of each reagent were delivered to each synthesis so final reaction volumes could be known with certainty. Most of these syntheses were based on the 1:1:2 dye ratio, although a synthesis of 1:1:1 (FITC:TR:GC-1-

23) NPs was also performed in order to assess whether the dye incorporation steps appeared to scale linearly with concentration. The following dye doping ratios were examined: 1:0:0, 1:1:0, 0:0:2, 1:0:2, 1:1:1, 1:1:2. Additional "blank" NP reactions were also carried out concurrently and in tandem with each "actual" NP synthesis; these syntheses were identical to the actual NP syntheses in every way except no TEOS was added. These "blank" NP reactions were carried out using the same dye doping ratios listed previously, and the absorption values from these syntheses were used to calculate the initial absorption values (A_I) used to determine the change in absorption. These were used as a surrogate for the "whole" NP solution in the determination of this value due to both the strong scattering that appears in NP absorption spectra (requiring deconvolution) as well as the possibility of changes in dye molar absorptivity upon incorporation into NPs (which could skew the calculated results). In order to determine the final absorption values, "whole" NP reactions were centrifuged as usual (30 min, 10,397 g) and supernatant aliquots were collected from the very tops of the centrifuge tubes prior to further NP cleaning steps. These collected supernatants were then subjected to a second centrifugation step (30 min, 17,000 g), and supernatants from the second centrifugation were further separated into new, clean tubes; these "super-supernatants" were used in the determination of the final absorption values (A_F) in order to ensure no NPs remained in these solutions. The A_I and A_F values so determined were used to calculate ΔA, and the ΔA values and molar absorptivities (ε) at each relevant wavelength (502 nm, 576 nm, 650 nm) were further used to estimate the concentrations of dyes incorporated into each of the NP samples.

The following discussion details the steps that may be taken to deconvolute individual dye concentrations in NPs doped with all 3 dyes (as this is the most complex case). At 650 nm, only GC-1-23-ICPTES (G) contributes significantly to the total absorption, thus [GC-1-23-

ICPTES] (C_G) may be calculated using Equation 4.8 after substituting in the change in absorption ($\Delta A_{tot} = \Delta A_G$) at this wavelength and the predetermined molar absorptivity of this dye (ε_G) at 650 nm. At 576 nm, both TR-APTES (T) and G contribute to the total absorption ($\Delta A_{tot} = \Delta A_T + \Delta A_G$ at 576 nm); the change in absorption at this wavelength can therefore be used to determine [TR-APTES] (C_T) as per Equation 4.9 after substituting in C_G (as determined using Equation 4.8) and the predetermined molar absorptivities of each dye at 576 nm (ε_G and ε_T). At 502 nm, all three of the dye-silane conjugates FITC-APTES (F), T, and G contribute to the total absorption ($\Delta A_{tot} = \Delta A_F + \Delta A_T + \Delta A_G$ at 502 nm); the change in absorption at this wavelength can be used to determine [FITC-APTES] (F) as per Equation 4.10 after substituting in C_G (as determined using Equation 4.8), C_T (as determined using Equation 4.9) and the predetermined molar absorptivities of each dye at 502 nm (ε_G, ε_T and ε_F).

$$C_G = \frac{\Delta A_{tot}}{\varepsilon_G b} \text{ (at 650 nm)} \qquad 4.8$$

$$C_T = \frac{\Delta A_{tot} - \varepsilon_G b C_G}{\varepsilon_T b} \text{ (at 576 nm)} \qquad 4.9$$

$$C_F = \frac{\Delta A_{tot} - \varepsilon_G b C_G - \varepsilon_T b C_T}{\varepsilon_F b} \text{ (at 502 nm)} \qquad 4.10$$

After determining the dye concentration in the NPs, the number of dyes per particle (N) could be determined by dividing the concentration of dye (C_X, in M, where X = F, T, or G) by the known concentration of NPs (C_{NP}, in M) in the solutions analyzed, as per Equation 4.11.

$$N = \frac{C_X}{C_{NP}} \qquad 4.11$$

The concentration of NPs in the synthesis solution (C_{NP}) was calculated using the molecular weight of the NPs (MW_{NP}, in g/mol) as determined from the TEM radius per Equation 3.9, the yield of the NPs (m_{NP}, in g) as determined using the drying process described in Section 3.3.3.3, and the total volume of the synthesis solution (V, in L). The relationship used to determine C_{NP} is illustrated in Equation 4.12.

$$C_{NP} = \frac{m_{NP}}{MW_{NP} \times V} \qquad 4.12$$

4.2.3 Estimation of average distance between dye molecules

After the NP size and number of dye molecules per NP has been calculated, it becomes possible to estimate the average distance between dye molecules. Particle volume V was determined from the TEM radii (r) assuming spherical particles ($V = \frac{4}{3}\pi r^3$). For a spherical shell (nanoparticle) of volume V containing N particles (dye molecules in this case), the average distance R between two dye molecules is given by Equation 4.13 as derived by Chandrasekhar and developed by Ardell and Bansal,.[9, 10] In this equation, Γ is the gamma function. Assuming the dye molecules to be point sources (a reasonable assumption given the very large volume differential between individual dye molecules and silica NPs and the unknown orientation of the dye molecules), Equation 4.13 simplifies to Equation 4.14 (Chandrasekhar's original derivation).

$$R = \left(\frac{3V}{4\pi N}\right)^{1/3} \Gamma\left(\frac{4}{3}\right) \qquad 4.13$$

$$R \approx 0.893 \left(\frac{3V}{4\pi N}\right)^{1/3} \qquad 4.14$$

4.2.4 Determination of Förster distance using spectral overlap

Once the number of dyes per NP has been calculated, it becomes possible to estimate the molar absorptivity (ε, in M^{-1} cm^{-1}) of dyes encapsulated into NPs using Beer's law (Equation 2.6) by measuring the (scattering-corrected) absorption of solutions containing known NP concentrations and known dye concentrations per NP. As mentioned previously, NP concentrations are determined per Equation 4.12; in this case, the volume (V) is the known resuspension volume of cleaned NPs. Following the calculation of acceptor molar absorptivities (ε_A) the overlap integral $J(\lambda)$ was calculated as per Equation 4.2. This calculation was carried out using a|e - UV-Vis-IR Spectral Software (v.2.2) using the overlap integral calculation functionality and inputting ε_A values and normalized fluorescence spectra (area sum = 1) from respective donors. Following determination of the overlap integral, the Förster distance R_0 was calculated as per Equation 4.3. Donor dye quantum yields (ϕ_D) measured in NPs as described in Section 4.2.1 were input into this equation along with the published refractive index of silica NPs ($\eta = 1.475 \pm 0.005$)[7] and the typical approximation for the dipole angular orientation of each molecule ($\kappa^2 = 2/3$).[3, 4] While this approximation is most accurate for dye molecules possessing rotational freedom as discussed in Section 4.1.2, it may hold to some extent for a population of (presumably) randomly oriented dyes encapsulated with the NP matrix due to the orientational averaging that is expected to occur.[4, 11]

4.2.5 Determination of Förster distance using energy transfer efficiency

The Förster distance R_0 calculated from the overlap integral (as per Section 4.2.4) was verified using an alternate approach. This secondary approach is based on the relationship written in Equation 4.4, which can be rewritten as Equation 4.15 in order to solve for R_0. In this

equation, R is the donor-acceptor distance and E is the FRET efficiency. The procedures used to determine R and E have been previously described in Sections 4.2.3 and 4.2.1, respectively.

$$R_0 = R \left(\frac{E}{1 - E}\right)^{1/6} \quad 4.15$$

4.3 Results and discussion

4.3.1 Determination of energy transfer efficiency

Quantum yields of donors FITC-APTES and TR-APTES were determined in NPs doped with 2-3 different dye species. Quantum yields of single dye-doped NPs were previously reported in Table 3.6. In all determinations of quantum yield reported for dyes copolymerized with NPs, the absorption values of dyes in dye-doped NPs were determined for quantum yield calculations by deconvolution (subtraction of normalized dye-free "blank" NP absorption spectra from the total dye-doped NP absorption). An example of spectral deconvolution is shown in Figure 4.4 for FITC-doped 1:0:0 NPs.

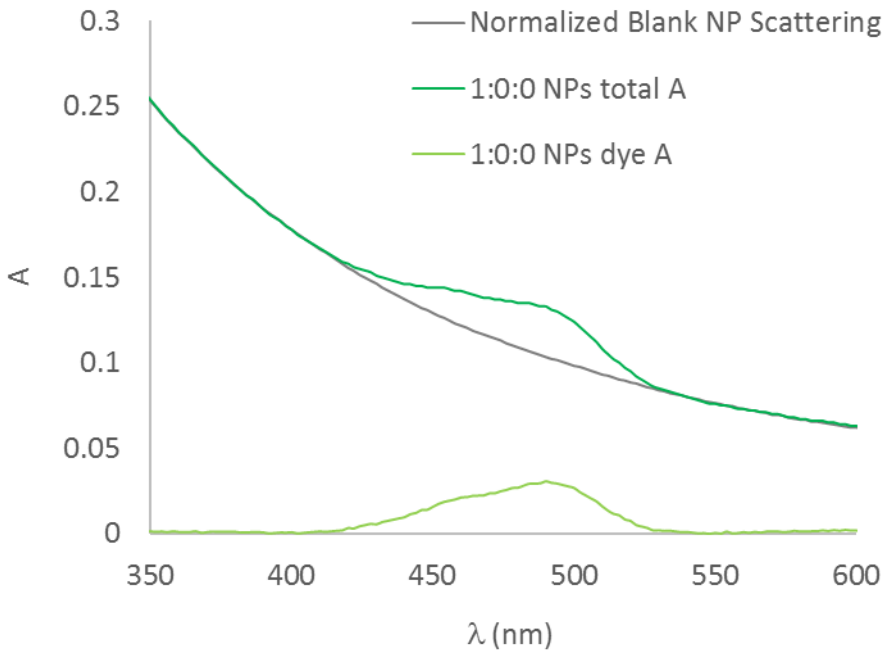

Figure 4.4: Spectral deconvolution of FITC dye absorption from nanoparticle scattering in 1:0:0 nanoparticles

Absorption normalization of the "blank" NPs is possible due to the linear relationship between blank NP concentration and light scattering at a given wavelength. A chart of "absorption" (scattering) at different wavelengths (A_λ) as a function of blank NP stock volume is provided in Figure 4.5. Wavelengths at which there is little absorption by the studied dye conjugates were chosen for this comparison. Note that the "volume" values of blank NP stock solutions provided on the x axis are proportional to the concentration of blank NPs since these volumes were made up to a constant total volume in EtOH. This linearity with respect to concentration supports the absorption deconvolution rationale. By adjusting ("normalizing") the absorption of a blank NP sample to equal that of the dye-doped NP absorption at a wavelength at which the dye does not absorb, the background scattering of the dye-doped NPs can be calculated at any wavelength and subtracted from the total absorption value.

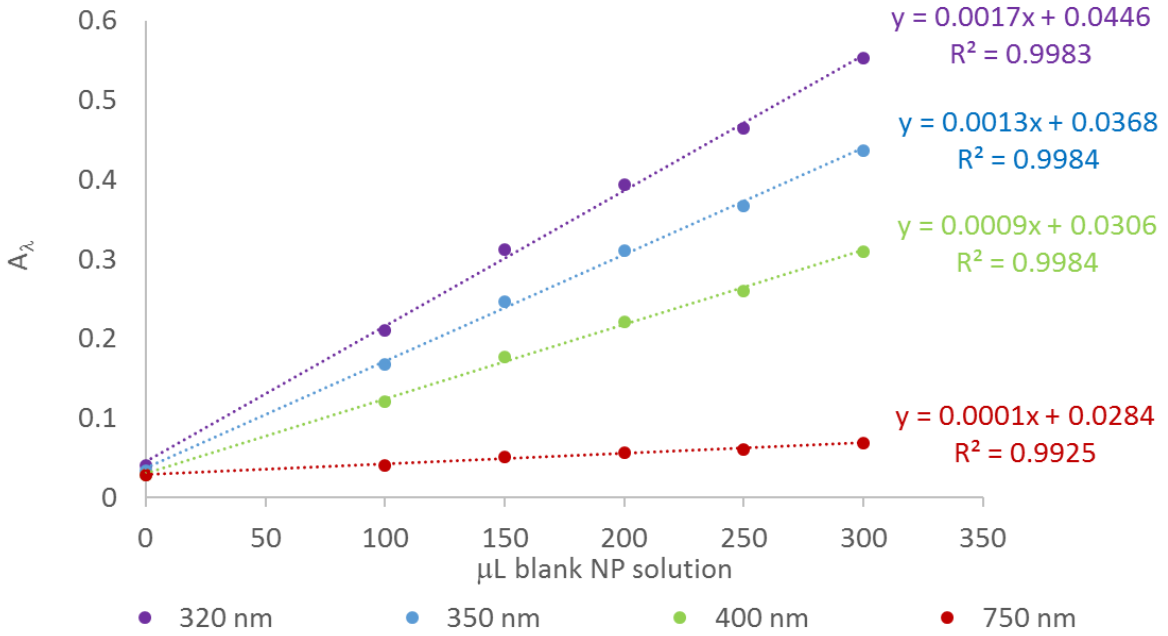

Figure 4.5: Linear relationship between NP scattering and volume of NP solution added (in this case volume is proportional to NP concentration)

Due to the necessity of subtracting the NP scattering from the absorption spectra, somewhat more concentrated NP solutions ($0.2 < A^{total}_{320\ nm} < 0.8$) were necessary in order to ensure adequate signal to noise for the "dye only" portion of the absorption. Solutions used for fluorescence measurements were prepared by diluting those used for absorption measurements by known ratios such that the total A (dye + NP) was <0.1 at the excitation wavelength (in order to minimize the inner filter effect). The acquired fluorescence spectra for multidye doped NPs also required some deconvolution due to the non-negligible spectral overlap as implicated in Figures 3.12, 3.14, and 3.15.

Quantum yields (determined in triplicate) for donor dyes (FITC and TR) in single (ϕ_D) and multidye NPs (ϕ_{DA}) are provided in Table 4.1 as averages ± standard deviations. The FRET efficiency (E) values calculated from these data are also provided in the table.

Table 4.1: Quantum yields (ϕ, n = 3) of donor dyes in single and multidye NPs and corresponding FRET efficiencies (E) for these dye combinations

Sample	Donor (D)	λ_{EXC} (nm)	$\phi_{D(A)}$	%Error $\phi_{D(A)}$	Acceptor(s) (A)	E	% Error E
1:0:0 NPs	FITC	450	$0.49_{23} \pm 0.014$	2.3%	N/A	N/A	N/A
1:0:1 NPs	FITC	450	$0.198_{7} \pm 0.0073$	3.3%	GC-1-23	$0.59_{63} \pm 0.028$	4.7%
1:0:2 NPs	FITC	450	$0.075_{59} \pm 0.0014$	1.0%	GC-1-23	$0.84_{64} \pm 0.029$	3.4%
1:1:0 NPs	FITC	450	$0.095_{61} \pm 0.0043$	4.2%	TR	$0.80_{58} \pm 0.042$	5.2%
1:1:1 NPs	FITC	450	$0.074_{26} \pm 0.0030$	3.7%	TR & GC-1-23	$0.84_{92} \pm 0.042$	5.1%
1:1:2 NPs	FITC	450	$0.036_{80} \pm 0.0015$	3.8%	TR & GC-1-23	$0.92_{52} \pm 0.046$	5.0%
0:1:0 NPs	TR	510	$1.04_{7} \pm 0.021$	2.0%	N/A	N/A	N/A
0:1:1 NPs	TR	510	$0.148_{2} \pm 0.0089$	5.8%	GC-1-23	$0.85_{84} \pm 0.055$	6.4%
0:1:2 NPs	TR	510	$0.069_{85} \pm 0.0020$	2.4%	GC-1-23	$0.93_{33} \pm 0.033$	3.5%
1:1:1 NPs	TR	510	$0.120_{0} \pm 0.0025$	1.4%	GC-1-23	$0.88_{54} \pm 0.026$	2.9%
1:1:2 NPs	TR	510	$0.062_{06} \pm 0.0025$	3.7%	GC-1-23	$0.94_{07} \pm 0.043$	4.6%

There are large observed decreases in FITC quantum yields in the presence of acceptor dyes TR and GC-1-23; the same is true of TR as a donor in the presence of GC-1-23 as acceptor. As expected, quantum yields decrease and FRET efficiencies increase more with increasing concentration of acceptor(s), due to both greater availability of acceptor dyes and greater proximity of the dye molecules promoting more efficient energy transfer.

The calculated FRET efficiency between FITC and GC-1-23 was substantial in the 1:0:1 and 1:0:2 NPs (60% and 85%, respectively) despite the fact that TR was not included as an intermediate donor and acceptor. The dye GC-1-23 exhibits a rather broad absorption band, and FITC exhibits a somewhat broad fluorescence band when encapsulated within the silica matrix; despite the large separation between donor absorption and acceptor fluorescence for these two species, there is still significant overlap between the donor fluorescence and acceptor absorption (as illustrated in Figure 3.12). When all three dyes are combined in ratios of 1:1:1 or 1:1:2, the apparent overall FRET efficiency increases further (85% and 93%, respectively) due to inclusion

of intermediate acceptor/donor TR and the reduced intermolecular distance between dyes. The FRET efficiency between FITC and TR in the 1:1:0 NPs (81%) was significantly higher than that observed between FITC and GC-1-23 when combined in the same ratio (1:0:1); this is as expected given the greater spectral overlap between these two species (Figure 3.12) and the higher molar absorptivity of TR.

Energy transfer efficiencies between TR and GC-1-23 were also determined to be quite substantial in the 0:1:1 and 0:1:2 NPs (86% and 93%, respectively) as a result of spectral overlap. Modest apparent increases beyond these values were observed in average FRET efficiencies between TR and GC-1-23 in the 1:1:1 and 1:1:2 NPs (89% and 94%, respectively), although these increases were not statistically significant. Nonetheless, an increase in the E value would be expected in these materials as a consequence of the decreased intermolecular distances, and it would further be expected that such theoretical gains would be relatively modest as a result of the sigmoidal relationship between intermolecular distance and energy transfer efficiency (Figure 4.2).

4.3.2 Determination of number of dye molecules per NP

As mentioned in the experimental section, some of the fluorescent NPs contained up to 3 dyes with partially overlapping absorption spectra; accordingly, it was necessary to identify wavelengths at which absorption (and therefore the concentration) of each dye could be deconvoluted. In the case of these 3 dyes, the identified wavelengths were: 650 nm, 576 nm, and 502 nm. Molar absorptivities (ε) determined in triplicate for each dye at each wavelength of interest after 20 h incubation in the NP synthesis solution are provided in Table 4.2; values are given as averages ± standard deviations with included percent relative standard deviations (%RSD).

Table 4.2: Summary of molar absorptivity values calculated for dye-silane conjugates in nanoparticle synthesis solution at wavelengths of interest (n = 3)

Dye	λ (nm)	ε (M^{-1} cm^{-1})	%RSD
GC-1-23-ICPTES	650	$(1.375_{1} \pm 0.0025)$E+04	0.18%
	576	$(9.3_{294} \pm 0.18)$E+03	1.9%
	502	$(2.5_{629} \pm 0.10)$E+03	3.9%
TR-APTES	576	$(4.2_{597} \pm 0.17)$E+04	4.0%
	502	$(1.55_{50} \pm 0.027)$E+04	1.7%
FITC-APTES	502	$(8.9_{366} \pm 0.36)$E+04	4.0%

The calculated molar absorptivities were reproducible (RSD = 0.2% – 4%). Notably, the values were found to be somewhat lower for all dye-silane conjugates in the NP synthesis solution than those published or determined for the unmodified dyes in other solvents for which values are published or have been previously determined. This is unsurprising given the derivatization of the dyes with trialkoxysilane, the high pH of the solution and the water content of the solvent, all of which are expected to modulate the spectroscopic properties of the dyes. The discrepancy is significantly lower for FITC-APTES conjugate, which may be attributable to the fact that published absorptivity values for this dye are typically given in basic solutions (either aqueous or alcoholic).

Experimentally determined molar absorptivities for dye-silane conjugates in NP synthesis solutions were used to calculate the concentrations of dyes incorporated into the NPs by the difference in absorption (prior to and following NP removal from the reaction solution) at the wavelengths of interest. The calculated numbers of dyes per particle (N) for selected reactions are provided in Table 4.3. Also provided in this table are average N values (± standard deviation) across the "X:X:2" series of NPs. Note that while the 1:1:1 NPs were not subject to TEM

analysis, the relatively low variation in average NP radius (Section 3.3.4.3) allowed an estimation of the molecular weight of these particles based on the averages calculated for other NPs.

Table 4.3: Calculated number of dyes per nanoparticle (N) for 1:1:1 nanoparticles and selected nanoparticles in the 1:1:2 series, and average number of dye molecules/NP (± standard deviation) across different sample syntheses

Sample	Calc'd N for dye-silane		
	GC-1-23-ICPTES	**TR-APTES**	**FITC-APTES**
1:1:1 NPs	694	696	591
1:0:0 NPs	0	0	646
1:0:2 NPs	1204	0	677
1:1:2 NPs	1229	555	510
1:1:0 NPs	0	686	674
0:0:2 NPs	1106	0	0
Average X:X:2 NPs	$(1.18_0 \pm .053)$E+03	$(6.4_{56} \pm 0.64)$E+02	$(6.1_{96} \pm 0.63)$E+02
%RSD	4.5%	9.9%	10%

There was good inter-reaction precision (RSD = 4.5% – 10%) despite the fact that different ratios of different dye conjugate species were incorporated into each synthesis. The N values appear to correlate well with the respective amounts of dye-silane conjugates added to the reaction regardless of dye-silane type, and furthermore, N values appear to scale reasonably well with the number of equivalents of dye added; the apparent quantity of GC-1-23 molecules per particle measured in all of the "X:X:2" particles is approximately twice that observed in the "1:1:1" NPs, and for a particle with an "X:X:X" molar ratio, when X = 1 equivalent, the number of dye molecules incorporated per particle is around 600. These observations indicate good reproducibility of dye incorporation for these dye-copolymerized particles regardless of fluorophore contents. Furthermore, the enhancement in the experimentally determined limits of detection (LOD) (Table 3.7) for dye-silane conjugates in NPs relative to those in solution

correlate reasonably well with these values when corrections are made for quantum yield (ϕ). More specifically, assuming a linear relationship between dye concentration and fluorescence intensity, the limit of detection for dye-doped NPs (Est. LOD_{NP}) may be roughly estimated as per Equation 4.16. In this equation, the indices "dye" and "NP" refer to dye-silane conjugates in solution and dye-copolymerized NPs, respectively.

$$\text{Est. } LOD_{NP} = \frac{LOD_{dye}}{N} \times \frac{\phi_{dye}}{\phi_{NP}} \qquad 4.16$$

A comparison of the estimated and experimentally observed limits of detection (Obs. LOD_{NP}) for dye-doped NPs is provided in Table 4.4. In this table, there is reasonably good agreement between the two values for all dye-silane conjugates; while the 13-16% differences are not negligible, the agreement between the values was nonetheless good, particularly given the number of calculations, extrapolations, and deconvolutions involved in determining the relevant values of LOD, ϕ, and N.

Table 4.4: Comparison of estimated and observed limits of detection for dye-copolymerized NPs

Dye-silane	FITC-APTES	TR-APTES	GC-1-23-ICPTES
N	620	646	1180
ϕ_{NP}	0.492	1.036	0.398
ϕ_{dye}	0.044	0.599	0.210
LOD_{dye} (M)	8.20E-10	6.33E-11	6.04E-09
Est. LOD_{NP} (M)	1.19E-13	5.67E-14	2.70E-12
Obs. LOD_{NP} (M)	1.38E-13	6.47E-14	3.16E-12
% Difference	15%	13%	16%

4.3.3 Estimation of average distance between dye molecules

The average distance between dye molecules (R) was estimated using the nanoparticle volume (V) determined from TEM radii and the calculated number of dyes per nanoparticle (N), as per Equation 4.14. The results of this calculation are provided in Table 4.5. The average distance between dye molecules of the same species (R_X) were also computed based on the number of dye molecules of the same species per nanoparticle (N_G) and the nanoparticle volume (V); these results are provided in Table 4.6. In this table, the general index "X" refers to the dye-silane conjugate of interest; X = G refers to GC-1-23-ICPTES, X = T refers to TR-APTES, and X = F refers to FITC-APTES.

Table 4.5: Determination of average distance between all dye molecules in NPs (R)

Sample	N	V ($Å^3$)	R (Å)
1:0:0 NPs	6.4_6 E+02	2.3_3 E+08	$39._4$
0:0:2 NPs	1.1_1 E+03	1.8_4 E+08	$30._5$
1:1:0 NPs	1.3_6 E+03	2.3_9 E+08	$31._0$
1:0:1 NPs*	1.2_1 E+03	2.2_3 E+08	$31._5$
1:0:2 NPs	1.8_8 E+03	2.4_9 E+08	$28._2$
0:1:1 NPs*	1.3_4 E+03	2.2_3 E+08	$30._5$
0:1:2 NPs*	1.8_3 E+03	2.2_3 E+08	$27._5$
1:1:1 NPs	1.9_8 E+03	2.3_2 E+08	$27._1$
1:1:2 NPs	2.2_9 E+03	1.9_9 E+08	$24._5$

*Value estimated based on average N or average V

Table 4.6: Determination of average distance between dyes of same species in NPs (R_X)

Sample	V (Å^3)	GC-1-23-ICPTES		TR-APTES		FITC-APTES	
		N_G	R_G (Å)	N_T	R_T (Å)	N_F	R_F (Å)
1:0:0 NPs	2.3_3 E+08	0	N/A	0	N/A	6.4_6 E+02	$39._4$
0:0:2 NPs	1.8_4 E+08	1.1_1 E+03	$30._4$	0	N/A	0	N/A
1:1:0 NPs	2.3_9 E+08	0	N/A	6.8_6 E+02	$39._0$	6.7_4 E+02	$39._2$
1:0:1 NPs*	2.2_3 E+08	5.9_0 E+02	$40._0$	0	N/A	6.2_0 E+02	$39._4$
1:0:2 NPs	2.4_9 E+08	1.2_0 E+03	$32._8$	0	N/A	6.7_7 E+02	$39._7$
0:1:1 NPs*	2.2_3 E+08	5.9_0 E+02	$40._0$	6.4_6 E+02	$38._8$	0	N/A
0:1:2 NPs*	2.2_3 E+08	1.1_8 E+03	$31._8$	6.4_6 E+02	$38._8$	0	N/A
1:1:1 NPs	2.3_2 E+08	6.9_4 E+02	$38._4$	6.9_6 E+02	$38._4$	5.9_1 E+02	$40._6$
1:1:2 NPs	1.9_9 E+08	1.2_3 E+03	$30._2$	5.5_5 E+02	$39._4$	5.1_0 E+02	$40._5$

*Value estimated based on average N or average V

In these tables, R values have been calculated for all NP samples for which N and V were experimentally determined as well as for selected NP samples for which N and/or V were estimated based on averages; samples falling into the latter category have been marked with an asterisk. The samples for which values were estimated were chosen based on their utility in the calculation of Förster radii (R_0) in subsequent Section 4.3.5. Estimation of the N and V values for these samples was possible due to the good reproducibility of the experimentally determined NP radii (from TEM, Table 3.5) and the number of dyes per NP (N, Table 4.3), although for these samples the uncertainty is nonetheless significantly higher due to the approximation. Apparent intermolecular distances between dye molecules in NPs (R) ranged between 25 and 41 Å; these values are well within the range typically required for FRET to occur (10-100 Å) and therefore corroborate the evidence for FRET discussed previously.[5] To the best of our knowledge, this is the first time such an approach has been used to estimate intermolecular distances in NPs.

4.3.4 Determination of Förster distances using spectral overlap

Förster distances were determined based on the spectral overlap J(λ) using Equation 4.3; calculated values are provided in Table 4.7. The first subsection of the table contains hetero-Förster distances for the intended donor-acceptor pairs (FITC:TR, FITC:GC-1-23, and TR:GC-1-23); the second subsection contains homo-Förster distances for individual dye species.

Table 4.7: R_0 values calculated from overlap integrals for hetero-FRET and homo-FRET in multidye-copolymerized NPs

RET Type	Donor	Donor ϕ	Acceptor	J(λ) ($nm^4\ M^{-1}\ cm^{-1}$)	R_0 (Å)
Hetero-FRET	FITC	0.49_2	TR	1.7E+15	47
	FITC	0.49_2	GC-1-23	4.6 E+14	38
	TR	1.04_7	GC-1-23	1.3E+15	51
Homo-FRET	FITC	0.49_2	FITC	2.6E+14	34
	TR	1.04_7	TR	2.1E+14	37
	GC-1-23	0.38_6	GC-1-23	5.6E+14	37

The calculated R_0 values fall at the shorter end of the expected range for typical FRET pairs (35-75 Å).[12] As expected, R_0 increases with extent of spectral overlap (Figure 3.12); dyes with greater overlap are capable of transferring energy with greater efficiency over longer distances. Furthermore, the calculated R_0 for the FITC/TR pair (47 Å encapsulated in NPs) shows some agreement with that published for fluorescein and rhodamine 6G (55 Å in a transmembrane protein helix; 51-66 Å in aqueous solutions depending on pH).[13, 14] The difference between these values may be attributable to spectroscopic differences due to disparities in environmental refractive index,[13] rotational restriction of the randomly oriented dyes encapsulated in NPs (resulting in deviations of κ^2),[6] and/or innate spectroscopic differences between the dye species; TR and rhodamine 6G are structurally and spectroscopically similar, but not identical.

The calculated Förster radii for self-quenching (homo-FRET) were smaller than for those calculated for hetero acceptors, indicating preferential resonance energy transfer from each donor to the acceptor dye species rather than to itself. The intermolecular dye distances calculated in Section 4.3.3 indicate that a mixture of homo-FRET and hetero-FRET is likely present in multidye-encapsulated NPs and that some homo-FRET occurs in single dye encapsulated NPs. The extent of homo-FRET can be estimated by a reevaluation of the data provided in Section 3.2.3.3. As mentioned in this section, the NP dye ratios were optimized for per-particle fluorescence intensity rather than per-dye fluorescence intensity. The data provided in Figure 3.10 may be recalculated in terms of per-dye fluorescence intensity relative to the mol% dye incorporated into NPs. Per-dye fluorescence intensities were calculated by taking the ratio of the fluorescence intensity and the mol% dye (vs. TEOS) at each data point; these values were then normalized to 100% to determine the percentage of the maximum per-dye fluorescence intensity (%I_F/Dye). The results of this calculation are provided in Table 4.8. The corresponding dye ratios (also provided in Table 3.3) have been included in this table for convenience of comparison. Based on this estimation, for the 1:1:2 FITC:TR:GC-1-23 dye ratio chosen for study throughout this text, there should be approximately 27% homo-FRET for FITC and 33% homo-FRET for GC-1-23. Interestingly, there is no evidence of quenching for TR in this dye ratio, and the 100% quantum yield observed for TR in the 0:1:0 NPs further corroborates a lack of self-quenching for this dye species when incorporated into NPs at the fluorescence-optimized concentration. This result is unexpected given the homo-FRET R_0 value calculated for TR using overlap integrals; while the discrepancy may once again be attributable to deviations in the orientation factor ($\kappa^2 \neq 2/3$), this observation nonetheless warrants further study.

Table 4.8: Determination of per-dye fluorescence intensities as a percentage of the maximum for individual dyes in multidye nanoparticles containing varying mole percentages (mol%) of dye relative to TEOS

Dye Ratio (FITC:TR:GC-1-23)	mol% Dye (vs. TEOS)	$\%I_F$/Dye FITC	TR	GC-1-23
0.5:0.5:0.5	0.012	100%	97%	88%
1:1:1	0.025	73%	100%	100%
2:2:2	0.05	26%	43%	67%
4:4:4	0.10	1.4%	9.0%	15%
8:8:8	0.20	0.26%	0.87%	4.7%
12:12:12	0.30	0.065%	0.20%	1.3%

4.3.5 Determination of Förster distance using energy transfer efficiency

Due to the uncertainty regarding the orientation factor (κ^2) in the calculation of Förster distances (R_0) from the overlap integral (Sections 4.1.2, 4.2.4, and 4.3.4), an alternate approach for determining R_0 was applied as a confirmation. Specifically, the relationship between R_0, energy transfer efficiency (E), and distance between dye molecules in NPs (R) illustrated in Equation 4.15 was applied in order to verify these values. Note that homo-Förster distances were not determined in this manner as E values could not be calculated for individual dye molecules using the specified approach (Section 4.2.1).

The results of this calculation are presented in Table 4.9 for relevant NPs containing two separate dye species (donor-acceptor pairs). The results have also been presented graphically as a plot of R_0 vs R in Figure 4.6; in this figure, energy transfer efficiencies for donor-acceptor pairs in the specified configurations are provided for each point, and average Förster radii for the donor-acceptor pairs are denoted with horizontal dashed lines.

Table 4.9: R_0 values calculated from intermolecular distances and energy transfer efficiency in multidye-copolymerized NPs

Sample	Donor	Acceptor	R (Å)	E	R_0 (Å)
1:0:1 NPs	FITC	GC-1-23	$31._5$	0.59_{63}	34
1:0:2 NPs	FITC	GC-1-23	$28._2$	0.84_{64}	37
1:1:0 NPs	FITC	TR	$31._0$	0.80_{58}	39
0:1:1 NPs	TR	GC-1-23	$30._5$	0.85_{84}	41
0:1:2 NPs	TR	GC-1-23	$27._5$	0.93_{33}	43

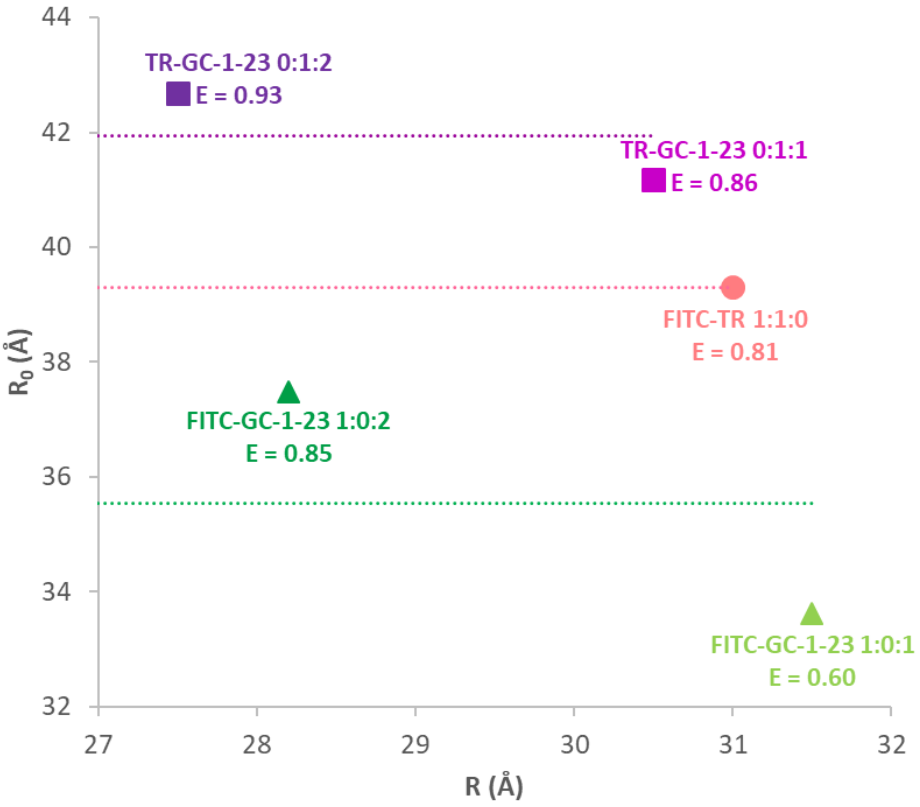

Figure 4.6: Graphical representation of calculated Förster radii (R_0) versus intermolecular distances between dye molecules (R) for donor-acceptor pairs, with included average R_0 values (horizontal lines) and energy transfer efficiencies (E)

The R_0 values calculated in this manner once again fall at the shorter end of the typical range for FRET pairs.[12] Because the value of R_0 is a constant for a given donor-acceptor pair in a given environment, calculated values should not change for NP samples containing the same donor-

acceptor pair in varying concentrations; upon comparison of NPs containing either 1 or 2 molar equivalents of GC-1-23 (i.e. 1:0:1 NPs and 1:0:2 NPs or 0:1:1 NPs and 0:1:2 NPs), very good agreement of the calculated R_0 values was in fact observed. The calculated R_0 values increase with increasing spectral overlap between donor and acceptor (indicative of the greater energy transfer efficiency); this trend was also observed for the R_0 values calculated using spectral overlap (Section 4.3.4).

A comparison of average R_0 values calculated using the overlap integral $J(\lambda)$ (Section 4.3.4) with those calculated using the present "energy transfer efficiency and donor-acceptor distance method" (E and R) is provided in Table 4.10, along with percent differences between values. Reasonable agreement was observed between these values, with calculated percent differences ranging from 6.8% to 19%.

Table 4.10: Comparison of R_0 values calculated using different approaches

Donor	Acceptor	R_0 (Å) from $J(\lambda)$	R_0 (Å) from E and R*	% Difference
FITC	TR	47	39	19%
FITC	GC-1-23	38	$35._5$	6.8%
TR	GC-1-23	51	42	19%

*R_0 values for donor-acceptor pair FITC and GC-1-23 are average of R_0 results calculated for 1:0:1 NPs and 1:0:2 NPs; R_0 values for donor-acceptor pair TR and GC-1-23 are average of R_0 results calculated for 0:1:1 NPs and 0:1:2 NPs.

The extent of agreement of R_0 values calculated for the donor-acceptor pair FITC and GC-1-23 using the two different approaches is somewhat better than those calculated for donor-acceptor pairs FITC and TR or TR and GC-1-23; the reason for this is not entirely clear. Part of the deviation between the two sets of R_0 values almost certainly results from errors arising from the series of measurements, deconvolutions, approximations, and calculations required to arrive at

each value. Another contributing factor is the presence of homo-FRET between donor dye molecules, although this is mitigated somewhat by the similar same species distances in both single and multidye NPs; similar same species distances should result in similar homo-quenching energy losses in both "donor only" and donor-acceptor systems. An additional likely contribution to the observed deviation may result from the approximation of the orientation factor ($\kappa^2 = 2/3$) used in the calculation of R_0 from $J(\lambda)$. As mentioned previously, this approximation is most applicable in cases where the dye molecules are capable of free rotation (and the rotational diffusion is faster than the fluorescence lifetime of the dye). In the case of these samples, the dyes are covalently bound to and incorporated within the solid NP matrix; rotation of the donor relative to the acceptor is thereby greatly hindered. This apparent limitation of R_0 determination using spectral overlap underscores the importance of the secondary means of R_0 calculation using energy transfer efficiency and donor-acceptor distance described herein.

4.4 Conclusions

Fluorescent silica NPs copolymerized with multiple dye species were characterized in terms of their resonance energy transfer parameters. For NPs containing FRET-paired species, the energy transfer efficiency (E) between dyes was found to be relatively high, ranging from 60% to 94% depending on dye content and concentration. The number of dye molecules per NP (N), as determined by change in absorption during NP synthesis, was found to scale relatively linearly with increases in added amounts of dye and to remain relatively constant regardless of dye-silane constituent added, with a calculated value of around 600 dye molecules for every ratio equivalent of dye added; in other words, for "X:X:X" NPs, when $X = 1$, $N \approx 600$. The limits of

detection determined in Section 3.3.4.7 were found to corroborate the calculated values of N relatively well, with calculated percent differences ranging from 13-16%.

Intermolecular distances between dye molecules (R) were calculated using a novel approach based on the "points in a sphere" distance relationship derived by Chandrasekar and developed by Bansal and Ardell. The previously determined numbers of dye molecules per particle and NP volumes (from TEM radii) were substituted into this equation in order to determine R. Calculated intermolecular distances fell within the typical range for FRET interactions, ranging from 25 to 39 Å.

The characteristic Förster distances (R_0) were then determined using two different methodologies for each of the donor-acceptor pairs used in the multidye copolymerized NPs; the common approach to R_0 calculation (based on overlap integral) was applied first, then the R_0 values obtained using this calculation were verified via the relationship between R_0, energy transfer efficiency, and donor-acceptor distance. Calculated R_0 values using either approach for donor/acceptor pairs FITC/TR, FITC/GC-1-23, and TR/GC-1-23 ranged from 36 – 51 Å. In both methodologies, R_0 increased as expected with increases in spectral overlap, signifying improved efficiency of energy transfer. The two approaches yielded percent differences ranging from 6.8% – 19% for given donor-acceptor pairs; the observed difference in values is thought to be largely attributable to inaccurate estimations of the orientation factor (κ^2) when R_0 is calculated based on the overlap integral, although homo-FRET may also play a role.

Multidye copolymerized NPs have been a subject of increased scientific interest recently due to their promising applications as barcoding tags for *in vivo* and *in vitro* multiplexing assays. The information discussed in this chapter provides a useful framework for the characterization of

FRET parameters of these types of nanomaterials, which should assist in future efforts to both better understand and optimize the spectroscopic properties of these fluorescent tags.

4.5 References

1. Hussain, S. A., An Introduction to Fluorescence Resonance Energy Transfer (FRET). *Sci. J. Phys.* **2012,** *2012*, sjp268.

2. Strieth-Kalthoff, F.; James, M. J.; Teders, M.; Pitzer, L.; Glorius, F., Energy transfer catalysis mediated by visible light: principles, applications, directions. *Chem. Soc. Rev.* **2018,** *47* (19), 7190-7202.

3. Lakowicz, J. R., *Principles of Fluorescence Spectroscopy*. 3rd ed.; Springer Science+Business Media, LLC: New York, 2006.

4. Valeur, B., *Molecular Fluorescence: Principles and Applications*. Wiley-VCH: Weinheim, 2001.

5. Gust, A.; Zander, A.; Gietl, A.; Holzmeister, P.; Schulz, S.; Lalkens, B.; Tinnefeld, P.; Grohmann, D., A Starting Point for Fluorescence-Based Single-Molecule Measurements in Biomolecular Research. *Molecules* **2014,** *19* (10), 15824.

6. Müller, S.; Galliardt, H.; Schneider, J.; Barisas, B.; Seidel, T., Quantification of Förster resonance energy transfer by monitoring sensitized emission in living plant cells. *Front. Plant Sci.* **2013,** *4* (413).

7. Khlebtsov, B. N.; Khanadeev, V. A.; Khlebtsov, N. G., Determination of the Size, Concentration, and Refractive Index of Silica Nanoparticles from Turbidity Spectra. *Langmuir* **2008,** *24* (16), 8964-8970.

8. Lakowicz, J. R., *Principles of Fluorescence Spectroscopy*. 2nd ed.; Kluwer Academic: New York, 1999.

9. Chandrasekhar, S., Stochastic Problems in Physics and Astronomy. *Rev. Mod. Phys.* **1943,** *15* (1), 1-89.

10. Bansal, P. P.; Ardell, A. J., Average nearest-neighbor distances between uniformly distributed finite particles. *Metallography* **1972,** *5* (2), 97-111.

11. Demchenko, A. P., Fluorescence Detection Techniques. In *Introduction to Fluorescence Sensing*, Springer International Publishing: New York City, 2015.

12. Götz, M.; Wortmann, P., *Manual: Single Molecule Förster-Resonance-Energy-Transfer*. Technische Universität München: Munich, 2013.

13. Saha, J.; Datta Roy, A.; Dey, D.; Chakraborty, S.; Bhattacharjee, D.; Paul, P. K.; Hussain, S. A., Investigation of Fluorescence Resonance Energy Transfer between Fluorescein and Rhodamine 6G. *Spectrochim. Acta A* **2015,** *149*, 143-149.

14. Merzlyakov, M.; Hristova, K., Chapter 6 Forster Resonance Energy Transfer Measurements of Transmembrane Helix Dimerization Energetics. In *Methods in Enzymology*, Academic Press: 2008; Vol. Volume 450, pp 107-127.

APPENDICES

Appendix A – NMR and HRMS spectra

Appendix A.1 - ^{1}H NMR

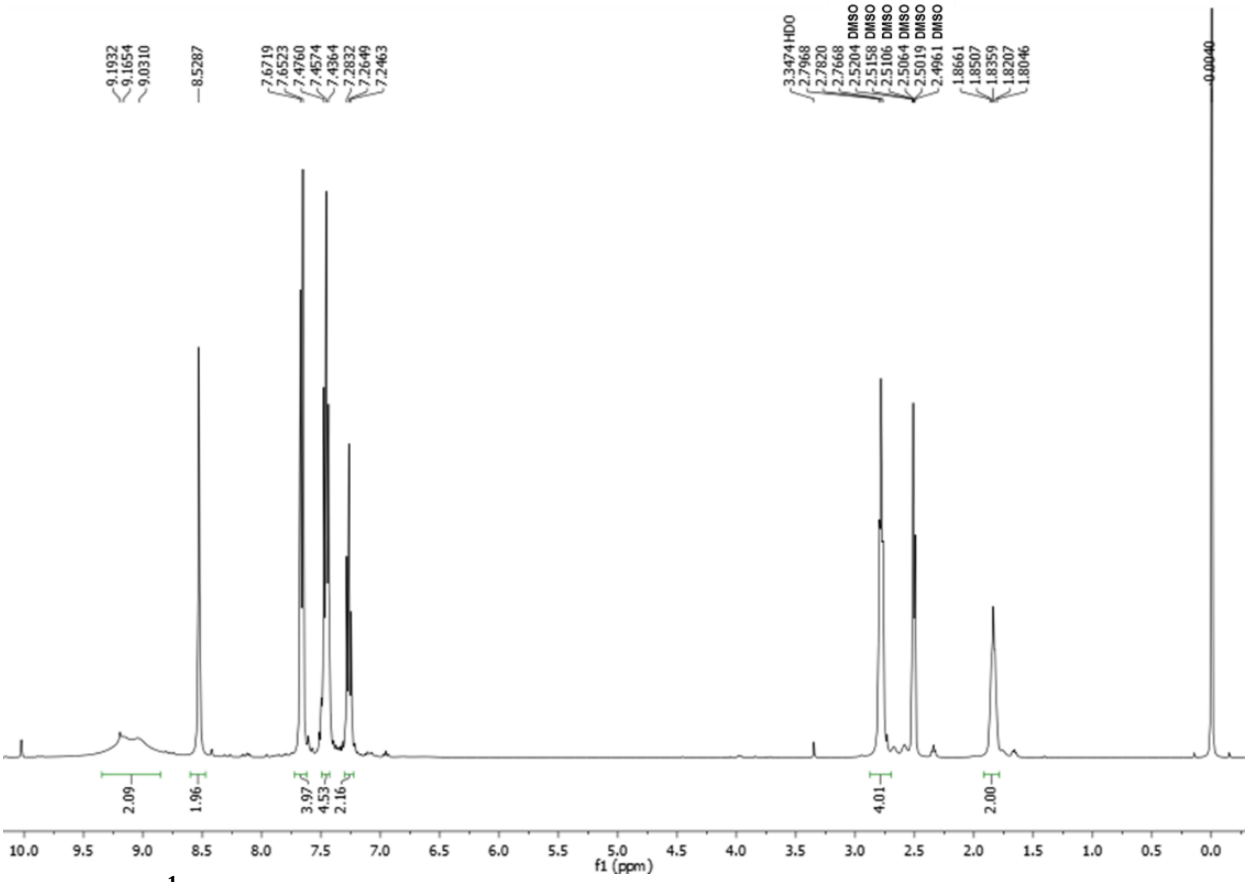

Figure A.1: ^{1}H NMR spectrum of Vilsmeier-Haack-Arnold reagent

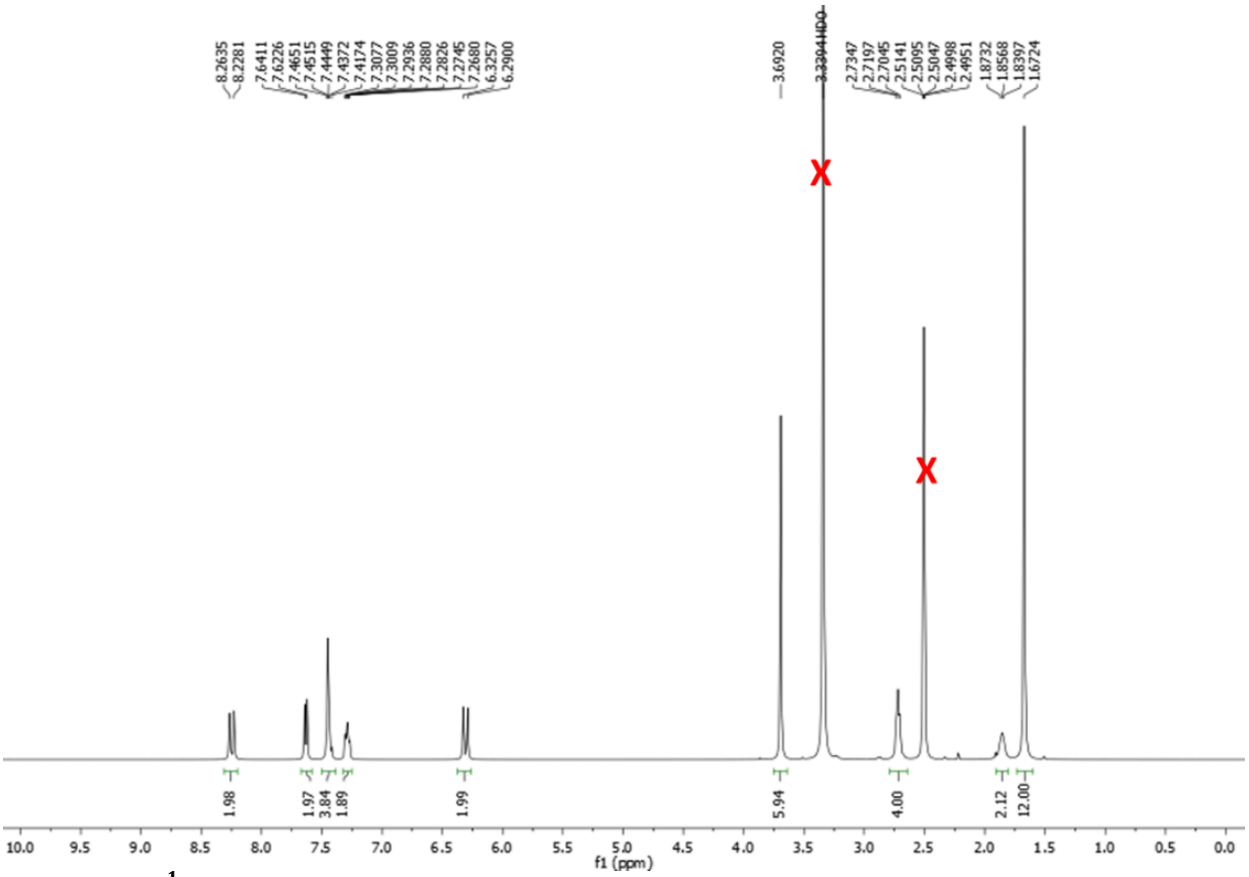

Figure A.2: ^{1}H NMR spectrum of IR-786

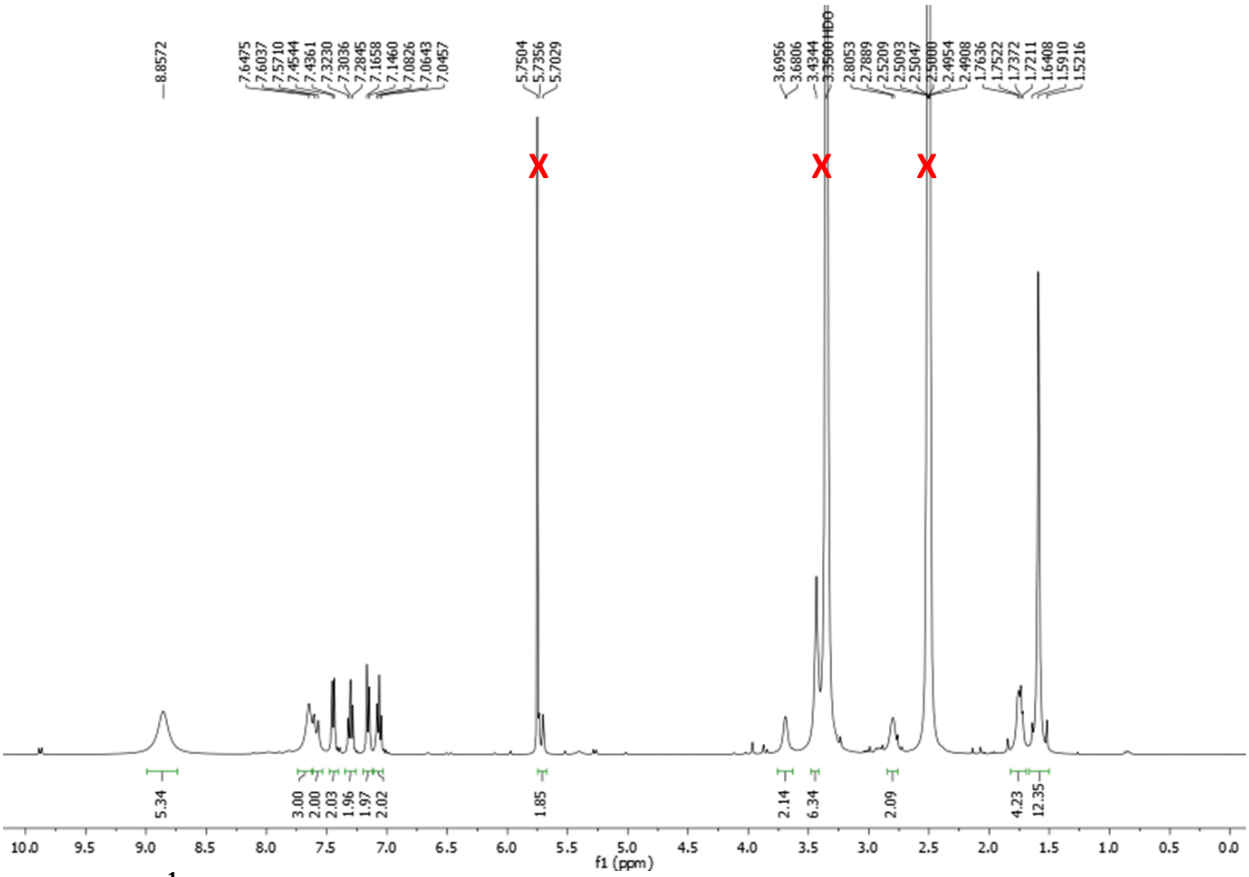

Figure A.3: ^{1}H NMR spectrum of GC-1-23

Appendix A.2 - ^{13}C NMR

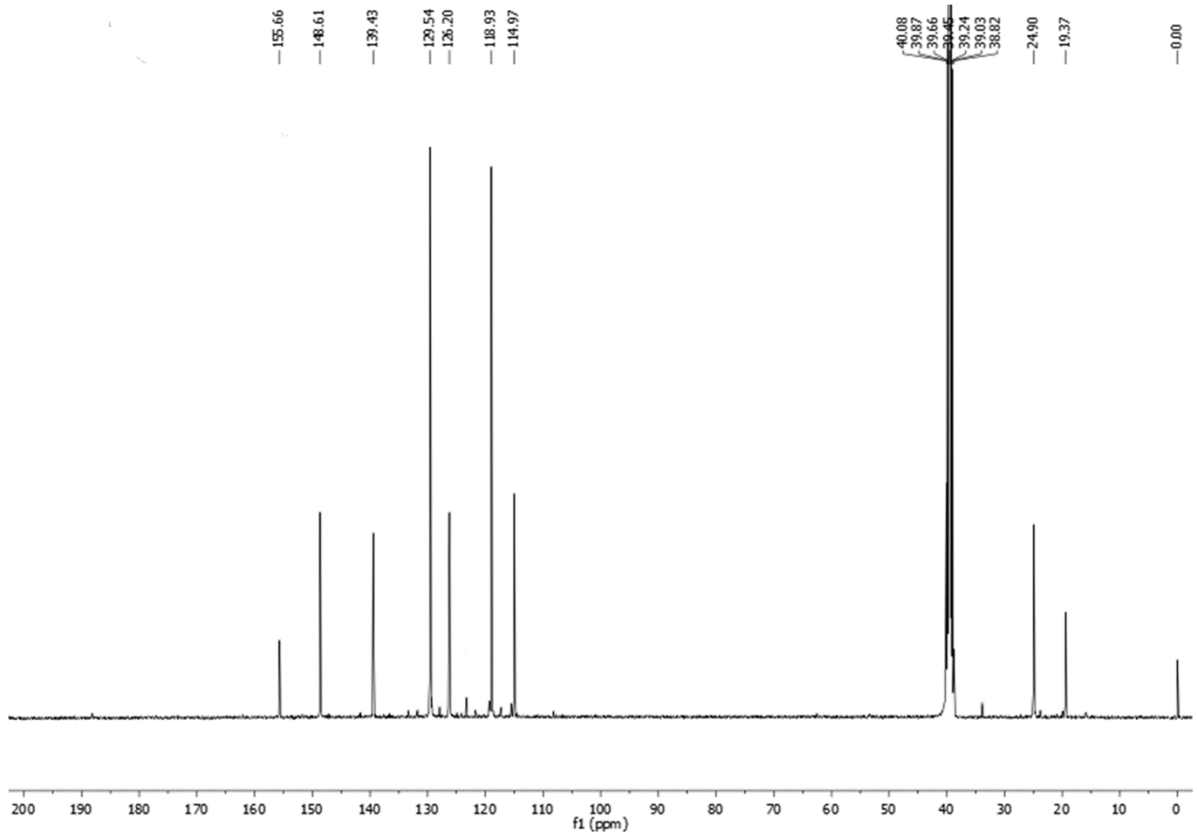

Figure A.4: ^{13}C NMR spectrum of Vilsmeier-Haack-Arnold reagent

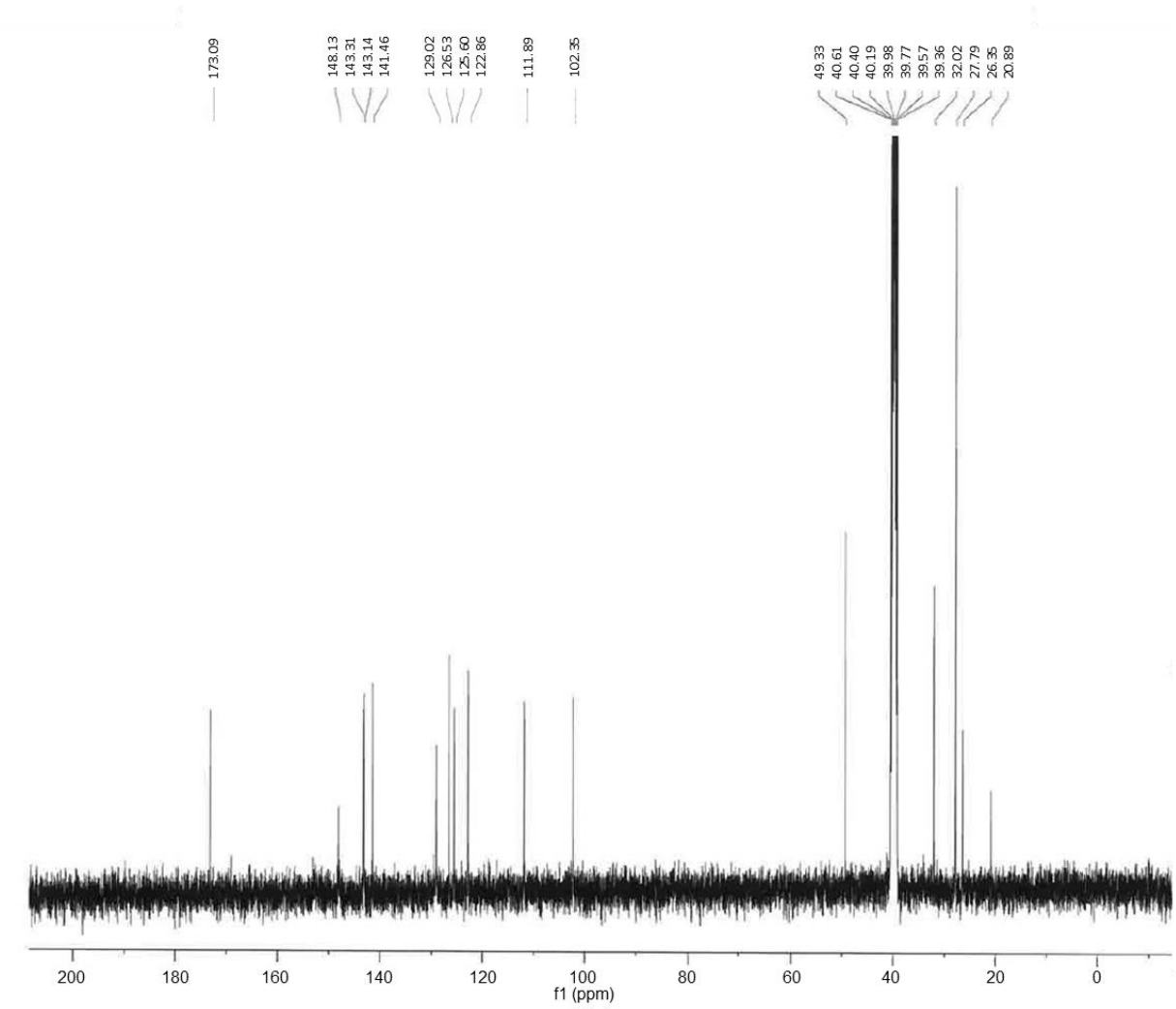

Figure A.5: ^{13}C NMR spectrum of IR-786

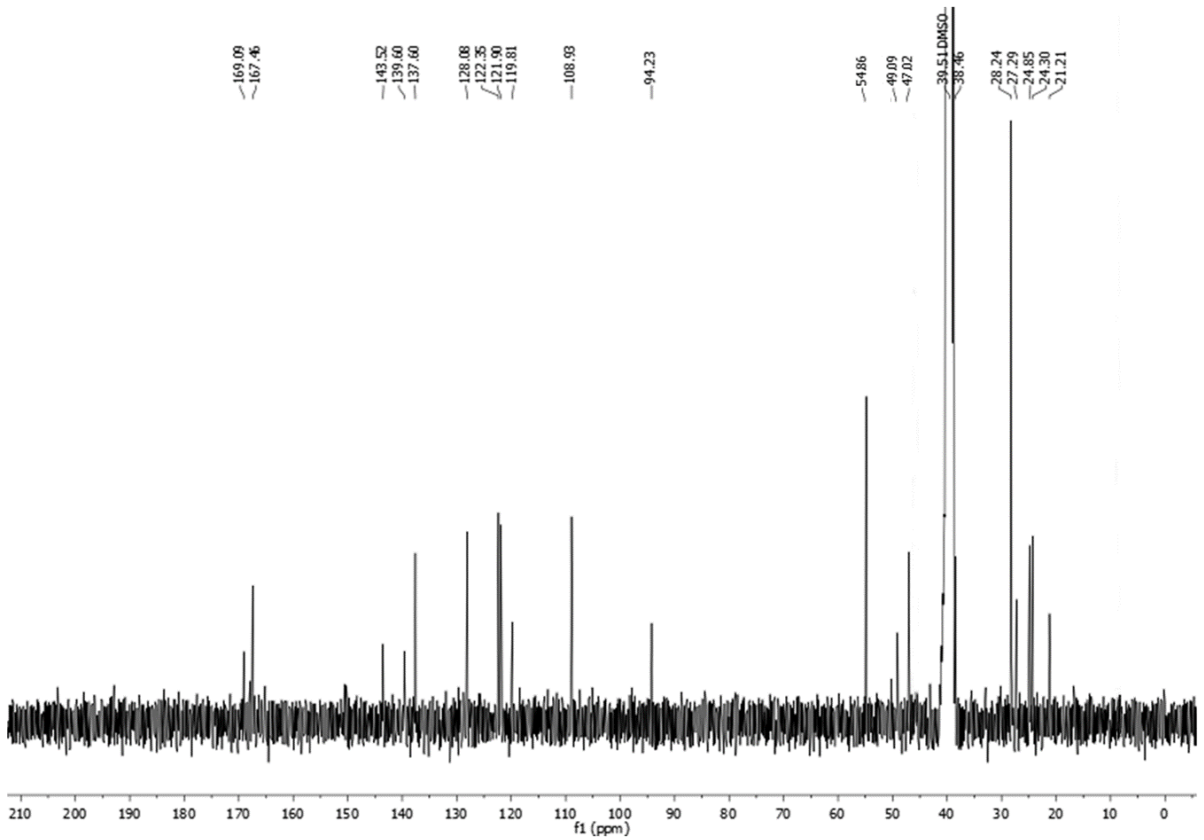

Figure A.6: ^{13}C NMR spectrum of GC-1-23

Appendix A.3 – HRMS

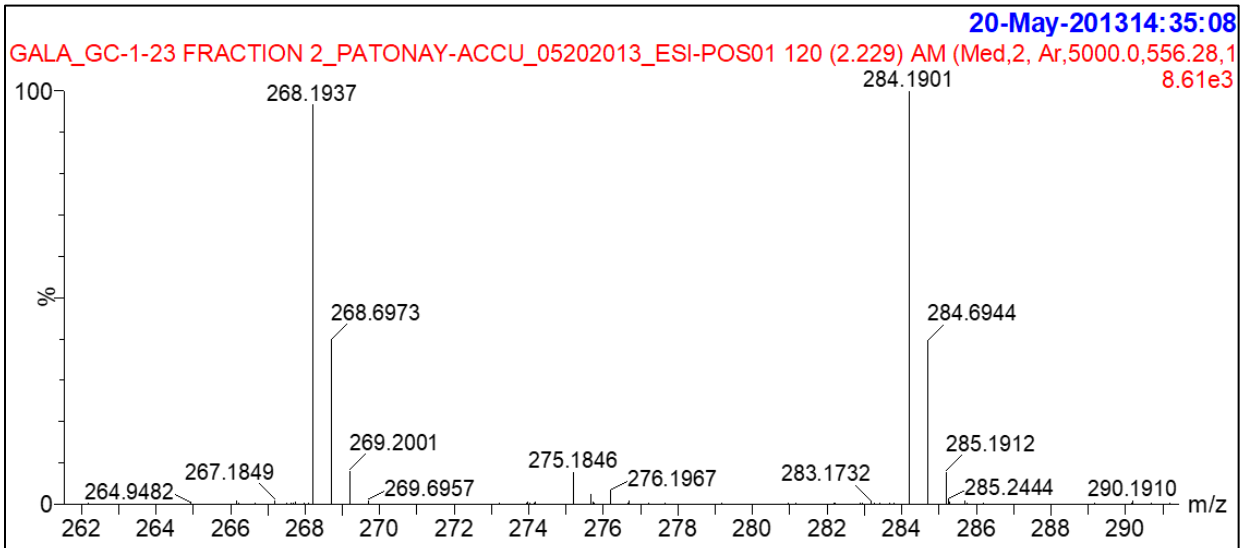

Elemental Composition Report
Single Mass Analysis
Tolerance = 5.0 PPM / DBE: min = -1.5, max = 50.0
Element prediction: Off
Number of isotope peaks used for i-FIT = 3
Monoisotopic Mass, Odd and Even Electron Ions
54 formula(e) evaluated with 2 results within limits (all results (up to 1000) for each mass)
Elements Used:
C: 1-150 H: 1-150 N: 1-30

Minimum:				-1.5		
Maximum:		5.0	5.0	50.0		
Mass	Calc. Mass	mDa	PPM	DBE	i-FIT	Formula
268.1937	268.1939	-0.2	-0.7	8.0	1260.8	C18 H24 N2
	268.1931	0.6	2.2	1.5	16.1	C H18 N17

Figure A.7: HRMS results GC-1-23 (intended aminocyanine product, second eluting blue fraction)

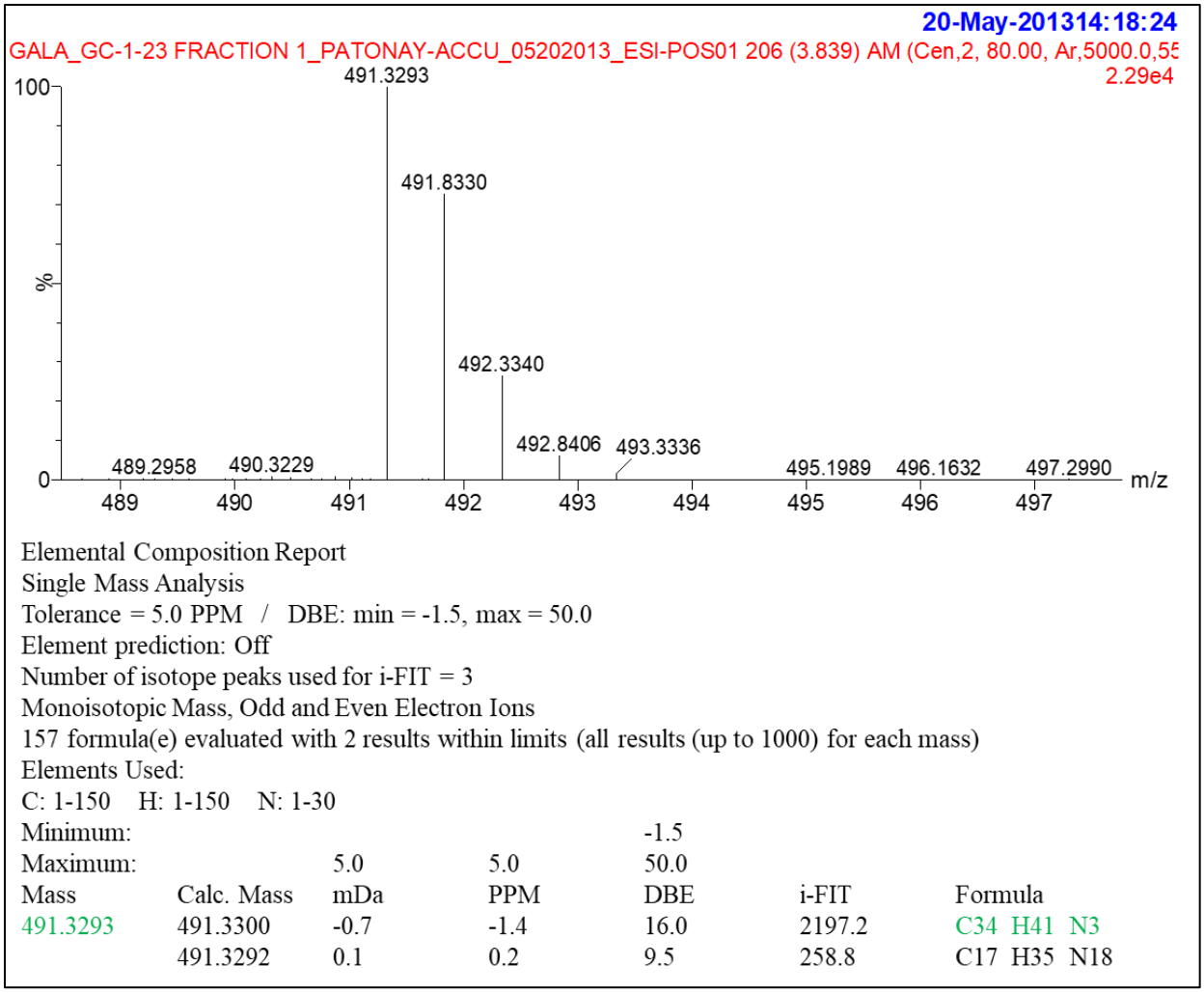

Elemental Composition Report
Single Mass Analysis
Tolerance = 5.0 PPM / DBE: min = -1.5, max = 50.0
Element prediction: Off
Number of isotope peaks used for i-FIT = 3
Monoisotopic Mass, Odd and Even Electron Ions
157 formula(e) evaluated with 2 results within limits (all results (up to 1000) for each mass)
Elements Used:
C: 1-150 H: 1-150 N: 1-30

Minimum:				-1.5		
Maximum:		5.0	5.0	50.0		
Mass	Calc. Mass	mDa	PPM	DBE	i-FIT	Formula
491.3293	491.3300	-0.7	-1.4	16.0	2197.2	C34 H41 N3
	491.3292	0.1	0.2	9.5	258.8	C17 H35 N18

Figure A.8: HRMS results GC-1-24 (bis-cyanine side product, first eluting blue fraction)

Appendix B – Supplementary information to Section 3.3

The content of this appendix is identical to parts of the supplementary material to the manuscript "Chapman, G., Patonay, G. NIR-fluorescent multidye silica nanoparticles with large Stokes shifts for versatile biosensing applications" published in *Journal of Fluorescence* (pre-print). The final authenticated version is available online at https://doi.org/10.1007/s10895-018-02339-z.

Appendix B.1 - Reproducibility of dye incorporation

Reproducibility of dye incorporation during synthesis was assessed by determining dye fluorescence ratios for three parallel syntheses of NPs containing silane conjugates of FITC, TR, and GC-1-23 in respective molar ratios of 1:1:2. The separate batches of NPs were prepared using the same dye-silane stock solutions. Fluorescence ratios were calculated from intensities measured at the wavelengths of maximum emission (λ_{EM}) for the constituent dyes in the NP matrix (512 nm for FITC, 589 nm for TR, and 745 nm for GC-1-23) using a single excitation wavelength (λ_{EXC}) of 450 nm; results are provided in Table B.1.

Table B.1: Batch-to-batch reproducibility of emission wavelength fluorescence intensity (I_F^{λ}) ratios for three concurrent syntheses of 1:1:2 NPs

Intensity Ratio	Ratio Value	%RSD
I_F^{512}/I_F^{589}	0.66 ± 0.015	2.3
I_F^{512}/I_F^{745}	1.09 ± 0.019	1.7
I_F^{589}/I_F^{745}	1.64 ± 0.011	0.67

Appendix B.2 – Dye leaching

The extent of dye leaching was assessed for a NP solution stored in EtOH for 205 days (at 4 °C) containing silane conjugates of FITC, TR, and GC-1-23 in respective molar ratios of

1:1:2. Supernatant was separated from a batch of 1:1:2 NPs and the fluorescence intensities of "whole" NP solution and of supernatant were assessed separately. Supernatant was isolated by running an aliquot of suspended NP solution through an Amicon Ultra centrifugal filter (10,000 Da) at 14,000 g for 20 minutes. The undiluted supernatant was used for fluorescence measurements to ensure a measurable signal. Separately, aliquots of unfiltered NP solution were diluted such that the absorption (A) at the λ_{EXC} was less than 0.1 in order to minimize errors due to the inner filter effect and then fluorescence measurements were acquired. The λ_{EXC} values were 450 nm for FITC, 510 nm for TR, and 650 nm for GC-1-23. Fluorescence intensities were acquired at wavelengths of maximum emission for each dye for both the supernatant and whole NP solution samples. Measured fluorescence intensities were blank subtracted (using EtOH as a blank). The fluorescence of the supernatant was calculated for each constituent dye at its corresponding λ_{EM} as a relative percentage of the total fluorescence of the whole (unfiltered) NP solution and corrected for dilution in order to determine the extent of dye leaching. Results are provided in Table B.2.

Table B.2: Calculated percent dye leakage (%Leach) for each dye component of 1:1:2 NPs after long term storage in ethanol (205 days, 4 °C)

Dye	%Leach
FITC	1.5%
TR	0.046%
GC-1-23	0.033%

Appendix B.3 – Quantum yield of NPs

Quantum yields of dye-silane conjugates and single dye copolymerized NPs in EtOH were determined in triplicate in EtOH as per Equation 2.7. Quantum yield fluorescence samples were prepared such that the total absorption (A) was below 0.1 in order to reduce contributions

from the inner filter effect. Absorption spectra of both blank and dye copolymerized NPs were acquired; the normalized blank NP spectra (Rayleigh scattering) were subtracted from absorption spectra of the dye-containing NPs in order to deconvolute and determine the dye absorption.

Appendix B.4 – Fluorescence enhancement of dye copolymerized NPs

The relative fluorescence signal enhancement was determined for single dye copolymerized NPs relative to their constituent dye-silane conjugates by a comparison of the detection limits (LOD) of each in EtOH. Limits of detection of dye-silane conjugates and corresponding NPs were determined in triplicate in EtOH using Equation B.1.

$$\text{LOD} = k s_{bi} S \tag{B.1}$$

In this equation, $k = 3$ (corresponding to a 3σ detection limit or a confidence level of approximately 90%), s_{bi} is the standard deviation of "blank" solvent measurements (n = 36), and S is the sensitivity or slope of the inverse calibration curve ($S = \Delta C / \Delta I_F$, where C = concentration (M) and I_F = fluorescence intensity at the λ_{EM}). Six point curves were constructed for each material in order to determine S values. The relative signal enhancement was then determined by dividing the calculated limits of detection for the dye-silane conjugates (LOD_{DYE}) by those determined for the dye-containing NPs (LOD_{NP}).

Appendix B.5 – Binding of BPNPs to streptavidin microspheres

Magnetic streptavidin microspheres were washed according to the manufacturer's instructions. The synthesized BPNPs were centrifuged and resuspended in syringe-filtered

phosphate buffer (PB, 11.8 mM, pH 7.4) thrice, with resuspension steps carried out via brief sonication in an ice bath. Following final resuspension, BPNPs were introduced to the washed streptavidin microspheres in excess to ensure binding site saturation (3×10^7 NPs/microsphere), and the reaction mixture was gently agitated at room temperature for 1 h. Following conjugation, a total of five wash steps using PB as wash buffer were employed in order to remove excess BPNPs from the reaction mixture and reduce the likelihood of nonspecific binding. Wash steps were conducted using a 3D printed magnetic separator fitted with neodymium magnets. A 3 min separation time was used; following this time the supernatant was removed, discarded, and replaced with an equivalent volume of fresh buffer. Following washing, the resultant BPNP-microsphere conjugate solution was spotted onto glass slides, outfitted with a coverslip, and left to dry for several hours prior to fluorescence microscopy imaging.

Appendix B.6 – Hemolysis assay

A hemolysis assay was carried out for bare and surface modified (PEGylated) NPs as an assessment of *in vivo* biocompatibility using slight modifications to a method described previously. To summarize, a 1.00 mL sample of human red blood cells (RBCs) from a freshly opened unit were centrifuge washed (500 g for 10 min) three times with 10 mL portions of sterile isotonic phosphate buffered saline (PBS, pH 7.4) and resuspended in 10 mL PBS to prepare an isotonic RBC stock suspension. Separately, three NP samples were washed and resuspended thrice in PBS to a concentration of 2 mg/mL. The representative NP samples studied all had a 1:1:2 dye ratio and differing surface modifications: bare 1:1:2 NPs, mPEG-only 1:1:2 PNPs, and 1:1:2 BPNPs with dual Bio-PEG-Sil and mPEG-Sil surface functionalization. For the surface modified PNPs and BPNPs, the total PEG surface coverage was 40 $\mu mol/m^2$; for the BPNPs, the

percentage of Bio-PEG-Sil was 10% (4 μmol/m^2). To prepare hemolysis study samples, 0.5 mL of the RBC stock suspension was combined with 0.5 mL of each NP sample, resulting in final NP concentrations of 1 mg/mL. Positive and negative controls contained equivalent concentrations of RBCs prepared in deionized water and PBS, respectively. The mixtures were incubated at 37 °C for 90 min with shaking. All samples were first centrifuged at 500 g for 10 min and to remove RBCs, then the collected supernatants were further centrifuged at 15,000 g for 20 min to remove NPs. Absorbance values at 530 nm were acquired for the supernatants obtained after this second centrifugation step in order to assess the percentage of hemolysis. Hemolysis percentage was calculated using Equation B.2. In this equation, A_S is the sample absorbance, A_{NEG} is the absorbance of the negative control, and A_{POS} is the absorbance of the positive (fully hemolyzed) control.

$$\text{Hemolysis } (\%) = \frac{A_S - A_{NEG}}{A_{POS} - A_{NEG}} \times 100\% \qquad \text{(B.2)}$$

Appendix B.7 – Protein adsorption study

A nonspecific binding study of serum proteins on bare and surface modified (PEGylated) NPs was conducted as an additional assessment of *in vivo* biocompatibility using slight modifications to a method described previously. The representative NP samples studied were the same as those listed for the hemolysis study (bare 1:1:2 NPs, mPEG-only 1:1:2 PNPs, and 1:1:2 BPNPs with dual Bio-PEG-Sil and mPEG-Sil surface functionalization). NP samples were prepared in the manner discussed previously for the hemolysis study except the NPs were resuspended to concentrations of 5 mg/mL (to ensure measurable changes in protein absorbance in the assessment of nonspecific binding). Human serum albumin (HSA) and immunoglobulin G

(IgG) were assessed as representative serum proteins for this study; protein stock solutions containing 1.0 mg/mL HSA and 0.90 mg/mL IgG were prepared in PBS. To prepare samples, 0.25 mL of each protein solution was combined with 0.25 mL of each NP solution, briefly mixed, then the samples were incubated at 37 °C for 90 min with shaking. Protein solution blanks were prepared by combining 0.25 mL of protein solution and 0.25 mL PBS. The mixtures were centrifuged (15,000 g for 20 min) and the absorbance of the supernatant was measured at 280 nm. Protein adsorption efficiency was calculated as a weight percent [AE (wt.%)] as described in Equation B.3. In this equation, C_N represents the concentration of NPs (in mg/mL), and C_I and C_F represent the respective initial and final protein concentrations (in mg/mL).

$$\text{AE (wt.\%)} = \frac{C_I - C_F}{C_N} \times 100\% \tag{B.3}$$

Concentrations of protein (in mg/mL) were verified from the absorbance (A) at 280 nm, the solution pathlength (b, in cm), the extinction coefficient (ε, in M^{-1} cm^{-1}), and the molecular weight (MW, in g/mol) as per Equation B.4.

$$\text{C (mg/mL)} = \frac{A}{\varepsilon\, b} \times \text{MW} \tag{B.4}$$